Spring 3-27-2013

Mechanics of blast loading on post-mortem human and surrogate heads in the study of Traumatic Brain Injury (TBI) using experimental and computational approaches

Shailesh Govind Ganpule
University of Nebraska-Lincoln, shailesh@huskers.unl.edu

MECHANICS OF BLAST LOADING ON POST-MORTEM HUMAN AND SURROGATE HEADS IN THE STUDY OF TRAUMATIC BRAIN INJURY (TBI) USING EXPERIMENTAL AND COMPUTATIONAL APPROACHES

by

Shailesh Govind Ganpule

A DISSERTATION

Presented to the Faculty of

The Graduate College at the University of Nebraska

In Partial Fulfillment of Requirements

For the Degree of Doctor of Philosophy

Major: Engineering

Under the Supervision of Professors Namas Chandra and Linxia Gu

Lincoln, Nebraska

March, 2013

MECHANICS OF BLAST LOADING ON POST-MORTEM HUMAN AND SURROGATE HEADS IN THE STUDY OF TRAUMATIC BRAIN INJURY (TBI) USING EXPERIMENTAL AND COMPUTATIONAL APPROACHES

Shailesh Ganpule, Ph.D.

University of Nebraska, 2013

Advisers: Namas Chandra and Linxia Gu

Blast induced neurotrauma (BINT) has been designated as the "signature injury" to warfighters in the recent military conflicts. The occurrence of traumatic brain injury (TBI) in blasts is controversial in the medical and scientific communities because the manifesting symptoms occur without visible injuries. Whether the primary blast waves alone can cause mechanical insult that is comparable to existing traumatic brain injury thresholds is still an open question, and this work is aimed to address this issue.

In the first part of this dissertation, mechanics of primary blast loading on Realistic Explosive Dummy (RED) head with and without helmets is studied using experiments and a validated numerical model. It is shown that geometry of the head and helmet, their configurations and orientations with respect to the direction of the blast govern the flow dynamics around the head; these factors in turn determine the surface pressures. The blast wave can focus under the helmet if there is a gap between the head and the helmet leading to an increase in surface pressures beneath the focused regions.

In the second part of this dissertation, the response of post-mortem human specimen (PMHS) heads is studied. Three PMHS heads are subjected to primary blast of varying peak incident intensities or overpressures (70 kPa, 140 kPa and 200 kPa). When

the incident blast intensity is increased, there is a statistically significant increase in the peak intracranial pressure (ICP) and total impulse ($p<0.05$). Further, for blast overpressures of 140 kPa and 200 kPa, ICP values exceed brain injury thresholds available in the literature based on blunt impacts. From the parametric studies on the validated human head model, it is seen that the wave propagation through skin-skull-brain parenchyma plays prominent role in governing ICP-time histories. The effect of helmets on PMHS head is also analyzed. The results suggest that based only on ICP blast mitigation offered by the current helmets may be marginal, if at all.

Dedicated to,

Aai and Baba

(my parents)

This work was not possible without your tremendous sacrifice for the family

Acknowledgements

I would like to take this opportunity to express my deepest gratitude to my advisor Dr. Namas Chandra. His guidance not only just remained in the professional research but also extended in many issues of life. I am profoundly indebted to Dr. Chandra for teaching me how to do science and for his selfless help throughout my Ph.D. study. I would also like to thank my co-advisor Dr. Linxia Gu for her guidance and supervision while developing computational framework of this work that includes MRI based head modeling and signature blast wave head interaction modeling using Fluid Structure Interaction (FSI). In addition, I also thank her for mentoring my research work from time to time and for her guidance while writing the papers. I would also like to thank my committee members Dr. Reqiang Feng, Dr. Mehrdad Negahban and Dr. Yong Rak Kim for their timely suggestions to improve this research work. I also took many classes with Dr. Reqiang Feng, Dr. Mehrdad Negahban; those classes helped in better conducting this research. In addition, Dr. Feng has provided many insightful guidelines while developing computational framework of this work.

I would also like to thank army research office for providing funding for this research. The research work was not possible without constant monetary support.

The atmosphere at the Trauma Mechanics Research Facility (TMRF), UNL has always been friendly and conducive to research. I would like to thank Aaron Alai, Nick Kleinschmit and Aaron Holmberg for conducting the experiments. I also thank my present and past colleagues Girish Khare, Dr. Guoxin Cao, Aravind Sundaramurthy, Dr. Erwan Plougonven, Veera Selvan, Dr. Maciej Skotak, Dr. Fang Wang. I also thank my

seniors Dr. Ashwani Goel, Dr. Goutam Ghoshal and Alireza Tofangchi for friendship and guidance during my Ph.D. qualifying exams.

My former roommates Apoorva Pandya, Sai Siddhartha Nudurupati, Uday Verma, Chaitanya Pathak, Dhairyashil Aher and Hardik Kundariya have contributed a lot in making my stay in Lincoln enjoyable. I would like to thank all of them.

My grandmother, parents and brother have always been extremely encouraging and accommodative. I can never thank them enough for their love and faith. I also thank my wife Prachi and her family for their encouragement and patience during the final stages of this work.

Contents

List of Figures

List of Tables

CHAPTER 1

INTRODUCTION

1.1 Motivation

Combat-related mild traumatic brain injury (mTBI) and posttraumatic stress disorder (PTSD) are identified as the "signature injuries" of recent conflicts in Iraq and Afghanistan. An estimated 320,000, or 19.5% of all U.S. service members deployed to Iraq and Afghanistan have symptoms related to blast induced neurotrauma (BINT), which accounts for over 92% of all battlefield injuries [1]. Explosive mechanisms (e.g., IEDs, landmines, rocket-propelled grenades) account for 88% of injuries during these operations. The ratio of sustained to fatal injuries (7.37:1) in these conflicts is higher than in any previous military conflict because of use of improved body armor and advances in battlefield medical response and evacuation. Many of those wounded would have died in past wars, and new clinical symptoms, such as those related to blast induced neurotrauma (BINT) are being manifested in this population [1]. Blast not only affects warfighters but also peace retrieving forces (e.g. UN) and other innocent bystanders.

Although invisible to the naked eye, BINT is reported to cause debilitating changes in mood, thought, and behavior. Medical symptoms associated with BINT include migraine headaches, insomnia, blurred vision, dizziness, vertigo, tinnitus, nausea and vomiting with exertion [2]. Other manifestations of BINT include memory and concentration problems, verbal and written language problems, emotional liability and depression, fatigue, light and noise intolerance, anxiety, and irritability [1]. About 5–15% of

individuals with BINT have persistent symptoms that require neurological evaluation and treatment [1]. It is postulated that all of the effects noted above can arise from a single mild blast exposure, though multiple explosions are more likely to be the cause. Simply feeling the blastwave is sufficient to cause injury, even without loss of consciousness [3].

The current literature on BINT in U.S. troops serving in Afghanistan and Iraq suggests conflicting views on its cause, pathophysiology, screening, diagnosis, treatment and care. BINT's lack of external trauma or invisible internal damage often results in BINT going unrecognized, unacknowledged, and underdiagnosed. Many experts have identified BINT as an emerging subspecialty of traumatic brain injury (TBI) [1]. This emerging phenomenon is controversial in the medical and scientific communities because the manifesting symptoms, occurring without external injury or structural damage visible on imaging, are not consistent with current medical knowledge. The scarcity of scientific studies on BINT's prevalence, neuropathophysiology and symptoms make it even more difficult for clinicians in terms of diagnosis, treatment and coordination of care. There is a huge knowledge gap in regards to BINT and opportunity to fill this knowledge gap is vast. While BINT is the likely cause for many field related injuries, direct evidence that pure blast causes mechanical insult to the brain and leads to TBI does not exist in the field; except in very rare circumstances multiple events simultaneously occur.

In this work, we study mechanical insult to the brain due to primary blast waves and investigate potential of primary blast waves alone in causing TBI. We study this phenomenon at macroscopic level using post-mortem human specimen (PMHS) and surrogate head models. By doing this, we hope to answer some of critical scientific

questions regarding BINT and also hope to contribute in generating new knowledge for both understanding the injury and managing the care.

1.2 Goals of the research effort

The overall goal of this research work is to investigate if primary blast causes traumatic brain injury (TBI) of mild or moderate type. Since accurate field data or medical biomarkers are not available, susceptibility to TBI is determined based on tissue level mechanical parameters that exceed acceptable brain injury threshold values. Following objectives are identified to fulfill this goal. The objectives are:

- To identify field conditions, and to accurately replicate such field conditions in the laboratory environment.
- To develop a computational framework that can simulate in field and in laboratory conditions.
- To develop surrogate head models and measurement methods that can accurately predict response of the head under the primary blast loading conditions.
- To understand the response of the surrogate and PMHS heads to primary blast using carefully designed and highly repeatable experiments.
- To quantify mechanical insult to the brain (due to primary blast) on the basis of existing brain injury criteria using experimental data and validated computational models.
- To identify key factors and mechanisms that are responsible for mechanical insult to the brain using experiments and computational models.
- To understand the effect of head orientation on mechanical insult to the brain.

- To study the role of personal protective equipment (PPE) in the mechanical insult experienced by the brain.

In order to achieve those objectives, the following hypotheses are postulated:

- When a blast wave encounters the head helmet complex, the flow field around the head is not uniform. The geometry of the head and the helmet, their configurations and their orientations with respect to the blast govern the flow dynamics around the head, the flow separation and the flow reunion; these factors in turn determine the surface pressures and surface loads.
- The magnitude of surface and intracranial pressures increase with increase in incident blast intensity, duration and impulse.
- Beyond a specific blast intensity, magnitudes of intracranial pressures (ICPs) and shear stresses exceed the available brain injury thresholds based on blunt impacts.
- Geometry and anatomical features of the head play an important roles in blast wave propagation and hence the spatial and temporal distribution of ICP.
- The intracranial response is governed by direct and indirect loads. Direct load is due to the blast wave and indirect load is due to skull deflection.
- With the PPE (i.e. helmet), surface pressures are only marginally reduced. The magnitudes of pressure reductions are statistically insignificant. With the PPE, only partial protection (behind the forehead) is achieved. Even in the presence of helmets, face remains important pathway of energy transfer to the brain.
- For the suspension type helmet, focusing effect accompanies a corresponding increase in intracranial pressure (ICP) beneath those regions.

1.3 Contents of the dissertation

Chapter 2 presents the survey of literature pertaining to various aspects of this dissertation. A review of blast field conditions, available laboratory experiments, computational models and brain injury thresholds is made. This chapter starts off with an overview of Traumatic Brain Injury (TBI) in general and focuses on blast induced traumatic brain injury in particular. This chapter then outlines the field conditions implicated in primary blast. The next part of this chapter reviews various laboratory experiments conducted thus far to understand blunt and blast induced mechanical insult to the brain. This is followed by the description of the three dimensional computational models used to simulate blunt and blast induced head injuries. The next part of this chapter describes brain injury mechanisms and various injury thresholds developed for blunt TBI. Studies conducted to investigate the role of helmets in reducing the risk of TBI are also reviewed. Key observations on the current state of TBI research are summarized in the final section.

Chapter 3 investigates how blast wave evolves inside and near the exit of the shock tube. Various aspects of the flow such as vorticity and subsonic jet wind are studied. How the evolution of the blast wave near the exit of the shock tube affects the loading conditions is also studied.

Chapter 4 describes anatomically accurate and surrogate computational head models developed to study the effect of primary blast. This chapter also describes the development of finite element methodology to simulate blast waves. Here, head models are validated under impact and blast loading conditions.

Chapter 5 describes the experiments on surrogate dummy head. The flow field on the surface of the head with and without PPE is investigated. The effect of orientation on the load experienced on the surface of the head is also studied.

Chapter 6 comprises experimental studies using PMHS heads, where the head is subjected to primary blast of varying intensities. Experiments are described in detail and key experimental results are presented. The results are discussed in conjunction with numerical simulations to address the various hypotheses. The effect of PPE on the mechanical insult to the brain is also investigated.

Chapter 7 describes parametric studies on the key aspects of bTBI conducted using validated numerical models. These aspects include the role of skull deformations, skull thickness and brain material properties on intracranial response. The loading pathways to the brain tissue are also identified.

Chapter 8 on conclusions includes contributions of this research work and recommendations for future work.

CHAPTER 2

LITERATURE REVIEW

2.1 Introduction:

This chapter reviews relevant literature associated with the theme of this dissertation; to understand the mechanics of the blast induced Traumatic Brain Injury (bTBI). In section 2.2, clinical aspects of TBI are discussed. In section 2.3, blast induced traumatic brain injuries (bTBIs) seen in the theatre are described. In order to study bTBI in the laboratory environment it is extremely important to replicate relevant field conditions implicated in bTBI, these field conditions are discussed in section 2.4. Next section of this chapter (i.e. section 2.5) reviews laboratory experiments conducted thus far for impact and blast TBI using PMHS heads. This is followed by a review of finite element human head models of impact and blast TBI in section 2.6. The next section of this chapter (section 2.7) describes mechanisms of TBI; this is followed by section on brain injury criterions (section 2.8). In section 2.9, studies conducted to investigate the role of helmets in reducing risk of TBI are reviewed. The key observations on the current state of TBI research are summarized in the final section on summary (section 2.10).

2.2 Definition, symptoms and care of Traumatic Brain Injury (TBI):

In 1995, the Centers for Disease Control and Prevention (CDC) published Guidelines for Surveillance of Central Nervous System Injury. It defined TBI in terms of ICD-9-CM (International Classification of Diseases, Ninth Revision, Clinical Modification) diagnostic codes [4]. TBI was defined as an occurrence of head injury that is associated

with decreased level of consciousness, amnesia, other neurological or neuropsychological abnormalities, skull fracture, diagnosed intracranial lesions, or death [5]. TBIs may be classified by severity as mild, moderate, or severe. The American Congress of Rehabilitation Medicine has defined mild TBI (mTBI) as a head injury resulting in at least one of the following: (1) loss of consciousness (LOC) for approximately 30 minutes or less; (2) post-traumatic amnesia (PTA) for less than 24 hours; (3) any alteration in mental state at the time of the accident; and (4) focal neurological deficit(s) that may or may not be transient. The 15-point Glasgow Coma Scale defines the severity of injury as mild (13-15), moderate (9-12), severe (3-8), and vegetative states (<3) [6] . A new classification specific to blast related TBI (bTBI) has been also proposed recently, in which a mild bTBI (mbTBI) is characterized by LOC for less than 1 hour and PTA for less than 24 hours following exposure to an explosive blast. Moderate bTBI is characterized by LOC for 1-24 hours and PTA for 1-7 days, and severe bTBI is characterized by LOC for more than 24 hours and PTA for more than 7 days [7]. Mild to moderate cases of bTBI, does not involve skull fracture; other pathophysiological markers in the brain are also well below the detectable levels with current neuro-imaging or serum biomarkers. The vast majority of TBIs in the civilian population are mild; the CDC has reported that up to 75% of TBIs that occur each year are mild [8], and a World Health Organization task force reported that 70-90% of all treated TBI were mild [9]. Mild TBI is typically not associated with abnormalities in brain imaging [10], and most patients with mild TBI recover fully in 4-12 weeks [11, 12]. However, mTBI patients with more severe injuries, such as those who experienced LOC lasting more than 10

minutes or PTA lasting more than 4-6 hours, may require months to years to recuperate [12]. In addition, some mTBI patients develop postconcussive syndrome (PCS), experiencing persistent cognitive, behavioral, and/or somatic symptoms [12-14]. Studies have shown that 15-35% of patients with mildTBI experience onset of above long-term disability [4, 12, 14].

Common symptoms of TBI include a variety of cognitive, behavioral, and physical/somatic changes. Cognitive changes may include disturbances in attention, memory, language, or executive functioning, such as poor planning, organizing, or sequencing, and/or impaired judgment and impulse control [9, 10, 15]. Behavioral changes may include mood changes, depression, anxiety, impulsiveness, emotional outbursts, irritability, or inappropriate laughter [10, 11]. Physical or somatic symptoms may include headaches, fatigue, sleep disturbances, dizziness, problems with motor skills, and sensitivity to light and noise [10, 11]. In addition, following TBI, some patients experience neuropsychiatric problems such as major depression, anxiety disorders, and psychosis [15], and up to 50% of patients with TBI suffer from impaired neuroendocrine function, particularly growth hormone deficiency [11]. For bTBI patients in particular, common symptoms include headache, blurring of vision, transient deafness, and psychoneuroses [16]. bTBI patients are also more likely than other TBI patients to report neurological disorders such as insomnia, impaired concentration, memory loss, and hypervigilance [3, 16].

Some of the symptoms of TBI can be treated by pharmaceuticals. For example, stimulants such as methylphenidate or dextroamphetamine are commonly used to treat

problems with attention or information processing. Selective serotonineuptake inhibitor antidepressants are sometimes prescribed for irritability or angry outbursts, and valproate is often prescribed for migraines and behavioral symptoms [10]. However, there is still lack of broad-based cure for TBI, in large part due to the complex nature of TBI. While a number of pharmacological agents, including calcium channel blockers, corticosteroids, magnesium, N-methyl-D-aspartate (NMDA) receptor antagonists, and progesterone have shown promise in preclinical studies, and some have even had encouraging results in phase II clinical trials, none have demonstrated efficacy in phase III clinical trials thus far [17, 18]. Similarly, no single biomarker of TBI has yet been identified, although it has been suggested that a combination of markers, such as S-1000, neuron specific enolase, glial fibrillary acid protein, myelin basic protein, cl-spectrin breakdown products, NMDA-R fragments, and anti-inflammatory cytokines could effectively detect TBI and predict outcomes [19].

2.3 Blast induced Traumatic Brain Injury (bTBI) in theater:

Traumatic brain injury (TBI) has been a major public health concern in the United States for decades; from 1995 to 2001, an average of 1.4 million Americans a year sustained a TBI, leading to 50,000 deaths, 235,000 hospitalizations, and 1.1 million emergency department visits [20]. Of these, an estimated of 80,000 to 90,000 experienced the onset of long-term disability [4, 20]. These TBIs were largely caused by falls, motor vehicle crashes, sports collisions, and firearm assaults [20].

Since Operation Enduring Freedom (OEF) began in Afghanistan in October 2001 and Operation Iraqi Freedom (OIF) began in Iraq in May 2003, the incidence of TBI among

U.S. service members has been significantly higher. A recent RAND report estimates that 320,000 service members or 20% of the deployed force (total deployed 1.6 million) potentially suffer from TBI [1]. However, out of this population, approximately 60% have never been assessed by a healthcare provider specifically for TBI. Department of Defense (DoD) based on data from 2004 to 2006 at selected military installations has estimated that 10-20% of (the total deployed) OEF/OIF service members potentially sustain mTBI [21]. Other studies also report the occurrence of TBI in OEF/OIF veterans. For example, a recent study has found that 22.8% of soldiers in an Army Brigade Combat Team returning from Iraq had clinically confirmed TBI [22]. A survey of OEF/OIF veterans, who had left combat theaters by September 2004, found that about 12% of the 2,235 respondents reported a history consistent with mTBI [13]. Among those who have been medically evacuated from theater, the proportions who have suffered a TBI is predictably higher. For example, Between January 2003 and February 2007, 29 percent of the patients evacuated from the combat theater to Walter Reed Army Medical Center in Washington, DC, had evidence of a traumatic brain injury (TBI) [23]. Of 50 OEF/OIF veterans treated at the Tampa Veterans Affairs Polytrauma Rehabilitation Center, 80% had incurred combat related TBI, with 70% of the injuries caused by improvised explosive devices (IEDs) [24]. For active duty military personnel in war zones, blasts are the primary cause of TBI [1]. Recent statistics from the conflict in Iraq show that several thousand of active duty United States soldiers have sustained TBI; 69% of these as a result of blasts [3]. Analysis of data collected (collection period: March 2004 and September 2004) from 115 patients from the Navy–Marine Corps that were identified

with TBI, have found that IEDs were the most common mechanism of injury responsible for 52% TBI cases overall [25]. The analysis also showed that intracranial injuries, particularly concussions, were the most common diagnosis category, especially among patients with nonbattle injuries (94%). Although multiple TBI related diagnoses were common, 51% of the patient group had only an intracranial injury with no accompanying head fracture or open wound of the head. It was also found that out of 115 patients analyzed, about 63% of patients were wearing helmet at the time of injury [25]. In addition to data reported above, Department of defense (DoD), in cooperation with the Armed Forces Health Surveillance Center (AFHSC) and Defense and Veterans Brain Injury Center (DVBIC), has consolidated the data of clinically confirmed TBI cases among service members and categorized them based on the severity of injury as shown in figure 1 [26]. mTBI contributes to more than 80% of the total reported brain injuries (Fig. 1) as exposure to repeated low level blasts is a common feature of the war zone personnel/civilian populations. Indeed, blast induced mild traumatic brain injury (bmTBI) has been identified as the signature injury of OEF and OIF [1, 3, 27, 28]. It should also be noted that number of TBI cases reported by DoD [26] are 10 times smaller than that estimated by RAND [1] study. This discrepancy is attributed to methodology used for estimating the numbers. RAND estimates are often based upon the subjective response to non-specific screening questions asked to several hundred individuals and then that resulting percentage was generalized to the entire deployed population. On the contrary DoD estimates are completed based on clinically confirmed TBI cases.

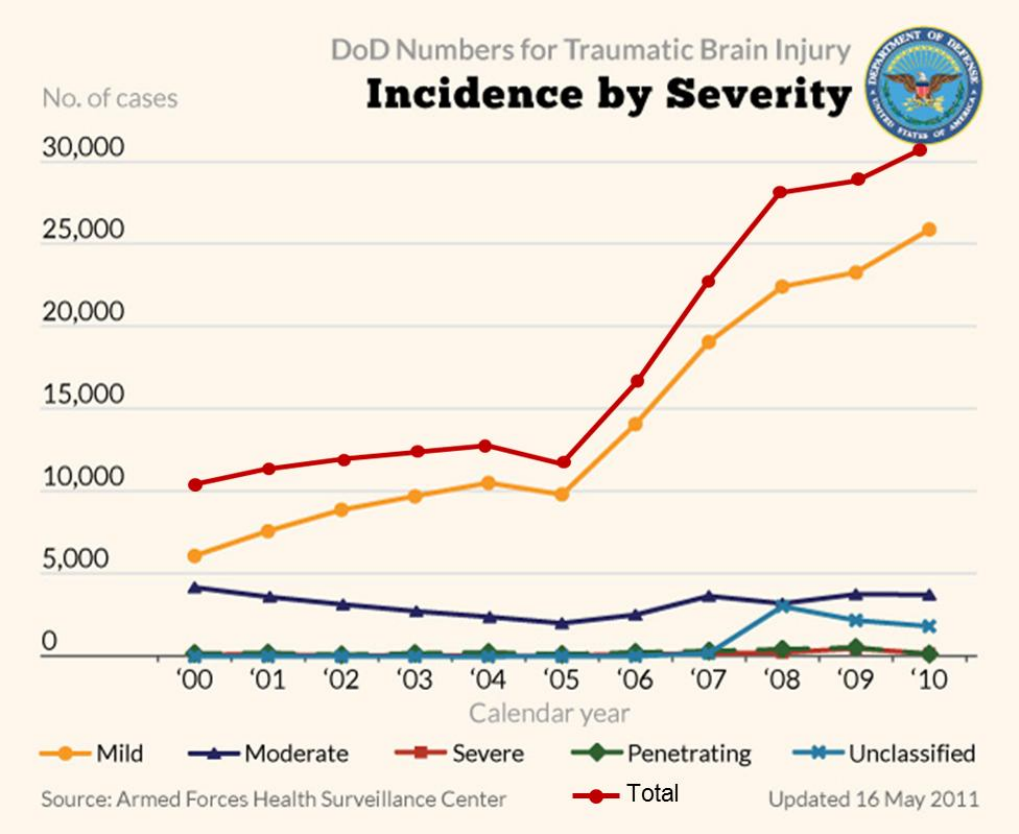

Figure 2.1: Blast Induced TBI in U.S. service members from year 2000 to year 2010 (source: Armed Forces Health Surveillance Center (AFHSC), [26]). These numbers are based on clinically confirmed TBI cases. mTBI contributes to more than 80% of the total reported brain injuries.

Given the high prevalence of TBI among U.S. service members, the cost associated with bTBI are enormous. RAND study estimated that through 2007, the cost of deployment related TBI were between $554 million and $854 million [1]. Final costs are unknown given the uncertainty over the length of the conflict. This trend is expected to continue as the US engages in asymmetric warfare as the new world order develops in the

coming years. One estimate of the financial burden, calculated by Harvard researchers, puts the number at $14 billion over the next 20 years [29].

One reason bTBI is so much widespread is because the current conflicts in Iraq and Afghanistan involve battling insurgents who favor cheap, easily concealed explosive weapons. As a result, approximately 60% of total combat casualties [7] and 67% of Army war zone evacuations [3] have been attributed to explosive blasts. The IED in particular has become the most common explosive weapon [7], accounting for about 40% of all casualties [1]. IEDs can be manufactured from materials ranging from 155 mm artillery shells to plastic explosives to barrels of gasoline [2]; they have evolved from relatively crude devices detonated by simple mechanisms to sophisticated devices capable of penetrating the armor of an M-1 Abrams tank [1]. Exposures to these blasts often lead to the head and neck injuries. For example, 97% of the injuries in one Marine unit in Iraq were due to explosions (65% to IEDs), with 53% involving the head and neck [30]. A study of 4,831 patients at a U.S. Army echelon II medical facility in Iraq between October 1, 2003, and June 30, 2004, found that 88% of U.S military personnel treated had been injured by IEDs or mortars, with up to 47% of those injuries involving the head [31]. According to the Joint Theater Trauma Registry compiled by the U.S. Army Institute of Surgical Research, 22% of wounded OEF/OIF service members who were admitted at the Landstuhl Regional Medical Center in Germany had injuries to the head, face, or neck [10]. Blast-related TBI has also gained visibility due to advances in military medicine and personal protective equipment (PPE) such as body armor that allow U.S. service members to survive blasts that previously would have been fatal. In the current

conflicts, the survival rates are dramatically higher than in previous conflicts. While 30% of wounded U.S. soldiers died in World War II and 24% of wounded U.S. soldiers died in the Vietnam conflict, only about 10% of wounded U.S. soldiers have died in Afghanistan and Iraq [32].

2.4 Field conditions implicated in bTBI:

While studying the mechanics and the mechanisms of bTBI, it is important to accurately reproduce injury causing field conditions. Blast explosions can result in primary (pure blast), secondary (interaction with shrapnel or fragments), tertiary (impact with environmental structures) or/and quaternary (toxic gases) effects [33-35]. At a sufficiently long distance from the source (i.e. in the far field range) only primary or pure blast effects are dominant [36]. It is conjectured that mild to moderate TBI seen in the theatre is due to primary blast effects alone as injuries were non-fatal, with neither head fracture nor open wound [3, 25, 30, 37]. In 2005, the U.S. military reported 10,953 IED attacks, at an average of 30 per day with (Iraq coalition casualty count). As mentioned earlier, these explosions were less fatal with much higher survivability rate than previous wars. Thus, we focus on the effect of primary blast alone.

In this dissertation we focus our attention on mild to moderate TBI and hence pure primary blast loading. Thus, we consider the characteristics of a spherically expanding blast wave formed by the detonation of an explosive (e.g., an uncased C4 of charge weight W). The effects of fireball, ground reflections and other artifacts are not considered as in the far field range of interest these effects are absent [36]. Other types of explosives or IEDs can be directly related to these charges using TNT equivalents. The

impulsive expansion of explosive product initiates first a shock wave propagating spherically outward in the surrounding air and then a family of infinite rarefaction waves propagating in the shock-compressed air. Across the shock front, pressure, density, particle velocity and temperature rise significantly and rapidly in less than a microsecond. As the radial propagation distance *r* increases, the surface area of the spherical shock front increases as r^2 and consequently its intensity decreases as $1/r^2$. The propagation of the shock front is supersonic with respect to the ambient air ahead (upstream) but subsonic with respect to the shocked air behind (downstream); the rarefaction waves remain supersonic with respect to the compressed air ahead (upstream) until the air compression is fully released. The sequential arrivals of the rarefaction waves at a given *r* make the release of shock compression. Hence, in the intermediate to far range of *r*, more and more rarefaction waves catch up the shock front giving rise to erosion of the shock front intensity with *r*, evolving nonlinear decay in overpressure *p* and even a period of underpressure (negative overpressure) afterward. The shock front diminishes eventually at large *r*. Therefore, the *p*–*t* profiles of the blast waves of interest have a shock front with a peak overpressure p^* followed by a nonlinear decay during positive overpressure duration of t^* and then a period of underpressure. This is confirmed through an open field testing conducted by the Trauma Mechanics Research Facility (TMRF) of University of Nebraska-Lincoln (UNL) (TMRF, UNL from here on) in conjunction with Army; this is further corroborated using ConWep [38] (figure 2). In addition, other experimental measurements support this theory [39-41].

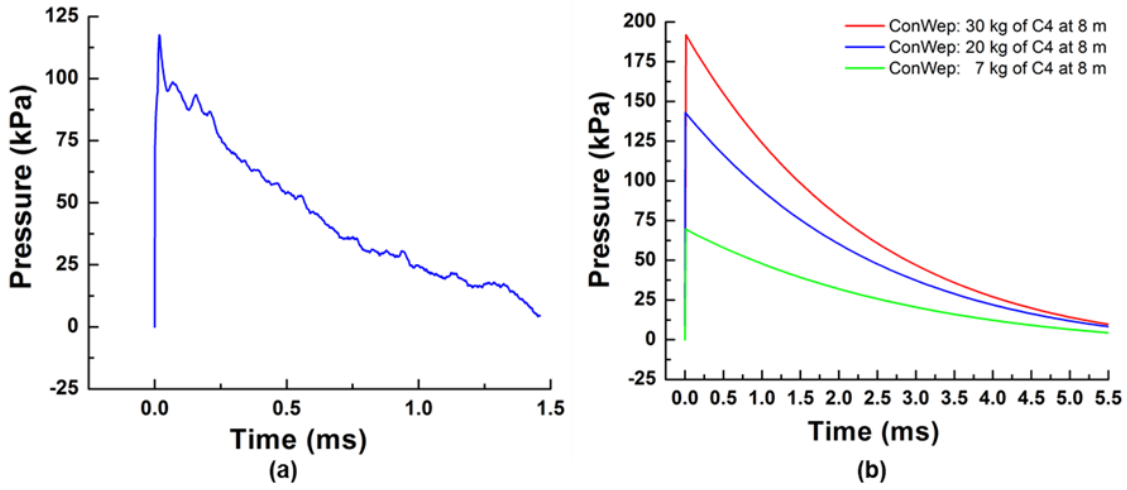

Figure 2.2: Pressure time profiles in a free field explosion: (a) Incident Pressure profiles measured using pencil gauge by a free field explosion of 1.81 kg of C4 @ distance of 2.8 m. The testing was conducted by TMRF, UNL in conjunction with Army. (b) Pressure profiles obtained using Conventional Weapons Effects calculations using ConWep [38]. ConWep profiles are comparable to one generated in our shock tube facility and used in this research; comparison will be shown in chapter 6.

Such *p–t* curves can be mathematically described by the so-called Friedlander waveform [42] given by the following equation.

$$p(t) = p^*(1 - t/t^*)\exp(-bt/t^*) \qquad (2.1)$$

where, *b* is the decay constant.

Friedlander waveform obeys characteristics of open field blast described above. A typical Friedlander wave profile is shown in figure 3. The integration of $p(t)$ over t^* gives the positive impulse per unit area I^*, which is an intuitively more useful alternative to b for a given positive overpressure duration. Hence p^*, t^*, and I^* are the three

independent parameters describing the essential characteristics of positive portions of the blast waves of interest. The ranges of p* and t^* that are of interest for bTBI are postulated to be 50-1000 kPa and 1-8 ms respectively [43]; however precise ranges are not available from the field data. It should be noted that during an actual explosion, the *p–t* curve can be more complex due to ground explosions, reflections from the ground, non-chemical explosives (e.g., delayed fusion, nuclear), or explosives that are cased and contain shrapnel. For the loading conditions relevant to bTBI, it is critical to isolate these as extraneous effects and generate the blast waves with the Friedlander type wave profile.

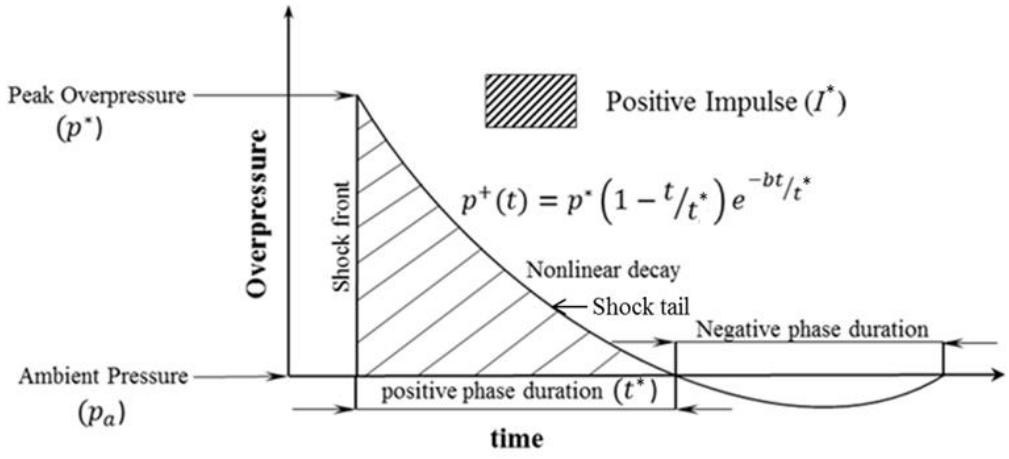

Figure 2.3: Mathematical representation of planar Friedlander waveform. Equation in the figure represents instantaneous overpressure p+ at given time t, where p∗ is the peak overpressure, t* is positive phase duration, I* is positive phase impulse and b is the decay constant.

Another important feature of the open-field blast waves in the intermediate to far range is that the sizes of wave front are much larger than that of a human body. The

interactions of such a blast wave with a human body are influenced strongly by the confinement of an effectively edgeless (no flat top) wave front. This characteristic must be recreated in the testing to realistically simulate field blast loading. As a spherical wave, the strain associated with the blast wave is actually triaxial. The circumferential strain component is given by d/r with d being the particle displacement and thus decreasing with increasing r. For a blast wave with a shock front speed up to Mach 2 (twice the sound speed = 686 m/s) at an ambient temperature of 20 °C, the particle velocity jump across the shock front is less than 429 m/s, the associated d less than 0.5 mm, and the associated circumferential strain component less than 10^{-4} for r beyond 5 m. Compared to 37.5% specific volume reduction (98% true compressive volume strain) across the front of a Mach 2 air shock wave, the circumferential strain component ($<10^{-4}$) is negligible. Therefore, a blast wave in the intermediate to far range can be well approximated with a (uniaxial-strain) planar Friedlander wave, within the ranges of p^*, t^*, and I^*shown in figure 3.

2.5 Experimental investigation of TBI events:

Over the years various researchers have studied the impact and blast TBI using experiments. However, there are only a handful of investigations using PMHS heads due to inherent difficulties in obtaining and testing PMHS. Majority of investigations either use numerical models of the human head (especially in impact TBI) or use experimental rodent animal models (especially in blast TBI). As the focus of this work is the human response, we will only consider PMHS studies. For animal experiments of TBI interested readers can refer to excellent reviews by Goldsmith et al. (impact) [44], O'Connor et al.

[45] and Xiong et al. [46] (blast) and references therein. For experiments using surrogate head models (e.g. spherical shell containing fluid) readers can refer to reviews by Goldsmith and Goldsmith & Monson [44, 47].

PMHS impact studies can be divided into two categories: the first category focuses on skull fracture tolerance or general head motion; and second category analyzes brain deformation and injury; although this division is somewhat arbitrary since early studies often equated skull fracture with brain injury. In this section, we will only consider studies that analyze brain deformation and injury. Cadaver experiments that studied skull fracture and hence severe head injury are not included here.

Nahum et al., in 1976 and 1977, conducted frontal head impact experiments on cadavers [48, 49]. In these experiments, seated, stationary cadavers were impacted by a rigid mass traveling at a constant velocity; the skull was rotated so that the anatomical plane was inclined 45 degrees to the horizontal, and the blow was delivered to the frontal bone in the mid-sagittal plane in an anterior–posterior direction. The cadavers were repressurized to in vivo brain pressure levels and were instrumented with pressure transducers to measure ICPs at five different locations: (1) the frontal bone adjacent to the impact contact area, (2,3) posterior and superior to the coronal and sequamosal sutures, respectively, in the parietal bone, (4) inferior to the lambdoidal suture in the occipital bone and (5) in the occipital bone at the posterior fossa. In addition, accelerations and forces were measured for impactor. For the measurement of head acceleration, accelerometer was mounted on the skull. All the measured data were filtered using 300 Hz 4 pole Butterworth filter. The cadavers were impacted with impactors of

varying masses (5.18 to 23.09 kg) and varying velocities (3.56 to 12.95 m/s). The experiments found high positive peak pressures at the impact site also referred as coup site. The pressure magnitudes decreased as we moved away from the impact site and eventually became negative opposite to the impact site also referred as countercoup site. A linear relationship was found between pressure and (translational) head acceleration. It was also found that rotational (angular) velocity was constant during the experiment resulting in zero rotational acceleration. This was further confirmed from high speed video images that head experienced pure translational motion during the impact event. Comparison of measured ICP and acceleration values with injury severity indices such as GSI and HIC resulted in reasonable correlations. It was however determined that more data points were needed to establish reliable correlations with these indices and therefore severity of injury. The measured ICP values by Nahum has been widely used to validate numerical/FE head models developed to study TBI. These ICP values were later used by Ward et al. [50] to develop brain injury criterion based on ICP values. The ICP based brain injury criterion proposed by Ward et al. [50] is discussed later in this chapter.

In 1992, Trosseille et al. [51] conducted a series of head impact experiments in which repressurized cadavers were hung in a sitting position with a harness and impacted in the anterior–posterior direction [90]. The main goal of the experiments was to produce data for finite element model validation. The cadavers were instrumented to measure input/impactor acceleration, acceleration of the head, intracranial pressures and intracranial accelerations. Data reduction and filtering techniques used were not specified. Intracranial pressures were measured in the frontal, parietal, and occipital

lobes, and for certain tests, in ventricles. In the tests, the impactor had a mass of 23.4 kg, the initial velocity ranged from 5 to 7 m/s. Impact locations included impacts to thorax, forehead and face. Reported intracranial pressure patterns were similar to one seen by Nahum and Smith [48, 49] for most of the tests. Intracranial accelerations varied widely from test to test and even from the sensor to sensor (for a given test) for some of the tests. Authors also recorded significant rotational accelerations (1474-7600 rad/s^2) and comparably less translational accelerations (12-102 G's). This is contrary to Nahum's findings wherein high translational accelerations (120-321 G's for impact velocities in the range of 5 to 7 m/s [49]) and no rotational accelerations were seen [48, 49]. This is probably due to the way cadavers were positioned. In Nahum et al.'s experiments [48, 49] cadavers were stationary with its back secured to a rigid vertical support to prevent gross motion of the upper torso subsequent to the impact event, whereas in Trosseille et al.'s [51] experiments cadavers were hung in a sitting position with a harness. No injuries were reported as a result of the experiments, which generated linear and angular accelerations < 60 G and <4.3 krad/s^2 and a minimum occipital pressure of —30 kPa. Trosseille's [51] experimental results, especially ventricular pressures, have also been used validate numerical head models.

Hardy et al. (2001, 2007) [52, 53] studied response of the PMHS to impact. The main focus of the work was to study the relative motion between the skull and the brain using high-speed biplane x-ray and neutral density technique. In the head impact tests, unembalmed cadaveric specimens were accepted shortly after the death. The head and neck were separated from the cadavers between the third and fourth thoracic vertebrae.

Two columns of five to six neural density targets (NDT's) were implanted in the temporoparietal and occipitoparietal regions. Typically, targets were spaced 10 mm apart. An inverted, repressurized, human cadaver heads were subjected to occipital impacts. A 152-mm diameter impactor with impact velocities ranging from 2 to 4 m/s was used to impact the occipital region. During impact, brain target motion was captured by the x-ray system at 250 frames/second (fps) to examine brain motion under the low-speed impact conditions. The general kinematic response of the head was determined using output from a Wayne State University (WSU) 3-2-2-2 accelerometer array mounted on the apex of the skull. The target data were filtered using a 50 Hz low-pass fourth-order Butterworth profile (SAE pseudo-channel class 30 Hz), and then interpolated to 2000 samples per second. It was shown that during the impact brain and skull experience relative displacement; which in these tests is approximately 5 mm after 20 to 30 ms. However, for first 3-4 ms relative displacement between the skull and the brain was negligible. Relative motion tends to follow looping pattern and this trend is consistent across median, coronal, and horizontal planes. In addition to NDT measurements, Hardy et al., during the second phase of experiments conducted in 2007, also measured intracranial pressures and calculated maximum principal strain, maximum shear strain from NDT measurements [53]. ICP pattern showed classic coup and contrecoup response. They also reported the highest average maximum principal strain of 8.8 %, and the greatest average maximum shear strain of 8.9 %. It was also seen that pressure and strain values did not vary with varying angular accelerations. These experimental results have been used to validate (relative) motion data of numerical models, especially in

impact simulations, where response over larger time interval is studied. However, for blast events relative motion between the skull and brain is likely to be negligible as the time scale of blast event is in the order of 3-10 ms. Other impact experiments using PMHS were mainly focused on head accelerations; some studies report ICP values at one or two locations inside the brain. These studies are not widely used for validation purposes as intracranial response is not extensively studied. However, for the sake of completeness, these studies along with studies described above are summarized in table 2.1. One important aspect that can be easily noticed from table 2.1 is huge variations in the reported data and its relation to injury severity.

Table 2.1: Experimental investigation of impact TBI

Author and year	**Study description**	**Input conditions**	**Reported head kinematics**	**Reported ICP values**	**Main findings**
Nahum et al. (1976) [49]	Impact tests on 10 seated cadavers. The cadavers were impacted with impactors of varying masses (5.18 to 5.38 kg) and varying velocities (3.56	Peak force : 2.9 to 12 kN, Durations: 3-18 ms impact velocities: 3.6 to 9.6 m/s	resultant linear acceleration : 44 to 327 G		Lesions type injuries were produced at linear accelerations of 195 G or more.

	to 9.6 m/s).				
Nahum et al. (1977) [48]	Impact tests on 8 seated cadavers. The cadavers were impacted with impactors of varying masses (5.23 to 23.09 kg) and varying velocities (4.36 to 12.95 m/s).	Peak force : 5.2 to 14.8 kN, impact velocities : 8.4 to 13 m/s	resultant linear acceleration : 155 to 433 G	Peak pressures Frontal: 427 kPa. Parietal: 9 to 221 kPa, and posterior fossa: -65 to -3 kPa.	Comparison of measured ICP and acceleration values with injury severity (as determined from pathologic examination) indices such as GSI and HIC resulted in reasonable correlation but scatter in the data was huge. It was determined that more data points were needed to establish clear relation with any measures and hence severity of injury
Stalnaker et al. (1977) [54]	Impact tests on 15 cadavers seated upright. Cylindrical impactor of	Peak force : 4.2 to 14.6 kN, Durations: 3.2 and 10.6	resultant linear acceleration : 125 to 532 G, peak angular velocities : 12	140 kPa	General agreement between load severity and degree of injury was found but specific

	diameter 152 mm and mass 10 kg and was used to deliver an impact.	ms	to 44 rad/s, and peak angular acceleration: 5.5 and 37.6 krad/s^2		correlations could not be identified due to scatter among a small number of samples. Pressurized heads shown improved coupling between the skull and the brain, suggesting that relative motion between the brain and skull is minimized in vivo.
Nusholtz et al. (1984) [55]	Impact tests on 9 cadavers. Cylindrical impactors of diameter 150 mm and mass of either 25 or 65 kg were used to deliver an impact.	Peak force : 0.8 to 10.2 kN, Durations: 8 to > 50 ms, impact velocities : 3.6 to 5.7 m/s	resultant linear acceleration : 25 and 459 G, peak angular velocities : 18 to 52 rad/s, and peak angular acceleration: 0.8 and 42 krad/s^2	180 kPa in the frontal region and -62 kPa occipital region	While no measured parameters correlated perfectly with injury severity, resultant linear and angular accelerations were the most predictive. Injuries were produced for translational head accelerations >161

					G or rotational head accelerations >7.2 krad/s^2.
Trosseille et al. (1992) [51]	Impact tests on 2 cadavers.	Impactor velocity : 5-7 m/s			No injuries were reported as a result for linear and angular accelerations < 60 G and <4.3 krad/s^2 and a minimum occipital pressure of —30 kPa.
Walsh et al. (1985) [56]	Lateral impacts in 18 cadavers simulating pedestrian contact by an automobile. Some cadavers were also directly impacted by 23.5 kg impactor.	Impactor velocity : 4 m/s	Peak linear accelerations : 60 to 280 G		No correlation between HIC and injury (as coded by AIS) could be found.
Mcintosh et al. (1993)	Impact tests on 17	Impactor velocity :			It was estimated that moderate brain

[57]	cadavers seated upright. Cylindrical impactors of diameter 150 mm and mass 25-28 kgs were used to deliver an impact.	2.8 to 6.1 m/s			injuries can be expected at resultant linear accelerations of 200 G.
Rizzetti et al. (1997) [58]	Impact tests on 14 cadavers with impactor of mass 23 kg and diameter 150 mm.	Peak force : 3.6 to 20 kN, Impactor velocity : 5.3 to 5.8 m/s	Peak linear accelerations: 70 to 92 G for padded impacts and from 130 to 160 G for unpadded impacts.	Contre coup pressures: -20 to -46 kPa	Injuries produced suggest that linear acceleration was more relevant as a severity predictor than rotational acceleration.
Got et al. (1978) [59]	42 free fall tests on fresh cadavers from heights of 1.83, 2.5, and 3 m	Impact force was measured but it was found unreliable.			It was also reported here that there was a minor chance of injury when HIC < 1500. Nahum et al. reported severe injuries with a HIC value as low as 657,

					indicating the enormous variability in reported values depending on the how the input load is imparted to the specimen, specimen condition and specimen preparation.
Hardy et al. (2001,2007) [52, 53]	Impact tests on cadavers. A 152-mm diameter impactor with impact velocities ranging from 2 to 4 m/s was used to impact the occipital region.	Impactor velocity < 4 m/s	peak linear acceleration : 12- 108 G, and peak angular acceleration: 2.5 and 7.5 krad/s^2		Study mainly focused on understanding relative motion between the skull and the brain.

Experimental investigations of blast using PMHS or sub human primates are rare in the literature, since bTBI gained attention only recently. In addition, obtaining and testing

PMHS specimens has become more cumbersome due to stricter government regulations. There are a few reports (mostly in the form of Ph.D. dissertations) from Wayne state University regarding blast studies using PMHS [60-62]. Rafaels et al. [63] from University of Virginia also used PMHS specimens in evaluating the performance of helmets under blast loading but that study was focused on understanding surface pressure response with and without the helmets with little emphasis on ICP. In addition, the test conditions used in Rafaels experiment may not represent pure primary blast.

Wayne state group [60-62] studied response of the PMHS subjected to simulated blast waves using shock tubes. Four cadaver heads were exposed to blast in four different orientations (front, back, right and left sides) at three incident blast intensities (69, 83, and 103 kPa). Unembalmed cadaver heads were placed in an inverted position inside a shock tube and were exposed to a total of fifteen simulated blasts, with changing pressure magnitudes and head orientations. Same test (i.e. same head, orientation and intensity) was never repeated hence statistical variations for a given test cannot be determined. Intracranial pressures (ICP) were measured at four locations in the brain (front, ventricle, parietal and occipital) using fiber optic pressure sensors and strain values were measured at five locations on the skull (frontal, zygomatic, temporal, parietal, and occipital bones) using strain gauges. The results from these studies suggest that the ICP values in the brain were controlled by the structural response dynamics of the coupled skull/brain system. Significant head to head variations in ICP values were seen. It was also suggested that skull flexure has a significant role in determining ICP values. While, there were some similarities between the skull and brain pressure profiles, there were enough differences

and authors suggested that further investigations are needed to thoroughly understand the role of skull deformations in governing ICP values. It was also suggested that the geometry and orientation of the head plays an important role in determining ICP values. Furthermore, results showed that significant ICP values were recorded in the brain even in the absence of a fully functioning vasculature and/or an intact body, refuting thoracic mechanism [64, 65] proposed as a primary mechanism of bTBI.

2.6 Finite element head models:

Given the difficulties associated with conducting experiments on post-mortem human subjects or human volunteers, computational modelling of human head to understand TBI has always been an easier choice. As a result, there are a large number of models reported in the literature over past five decades. The first modeling effort date backs to 1943 when Anzelius developed the first mathematical model of human head [66]. He considered the effect of a blow to a free-floating rigid closed spherical shell with irrotational, inviscid fluid inside. His formulations involved an axisymmetric solution of the wave equation in spherical coordinates. He concluded that the initial velocity input produced a compression wave at the point of impact (coup); however, because the shell was assumed rigid, the effect was instantaneously transmitted to the contrecoup region where a tension wave was simultaneously developed. The collision of the two waves at the center produced large pressure gradients, which was considered the mechanism of damage. Since then, modeling efforts have evolved tremendously; current head models using state of art finite element (FE) methods are solved using very powerful computers. In this section, we will only focus on advanced three dimensional FE models developed over the

years using actual geometry of human head. The models are summarized in Table 2. It should be noted that while referencing the models only original studies/papers describing models are cited; subsequent studies are only cited wherever necessary. For other modeling efforts prior to 1994 readers are referred to the review by Voo et al. [67].

Geometry related aspects:

The early three dimensional models were developed from human atlas [68-72] and included 2 to 3 components (or anatomical structures) of the head [68]. Over the years, the level of complexity was gradually increased and the current finite elements models are state of the art models that are based on CT and MRI images [34, 73-79]. Using CT and MRI images, one can segment the human head to the minute details. However, the use of segmented (anatomical) structures is infructuous since many of the segmented structures do not have the right material models and parameters. The very first 3D head model contained three layered skull [68]; however, in later models the three layered skull was changed to a single layered skull and equivalent modulus was assigned [69-71, 80]. This assumption was justified by citing Hubbard's work [81], who from his three point bending experiments, concluded that homogenous skull material of same total thickness with equivalent modulus responds similar to that of a layered skull material. Over the years, researchers have included various anatomical components, such as scalp/skin, dura, falx, tentorium, pia, subarachnoidal space (includes CSF), sinuses, brain stem, bridging veins and cisterns in order to make head model more anatomically accurate. However, the role of modeling these anatomical components on intracranial response is never extensively studied (in three dimensional setting) nor reported in the literature.

Claessens et al. [82] suggested that detailed modeling of these structures has little influence on the predicted intracranial response. In some investigations, these components were specifically added to evaluate the injury risk by certain type of failure. For example, e.g. Zhou et al. [71] added bridging veins to evaluate rupture risk of bridging veins. They predicted that the bridging veins in the central part of the superior sagittal sinus were at higher risk of rupture due to impact. More recently, Moore et al. segmented the head model into 11 distinct head structures, these structures are: cerebrospinal fluid (CSF), eyes, glia, ventricles, venous sinus, air sinus, muscle, skull, skin/fat, white matter, and gray matter. However most of these 11 structures were described by using just 4 different materials, questioning the validity of this division.

The number of elements modeled in the head models varies from 1110 in Ruan et al.'s [68] model to 6,850,560 in Taylor and Ford's model [79]. In Taylor and Ford's model using very fine grids of 1 mm^3. Shock physics wave code CTH (CTH is a Eulerian finite-volume computer code), was used to solve the head model. Due to excessive number of elements one blast simulation required 31 hours of CPU time using 64 processors on the Sandia National Laboratories Thunderbird computer to integrate out to a time of 2 ms. The average number of elements used by other researchers is around 50,000 (see table 2). The head model was meshed using both solid and shell elements and in some cases one dimensional elements were also used. Typically, linear hexahedral elements or quadratic tetrahedral elements were used to model skin, skull, CSF, brain and face and dura, falx, tentorium. Membranes were modeled with shell elements. In some cases, facial bones

were also modeled using shell elements [71, 73]. Bridging veins, if included, were either modeled using string elements [71] or using beam elements [83].

Modeling of interface between the skull and the brain has always been challenging, especially while matching simulation results to experimental data. Two different approaches have been proposed to model skull-brain interface. In the first approach, skull and brain share common nodes and elements at the skull brain boundary (i.e. interface) were assigned lower shear modulus (mimicking subarachnoid CSF). This approximation has been used by several researchers [68, 71, 84]. An alternative way of modeling the brain-skull interface includes contact algorithms between the brain and the skull. The contact can be defined in different ways ranging from completely fixed (tied) to frictionless sliding. Several parametric studies have been performed, wherein the effects of different interface/contact conditions between the brain and skull have been studied [85-87]. These studies indicate that the impact response of the human head, especially the countercoup pressure is sensitive to the interface modeling condition. The (tangential) sliding with (normal) separation contact algorithm was found to be inadequate for modeling brain-skull interface as the negative pressures seen experimentally in the contrecoup region were not obtained with this algorithm. Instead, with this algorithm, separation occurred between the skull and the brain in countercoup region due to incapability of the algorithm to transfer tensile loads. Tangential sliding with no normal separation and tied contact algorithms allow tensile loads to be transferred and hence negative pressures can be generated in the countercoup region. This is consistent with experimental findings. Kleiven and Hardy [77], from their extensive study on skull-brain

interfaces, found that ICP response is sensitive to the interface conditions (which was consistent with other studies). They also found that relative motion between the brain and the skull is relatively insensitive to interface conditions. Kleiven and Hardy concluded that tied interface provided the best correlation with the experiments [48, 52].

Material models and material parameters used:

Material model of biological tissue is always a challenge since the live tissue is more a liquid than a solid. There are two aspects to material modeling of biological tissues: choice of material model, and the selection of the right material parametric values. Majority of the components of the head model were conventionally modeled as linear, elastic, isotropic materials, expect brain and in a few cases the skull. It should be also be noted that Moore et al. [34] and Nyein et al. [78] modeled all components of the head using equation of state (EOS), presumably due to the limitation of their solver in modeling elasticity. Adaptive Mesh Refinement in Object Oriented C++ (AMROC) and the Eulerian fluid solver were used for simulating blast wave head interactions by these researchers.

Very few studies modeled skull as an elastic-plastic material in order to capture skull fracture [74, 79]. Kang et al. [72] modeled skull as an elastic brittle material capable of fracture. All other head models reported here modeled skull as purely elastic material [68, 71, 73, 75-77, 83, 88].

Earlier head models assumed linear, elastic, isotropic behavior for brain tissue [68, 71], As more experimental data on brain characterization became available, head models favored linear viscoelastic model for shear response and linear elastic model for bulk

response [69, 70, 72, 73, 75, 76, 79, 83]. This is due to the fact that majority of studies of brain characterization were focused on response of brain in shear (see table 3) and hence viscoelastic response of the brain is only available in shear. There is a strong need for viscoelastic characterization of the brain in (unconfined) compression, especially at high frequency ranges. To account for large deformations, some researchers modeled the brain in non-linear setting; however, viscoelastic response/component still remained linear [77, 88]. El-sayed et al. [74] used variational constitutive model for brain tissue. This was developed by them for soft biological tissues. The material response included elastic-plastic and viscoelastic components and included rate effects, shear and porous plasticity, and finite viscoelasticity. However, the motivation behind selection of this model for brain tissue was not provided. In addition, no justification was provided for material parameters selected. Some researchers also modeled brain using equation of state (EOS) most probably due to limitations of the solver [34, 78, 79]. CSF was modeled either as elastic material [68-73, 75, 76, 88] or using EOS [34, 78, 79].

The second important aspect of head modeling is the choice of material parameters for a given tissue, having selected the material model. For skin and the skull reported material parameters are consistent across the studies. However, for brain tissue huge variations in material parameters are seen. The bulk modulus in the order of MPa to GPa has been used in different research works. In the lower ranges, Claessens et al. (0.83 to 83.3 MPa) [86], El Sayed et al. (2.19 MPa) [74], Nahum et al. (4.5 MPa) [48], Belingardi et al. (5.625 MPa) [73], Zoghi-Moghadam and Sadegh (50 MPa) [89] have used values in MPas. Values of the order of GPa have been used by Takhounts et al. (0.56 GPa) [83],

Zhang et al. (2.19 GPa) [69, 70], Kleiven and Hardy (2.1 GPa) [77], Willinger et al. (2.19 GPa, but the bulk modulus of subarachnoid space used was low (0.21 MPa)) [84]. Many of these values were obtained as fitting parameters in computational simulations to match available experimental results of Nahum et al. [48], though some papers quote previous experimental data [90, 91]. Ruan et al. [68] recommended value of bulk modulus between 21.9 to 219 MPa based on parametric studies on three dimensional finite element head model. Nahum et al. [48], Ruan et al. [68], Khalil and Viano [92], Nusholtz et al. [93] have suggested that compressibility of brain tissue and subarachnoidal space (i.e. values of bulk modulus for brain and/or CSF) are critical in accurately predicting intracranial pressures. On the contrary, Horgan et al. [76] suggested that the bulk modulus of the brain has little effect on the predicted intracranial pressures. He suggested that the shear modulus of the brain has very large effect on the predicted intracranial pressures. In this work, widely accepted value of 2.19 GPa is used. However, parametric studies are carried out using different bulk moduli.

Loading and Boundary conditions:

For validation purposes, most of the computational head models simulated the actual experiments conducted by Nahum et al. [48, 49], Trosseille et al. [51] and Hardy et al. [52, 53]. In order to simulate these experiments either actual experiment was replicated in the simulations or experimentally measured input force was applied as a pressure boundary condition. Once validated these models were used for other loading conditions. For example, to simulate head to head football collisions, Zhang et al. applied experimentally measured translational and rotational acceleration profiles at the CG of

the head [80]. For simulating blast loading conditions actual explosion was modeled by Chafi et al. [88] whereas shock tube pressure loading were used by Ganpule et al. [75] and Taylor et al. [79] . For studies where actual explosion was simulated the explosives were modeled using Jones–Wilkins–Lee (JWL) EOS.

Table 2.2: Summary of major three dimensional finite element head models

Author & year	**Model Features**	**Number of Elements**	**Main findings**
Ruan et al. (1994) [68]	Model was developed from brain atlas [68]. Model contained three layered skull (outer table, dipole and inner table), CSF, and brain.	1,110	It was found that compressibility of CSF/subarachnoidal space was critical to accurately match experimental pressures. It was also found that variations in the Young's modulus of the skull and bulk modulus of the brain and CSF affected intracranial pressure response. As the skull stiffness was increased, peak positive ICP in the brain decreased and peak negative ICP in the brain increased.
Zhou et al. (1995) [71]	Ruan's [68] model was modified. Specific modifications include separation of brain into grey and white matter purely based on geometrical	22,995	Model was used to compare response of homogenous and non-homogenous (i.e. containing grey and white matter) brain [71]. It was concluded that while shear stress pattern was different in homogeneous vs. non-homogenous brain the ICP pattern in the brain remains unchanged. Rupture risk of the

	approximations. Other anatomical components like scalp/skin, dura, falx, tentorium, pia, sinuses, brain stem and bridging veins were also added. skull was changed from three layers to single layer to reduce computational time		bridging veins was also evaluated and it was concluded that subdural hematoma could be important injury mechanism. The model was also used to compare brain's response to front and lateral impact [70]. It was concluded that lateral impacts result in larger skull deformation, higher intracranial pressure, and larger shear deformation than frontal impacts.
Zhang et al. (2004) [80]	Zhou's [71] model was remeshed using much finer mesh. Model was extensively validated against available experimental data.	314,500	Model was used to simulate 24 head-to-head football collisions. The model was used to develop injury threshold for mTBI. It was found that the maximum shear stress response at the brainstem provided the strongest correlation with occurrence of mTBI, and a shear stress of 7.8 kPa was proposed as the tolerance level for a 50% probability of sustaining an mTBI.
Kang et al. (1997) [72]	The skull geometry was obtained by digitizing the internal and external surfaces of an adult human skull, and geometry of the brain	13,208	Model was used to replicate a head impact caused by a motorcycle accident; high shear stress regions predicted by the model appeared in good correspondence with actual observed sites of contusion in the right temporal lobe. The model was also used to

	was obtained using data from an anatomical atlas.		simulate 64 real world accidents and brain von Mises stresses of 18 kPa and 38 kPa were proposed as a 50% risk of moderate and severe injuries respectively.
Horgan et al. (2003) [76]	The geometries of the skull and the brain were obtained from CT and MRI images respectively.	Two models were generated with 9,000 elements to 50,000 elements respectively	Based on parametric studies of material parameters it was found that the short-term shear modulus of the brain had large effects on intracranial pressure and von Mises stress, but the bulk modulus of the brain had little effect on either pressure or von Mises response.
Belingardi et al. (2005) [73]	The geometries of the skull and the brain were obtained from CT and MRI images of the patients with brain trauma.	55,264	High shear stresses were seen in the brainstem and corpus callosum.
Kleiven and Hardy (2002) [77]	Model was constructed using medical imaging data from visible human project (VHP)	18,416	The model was used to investigate the effect of head size on impact induced head trauma [94]. It was found that intracranial stresses increase with increasing head size under impact loading conditions.

El Sayed et al. (2008) [74]	Model was developed from MRI images available in Harvard Medical School's whole brain atlas.	39,047	Model was subjected to frontal and oblique (rotational accelerations) impacts. Oblique impact resulted in higher ICP values as well as shear stress than front impact. Shear stress values were up to 10 times higher than those observed during frontal impact.
Takhounts et al. (2003) [83]	Simplified FE head model was developed for use with the Simulated Injury Monitor (SIMon) software package. The skull was assumed to be rigid.	7,852	The head model was subjected to frontal and side impacts using test data from the U.S. National Highway Traffic Safety Administration (NHTSA) database; it was found that the brain experienced greater deformations in side impact tests than frontal impact tests.
Taylor et al. (2009) [79]	The model was constructed from high-resolution photographic data of a cryogenically frozen human female available from the VHP	6,850,560	Model was subjected to a 1.3 MPa incident blast wave for three orientations (front, side and back). Within the head, it was found for all blast orientations that maximum positive ICP occurred at the coup site, closest to the blast source, and negative ICP occurred at the contrecoup site; ICP values of 3-4 MPa at the coup site and -0.8 MPa at the contrecoup site were seen. The highest coup pressures were produced in the side blast scenario. The results of this study thus demonstrated that blasts could lead to the development of

			significant levels of ICPs, and shear stress, possibly contributing to the development of TBI, on a time scale much shorter than that associated with impact event.
Chafi et al. (2010) [88]	The model was developed from head atlas.	27,971	Explosion of 0.0838, 0.205, and 0.5 lbs of TNT at a distance of 0.8 m was simulated. These results demonstrated that blast waves could generate significant levels of pressure prior to any head movement. Based on proposed concussion thresholds in the literature, it was found that the peak ICP values in the 0.5 and 0.205 lb TNT scenarios exceeded the concussion threshold of 235 kPa at the coup and contrecoup sites. The major limitation of this study is that simulated standoff distance was too small and simulation mimics the near field range whree blast wave is non-planar, transient and contains fireball.
Moore et al.(2009) [34]; Nyein et al. (2010) [78]	The model was developed using high resolution medical imaging data obtained from a Montreal Neurological Institute.	743,341	The head model was subjected to frontal blast with incident blast intensities of 0.6 MPa and 3 MPa and later impact of velocity 5 m/s. It was found that blast waves transmit into the brain through cranial cavity. Authors also suggested that geometry of the head plays important role in producing nonuniform

			pressure field inside the brain. From comparison of blast event with impact event it was seen that peak ICP values experienced in the 0.6 MPa blast simulations were mostly similar and equivalent to the 5 m/s lateral impact case. Nyein et al. [78] also evaluated role of ACH padded helmet in blast mitigation. The results suggested that the ACH provided only minimal protection against blasts because it failed to block major pathways of load transmission from the blast to the brain. A more effective blast mitigation strategy in the form of face shield was suggested.
Grujicic et al. (2011) [95]	The model was develped from the CAD model of the head that was purchased from 3DCAD.com.	510,000	The head model was subjected to frontal blast with incident blast intensities of 0.52 MPa and 1.86 MPa. The results suggested that when shock waves interacted with the head, it gave rise to longitudinal and shear waves traveling through the skull and the brain whose propagation and reflections from head boundaries gave rise to very complex spatial distributions and temporal evolutions of stresses within the brain. The Role of ACH padded helmet in blast mitigation was also evaluated. The results suggested that ACH

			provided only partial protection to the brain.
Sharma & Zhang (2011) [96] ; Zhang et al. (2011) [97]	Zhang 's [80] model was used for blast simulations. The blast was simulated using explosion of TNT. Four different blast intensities were simulated.	314,500	The head model was subjected to frontal, backward and lateral blasts of incident blast intensities of 0.21, 0.35, 0.46 and 0.66 MPas. The model results suggested that the pressure wave was directly transmitted into the brain. The highest peak ICP was seen at the coup site in frontal cortex region (values of 0.7-1.8 MPa were seen at coup site as incident blast intensity is increased). The model was further used to evaluate role of ACH padded helmet in blast mitigation. Model results revealed that ACH provides some degree of protection/mitigation at coup site but ICP values remained unaltered for the brainstem and occipital regions. Among three blast loading directions with helmet, the highest reduction in peak intracranial pressures (30%) was seen in backward blast scenario.

Table 2.3: Summary of major experimental studies on brain tissue characterization

Study and year	**Experiment**	**frequency /strain rate**	**strain**	**Brain Matter**
Estes and McElhaney (1970) [98]	constant strain rate test-compression load	0.08, 0.8, 8, 40 s^{-1}	-1 %	human-white mater (in vitro)
Shuck and Advani (1972) [99]	oscillatory shear experiment	5 to 350 Hz	1.3 %	human-white and gray mater (in vitro)
Donnelly and Medige (1997) [100]	constant strain rate test-shear load	30, 60, 90, 120, 180 s^{-1}	0.28–12.5 %	human-white and gray mater (in vitro)
Arbogast et al. (1995) [101]; Arbogast and Margulies (1997,1998) [102, 103]	oscillatory shear experiment, stress relaxation test and constant strain rate test	20–200 Hz	2.5, 5, 7.5 %	porcine-white and gray mater (in vitro)
Bilston et al. (1997,2001) [104, 105]	oscillatory shear experiment and stress relaxation test	0.01–20 Hz 0.055, 0.2335,	0.015–2 % 2000 %	bovine-white mater (in vitro)

		0.947 s^{-1}		
Brands et al. (1999,2000) [106, 107]	oscillatory shear experiment	0.1–16 Hz	0.1-10 %	porcine - gray mater (in vitro)
Miller (1997) [108]; Miller and Chinzei (2002) [109]	constant strain rate test and indentation-compression and tension loads	0.64–64e-7 s^{-1}	–34 to 48 %	porcine- white and gray mater (in vitro and in vivo)
Darvish and Crandall (2001) [110]	oscillatory shear experiment	0.5–200 Hz	1–20 %	bovine - white mater (in vitro)
Lippert, Rang and Grimm (2004) [111]	ultrasonic method -"wave-in-a-tube"	100 kHz - 10 MHz	-	human- white mater (in vitro)
Nicolle et al. (2004,2005) [112, 113]	oscillatory shear experiment and stress relaxation test	0.1–6320 Hz	0.01–10 %	Porcine & human- white and gray mater (in vitro)
Hrapko et al. (2006) [114]	oscillatory shear experiment and stress relaxation test	0.04–16 Hz	1 %	porcine - gray mater (in vitro)
Franceschini et al.	constant strain rate test	5.5–9.3 s^{-1}	–26 to 33.5	human-

(2006) [115]	and creep test- tension and compression loads		%	white and gray mater (in vitro)
Pervin and Chen (2009) [116]	split Hopkinson pressure bar (SHPB)	0.01 to 3000 s^{-1}	70 %	bovine- white and gray mater (in vitro)
Prevost et al. (2011) [117]	unconfined compression under loading/unloading followed by stress relaxation	0.01 to 3000 s^{-1}	50 %	porcine gray/white tissue (in vitro)

2.7 Brain Injury Mechanisms:

There are three main mechanisms of TBI and these mechanisms are: 1) cerebral Contusion 2) Diffuse Axonal Injury (DAI) 3) subdural hematoma. Cerebral contusion (see figure 4 (a)) is a bruise of the brain tissue. Like bruises in other tissues, cerebral contusion can be associated with multiple microhemorrhages, small blood vessel leaks into brain tissue. Cerebral contusions generally occur in coup (behind the site of impact) and countercoup (opposite to site of impact) regions. The cerebral contusion is often associated with volumetric change (i.e. tension and compression) of neuronal cells and corresponding biomechanical parameter used to quantify cerebral contusion is increase in intracranial pressure (ICP). Diffuse axonal injury (DAI) (see figure 4 (b)) occurs due to shearing of axons and small vessels, which in turn, lead to impaired axonal transport and subsequent focal axonal swelling and eventual disconnection of axons. The most common locations for this type of DAI are deep gray matter, gray matter-white matter

interface, internal capsule, upper brainstem and corpus callosum [30]. Shearing strain, shearing stress and von Mises stress are used as a biomechanical parameter for quantifying DAI. Subdural hematoma (see figure 4 (c)) occurs due to tearing of bridging veins. In subdural hematoma, blood gathers within the outermost meningeal layer, between the dura mater, which adheres to the skull, and the arachnoid mater, which envelops the brain. Subdural hematoma is quantified using either increase in ICP or using relative motion between the skull and the brain.

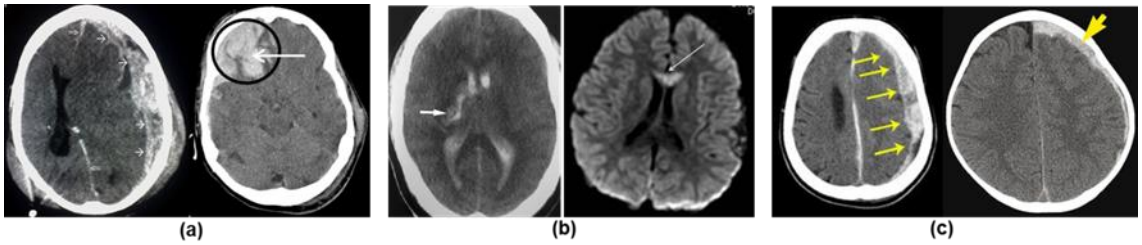

Figure 2.4: Brain injury mechanisms: (a) cerebral Contusion (b) Diffuse Axonal Injury (DAI) (c) subdural hematoma

2.8 Brain Injury Criterions:

Over the last five decades, several brain injury criterions were developed. Different researchers used different mechanical parameters to relate mechanical insult to the degree of injury. The fundamental parameters defining mechanical insult are: head acceleration, strain, intracranial pressure (ICP) and shearing stress. The earlier research into head injury biomechanics used head acceleration as the only criteria to assess head injuries; resultant global acceleration was measured either on the head or on the head protection device (i.e. helmet). As the understanding of head injury biomechanics got better, more sophisticated injury criterions were developed to assess brain injury.

The very first head injury criterion was developed in the form of Wayne State Tolerance Curve (WSTC) [118]. WSTC was developed to understand head injury tolerance in automotive frontal crashes. WSTC was generated by dropping embalmed cadaver heads onto unyielding, flat surfaces, striking the subject on the forehead. WSTC defines nominal tolerance limit on the basis of a peak translational acceleration and duration of impact (figure 5); for example, acceleration of 200g for 3 ms constitutes nominal tolerance limit. While developing WSTC, the onset of skull fracture (rather than brain injury) was used as the basis for injury. Thus WSTC was specifically limited to severe brain injury associated with skull fractures. Gadd Severity Index (GSI) [119] and Head Injury Criteria (HIC) [120] that are derived from WSTC were also used to quantify the brain injury. GSI was proposed by Charles Gadd of General Motors. He hypothesized that weighted integration of acceleration pulse is a better indicator of injury than just peak acceleration. He developed an injury severity index based on this weighted integration of acceleration (also known as weighted impulse); a value of 1,000 was associated with the serious head injury. HIC proposed by National Highway Traffic Safety Administration (NHTSA) is an improved version of GSI; the improvement is based on maximization procedure. NHTSA initially proposed a HIC value of 1000 for 36 ms as nominal tolerance limit, this value was later modified to HIC of 700 for 15 ms. GSI and HIC were also limited to severe brain injury. Most of the head protection standards for automotive impacts were developed based on these three (i.e. WSTC, GSI and HIC) criterions.

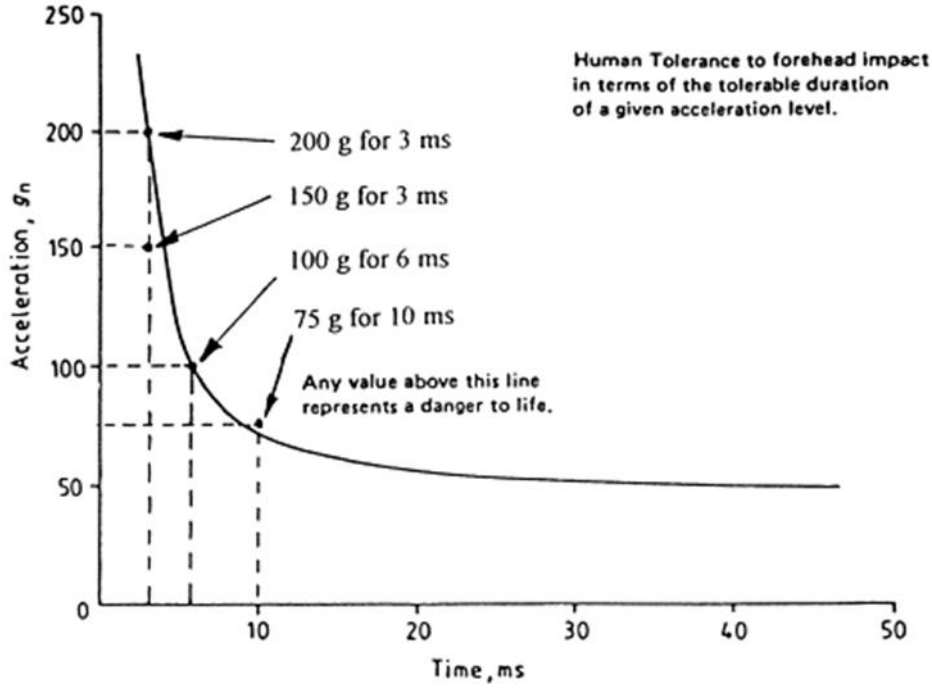

Figure 2.5: Wayne State Tolerance Curve

Over the years, U.S. military has adopted various automotive standards to test their helmets for blunt impact protection. These standards were originally developed as performance requirements for motorcyclists helmets. These standards and corresponding acceleration threshold limits that were used as a pass-fail criteria are listed in table 4. Peak acceleration limit of 300 g was intended to prevent serious head injury only, and does not meant for mTBI. Since blast and possibly many blunt impacts can cause mTBI, Department of Defense is interested in establishing standards for mTBI. In order to account for mTBI, the standard was modified as follows: (1) mean peak acceleration at the C.G. of the headform for all impact sites (orientations) should not exceed 150 G and (2) maximum individual peak acceleration at the C.G. of the headform for all impact sites (orientations) should not exceed 300 G. Neither time duration nor weighted index is used

in the acceptance standard. This new criterion was adopted for U.S. army aviator helmets and currently being used in testing of all other military helmets.

Table 2.4: Protective helmet impact test standards and acceleration thresholds

Reference standard	**Standard developing agency**	**Translational acceleration level (g)**	**Time limit**	**Measurement location**
FMVSS 571.218	U.S. federal Motor Vehicle Safety Standard (motor cycle helmet)	400	peak	At the C.G. of the head
		200	2 ms	
		150	4 ms	
ANSI-Z90.1	American National Standards Institute (ANSI)	300	peak	At the C.G. of the head
Snell M2000	Snell foundation	300	peak	At the C.G. of the head

Injury thresholds for sports (especially American football) related concussions were developed using helmet kinematics and reported concussion data from the field. Helmet kinematics was determined by using a combination of videotapes and accelerometer measurements within a head using head impact telemetry (HIT) system. Table 2.5 shows the summary of football concussion studies over the last 15 years. It should be noted that only studies that contain head injury tolerance limits are considered in the table. The average translational and rotational acceleration tolerance limits are (barring Funk's [121, 122] data) 96 ± 8 g and 5684 ± 630 rad/s^2 respectively. Proposed nominal tolerance limit

for translational acceleration is fairly consistent across the studies whereas large discrepancies are observed in the rotational acceleration limits. Funk's tolerable limits are much higher than other studies (see table 5). Funk, argues that other studies are biased towards concussions, and hence are more conservative. From table 5 it can be seen that out of 502,227 collisions, concussions were reported in 84 collisions only. Forbes et al. [123], from the analysis of most of the reported literature on football concussions, found that while approximately 3 % of collisions exceed mean translational accelerations necessary for the onset of concussion, only about 0.02 % of collisions actually result in a concussion. Based on this observation, he questioned the ability of accelerations alone to reliably predict the incidence of concussion.

Table 2.5: Summary of football concussion studies

Author and year	**Study group**	**Helmet kinematics measurement method**	**No. of impacts**	**No. of concussions**	**Description of injury**	**Mean translational acceleration in g's**	**Mean rotational acceleration (rad/s^2)**	**HIC**
Pellman et al. (2003) [124]	professional football players	videotapes	NA (only concussion cases were studied)	182	50% risk of injury	85	6000	250
					10% risk of injury	45	NR	47
Guskiewicz et al. (2007) [125]	collegiate football players	accelerometers embedded in the helmets	104,714	13	nominal tolerance value	102.8	5311.6	NR
Brolinson et al. (2006) [126]	collegiate football players	HIT	11,604	3	nominal tolerance value	103.3	NR	NR
Funk et al.	collegiate	HIT	37,128	4	10% risk of injury	165	9,000	400

(2012, 2007) [121, 122]	football players							
Rowson et al. (2012) [127]	collegiate football players	HIT	301,034	57	nominal tolerance value	NR	5022	NR
					50% risk of injury	NR	6383	NR
Broglio et al. (2012) [128, 129]	high school football players	HIT	101,994	20	nominal tolerance value	93.6	6,402.6	NR
Total			502,227	84 (~0.02 %)				

Some other researchers have also proposed acceleration based concussive head injury thresholds from experimental studies on sub-human primates. These thresholds are summarized in table 6. Large discrepancies in the reported (tolerable) rotational accelerations are also seen from these studies. Ono's [130] study also highlights the importance of impact duration on tolerable acceleration limit. They proposed two

different tolerable limits based on the duration of impact (220g for 2 ms, 90g for 9 ms). This might also explain difference between Funk's [121, 122] tolerance limits with other studies involving football concussions. No football concussion study considers impact duration while developing tolerable limits.

Table 2.6: Acceleration based injury thresholds from experimental investigations

Study	**Injury type**	**Injury criterion**	**Stated tolerance level**	**Method**
Ono et al. (1980) [130]	Concussive injury	Resultant head acceleration	220 G (for 2 ms) and 90 G (for 9 ms)	Experimental studies on sub-human primates
Gurdjian (1964) [131]	Concussive injury	Resultant head acceleration	90 G	Animal experiments
Ommaya et al. (1971) [132]	50% Probability of concussion	Rotational acceleration	1800 rad/s^2	Experimental studies on sub-human primates
Margulies and Thibault (1992) [133]	Moderate to severe brain injury	Rotational acceleration	16000 rad/s^2	Experimental study on baboon, physical model, analytical simulation

Brain (internal parameters) based injury thresholds:

Stretching of neurons was always believed to be a fundamental mechanism of brain injury due to mechanical insult. Thus strain based injury criterion was always favored in the brain injury literature. Various attempts have been made to quantify brain injury in the form of strain; both at cellular and tissue level. Table 7 summarizes the brain injury thresholds with strain as an injury criterion. It should be noted that value of reported tolerable strain varies from 0.3 % to 38%. The wide range of reported value highlights the dependence of reported strain on the test methodology (tissue, cellular, and organ level testing), testing protocol and rate of loading.

Table 2.7: Strain based injury thresholds for traumatic brain injury

Study	**Injury type**	**Injury criterion**	**Stated tolerance level in % strain**	**Method**
Bain and Meaney (2000) [134]	Severe criterion	Strain to cause functional impairment	13	dynamic stretching of the right optic nerve of an adult male guinea pig
	Optimal criterion		18	
	Liberal criterion		28	
	Severe criterion	Strain to cause morphological damage	14	
	Optimal criterion		21	

	Liberal criterion		34	
Morrison III et al. (2003) [135]	Injury to hippocampal slice cultures	strain	> 10	Dynamic loading on hippocampal slice cultures
Ellis et al. (1995) [136]	injury of astrocytes	strain	31 - mild, 38 - moderate and 51 - severe	Dynamic loading on astrocyte cell cultures to evaluate injury of astrocytes
Deck et al. (2008) [137]	50% probability of mild brain injury	First principal strain	31	finite element reconstruction of motor sports, vehicle, football and pedestrian accidents
	50% probability of severe brain injury		40	
Kleiven (2007) [138]	50% probability of concussion	First principal strain (corpus callosum)	21	Finite element reconstruction of football collisions
		First principal strain (gray	26	

		matter)		
Margulies et al. (1992) [133]	Moderate to severe DAI/brain injury	Strain	5–10	Experimental study on baboon (monkey), physical model and analytical simulation
Stalnaker and Mcelhaney (1970) [139]	Severe brain injury	Maximum strain	0.329	Experiments on human cadaver skull and mathematical analog of skull-brain system

Various researchers have developed brain injury criterion to address specific injury mechanism. Ward et al. [50] developed brain injury criteria based on the occurrence of brain contusion and hemorrhage. It was derived from combined experimental and computational investigations of intracranial pressures and contusions. It was hypothesized that the increase in intracranial pressure is a cause of contusion and hemorrhage. Overall injury severity obtained from the experiments was correlated with intracranial pressures. It was proposed that ICP of 235 kPa will result in severe head injury and ICP of 173 kPa will result in moderate brain injury. Kleiven et al. proposed value 66 kPa (for 50% risk of concussion), based on finite element reconstruction of football collisions. Stalnaker et al. [139] hypothesized that negative ICP is responsible for contusions. Stalnaker et al. [139], from their experiments on sub-human primates, observed severe brain contusions for negative ICP of 68 kPa or more.

Several researchers (see table 8) have developed injury criterions to quantify diffuse axonal injury (DAI); it was hypothesized that shearing of axons cause diffuse axonal damage. Various biomechanical parameters such as shearing stress, von Mises stress, cumulative strain damage measure (CSDM), strain energy density (SED) measure were used to quantify diffuse axonal injury. Cumulative strain damage measure (CSDM) defines brain injury in terms of brain volume exceeding a given strain. CSDM and SED measures are not very popular among head injury researchers due to lack of its correlation with the experiments. Studies involving injury threshold for DAI are summarized in table 8. Viano et al. [140] hypothesized that viscous response of brain tissue is responsible for brain injury (both contusions and DAI); authors however failed to explain the rationale for this hypothesis and its connection to particular damage mechanism. They proposed product (of) strain and strain rate ($\varepsilon \cdot {}^{d\varepsilon}/_{dt}$) as a global parameter for brain injury. Based on the analysis of brain injury data from ferrets subjected to a linear impact they proposed strain of 0.25 and product of strain and strain rate ($\varepsilon \cdot {}^{d\varepsilon}/_{dt}$) of 45 s^{-1} as a nominal tolerance limit. Kleiven et al. (2008) proposed a strain rate value of 10.1 s^{-1} (for 50% risk of concussion), based on finite element reconstruction of football collisions. This measure (i.e. $\varepsilon \cdot {}^{d\varepsilon}/_{dt}$) is also not popular among head injury researchers due to inherent limitations stated above. Relative motion between the skull and the brain is used to quantify subdural hematoma; but injury threshold is not yet available for this type of damage.

Table 2.8: Injury thresholds for diffuse axonal injury

Study	**Injury type**	**Injury criterion**	**Stated tolerance level**	**Method**
Yao et al. (2008) [141]	Severe brain injury (AIS: 3)	von Mises stress	14.8 ± 4.5 kPa	finite element reconstruction of vehicle and pedestrian accidents
		shear stress	7.9 ± 1.6 kPa	
Deck et al. (2008) [137]	50% probability of mild DAI	von Mises stress	26 kPa	finite element reconstruction of motor sports, vehicle, football and pedestrian accidents
	50% Probability of severe DAI	von Mises stress	33 kPa	
Zhang et al. (2004) [80]	50% Probability of mild TBI	Shear stress	7.8 kPa	finite element reconstruction of football collisions
Kang et al. (1997) [72]	Severe TBI	von Mises stress	11–16.5 kPa	finite element reconstruction of motorcycle accident
Anderson et al. (2003) [142]	Severe TBI	von Mises stress	8-16 kPa	experimental and numerical studies on sheep.
Shreiber et al. (1997) [143]	50% probability of DAI	von Mises stress	6-11 kPa	finite element reconstruction of rat model
		Strain energy	0.8-1.9 kJ/m^3	

		density			
Kleiven et al. (2008) [144]	50% probability of DAI/concussion	von Mises stress	8.4 kPa		finite element reconstruction of football collisions
		Strain energy density	2.1 kJ/m^3		
Takhounts et al. (2003) [83]	50% Probability of DAI	Cumulative strain damage measure (CSDM). Defines brain injury in terms of brain volume exceeding given strain.	% volume	% strain	Validated finite element model. These threshold values are based on just observation and lacks statistical basis.
			55	15	
			36	20	
			21	25	
			13	30	
Kleiven et al. (2008) [144]	50% probability of DAI/concussion		47	10	

2.9 Helmets and TBI:

There are very few investigations that have studied the role of helmets in reducing risk of TBI, in impact events. Willinger et al. [145] studied the response of head, with and without helmet, for a frontal impact with velocity of 7.5 m/s. It was found that peak head acceleration was reduced by 20 % with the helmet. It was suggested that von Mises stress values were only slightly reduced with the helmet (but no quantitative data was provided on the reductions) and the stress values in the brain exceeded injury tolerance limit

proposed by Kang et al. [72] even with the helmet. Pinnoji et al. [146] studied response of the head for two types of helmets, namely metal foam helmets and conventional thermoplastics helmets. Response of the helmeted head is studied for a frontal impact with velocity of 7.5 m/s. It was found that for both types of helmets von Mises stress in the brain was within the injury tolerance limit proposed by Kang et al. [72] based on real world accidents reconstructions. This is exactly the opposite to Willinger's [145] finding; both these studies used same input conditions. Pinnoji's study used helmets that were significantly modified to dissipate energy than the one used in Willinger's study. It was also found that von Mises stress in the brain is reduced by approximately 25% in the metal foam helmet as compared to conventional thermoplastic helmet. The metal foam helmet is recommended as it lighter in weight and showed improved performance over conventional thermoplastic helmet. Various researches [78, 95-97] also evaluated the role of padded helmet in blast mitigation. All these studies concluded that padded helmet provides only some degree of protection to the head. Reductions were noticed in coup region while in other areas (e.g. brainstem) the values of ICP, shear stress and strain remained unchanged compared to no helmet case.

2.10 Summary:

In this chapter on literature review, literature relevant to this research work is reviewed. Clinical data clearly indicate that many of the warfighters engaged in recent conflicts in Iraq and Afghanistan suffer from mild to moderate TBI, due to explosion induced blast waves. It is also postulated, in the literature, that field conditions implicated in the primary blast induced TBI (bTBI) are free from secondary, tertiary and quaternary

effects and blast wave profile assumes Friedlander type waveform typically seen in the far field range. The literature on the bTBI is scarce due to lack of evidence of such injury until recently. On the contrary, ample amount of literature is available on impact induced traumatic brain injury. In order to comprehend the state of knowledge of the traumatic brain injury due to mechanical insult both impact and blast TBIs are thoroughly reviewed. The literature survey based on impact induced brain injury suggested that translational and rotational accelerations of the head occurring on a time scales of the order of 30-50 ms are responsible for impact TBI. The injury severity was defined based on PMHS response and for a given severity head accelerations were reported as a tolerance limits. However significant variations exist in reported tolerable head accelerations depending on the test methodology, testing protocol and PMHS condition. The analysis of ICPs showed the coup-countercoup type of pressure pattern inside the brain. However, very few injury threshold limits are available based on ICP as an injury criterion, mainly because acceleration was regarded as a mechanism of injury. Numerical models were also developed to study impact induced TBI. The main challenge for numerical models were proper representation of geometry of the head, correct set of material properties and loading and boundary conditions. While significant progress has been made on the accurate representation of the geometry of the head, accurate material properties of the various tissues of the head still remain a challenge. The numerical models were typically validated against experimental data and further used to establish injury thresholds or to conduct parametric studies. There exist significant variations in the data reported from the numerical models mainly due variations in the geometry,

materials, interface and boundary conditions. The literature survey based on blast induced brain injury suggested that a significant amount of mechanical insult to the brain is possible due to exposure to the blast based on animal experiments and this mechanical insult can cause functional and immunological changes in the animal brain. However, there is still lack of direct evidence of mechanical insult experienced by the brain under primary blast loading conditions, based on PMHS experiments. Computational studies on bTBI suggest that stress wave propagation in the skin-skull-brain parenchyma plays an important role in governing mechanical insult to the brain. It is also suggested that current military helmets provide marginal protection against blast.

CHAPTER 3

EVOLUTION OF BLAST WAVE PROFILES IN SIMULATED AIR BLASTS

3.1 Introduction:

As mentioned in chapter 2, due to the increased use of improvised explosive devices (IEDs) in military conflicts, there has been a major increase in the number of traumatic brain injuries due to the blast waves [147]. A major limitation of the current state of bTBI is the paucity of information on the pathophysiology of BINT [148]. This has led to an increase in blast studies in recent years through animal models, head surrogates and human cadavers using shock tubes [63, 149-160]. In this work the attention is focused on compressed gas (e.g. Helium, Nitrogen) driven air shock tubes, which are extensively used as the standard research tool. The energy to drive the air shock can also be obtained from small explosives [161], [150] as well as combustible fluids like oxy-acetylene [162].While explosives yield higher overpressures, the test specimens will be subjected to smoke and chemical residues. The combustible shock tubes can easily generate high pressures with less kinetic energy; however, varying both overpressure and duration independently is a challenge. In all these research efforts, the effect of sample placement (or discussion of consideration of sample placement) along the length of the shock tube is not critically analyzed. The locations include placement of the sample at various locations inside and outside of the shock tube. Placement of the sample outside the shock tube is preferred by researchers, as typically the dimensions of the sample are equivalent

or larger than the cross sectional dimensions of the shock tube [63, 155]. Or conversely, for a given specimen dimension smaller shock tube can be used. It is known that the pressure profiles continuously change along the length of the shock tube [163], which in turn can change the biomechanical response of the sample (e.g. animal, cadaver) in terms of injury type, severity and lethality. Thus in order to create an accurate representation of a blast wave generated from an IED in the far field range, the sample placement must be carefully considered. It is important to understand blast wave evolution along the length of the shock tube with particular emphasis on the evolution when blast wave exits the shock tube. This issue is critical and addressed in this chapter as proper placement of specimen/test object along the length of the shock tube is needed to ensure that we replicate specified field conditions. The knowledge gained through this analysis is used for developing proper test protocols in studies using dummy and cadaver heads that are essential ingredients of this work. Some of the protocols (i.e. do's and don'ts) on testing and simulation of BINT events using shock tube technique are outlined in this chapter. Many outcomes detailed in this chapter have evolved over time at TMRF, UNL and the author does not stake an exclusive claim.

In a typical free field explosion, a blast wave propagates radially from the source of the explosive. Close to the source of the explosion, the pressure history is turbulent and unpredictable, but further away from the center, the blast wave takes the form of a Friedlander wave [164]. This wave has the characteristics of a shock front followed by a nonlinear decay as shown in figure 3.1. In this work we focus on Friedlander wave (positive phase) implicated in BINT.

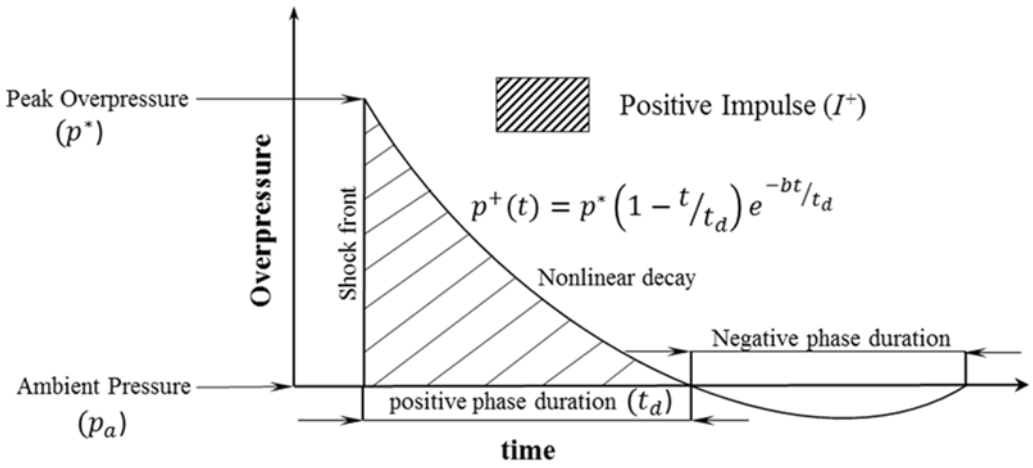

Figure 3.1: Mathematical representation of a planar Friedlander waveform. Equation in the figure represents the instantaneous overpressure p^+ at given time *t*, where p^* is the peak overpressure, t_d is positive phase duration and *b* is decay constant.

3.2 Review of shock tube theory:

Although individual shock tubes for blast wave simulation may have different features for different purposes, the essential wave physics can be understood by analyzing the wave propagation in a generic shock tube configuration as shown in figure 3.2. A typical (compression driven) shock tube consists of a driver section of pressurized gas and a driven section of air at atmospheric pressure with the two sections separated by a set of membranes. When the membranes burst, the driver gas expands rapidly and compresses the atmospheric air (i.e. driven gas) in front to a shocked state, which propagates forward as an air shock wave. Meanwhile, the driver gas expansion initiates a

family of infinite rarefaction waves (expansion fan). These rarefaction waves first travel towards closed end, get reflected at the closed end, and then travel towards open end. Their sequential arrivals at a given location of driven section produce a nonlinear decay (see wave profiles a-c of figure 3.2). The wave profile evolves with propagation distance to that of a Friedlander wave (curve c of figure 3.2) when the fastest rarefaction wave (which is faster than the shock front) catches the shock front at $x = x^*$, where the shock front intensity is eroded the least by the rarefaction waves. Hence, at $x = x^*$, peak overpressure p^* has the maximum value with a Friedlander wave profile. The time for the nonlinear decay to reach $p = 0$ gives overpressure duration t^*, which has the minimum value at $x = x^*$. Before the initial catch-up, $x < x^*$ (curves a and b of figure 3.2) the blast wave assumes a flat-top shape as rarefaction wave reflected from the closed end has not reached shock front yet. The flat-top duration is given by the difference in the arrival times of the shock front and the fastest rarefaction wave. In the range $x^* < x < 0$ where $x = 0$ represents the shock tube exit, more and more rarefaction waves catch up the shock front causing decreasing p^* and increasing t^* with increasing x. The pressure-time (*p*-*t*) profile near (outside) the exit is shown by curve d of figure 3.2; notice that the waveform is changed significantly (low p^*, low t^*, followed by jet wind).

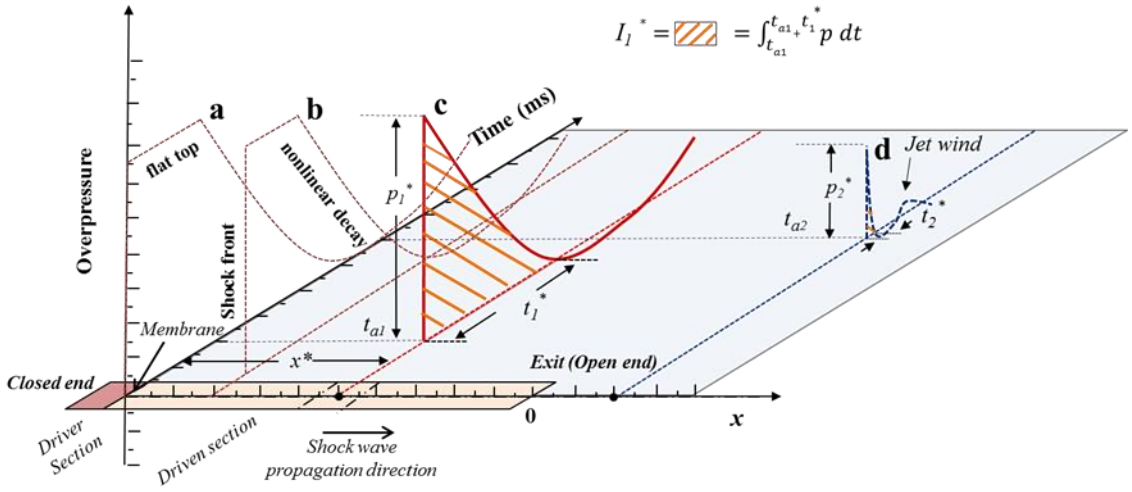

Figure 3.2: Evolution of shock wave in a generic shock tube

Studies on the evolution of the shock wave at the exit or open end have attracted researchers over the years, due to numerous flow phenomena occurring at the exit [165-171]. It is shown in these studies that at the exit of the shock tube, the shock wave evolves from planar to three dimensional spherical with other effects like vortex formation, secondary shock formation, Mach disc, subsonic jet flow, shock-vortex interaction and impulsive noise. All of the above effects may or may not been seen depending on the shock wave strength and geometry of the exit. Most of these studies, however have focused on the flow dynamics aspects with no emphasis on qualitative or quantitative analysis of shock/blast wave profiles (e.g. pressure-time (*p*-*t*) profiles). This becomes particularly important when one wants to use shock tube to generate the desired dynamical mechanical load both in terms of shape and magnitude. Here we focus on the shape and magnitude aspect of pressure time profile (referred as pressure profile/(s) from here on) of blast wave along the length of the shock tube, both inside and outside from

the exit (open end). Such studies of blast waves are important in the basic understanding of shock/blast wave dynamics and in engineering applications (e.g. in the study of blast-structure or blast-human interactions) as well.

3.3 Methods:

3.3.1 Experiments

The shock tube used to generate the blast waves for this study is located at the University of Nebraska-Lincoln's blast wave generation facility [172]. The three main components of the shock tube are the driver, transition and driven sections. The circle-to-square transition is used to change the cross-section of the tube from a circular cylinder (driver section) to a square (driven sections); the square section is a design element to observe events in the test section (which is part of driven section) with high speed video imaging (600, 000 frames per second). The length and diameter of the driver section is 295 mm and 101 mm respectively. The transition is composed of 6.35 mm thick hot rolled steel. It was brake-formed in two pieces and welded together. It has a 5.9-degree taper from the driver to the driven section. This angle is selected so as to minimize turbulence caused by boundary layer separation as the driver is discharged. The driven section has a cross section of 230 mm x 230 mm and the length of 6225 mm (figure 3.3 (a)).

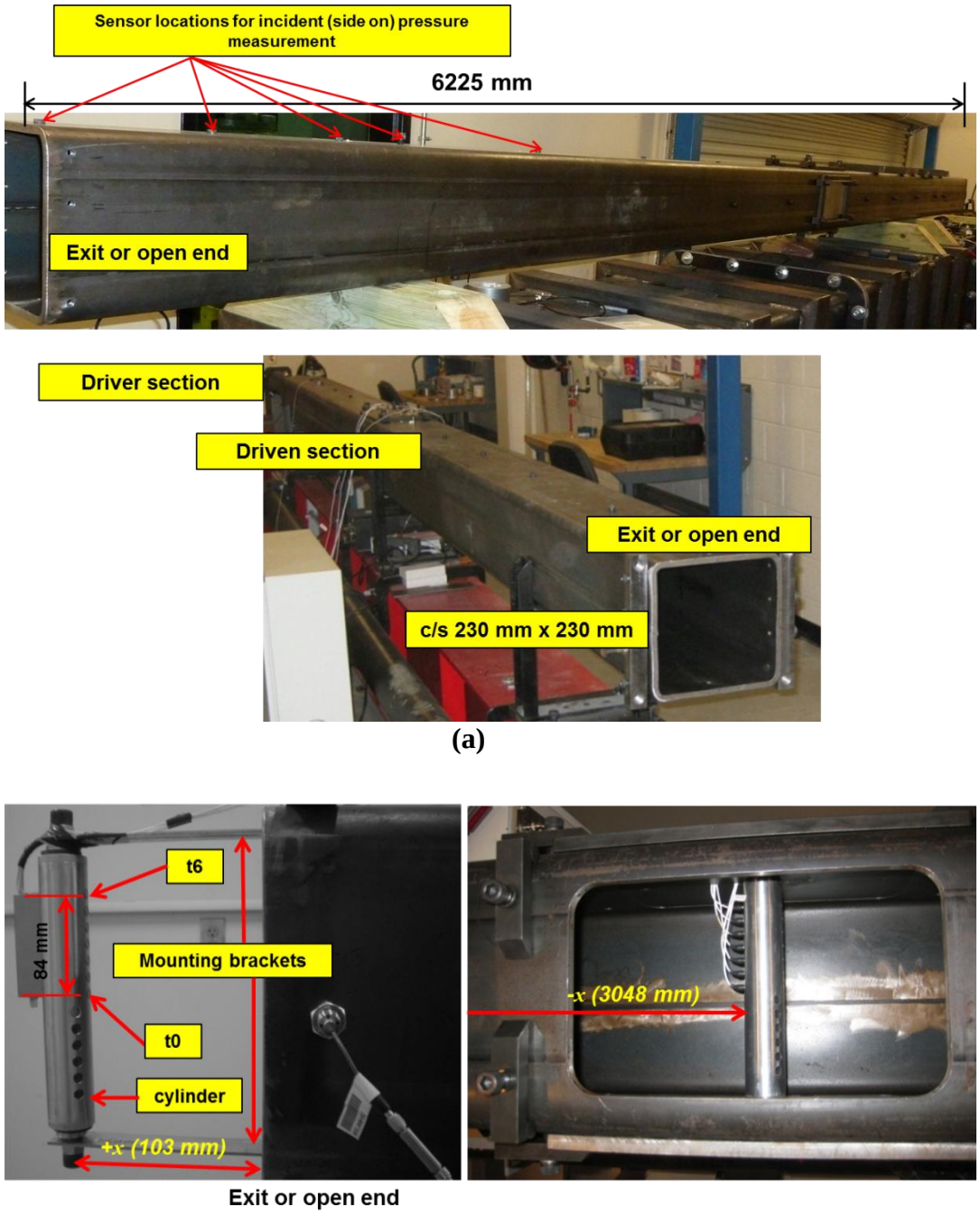

Figure 3.3: (a) Photographs of 230 mm x230 mm square shock tube used in this work. (b) Experimental setup to measure evolution of the shock wave along the length of the

shock tube. Placement of the cylinder at two representative locations along the length of the shock tube is shown.

The unique features of UNL shock tube lies in its ability to produce a range of peak overpressures, durations and impulses that can all be independently controlled within reasonable limits. These are achieved by having variable driver length, placing the test specimens at many selected locations along the driven section (with the ability to capture live videos), and an end plate modifier that can alter the wave profiles. Further wave tailoring is also achieved by using different driver gases and burst pressures (by altering the thickness of the membranes). The working fluid is always air, as the driven gas stays well within a few diameter of the driver. Though the pressure-time profile in this work emphasizes all positive pressures, experiments with negative pressures have been obtained by changing gas pressure, transitions and specimen placements.

In addition to the above, the generation of shock-blast wave profile is affected by a number of tube parameters; length and diameter of the driver; length and diameter of the driven; transition section if the driver and driven are of different shape or size; type of driver and driven fluids and their pressures. In order to obtain higher peak overpressures, one can either increase the burst pressure, or use Helium instead of Nitrogen or air, heat the driver gas or reduce the pressure in the driven section to partial vacuum. Further, when the diameter of the driven is increased, higher driver volume of gas at high pressure is required to reach the same peak overpressure profile. As the driver dimension increases, the location of optimal test location changes based on the driver gas, driver pressure, and the transition design. As the peak overpressure decreases and duration

increases downstream of optimal test location, having a longer length leads to lower peak overpressure and longer duration; however, if the length is too short, then the shock is not fully developed (the rarefaction wave from the driver has not reached the leading edge of the shock) the shock assumes a flat-topped wave shape.

In the patented UNL design, pure pressurized nitrogen was used as the driver gas, and the driven gas was air at ambient laboratory conditions (temperature range of 23° +/- 2° C). The evolution of the blast wave along the length of the shock tube was measured using an aluminum cylinder (length = 230 mm and diameter = 41.3 mm). All the experimental work reported in this chapter has been performed by N. Kleinschmit [173] as a part of his thesis work; however computational work and interpretations forms part of overall work. In order to measure the evolution of the blast wave along the length of the shock tube, the cylinder was placed along the longitudinal axis of the shock tube at various offset distances from the exit (open end) both outside ($+x$) and inside ($-x$) (figure 3.3 (b)). Seven holes were drilled and tapped to locate seven Dytran model 2300V1 piezoelectric pressure sensors used in conjunction with Dytran model 6502 mounting adapters. The location labeled t0 was centered between the two end surfaces of the cylinder, and the rest of the holes were evenly spaced for a total span of 84 mm (figure 3.3 (b)). The cylinder was mounted (i.e. firmly secured) using brackets made out of flat steel bar. In addition to the gauges mounted on the cylinder there were set of gauges (PCB pressure sensor model 134A24) mounted at various locations on the shock tube (along the length) which measure the incident (side-on) pressures (figure 3.3 (a)).

Experiment was repeated three times at each location along the length of the shock tube (N=3).

3.3.2 Computational Modeling

Finite element (FE) based numerical approach is used to depict the experiments and to simulate the flow inside and outside of the shock tube. The numerical techniques like finite element method (FEM) and computational fluid dynamics (CFD) were effectively used to study flow fields at the exit of the shock tube in the past [166-168, 174]. The main goal of the numerical simulation(s) in this chapter is to understand the flow field as the blast wave exits the open end of the square shock tube. The effect is seen not only outside but also inside the tube. Simulations are carried with cylinder placed at various locations inside and outside of the shock tube. An additional simulation is carried out without the cylinder, in order to understand mechanics of the undisturbed flow field.

3.3.2.1 FE discretization:

In our FE modeling, the blast wave propagation and its interaction with the cylinder is treated as a fluid structure interaction (FSI) problem. The air inside and outside of the shock tube is modeled as Eulerian elements and the cylinder and mounting bracket are modeled as Lagrangian elements. Eulerian framework allows for the modeling of highly dynamic events (e.g. shock) which would otherwise induce heavy mesh distortion. The size of the Eulerian domain is 7000 x 5000 x 5000 mm^3. The size of the Eulerian domain is selected such that the reflections from domain boundaries are negligible during total simulation time of interest. This Eulerian domain is meshed with 7,016,115 hexahedral elements. Biased meshing is used to reduce the total number of elements. The cylinder

and mounting brackets are meshed to generate 23,948 hexahedral elements. The experimental pressure boundary condition (i.e. experimentally measured pressure-time (p-*t*) profile deep inside the shock tube) is used as an input for the FE simulations. Figure 3.4 shows the simulation setup (2D section in transverse plane is shown for simplicity). The displacement perpendicular to each face of the shock tube is kept zero in order to avoid escaping/leaking of air through these faces. This will maintain a planar shock front traveling in the longitudinal direction with no lateral flow. In addition, displacement perpendicular to the external boundaries of Eulerian domain is also kept zero in order to avoid escaping/leaking of air through these faces. The tied constraint is used between open end of the shock tube and mounting brackets and cylinder and mounting brackets.

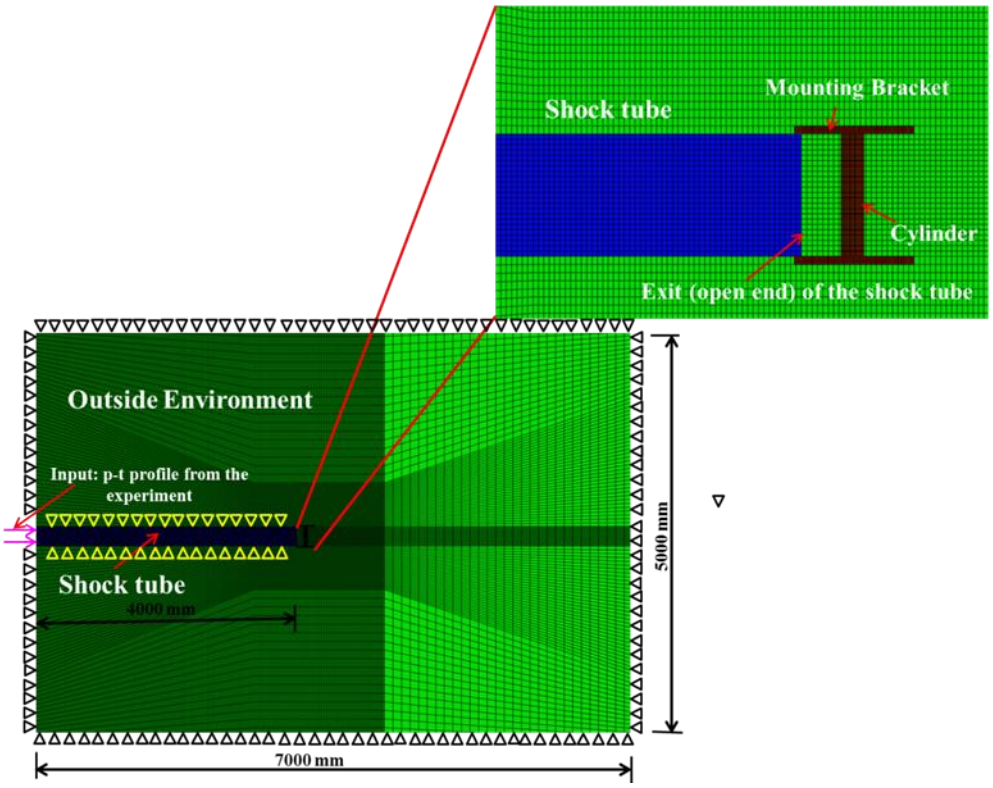

Figure 3.4: Simulation setup. Cut view in transverse plane.

3.3.2.2 Material models:

Air is modeled as an ideal gas equation of state (EOS). The Mach number of the shock front from our experiments is approximately 1.5; hence the ideal gas EOS assumption is acceptable, as the ratio of specific heats do not change drastically at this Mach number. Cylinder and mounting brackets are modeled as linear, elastic, isotropic solids.

3.3.2.3 Solution scheme:

The finite element model is solved using nonlinear transient dynamic procedure with Euler-Lagrangian coupling method (Abaqus®). In this procedure, the governing partial differential equations for the conservation of momentum, mass and energy along with the material constitutive equations and the equations defining the initial and the boundary conditions are solved simultaneously. An enhanced immersed boundary method is used to provide the coupling between the Eulerian and the Lagrangian domains. Here, the Lagrangian region resides fully or partially within the Eulerian region and provides *no-flow* boundary conditions to the fluid in the direction normal to the local surface. Further, the Eulerian region provides the pressure boundary conditions to the Lagrangian region. Thus, a combination of fixed Eulerian mesh and solid-fluid interface modeling through the enhanced immersed boundary method allows for the concurrent simulations of the formation and propagation of a primary blast wave in a fluid medium and accounts for the aerodynamic effects once the blast wave encounters a solid. A typical simulation required about 2 hours of CPU time, run on a dedicated 64 Opteron parallel processors (processor speed 2.2 GHz, 2 GB memory per processor) for an integration time of 20 ms.

3.4 Results and Discussion:

All experimental results presented in this work are for sensor t0, 0° orientation (unless stated otherwise) and are based on average over three shots (N=3) for each placement location. The experimental conditions were selected so that the pressure-time profiles remain positive (all compressive). However, the shock tube is capable of producing negative pressure by selecting shorter driver length and locating specimens close to the driver; the negative pressure effect can be a factor in BTBI, and will be studied in the future. In the current experiments, each shot is well controlled and the experimental measurements are repeatable with only slight variation (<5%) in peak to peak variation in blast over- pressures. Arrival of a shock wave at sensor t0 is set as t=0 for each placement location.

3.4.1 Pressure and impulse profiles along the length of the shock tube:

Figure 3.5 (a) and (b) respectively shows the reflected pressure profiles for cylinder placement locations inside and outside of the shock tube. The reflected pressure measures total pressure (both kinetic and potential energy components) at a given point. The reflected pressure profiles for placement locations inside the shock tube show the gradual decay in pressure and pressure profiles follow the Friedlander waveform. Small secondary peak in pressure profiles is due to reflection from walls of the shock tube; however these wall reflections do not significantly affect pressure profiles. The reflected pressure profiles for placement locations outside the shock tube show rapid pressure decay that do not conform to the Friedlander waveform, shock front and pressure decay rather looks like delta function. This is followed by long duration, relatively constant low

pressure regime (starting points of which are demarcated by cross symbols). This long duration, relatively constant low pressure regime is referred as subsonic jet wind in this work. This jet wind is an artifact of the shock tube exit effect and does not occur in free field blast conditions.

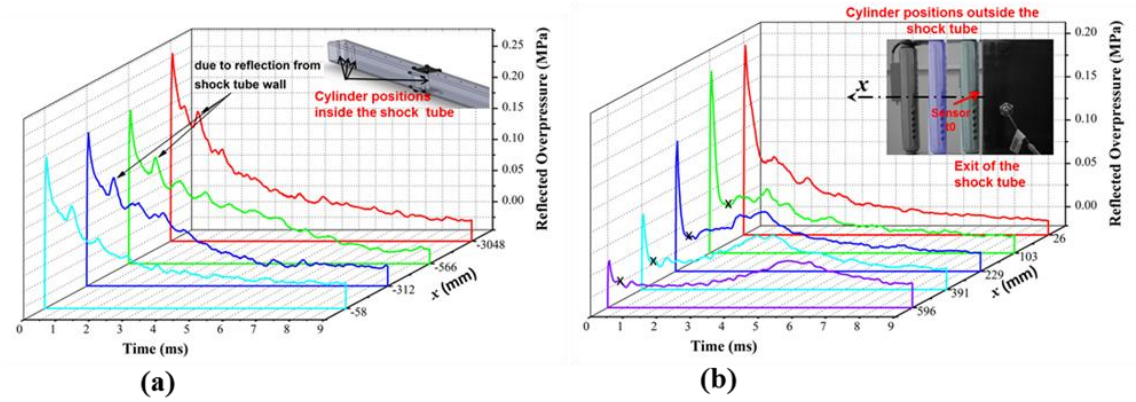

Figure 3.5: (a) Experimentally measured p-t profiles at various x locations inside the shock tube. p-t profiles follow Friedlander waveform fairly well. (b) Experimentally measured p-t profiles at various x locations outside the shock tube. In these profiles the trends do not follow Friedlander waveform and peak overpressure drastically reduces as we move away from the exit. The starting points of subsonic jet wind are demarcated by cross symbols.

Figure 3.6 (a) and (b) respectively shows the impulse profiles for cylinder placement locations inside and outside of the shock tube. The total impulse is reduced significantly for outside placement locations when compared with inside placement locations. The shape of impulse profiles for placement locations inside the shock tube is relatively constant (i.e. gradual increase) as opposed to non-gradual (i.e. with slope changes) for

outside placement locations. The contribution of subsonic jet wind to the impulse is high starting points of which are demarcated by cross symbols.

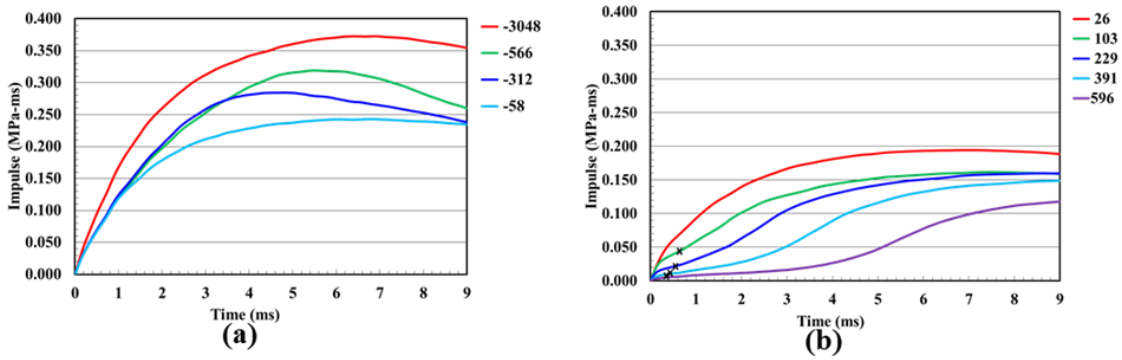

Figure 3.6: (a) Impulse profiles at various *x* locations inside the shock tube obtained by integration of experimentally measured *p-t* profiles. (b) Impulse profiles at various x locations outside the shock tube obtained by integration of experimentally measured p-t profiles. Contribution of the subsonic jet wind to the impulse is demarcated by cross symbols.

3.4.2 Comparison of experiments and numerical simulations:

Figure 3.7 shows the pressure-time (*p-t*) profiles from the shock tube experiments and numerical simulations for sensor t0 for cylinder placement locations inside (566 mm) and outside (26, 103 and 229 mm) of the shock tube. These distances (inside and outside) correspond to possible placements of specimens in experiments; further, these data are also used to analyze for trends and to compare with numerical results. The inside locations correspond to distances, where side-on pressure sensors were already mounted. There is a good agreement between the experiments and numerical simulations in terms of peak overpressures, nonlinear decay and positive phase durations which is also evident

from table 3.1. In general, pressure decay from experiments is faster than that of simulations. The simulations are able to capture majority of the features well, including the shock front rise time, secondary reflections, subsonic jet wind. The arrival of shock wave at sensor t0 from both experiments and simulations is set to zero for ease of comparison of different features of the pressure-time (*p*-*t*) profile. There is a slight difference in arrival times between the experiments and the simulations of the order of 0.3 ms, at most. Difference in arrival time indicates difference in shock wave speed and does not change the pressure and impulse experienced by the cylinder. The difference in arrival time between experiments and simulations can be attributed to the ideal gas equation of state modeling assumption, membrane rupture pattern, friction along the inner wall of the shock tube and misinterpretation of the vibrations of the shock tube itself as pressure readings by the pressure sensors [175]. The structural design at UNL is made extra stiff by the use of 0.5 in steel plates and reinforcing the structure with stiffeners every 18 inches to avoid vibrations. Zhu et al. [175] also found similar differences in arrival times from their experiments and numerical simulations due to the reasons stated above. The similar agreement in pressure-time (*p*-*t*) profiles is observed at other cylinder placement locations and for all other sensors (not shown for brevity).

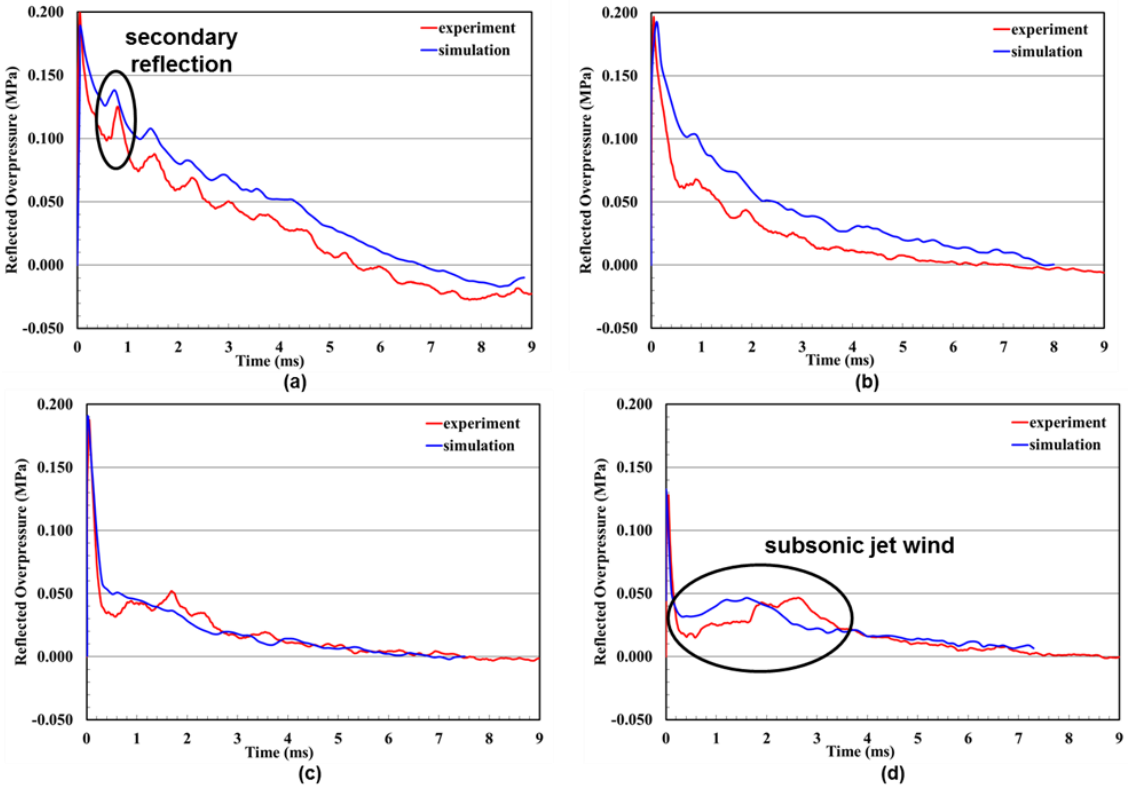

Figure 3.7: Comparison of pressure time history from experiments and simulations for sensor t0 for various cylinder placement locations inside and outside of shock tube: (a) *x*= -566 mm (b) *x*= 26 mm (c) *x*= 103 (d) *x*= 229.

Table 3.1: Comparison of peak overpressures and positive phase durations from experiments and simulations

Cylinder placement location (mm)	Peak overpressure (MPa)			Positive phase duration (ms)		
	experiment	simulation	% difference	experiment	simulation	% difference
x= -566	0.201	0.189	6.09	5.45	6.75	23.85
x= 26	0.198	0.192	3.03	6.06	7.7	27.06

x= 103	0.188	0.186	0.88	6.67	6.81	2.10
x= 229	0.128	0.133	3.77	-	-	-

3.4.3 Analysis of the flow field at the exit of the shock tube:

Flow field at the exit of the shock tube is studied using numerical simulations. No cylinder case is used to study/demonstrate the flow field at the exit that is free from any artifacts created by the cylinder. Figure 3.8 shows the pressure and velocity (vector) fields at the exit of the shock tube (no cylinder case). As the blast wave exits the shock tube, the flow changes from planar to three dimensional spherical (figure 3.8 (a)). Rarefaction wave and vorticities at the corners mix with blast and remaining air ejects as subsonic jet wind; which is evident from velocity vector field of figure 3.8 (b). This jet wind effect is not present deep inside tube. Further, to clearly demonstrate this, figure 3.9 shows the nodal velocities at various locations inside and outside the shock tube. Since fixed Eulerian mesh is used for modeling, velocity at a given mesh node corresponds to the instantaneous velocity of the material point coincident at given time '*t*' with the considered node. High velocity jet wind is recorded in nodal history for locations outside the shock tube. Particle velocity associated with this jet is higher than particle velocity associated with the shock (figure 3.9 (b)). Locations inside the shock tube that are close to the exit also show second peak in velocity due to rarefaction wave moving into the tube but magnitude of this second peak is lower than particle velocity associated with the jet for outside locations. In addition, magnitude of this second peak gradually reduces as

we move inside the shock tube away from the exit (open end). Deep inside the shock tube (x= -3048 mm) second peak is completely absent.

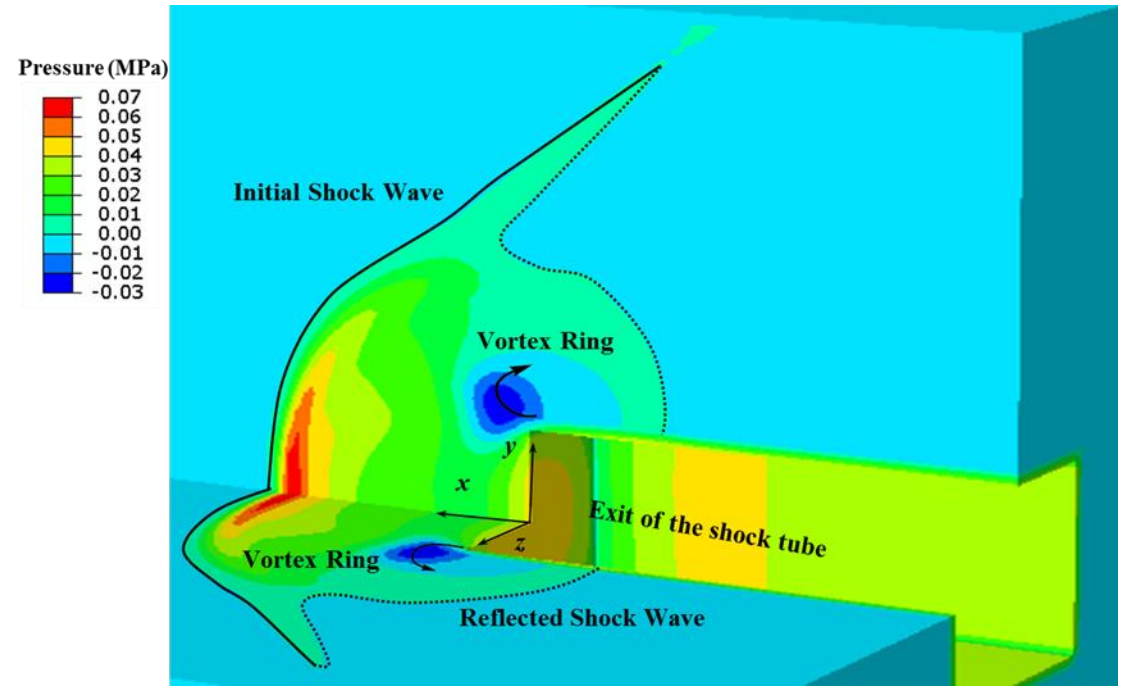

(a)

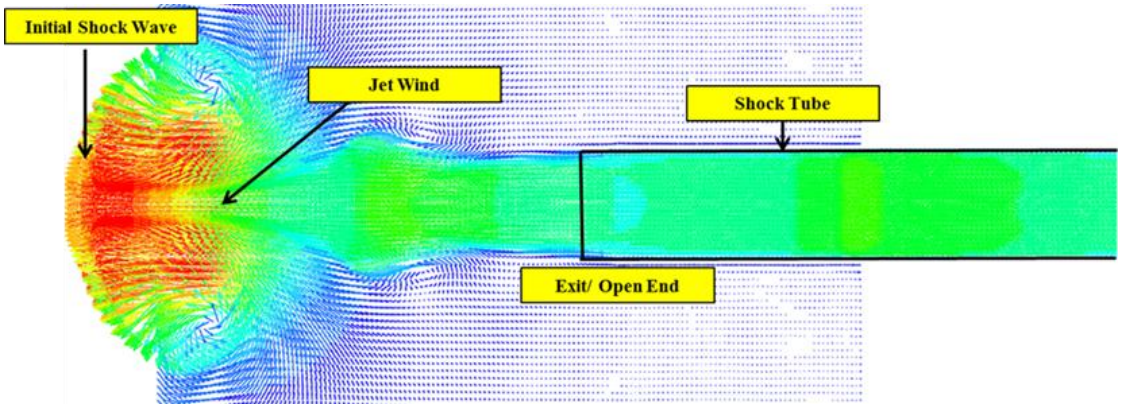

(b)

Figure 3.8: (a) Pressure field near the exit of the shock tube. Three dimensional expansion of shock wave along with vortex formation is seen at the exit. (b) Velocity

vector field near the exit of the shock tube. Jet wind is clearly visible in velocity vector field. Representative vector field is shown; jet is also observed at other locations close to the exit at earlier times.

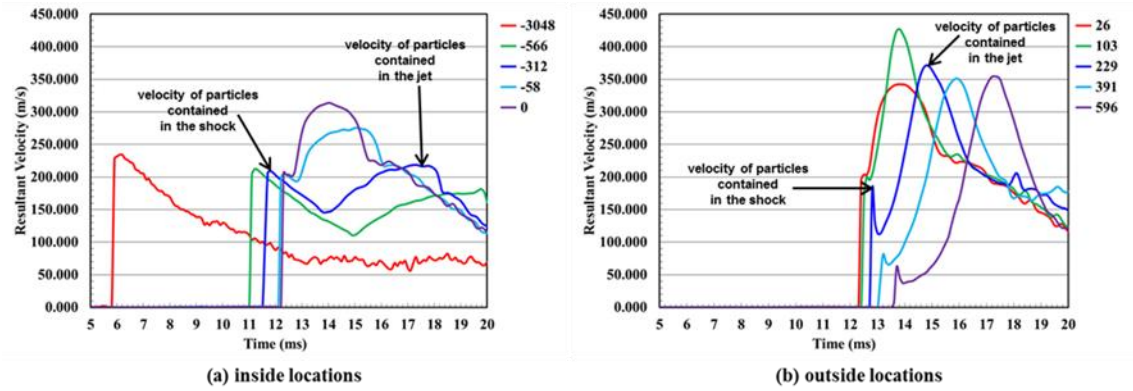

Figure 3.9: Nodal velocities at various locations inside and outside the shock tube. Since fixed Eulerian mesh is used for modeling, velocity at a given mesh node corresponds to the instantaneous velocity of the material point coincident at given time '*t*' with the considered node.

To clearly exhibit transition of blast wave from planar to three dimensional spherical, figure 3.10 shows the pressure distribution at the exit of the shock tube for sequence of times. The black arrows indicate the (velocity) vector field. In each figure outer red contour indicate the primary shock wave and inner green portion indicates primary vortex loop. The primary shock wave at first appears to be square shape with rounded corners as shown in figure 3.10 (i). These corners become significantly rounded and straight parts at the shock tube walls are shortened (figure 3.10 (ii), (iii), (iv)). This indicates that the primary shock wave is planar at the exit (open end) of the shock tube and evolves three dimensionally into spherical one as time elapses. This process is called as shock wave diffraction that affects the flow expansion behind it [168]. Similar arguments can be used

to show the three dimensional nature of primary vortex loop which is evident from green color of figure 3.10.

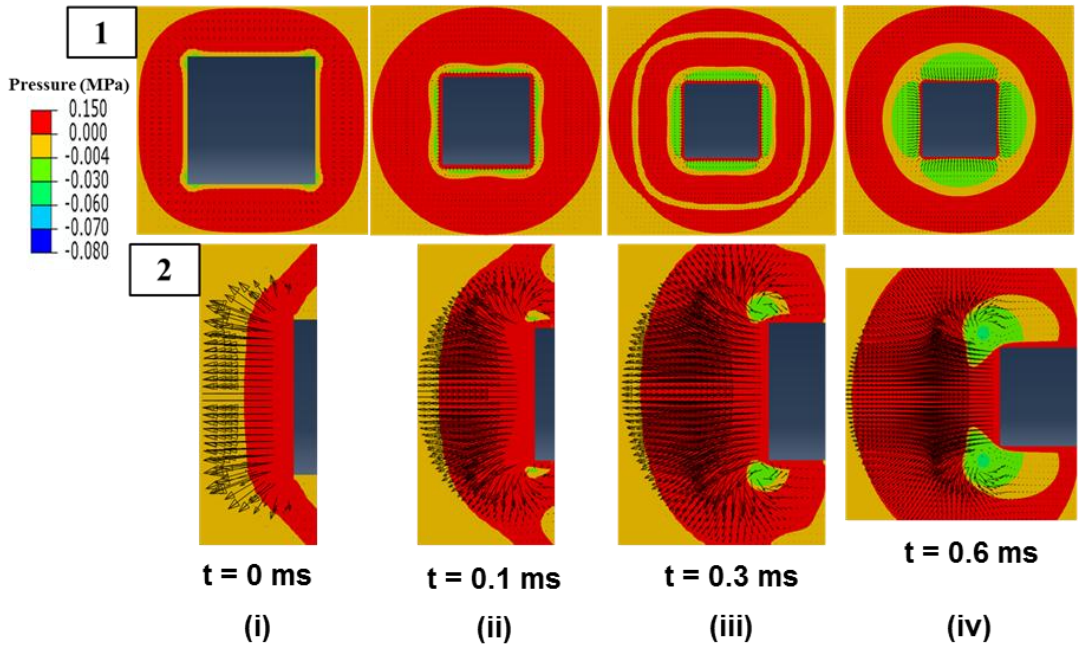

Figure 3.10: Flow fields illustrating physics of shock wave diffraction. Row 1 shows the axial view and row 2 shows the top view. Arrival of shock wave at the exit is marked as t=0.

3.5 Summary:

Shock tubes have been effectively used in the past to generate explosion type loading. In the event of BINT a key question is how to best replicate the field conditions in controlled and repeatable manner. This study has presented the evolution of the blast wave at various locations along the length of the compression driven air shock tube. Some of the key findings of this work are:

- Pressure profiles inside the shock tube follow the Friedlander waveform fairly closely. For locations very close to exit (but inside) the pressure profile is affected by rarefaction wave from the exit. For our shock tube design, optimal pressure profile with minimum artifacts is obtained deep inside the shock tube which happens to be approximately equidistant from the driver and exit (open end) of the shock tube. This location is considered as the best location to conduct BTBI/BINT studies.
- Upon approaching the exit of a shock tube, an expansion wave significantly degrades the measured pressure profiles. The peak pressures and shape of the pressure profiles significantly changes with distance from the exit of the shock tube.
- As the blast wave degrades, the remaining flow is ejected as subsonic jet wind.
- Results from numerical simulations visually indicate the presence of vortices and jet wind of a blast wave upon exiting the shock tube. In addition, nodal velocity histories confirm that particle velocity associated with the jet wind is higher than particle velocity associated with the shock blast.
- Based on these measurements, it is suggested that caution should be used when testing samples outside of the shock tube because of the non-uniformity of the loading in this region and since the majority of the loading comes from subsonic jet wind which is not part of IED primary blasts.

CHAPTER 4

DEVELOPMENT AND VALIDATION OF THREE DIMENSIONAL HUMAN AND DUMMY HEAD MODELS

4.1 Introduction:

In this chapter, we describe the development of MRI based finite element model of human head as well as development of surrogate dummy head model. In addition, computational framework for blast simulations is also described. Finite element (FE) discretization, material models for MRI based human head and surrogate dummy head are described in sections 4.2 and 4.3 respectively. Computational framework for blast simulations based on Euler-Lagrangian coupling is described in section 4.4. Boundary conditions are described in section 4.5 and the method of solution (including method of Euler-Lagrangian coupling) is described in section 4.6. In the next section, validations of both MRI based human head model and surrogate dummy head model are presented (section 4.7). The MRI based head model is validated against impact and blast experiments; validated parameters include surface and intracranial pressures, and surface/skull strains. Surrogate dummy head model is validated using surface pressures. The key observations are summarized in the final section on summary (section 4.8).

4.2 Development of the Head Model

4.2.1 FE discretization:

The three-dimensional human head model is generated from segmentation of high resolution MRI data obtained from the Visible Human Project [176]. The MRI data consists of 192 T1-weighted slices of 256^2 pixels taken at 1 mm intervals in a male head. The image data is segmented into four different tissue types: 1) skin, 2) skull, 3) subarachnoidal space (SAS) and 4) brain (for which material properties are available). Brain includes all important sections: frontal, parietal, temporal and occipital lobes, cerebrum, cerebellum, corpus callosum, thalamus, midbrain and brain stem. It is not possible to separately segment cerebrospinal fluid (CSF) and structures such as membranes and bridging veins due to the resolution of the MRI data; as such they are considered a part of the SAS. The segmentation uses 3D image analysis algorithms (voxel recognition algorithms) implemented in Avizo®. The segmented 3D head model is imported into the meshing software HyperMesh® and is meshed as a triangulated surface mesh. The volume mesh is generated from this surface mesh to generate 10-noded tetrahedrons. Tetrahedron meshing algorithms are robust than hexahedral meshing algorithms, and can model complex head volumes like brain and SAS faster and easier [177-179]. Modified quadratic tetrahedral element (C3D10M) available in Abaqus® is very robust and is as good as hexahedral elements (Abaqus user's manual) as far as accuracy of results is concerned [180-182]. In addition, hexahedral elements can suffer from the problem of volumetric locking for highly incompressible materials like brain. The problem of volumetric locking is not present for modified quadratic tetrahedral element (C3D10M) (Abaqus user's manual). Due to these reasons we chose modified quadratic tetrahedral element. The use of specialized 3D image processing (Avizo®) and

meshing software (HyperMesh®) allowed for the development of a geometrically accurate FE model. Table 4.1 shows the number of nodes, number of elements and element types for each component of the FE model. FE discretization is schematically shown in figure 4.1. While simulating blast events, hybrid III neck is also added to current FE model.

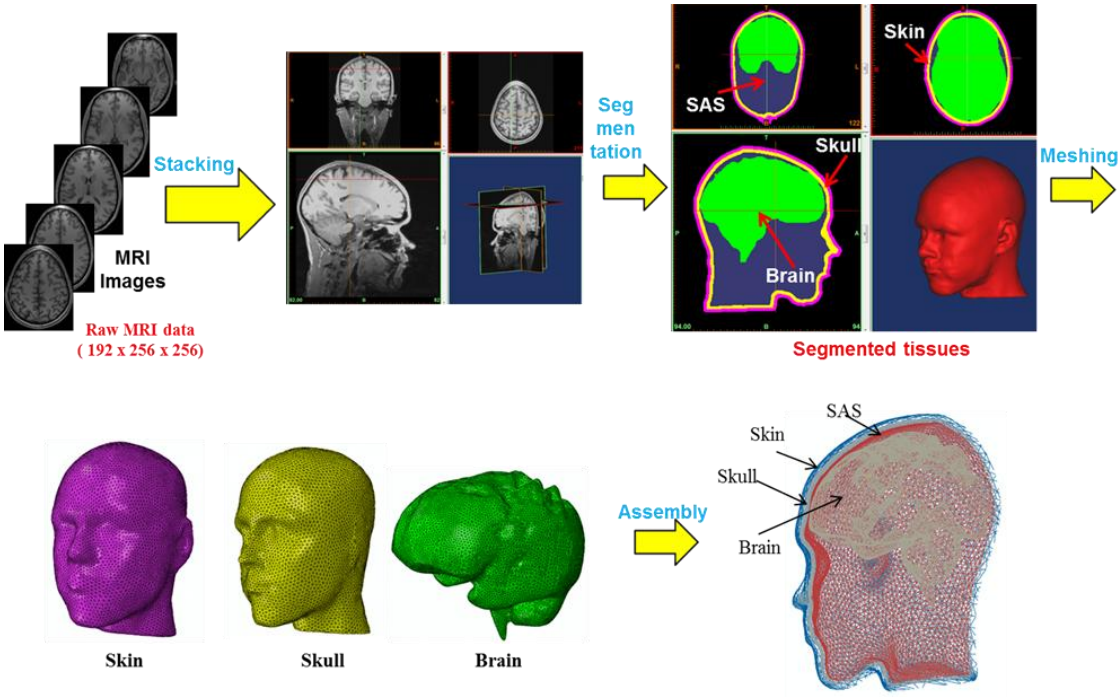

Figure 4.1: Finite Element (FE) discretization

Table 4.1: Details of the FE head model

Component/ Tissue type	No. of nodes	No. of elements	Type of element
Skin	106,915	54,094	10 noded tetrahedron
Skull	72,426	36,213	10 noded tetrahedron

Subarachnoidal space (SAS)	242,141	144,386	10 noded tetrahedron
Brain	271,552	175,460	10 noded tetrahedron
Neck	12,691	11,340	8 noded brick

4.2.2 Material models and material parameters used in the head model:

The skin, skull and SAS are modeled as linear, elastic, isotropic materials with properties adopted from the literature. Elastic properties in general, are sufficient to capture the wave propagation characteristics for these tissue types and this approach is consistent with other published works [34, 78, 88, 95, 183, 184]. For elastic material stress is related to strain as:

$$\sigma_{ij} = \lambda E_{kk}\delta_{ij} + 2\mu E_{ij} \tag{4.1}$$

Where,

σ is a Cauchy stress, E is a Green strain (also known as Green-Lagrange strain), λ and μ are Lame constants and δ is a Kronecker delta.

Brain is modeled with an elastic volumetric response and viscoelastic shear response. Viscoelastic response is modeled using Maxwell model. The associated Cauchy stress is computed through:

$$\sigma_{ij} = J^{-1}F_{ik}.S_{km}.F^{T}_{mj} \tag{4.2}$$

where σ is a Cauchy stress, F is a deformation gradient, J is a Jacobian, and S is the second Piola-Kirchhoff stress, which is estimated using following integral:

$$S_{ij} = \int_0^t G_{ijkl}(t-\tau)\frac{\partial E_{kl}}{\partial \tau} d\tau \tag{4.3}$$

where E is the Green strain, and G_{ijkl} is the tensorial stress relaxation function. The relaxation modulus for an isotropic material can be represented using Prony series:

$$G(t) = G_\infty + \sum_{i=1}^{n} G_i e^{-\beta_i t} \tag{4.4}$$

where G_∞ is the long term modulus and β is the decay constant.

For material parameters of the brain tissue, widely accepted bulk modulus value of 2.19 GPa is used in this work. This value is motivated from the works of Stalnaker [91] and McElhaney [90]. The shear properties of the brain tissue are adopted from Zhang et al. [70], who derived shear modulus from the experimental work of Shuck and Advani [99] on human white and grey matter. For material parameters, we relied on widely accepted values in the literature for base simulations. In addition, parametric studies are conducted to account for reported variations in the brain material properties. The material properties of the head model along with longitudinal wave speeds are summarized in table 4.2.

Table 4.2: Material Properties

(a) Elastic material properties

Tissue type	Density (kg/m^3)	Young's Modulus (MPa)	Poisson's Ratio	Longitudinal wave speed, C_L (m/sec)
Skin	1200	16.7	0.42	188.48
Skull	1710	5370	0.19	1856.79
SAS	1000	10	0.49	413.69
Neck	2500	354	0.3	436.60
		Bulk Modulus (MPa)		
Brain	1040	2.19	0.49999	1451.15

(b) Viscoelastic material properties of the brain

	Instantaneous Shear Modulus (kPa)	Long-term Shear Modulus (kPa)	Decay Constant (sec^{-1})
Brain	41.0	7.8	700

4.3 Realistic Explosive Dummy (RED) model development:

The Realistic Explosive Dummy (RED) head, used as the surrogate, is based on the Facial and Ocular CountermeasUre Safety (FOCUS) head [185]. The FOCUS head is

modified from the Hybrid III dummy head, the latter used in frontal impact studies in automotive accidents. The external geometry of the FOCUS headform (and hence the RED head) is designed to replicate a 50^{th} percentile male soldier across the three branches of the military (Army, Navy and Air Force) [186]. The RED head consists of a hard polyurethane skull with an opening for the brain and cerebrospinal fluid and is attached to the neck through the base plate. The RED head is used in conjunction with the Hybrid III neck in this work while intracranial contents are not included. The main advantage of the RED head over other dummies is that, RED head represents the anthropometry of the warfighter population under this research effort. In the present work, only skull is used. The RED head is modeled directly from the design (CAD) drawings and meshed with 10 noded tetrahedral elements using meshing software HyperMesh. The RED head contained total 74,856 nodes and 41,057 elements. Meshed RED head model is shown in figure 4.2. The RED head is modeled as linear, elastic, and isotropic with material properties adopted from literature [185]. These properties are: density- 1210 kg/m^3, Elastic Modulus- 2380 MPa and Poisson's Ratio-0.37. Further details on the RED head can be found in Hossain [187].

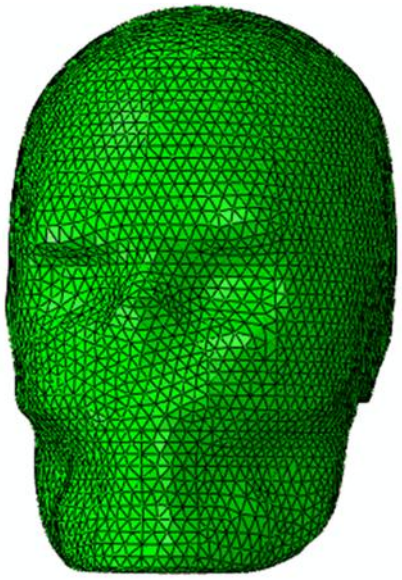

Figure 4.2: Meshed model of the RED head

4.4 Computational framework for blast simulations:

Blast simulations were carried out using shock tube setup. To this end, we have developed a numerical model utilizing the Euler-Lagrangian coupling method. In this method, an Eulerian mesh is used to model shock wave propagation inside the shock tube and a Lagrangian mesh for the head and the neck. This computational environment allows accurate concurrent simulations of the formation and propagation of blast wave in air, the fluid-structure interactions between the blast wave and the head model, and the stress wave propagation within the head. Computational framework is shown in figure 4.3.

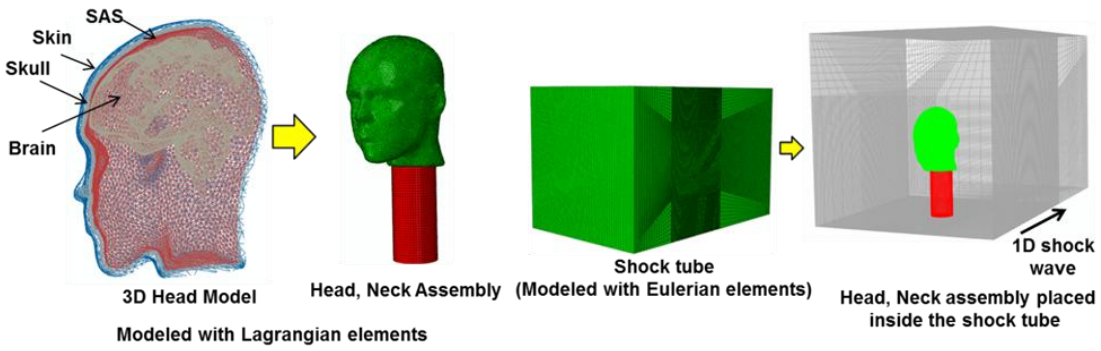

Figure 4.3: Computational framework for blast simulations

Shock tube that is used in the modeling is based on our experimental shock tube. The cross sectional dimensions of this shock tube are 711 mm X 711 mm (28”X28”). The head and neck assembly is placed inside the shock tube and subjected to blast wave profile of interest. The head and neck are modeled with Lagrangian elements, details of the head model are described in the earlier section. Air inside the shock tube in which the blast wave propagates is modeled with Eulerian elements (figure 4.3). The Eulerian domain (air inside the shock tube) is meshed with 8 noded brick elements, with appropriate mesh refinement near the regions of solid bodies to capture fluid-structure interaction (FSI) effects. Parametric studies on mesh size have been performed and it is found that mesh size of 3 mm is appropriate to capture flow field around the head (i.e. pressures, velocities) and fluid-structure interaction (FSI) effects. For Eulerian elements, mesh convergence is achieved at this element size; thus element size of 3 mm is used near the regions of solid bodies and along the direction of blast wave propagation. The total number of Eulerian nodes and elements contained in the model are 1,259,895 and 1,223,040 respectively. Air is modeled as an ideal gas equation of state (EOS) (see

equation 5) with following parameters: density- 1.1607 kg/m^3, gas Constant- 287.05 J/(kg-K) and temperature 27 °C.,

$$P = (\gamma - 1)\frac{\rho}{\rho_0}e \qquad (4.5)$$

where, P is the pressure, γ is the constant-pressure to constant-volume specific heat ratio (=1.4 for air), ρ_0 is the initial air mass density, and ρ is the current mass density and e is the internal volumetric energy density. The Mach number of the shock front from our experiments is approximately 1.4, and hence the ideal gas EOS assumption is acceptable, as the ratio of specific heats do not change drastically at this Mach number.

4.5 Loading, interface and boundary conditions:

We conducted numerical experiments on the head models (developed from MRI images and surrogate RED head) by subjecting it to blast in the frontal direction. In order to numerically reproduce the experiment, there are two possible techniques to impose the boundary conditions: technique (a) Modeling of the entire shock tube, in which driver, transition and extension sections are included in the model so that events of burst, expansion and development of a planar of the blast wave are reproduced; technique (b) Partial model with experimentally measured (*p*-*t*) history is used as the pressure boundary condition, where the numerical model comprises the downstream flow field containing the test specimen. Technique (a) is computationally very expensive. For example, a full scale simulation of 711 mm X 711 mm cross section, 9880 mm long shock tube (excluding catch tank) with cylindrical to square transition requires about 5 million eight-noded brick Eulerian elements and takes about 147 CPU hours on a dedicated 48

processors. These simulations reach the limits of computing power in terms of memory and simulation time. On the other hand, technique (b) requires about 1.26 million elements with 10 CPU hours. The pressure, velocity and temperature profiles obtained using technique (b) match well with the profiles that are obtained using full scale model (technique (a)) at the boundary and downstream locations. Hence technique (b) is capable of capturing the pressure, momentum and energy of the shock wave and is used here to save time without scarifying accuracy. Additional details and comparison of the field variables using both these techniques are provided in the appendix. Approach similar to technique (b) has been widely used in shock dynamics studies using shock tubes [166, 168, 169].

The velocity perpendicular to each face of Eulerian domain (shock tube) is kept zero in order to avoid escaping/leaking of air through these faces. This will maintain a planar shock front traveling in the longitudinal direction with no lateral flow. The bottom of the neck is constrained in all six degrees of freedom to avoid rigid body motion. The interface between all head components is modeled as tied (i.e. no tangential sliding and no separation) contact. It should also be noted that interface modeled as frictionless (tangential) sliding with no (normal) separation resulted in similar response as tied interface. An enhanced immersed boundary method is used to provide the coupling between the Eulerian and the Lagrangian domains. Here, the Lagrangian region resides fully or partially within the Eulerian region and provides *no-flow* boundary conditions to the fluid in the direction normal to the local surface. Further, the Eulerian region provides the pressure boundary conditions to the Lagrangian region. Thus, a combination of fixed

Eulerian mesh and solid-fluid interface modeling through the enhanced immersed boundary method allows for the concurrent simulations of the formation and propagation of a primary blast wave in a fluid medium and accounts for the effects of both fluid-structure interaction and structural deformations once the blast wave encounters a solid. The interactions (contact conditions) between Eulerian (containing air and a propagating blast wave) and Lagrangian regions are defined using 'general contact' feature (card) in Abaqus®. In general contact, contact constraints are enforced through the penalty method with finite sliding contact formulation. Various contact property models are available in general contact. In the present work, frictionless tangential sliding with hard contact is used as contact property model.

4.6 Solution scheme:

The finite element model is solved using the nonlinear transient dynamic procedure with the Euler-Lagrangian coupling method (Abaqus®). In this procedure, the governing partial differential equations for the conservation of momentum, mass and energy (see equations 6-8) along with the material constitutive equations (described earlier) and the equations defining the initial and boundary conditions are solved simultaneously.

Conservation of mass (continuity equation):

$$\rho \frac{\partial v_i}{\partial x_i} + \frac{\partial \rho}{\partial t} + v \cdot \nabla \rho = 0 \qquad (4.6)$$

Conservation of momentum (equation of motion):

$$\frac{\partial \sigma_{ij}}{\partial x_j} + \rho b_i = \rho a_i \qquad (4.7)$$

Conservation of energy (energy equation):

$$\rho \frac{\partial e}{\partial t} + v \cdot \nabla e = \sigma_{ij} \frac{\partial v_i}{\partial x_j} - \frac{\partial q_i}{\partial x_i} + \rho q_S \qquad (4.8)$$

where, ρ is a density, x, v and a are displacement, velocity and acceleration of a particle respectively, σ is a Cauchy stress, b is a body force, e is a internal energy per unit mass, q is a heat flow per unit area and q_S is a rate of heat input per unit mass by external sources.

In Eulerian-Lagrangian method, we are actually solving the whole model (i.e. both Eulerian and Lagrangian domains) with the same Lagrangian equations. The notion of a material (solid or fluid) is introduced when specific constitutive assumptions are made. The choice of a constitutive law for a solid or a fluid reduces the equation of motion appropriately (e.g., compressible Navier-Stokes equation, Euler equations etc.). For the Eulerian part/domain in the model the results are simply mapped back to the original mesh with extensions to allow multiple materials and to support the Eulerian transport phase for Eulerian elements. Eulerian framework allows for the modeling of highly dynamic events (e.g. shock) which would otherwise induce heavy mesh distortion. In Abaqus® the Eulerian time incrementation algorithm is based on an operator split of the governing equations, resulting in a traditional Lagrangian phase followed by an Eulerian, or transport phase. This formulation is known as "Lagrange-plus-remap." During the Lagrangian phase of the time increment nodes are assumed to be temporarily fixed within the material, and elements deform with the material. During the Eulerian phase of the time increment deformation is suspended, elements with significant deformation are

automatically remeshed, and the corresponding material flow between neighboring elements is computed. As material flows through an Eulerian mesh, state variables are transferred between elements by advection. Second-order advection is used in the current analysis. The Lagrangian (solid) body can be a deformable body and can deform based on the forces acting on it and the deformation of the Lagrangian solid influences the Eulerian part/domain. In current analysis 8 noded brick elements are used for Eulerian elements and 10 noded tetrahedron for Lagrangian elements. These elements use isoparametric interpolation functions.

A typical 3D simulation requires about 7 hours of CPU time on 48 dedicated Opteron parallel processors (processor speed 2.2 GHz, 2 GB memory per processor), for an integration time of 2.5 msec. The simulation time is selected such that the peaks due to stress wave action have been established. A time step of the order of 5×10^{-7} sec is used to resolve and capture wave disturbances of the order of 1 MHz, which increases the overall computational effort for the total simulation time of interest.

4.7 Model Validations:

4.7.1 Validation of the MRI based human head model against cadaveric impact experiments

The anatomically detailed human head model developed from the MRI dataset is validated using the frontal cadaveric impact experiment of Nahum et al. [48]. Nahum's experiment has become a de-facto standard [68, 70, 76, 84, 86, 89, 94, 183] to validate head/brain numerical models. As mentioned in the chapter 2 on literature review, in Nahum's experiments seated stationary cadaver subjects were impacted at the frontal

bone of the skull in the mid-sagittal plane in an anterior-posterior direction by a rigid mass traveling at a constant velocity. They measured intracranial pressure at five different locations: (1) the frontal bone adjacent to the impact contact area, (2,3) posterior and superior to the coronal and sequamosal sutures respectively in the parietal bone, (4) inferior to the lambdoidal suture in the occipital bone and (5) in the occipital bone at the posterior fossa. To simulate Nahum's experiment, the measured impact force from the cadaver test is applied to the mid-frontal area of the numerical human head model in the anterior-posterior direction, in the form of a distributed load over an area of 1,470 mm^2 as shown in figure 4.4(a). Pressures are measured at points corresponding to the experimental locations described above (figure 4.4(b)). Comparisons of pressure-time histories between model predictions and experimental measurements (test no 37) are shown in figure 4.4(c) and pressure pattern predicted by the brain is shown in figure 4.4(d). The agreement between pressure-time (*p*-*t*) profiles at frontal and occipital locations is good. The pressure pattern shows typical coup countercoup pattern and pressure varies continuously along the sagittal plane. Similar pattern is reported by various researcher's under frontal impact loading conditions (e.g. [70]).

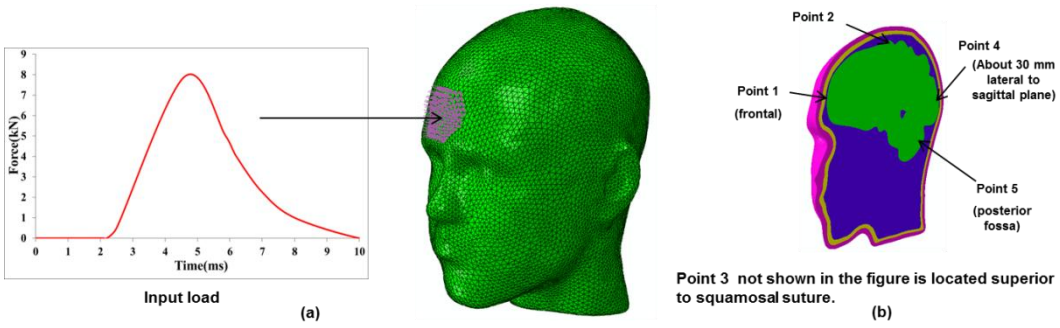

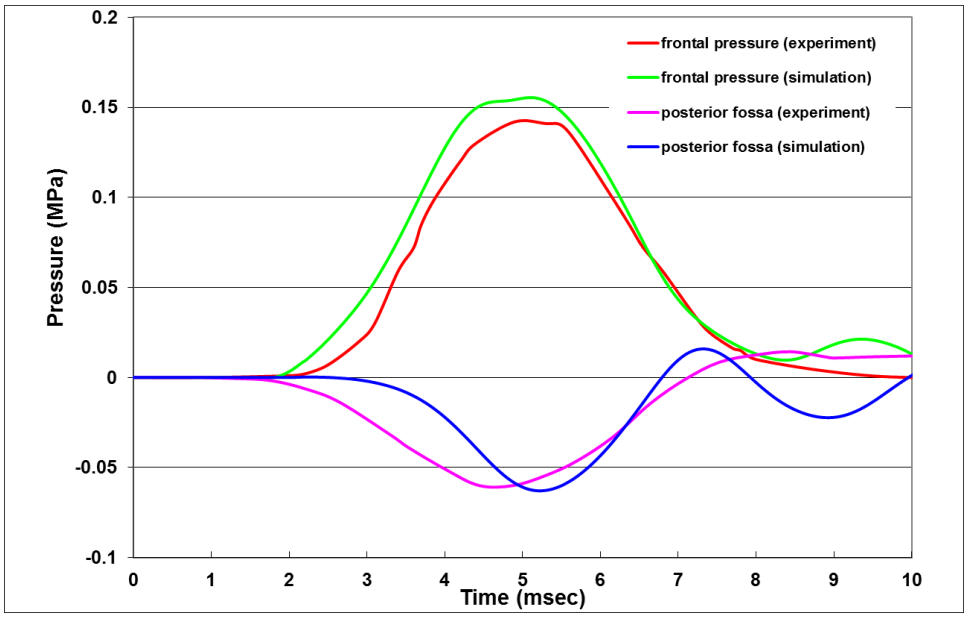

(c)

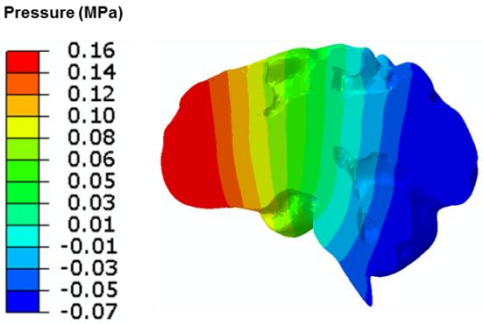

(d)

Figure 4.4: Validation of MRI based head model with Nahum's experiment (a) Head model subjected to Nahum's impact (b) locations at which pressure comparisons are made against experimental pressures (c) Pressure-time (*p*-*t*) profile comparisons at frontal and occipital locations with experimentally measured pressures (d) Pressure pattern in the brain at t=5.1 msec.

Table 4.3(a) shows the comparison of peak pressures and peak head accelerations between experiments and numerical simulations for various test cases of Nahum et al.

[48]. Acceleration is based on resultant nodal acceleration at center of mass of the head. The agreement between experiments and numerical simulations is good for these test cases as well. The small differences in peak pressures and peak head accelerations can be attributed to the discrepancy in geometry and materials, imprecise information on neck boundary conditions and pressure transducer locations. In addition, the head model is also validated against impact experiments of Trosseille et al. [51] and the results are shown in table 4.3(b). The reasonable agreement is seen between experimental and simulation intracranial pressures. Since, ventricles are not explicitly modeled in this work the elements in the ventricle region are approximately selected based on the knowledge of head anatomy.

Table 4.3(a): Head model validation against tests of Nahum et al. [48]

Test No.	input load* (kN)	Experiment				Simulation				% difference (absolute)			
		peak head acceleration (m/s^2)	Peak Pressure (kPa)			peak head acceleration* (m/s^2)	Peak Pressure (kPa)			peak head acceleration (m/s^2)	Peak Pressure (kPa)		
			frontal	parietal	posterior fossa		frontal	parietal	posterior fossa		frontal	parietal	posterior fossa
37	7.9	2000	141.19	73.59	- 60.26	2046.94	154.5	61.93	-63.2	2.35	9.43	15.85	4.87
41	14.84	3900	427.56	188.52	-56.80	3857	414	186.34	-59.31	1.10	3.17	1.16	4.43
42	5.2	1590	-	-	-43.86	1510.74	-	-	-46.33	4.98	-	-	5.62
54	10.84	2340	274.51	180.52	-64.39	2393.64	247.18	141.93	-66.5	2.29	9.96	21.38	3.27

* The stiffness of the padding material in front of the impactor for cases 37, 41, 42 and 54 is not known. Hence, for cases 41, 42, and 54, the shape of the pressure time profile as that of case 37 is conserved. The pressure pulse is scaled to match peak input force in cases 41,42 and 54.

** Acceleration is based on resultant nodal acceleration at center of mass of the head.

Table 4.3(b): Head model validation against tests of Trosseille et al. [51]

Test No.	Experiment					Simulation					% difference (absolute)				
	Peak Pressure (kPa)					Peak Pressure (kPa)									
	frontal	lateral ventricle	3rd ventricle	occipital	parietal	frontal	lateral ventricle	3rd ventricle	occipital	parietal	frontal	lateral ventricle	3rd ventricle	occipital	parietal
MS428-1	>60	30	25	-13.5	12.4	72	36.22	30.9	-17	15.2	-	20.73	23.6	25.93	22.58
MS428-2***	88	40	35	-11	10.5	84	43.23	38.56	-13.5	13	4.55	8.07	10.17	22.72	23.81

*** For test No. MS428-2 acceleration time history at the center of mass as reported in Zhang et al. [69] is used.

4.7.2 Validation of the RED head against blast experiments

Figure 4.5 shows the comparison of the *p-t* profiles between the experiment and the simulation when RED head is subjected to blast. From figure 4.5, it can be seen that, there is a reasonably good agreement between the experiment and numerical simulation, in terms of peak pressures (maximum difference 14.55 %) and nonlinear decay. The simulation is also able to capture majority of the features well, including the shock front rise time, the small peaks and valleys, secondary reflections (e.g. sensors T3 and RH). The arrival time of the experiment at each sensor location is shifted to match the arrival time of the numerical simulation for ease of comparison of the different features of the *p-t* profile. There is a slight difference in arrival time between the experiment and the numerical simulation, of the order of 0.05 msec (50 μsec). Difference in arrival time indicates the difference in the shock wave speed and does not change the pressure and the impulse experienced by the head. The difference in the arrival time between experiment and simulation can be attributed to the ideal gas equation of state modeling assumption, the membrane rupture pattern, the friction along the inner wall of the shock tube and the misinterpretation of the vibrations as pressure readings. Zhu et al. [175] have also found similar differences in arrival time from their experiment and numerical simulations due to similar reasons. A similar agreement between experiment and simulation is observed for all the other head orientations to the blast. Comparison between experiment and simulation for the padded helmet case is not possible as the constitutive equations of pads are not available.

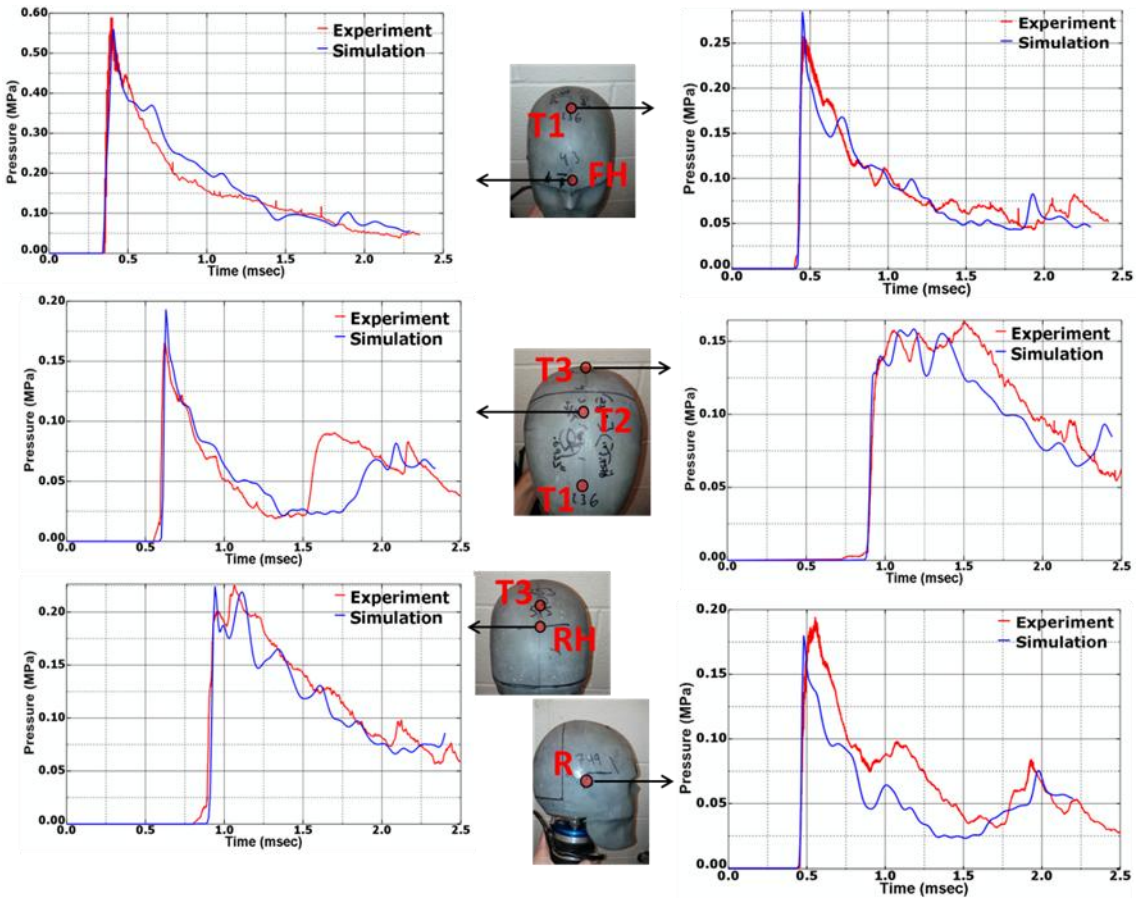

Figure 4.5: Comparison of (surface) pressure-time (*p*-*t*) history from experiment and numerical simulation on the surrogate RED head. Results from front orientation no helmet case are shown as sample case.

4.7.3 Validation of the MRI based human head model against blast experiments:

The head model is validated against PMHS experiments conducted at University of Nebraska-Lincoln's Trauma Mechanics Research facility [172]. PMHS specimens (N=3) were subjected to primary blast of incident intensities 70 kPa, 140 kPa and 200 kPa respectively using 28" shock tube. The numerical model is validated against surface pressures, surface/skull strains and intracranial pressures obtained from these

experiments. In the PMHS experiments, dura, subarachnoidal space and brain were removed and intracranial contents were backfilled with ballistic gel whose wave speed is calculated at 1583±118 m/s, which was close to the longitudinal wave speed of water. Thus for head model validation purposes only, SAS and brain were assigned same bulk modulus value of 2.19 GPa. The validation results are presented for incident intensity of 200 kPa, but similar agreement in the simulation and experimental results are seen for other intensities. The arrival time of the experiment at each sensor location is shifted to match the arrival time of the numerical simulation for ease of comparison of the different features of the *p-t* profile. The experimental profiles are based on average of three shots (experiments) for head 1.

Figure 4.6 shows comparison of surface pressure profile for front location. For front location (i.e. Forehead SM), good agreement is seen between the experiment and the simulation both in terms of peak pressure and nonlinear decay. The surface pressure profile at temple location is not presented and compared (with experiments) as the obtained profile (i.e. shape of the profile) was not consistent even within the experiments when PMHS specimen was changed. This non-repeatability in obtained profile within experiments is attributed to following reasons: (i) geometry of the PMHS is different from specimen to specimen. The flow field around the head is complex that is influenced by a number of geometric and process parameters and their shock-structural interaction occurring at micro-second to millisecond time scale. (ii) since the temple surface pressure gauge is mounted on the soft skin it is sensitive to small changes and affected by the ripple (undulating surface wave motion) effect of the skin; this is dependent on structural

rigidity of each PMHS specimen (iii) the results are also affected by precise location of temple surface gauge and its adherence to skin (i.e. mounting surface) for each PMHS specimen. Thus further testing is needed in order to accurately determine the pressure profile at temple location. Despite these facts, peak values of surface pressure at temple location are fairly consistent across the tested PMHS specimens in the experiments and the mean peak value compares reasonably well (difference < 20 %) with peak value obtained from the simulation.

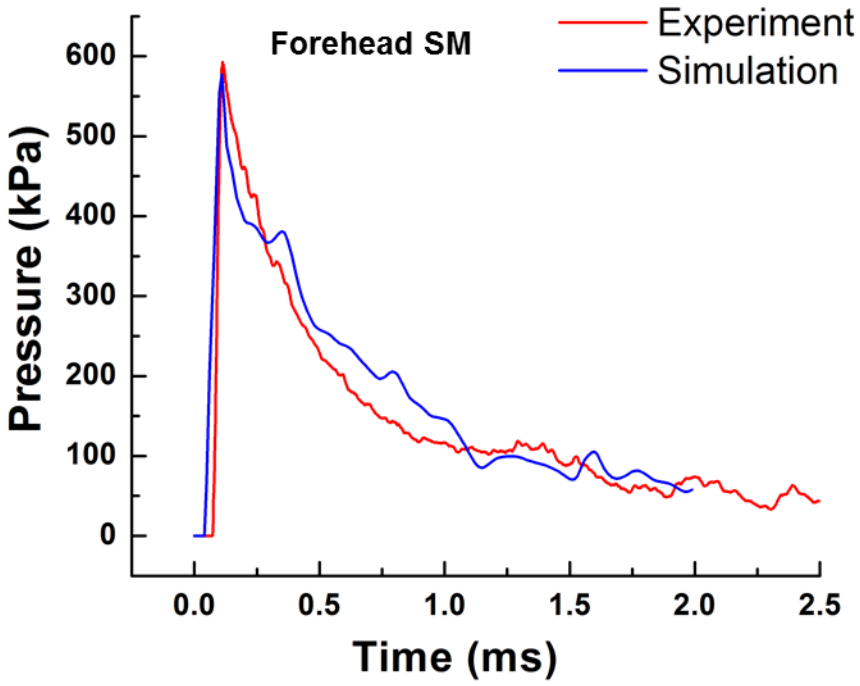

Figure 4.6: comparison of surface pressure profile between experiment and simulation for forehead location

Figure 4.7 show the comparison of ICP profiles between the experiment and the simulation. Both experimental and simulation data is filtered using 10 kHz four pole Butterworth filter. From figure 4.7, it can be seen that, there is a reasonably good

agreement between the experiment and numerical ICP profiles both in terms of peak values (maximum % difference in peak ICP value is 17%) and shape of the profiles. In general, simulation ICP profiles show more oscillatory behavior than experimental ICP profiles. This can be attributed to following: (i) lack of material characterization for ballistic gel. It is possible that the response of ballistic gel to shock loading is much more complex (due heterogeneity, rate dependent behavior, effect of curing, wave propagation and dispersion in three dimensional setting) than assumed here (ii) frequency response of ICP pressure probes (gauges) embedded in the ballistic gel is not known; it is possible that frequency response of the gauge is slower because of which behavior is less oscillatory in the experiments. Due to these artifacts discrepancies in the oscillatory pattern are to be expected between the simulation and the experiment. In fact it is also common that the repeated experiments will show small variations in the oscillatory pulse patterns from shot to shot. Due to these reasons it is improbable if not impossible to match every aspect of experiment with the computational simulation. With these considerations in mind some aspects of comparison between experimental and simulation ICP profiles are discussed.

For forehead ICP, simulation is able to capture major trends including initial sharp rise (rise time = 40 μs) associated with the shock front, initial decay (till t=0.15 ms), abrupt pressure increase (second peak) during initial decay (at t=0.07 ms) and subsequent pressure pattern. Secondary (loading) pulse seen in the experiment after 1.0 ms is not seen in the simulation profile for forehead ICP. For nose ICP, fair agreement is seen between the experiment and the simulation. The distinct secondary peak seen during the

decay (at t= 0.25 ms) is delayed in the simulation. This secondary peak is due to wave transmission from eye socket. The delay in this transmission between simulation and experiment is attributed to difference in geometry of the eye socket between the simulation and the experiments. Center ICP also shows fair agreement between the simulation and experiment. The rise time is shaper in the simulation than the experiments. In addition peak ICP value is slightly higher (20% difference) in the simulation. These discrepancies are expected considering complex set of direct and indirect loadings experienced by the center location. The center location experiences complex set of direct and indirect loadings emanating from different sources (e.g. blast wave transmission, reflections from tissue interfaces, skull deformation) at different points of time. These disturbances continuously propagate into the brain as waves. Constructive and deconstructive interferences of these waves control the pressure history deep inside the brain. We believe the obtained match between experiment and simulation for center ICP is reasonable considering these complexities. Back ICP also shows reasonably good agreement between experiment and simulation. The countercoup phase seen in the experiments is replicated in the simulation. Table 4.4 summarizes values of peak ICP and ICP impulse for experiment and simulation and % difference between them.

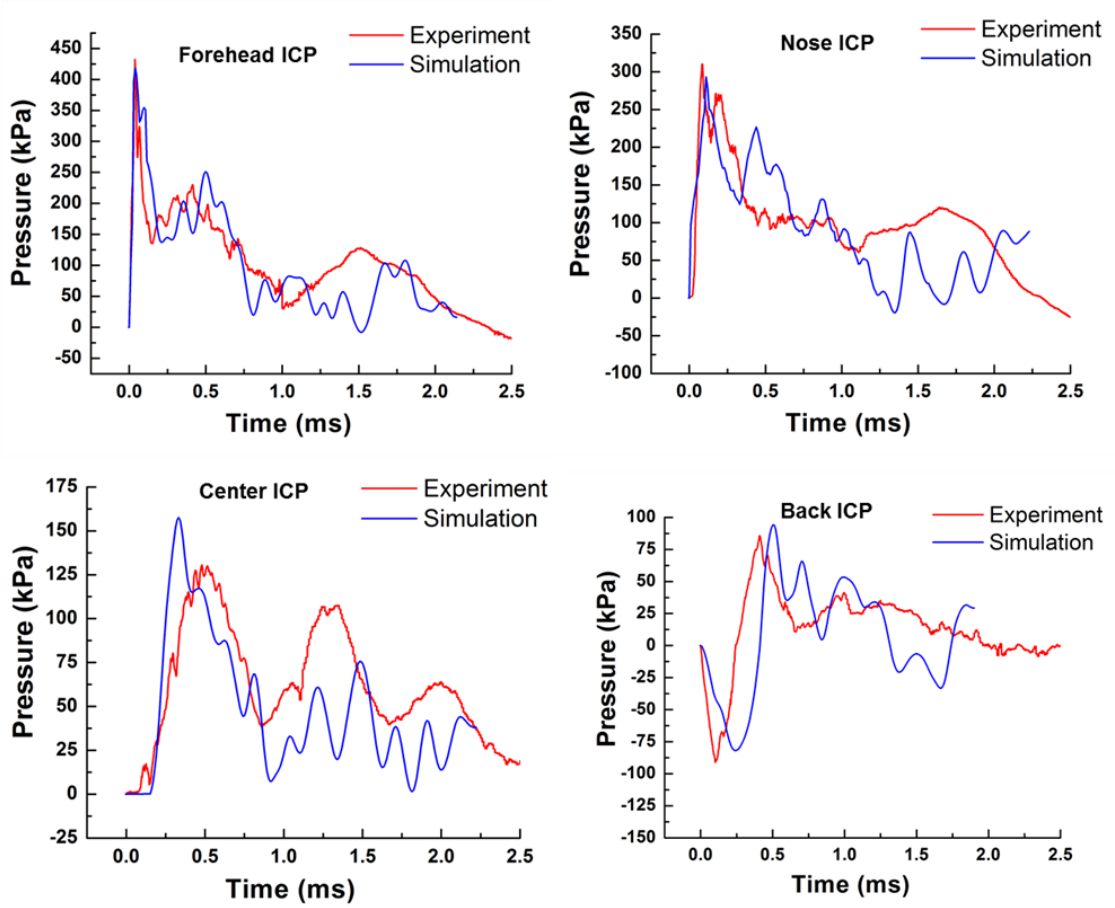

Figure 4.7: comparison of ICP profiles between experiment and simulation

Table 4.4: Comparison of peak ICP and ICP impulse values between experiment and simulation

	Peak ICP (kPa)						**Positive phase ICP impulse (kPa-ms)**					
	Forehead	**Nose**	**Center**	**Temple**	**Back (+ve)**	**Back (-ve)**	**Forehead**	**Nose**	**center**	**Temple**	**Back (+ve)**	**Back (-ve)**
Experiment	430	311	130	276	84	-88	241	227	166	144	43	-12
Simulation	417	293	157	265	94	-81	218	200	107	120	37	-20
% difference	3.02	5.79	-20.77	3.99	-11.90	7.95	9.54	11.89	35.54	16.67	13.95	-66.67

During PMHS experiments (circumferential) skull strains were also measured at four locations front, temple, top and back as shown in figure. Table 4.5 compares the peak skull strains obtained from the simulation with that of experimentally measured skull strains at various locations. The maximum peak strain is seen at front location and the strain value at this location is less than 0.1%. It should be noted that, the Standard Deviations (S.D.) in experimentally obtained skull strain values are huge. Standard deviations upto 100% of mean values are seen certain strain measurements. Such standard deviations are normal during strain measurements, especially when strain values are very small. Obtained strain values from the simulations fall within the range of experimentally obtained strain values. The experimental and numerical strain-time profiles are not compared as the obtained profiles were not highly repeatable during the experiments.

Table 4.5: Comparison of peak circumferential strains at various locations of the skull

Location	**Peak strain in %**	
	Experiment (Mean ± S.D.)	**Simulation**
Front (compressive)	0.09 ± 0.04	0.06
Front (tensile)	0.01 ± 0.01	0.018
Right temple (compressive)	0.04 ± 0.03	0.045

Right temple (tensile)	0.04 ± 0.02	0.028
Top (compressive)	0.04 ± 0.03	0.042
Top (tensile)	0.035 ± 0.02	0.02
Back (compressive)	0.04 ± 0.02	0.03
Back (tensile)	0.02 ± 0.02	0.03

4.8 Summary:

A biofidelic model of the human head is generated from high-resolution medical imaging data. The head model was segmented into four different structures/components namely skin, skull, SAS and brain and adequate material response is modeled that is consistent with the data reported in the literature. Computational methodology based on Euler-Lagrangian coupling method is developed to simulate blast events and this methodology is subsequently optimized to reduce computational time and resources. This computational methodology allows accurate concurrent simulations of the formation and propagation of the blast wave in the air, the fluid-structure interactions between the blast wave and the head model, and the stress wave propagation within the brain. The biofidelic human head model is validated against impact and blast experiments. The experiment and simulation response is compared using surface pressures, surface/skull strains and intracranial pressures (ICPs). Reasonably good agreement is seen between the experiments and simulations for both impact and blast events. In addition to biofidelic human head model, the surrogate RED head model is also developed. This model does

not contain intracranial contents. Surrogate RED head model is also validated using blast experiments. Response of RED head is compared using surface pressures and good agreement is seen between experiments and simulations. Validated computational framework for modeling blast TBI events not only provides the tool for interpreting experimental observations but also forms the basis for additional numerical experiments that are critical in understanding blast TBI. These models and computational methodology will be used for these purposes in subsequent chapters.

CHAPTER 5

ROLE OF HELMET IN THE MECHANICS OF BLAST WAVE HEAD INTERACTIONS: FLOW FIELD ANALYSIS ON THE SURFACE OF THE HEAD

5.1 Introduction:

As mentioned earlier, Blast induced Traumatic Brain Injury (bTBI) has been identified as the signature wound of recent conflicts in Iraq and Afghanistan [188]. Armed Forces Health Surveillance Center (AFHSC) has reported 233,425 clinically confirmed TBI cases within the U.S. service members from 2000 to 2011 [189]. In order to understand the mechanisms of bTBI and to develop injury thresholds for blast loading conditions, there has been a continual increase in the number of blast studies in recent years on animal models, head surrogates and human cadavers [19, 150-155, 157, 159, 160, 190-195]. Still, our current understanding of the pathophysiology of bTBI is incomplete [148]. How the blast wave interacts with the head helmet configuration and induces biomechanical loading of the brain are not fully understood. In addition, the role of helmets in blast mitigation is not fully known as helmets have been conventionally designed for blunt and ballistic protections [10, 29, 196, 197]. There are several studies that show that blast waves can focus under the helmet and enhance the pressure in the head-helmet subspace (gap) [41, 156, 184]. To the extent that pressure in the head/helmet subspace is predictive of injury, these data suggest that changes in the helmet configurations which result in different pressure distributions and magnitudes may have

influence on the location and severity of injuries. This does not preclude the use of the helmets that provide critical protection against blunt and penetrating conditions.

Many studies have shown that the orientations of the head play an important role in determining the intracranial pressures (ICPs) and the degree of injury [70, 198-200] for impact loadings. Gennarelli et al. [198] and Zhang et al. [70] have concluded that load in the lateral direction is more likely to cause diffuse axonal injury than the load in the frontal direction. Zhou et al. [200] have suggested that subdural hematoma is more likely to be produced in an occipital impact than in corresponding frontal impact. But there are only a limited number of studies [41, 63, 79, 201, 202] regarding orientation dependent response of the head under blast loading conditions. These studies predict different patterns of intracranial pressures (ICPs) depending on the orientation of the head to the blast. However, most of these studies lack critical understanding in terms of flow field around the head, mechanics of load transfer and subsequent biomechanical loading of the brain.

The goal of this chapter is to understand blast wave head interactions with and without the helmets for various head orientations. This becomes particularly important when evaluating current mitigation stratagems offered by the helmets under blast loading conditions. The basic hypothesis is that external pressure field on the head depends on head helmet configuration (e.g. suspension, padded or no helmet). Further, it is postulated that the orientation of the head to the blast wave (e.g. front, back, side or 45°) governs the pressure field experienced by the head. An integrated experimental computational approach is employed to test these hypotheses.

This chapter is organized as follows: In the methods section (section 5.2), we describe the specially designed shock tube capable of generating idealized primary blast loading conditions in the form of Friedlander wave and the experimental test configurations using surrogate head. We also briefly describe the finite element modeling framework used to interpret the experimental data. In the next section (section 5.3) on results and discussions, the results of the experimental and numerical analysis are presented and discussed in terms of mechanics of blast wave head interactions with and without the helmets. The validations of the surface pressures on the surface of the head with the helmets are also provided. Effect of curvature, head orientations, head-helmet gap size and incident peak pressure intensity on the surface pressures is also studied. Broad conclusions about blast wave head interactions and performance of the helmets under blast loading conditions are made in the section 5.4 on the summary.

5.2 Methods:

5.2.1 Experiments:

Experiments are carried out in the 711 mm X 711 mm (28”X28”) cross section shock tube designed and tested at the University of Nebraska-Lincoln's blast wave generation facility [172]. The four main components of the shock tube are: driver, transition, straight/extension sections (includes test section), and catch tank (figure 5.1(a)). The driver section contains pressurized gas (e.g. Nitrogen or Helium) which is separated from the transition by several 0.025 mm thick Mylar membranes, while the remaining sections contain air at atmospheric pressure and at room temperature. The transition section is used to change the cross-section of the tube from a cylinder (driver section) to a square

(extension sections); the square section is a design element to observe events in the test section with high speed video imaging. Upon membrane rupture, a blast wave is generated which expands through the transition; it develops into a planar shock-blast wave in the extension section(s). The test section is strategically located to expose specimens to the blast wave profile of interest (Friedlander in this case). Finally the blast wave exits the shock tube and enters the catch tank which absorbs and releases the blast wave energy while reducing the noise intensity. In addition, the catch tank is designed to reduce rarefaction waves from re-entering the shock tube. The shock tube is designed and built such that a fully developed planar shock-blast wave is obtained in the test section located approximately 2502 mm from the driver end; the total length of the shock tube is 12319 mm. The cross sectional dimensions of this shock tube are designed such that a head-neck surrogate (e.g. Anthropomorphic Test Dummies (ATD's) or cadaver head) experiences a planar blast wave without significant side-wall reflections [173]. The planarity of the blast wave has been verified by pressure measurements across the test section of the shock tube [173].

The Realistic Explosive Dummy (RED) head is used as the surrogate head in the experiments. Personal Armor System for Ground Troops (PASGT) helmet and ACH padded helmets (size: Medium; vendor: BAE systems) are used in the helmeted experiments [203].

The RED head, helmet and neck assembly are placed in the test section of the shock tube as shown in figure 5.1(b); and are subjected to front (anterior) blast loading scenario. To study effect of orientation on blast wave head interactions experiments are also

conducted for back (posterior), side (lateral) and 45° blast loading scenarios. The response of the RED head to planar Friedlander wave [156, 164] is studied. Friedlander wave is characterized by the following parameters: peak pressure, duration and total impulse (both positive and negative). In this work, only positive phase of the Friedlander wave is considered. The shape, overpressure and duration of the incident blast wave at a given location were known a priori. This is achieved through sample trials in the shock tube conducted without the surrogate head, the neck and the helmet. Three head helmet configurations are considered: no helmet, suspension helmet and padded helmet. For the suspension helmet configuration, there is a gap between the head and the helmet and the helmet is loosely connected to the head; for the padded helmet configuration, the helmet is connected to the head through a seven pad system. Suspension type helmets are currently used by the British military [204], while padded helmets are used by the U.S. military (source: http://www.defense.gov/).

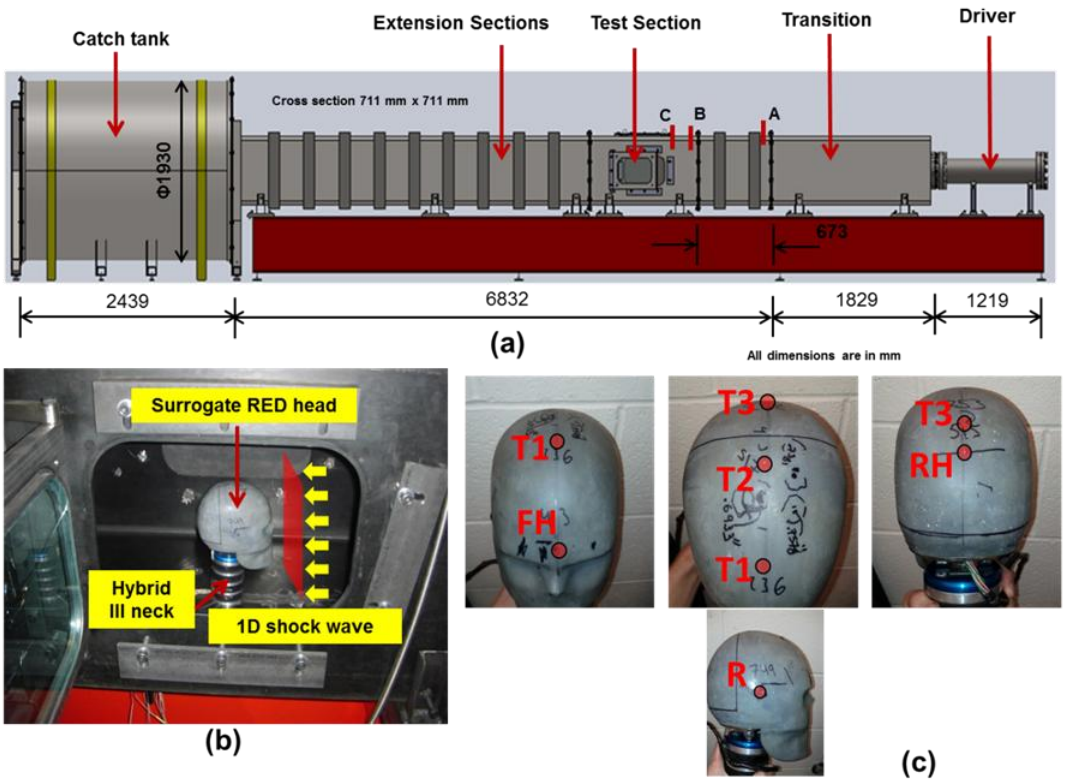

Figure 5.1: Experimental setup (a) Schematic of the 711 mm x 711 mm shock tube system (b) Realistic Explosive Dummy (RED) head with hybrid III neck placed inside the test section of the shock tube (c) Sensor locations on the RED head. FH: forehead, T1: top 1, T2: top 2, T3: top 3, RH: rear head, R: right.

Each scenario is repeated three times (N=3), thus there are a total of 36 (3x4x3) shots. Blast wave head interactions are studied by monitoring the surface pressures on the RED head. Surface pressures are measured at different locations on the surface of the head along the midsagittal plane using Kulite pressure sensors (model LE-080-250A). In addition, surface pressures are also measured on the right (all orientations) and left (only for side orientation) sides of the head. The sensor locations are shown in Figure 5.1(c). Surface pressures measure the reflected pressures that account for both the kinetic and the

potential energy components. Surface pressures reported in this work are gauge pressures or overpressures. The Kulite pressure sensor can measure the absolute pressure from 0-250 psi (0-1.72 MPa) with a nominal calibration of 0.400 mV/psi (58.02 mV/MPa) using 10 volts excitation. In addition to surface pressures, incident (side-on) blast wave pressures are measured at various locations along the length of the shock tube (which also includes location just before blast wave encounters the head-helmet-neck assembly) using PCB pressure sensors (model 134A24). Experimental data is collected at the sampling rate of 1MHz using two National Instruments PXI-6133 data acquisition cards, which have eight analog channels each. The data acquisition cards are capable of 14 bit sampling at up to 2.5 MHz. Pressure sensors are connected to the data acquisition system through 1 MHz differential amplifier. No anti-aliasing filters are used during data collection and post processing; instead a simple moving average (SMA) over 25 points is performed on the raw data.

All pressure sensors used in the experiments are calibrated under shock dynamic loading conditions using a separate 101 mm (4”) diameter shock tube. Accurate calibrations are achieved by generating precisely controlled shock wave velocities, and by invoking the Rankine-Hugoniot jump conditions that relate shock wave velocities to shock wave overpressures. Shock wave speed computed from the simulation correlate well with the measured shock wave speed from the experiments.

Data analysis

Experimental data is presented as mean ± Standard Error of the Mean (SEM). Unpaired two-tailed Student’s *t*-test with unequal variance is performed in order to assess

statistical significance between various cases, and *p*-values of <0.05 are considered statistically significant.

5.2.2 Computational Modeling:

The Finite Element (FE) modeling technique is used to simulate the propagation of the planar blast wave through the shock tube; and to study the response of the head to such a loading. The goal of the finite element models is to understand/elucidate experimental results. The computational framework remained the same as described in chapter 4. For helmeted simulations, helmet assembly (i.e. helmet and foam pads) is added to the current computational setup described in chapter 4. Helmet assembly was modeled using CAD drawing. The CAD model of the helmet assembly is imported into the meshing software HyperMesh® and a triangulated surface mesh is generated for each component. The volume mesh is generated from the surface mesh to generate 10-noded tetrahedrons. Helmet contains 52,491nodes and 27,046 elements and foam pad contains 34,726 nodes and 19,625 elements. The Kevlar helmet is modeled as transversely isotropic elastic material with properties obtained from Aare and Kleiven [205] . The foam pads are modeled with a linear bulk response and a viscoelastic shear response. The properties of foam pads are taken from Moss et al. [184], who obtained the properties from low rate compression and acoustic testing of the military foam pads. The material properties are listed in table 5.1. The head and the helmet are assembled together with an offset of ~13 mm (g=13 mm) from the skull as per ballistic standard (Reynosa 1999). For the case of foam padding between the helmet and the head, the head is partially connected to the helmet through seven pads suspension system. The

computational setup is shown in figure 5.2. In addition to three dimensional computational models, two dimensional plain strain models of simplified head and helmet are developed to conduct parametric studies. Two dimensional (2D) models are very useful for parametric studies as it drastically reduces computational time and as results of parametric studies are only used to study qualitative trends. For 2D cases, the head is simplified as a circular cylinder and the helmet as a semicircular cylinder with a constant offset from the head.

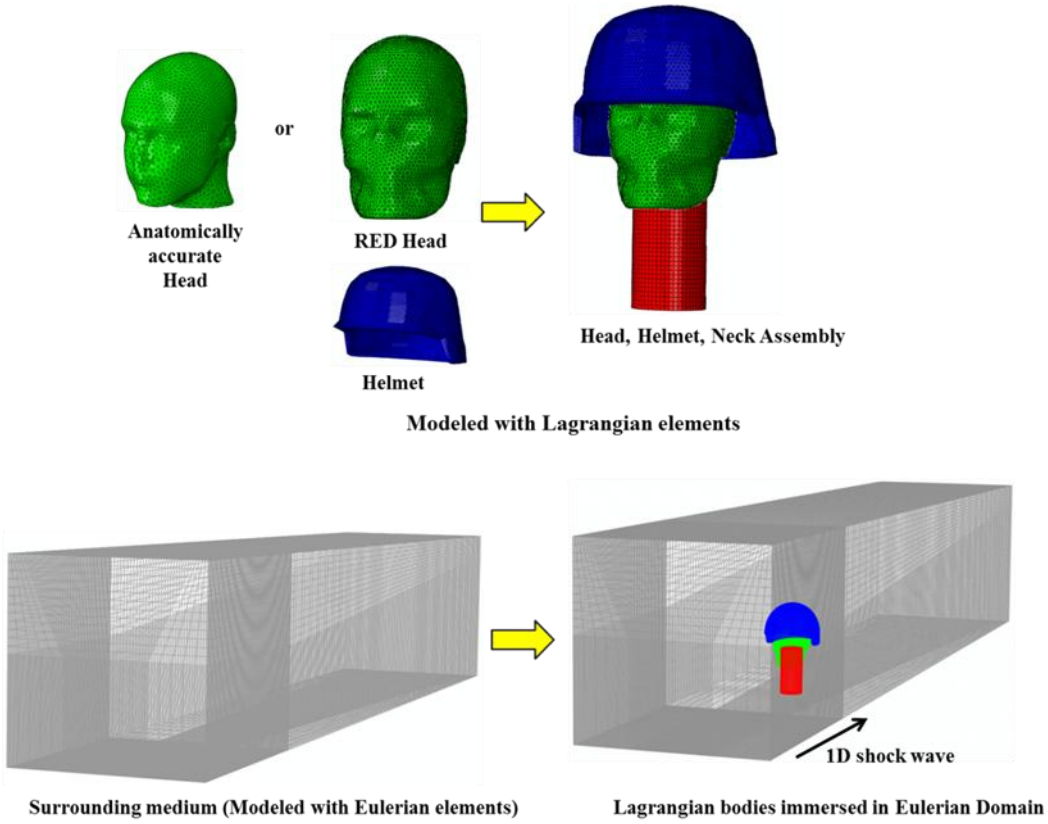

(a)

Seven pad suspension system

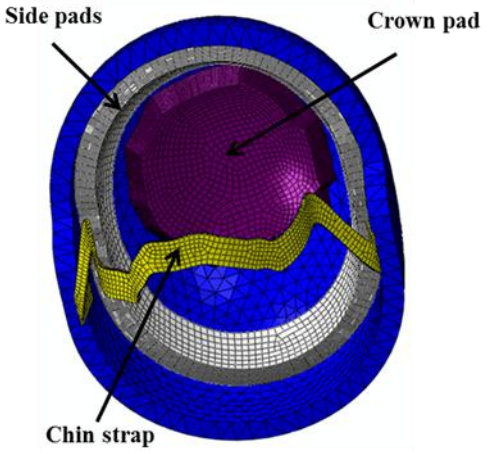

FE approximation of suspension system

(b)

Figure 5.2: (a) Computational setup for helmeted simulations (b) Pad suspension systems and FE approximation

Table 5.1: Material Properties of the helmet and foam pads

(a) Elastic material properties

	Density (kg/m^3)	**Elastic Modulus (MPa)**	**Poisson's Ratio**
Helmet	1230	See c	See c
		Bulk Modulus (MPa)	
Foam Pads	136	1.3	

(b) Viscoelastic material properties

	Instantaneous Shear	**Long-term**	**Decay Constant**

	Modulus (kPa)	Shear Modulus (kPa)	(sec^{-1})
Foam Pads	2000	20.1	100

(c) Transversely isotropic elastic material properties

	E_1 (MPa)	E_2 (MPa)	E_3 (MPa)	G_{13} (MPa)	G_{23} (MPa)	ν_{12}	ν_{13}	ν_{23}
Helmet	18500	18500	6000	2720	2720	0.25	0.33	0.33

5.3 Results and Discussion

5.3.1 Mechanics of Blast wave human head interactions without the helmet:

The mechanics of the blast wave head interactions can be studied by monitoring the flow field on the surface of the head. Figure 5.3 (a) and (b) respectively shows the experimentally measured peak pressures and shock wave velocities on the RED (surrogate) head. Mean incident pressure is measured at sensor C (see figure 5.1(a)) and surface pressures are measured at sensor locations shown in figure 5.1(c). Incident peak overpressure corresponding to sensor C is 0.23 MPa. The peak surface pressure at location 1 (forehead) is 0.553 MPa, thus the pressure amplification (the ratio of reflected pressure to incident pressure) is 2.40 due to fluid-structure interaction effects (i.e. $\Lambda = 2.40$). The peak surface pressure gradually decreases from locations 1 to 4 as the shock wave traverses the head. The pressure in the top region falls below the incident pressure ($\Lambda = 0.72$ for sensors 3 and 4). The sensor on the back side of the head record a higher pressure than those on the top and this pressure is equivalent to incident pressure

($\Lambda = 1.01$ for sensor 5). The shock wave velocity at incident blast site also increases over free field velocity due to fluid-structure interaction effects; and then gradually decreases as the shock wave traverses the head. The shock wave velocity between location 3, 4 and 5 falls below the free field shock wave velocity.

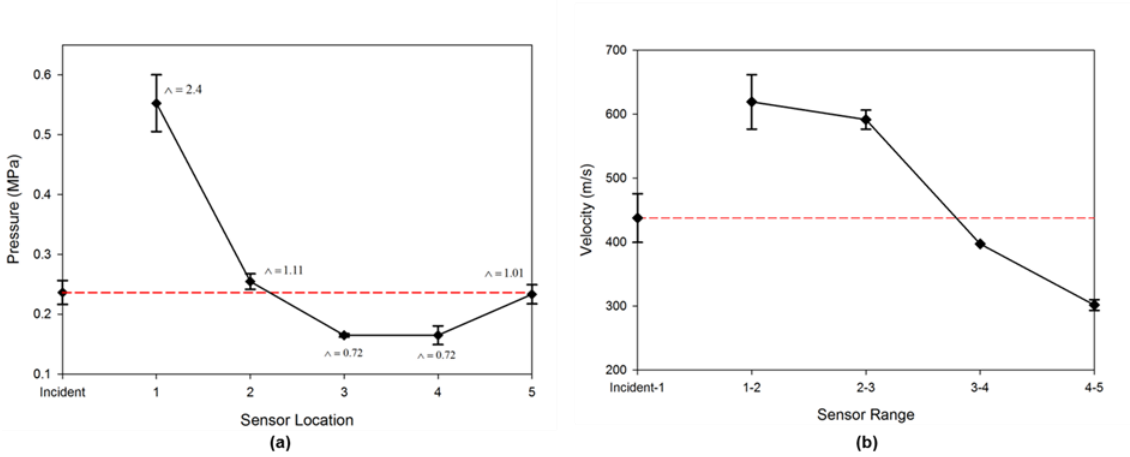

Figure 5.3: Mechanics of the blast wave head interactions for the surrogate head (a) experimentally measured incident (at sensor C) and surface pressures (corresponding to sensor locations of Fig. 5.1(c)) (b) Calculated incident and surface pressure velocities based on arrival times and distance between sensors

In order to assist in the understanding of this complex flow field, numerical simulations are carried out. The validation studies of the numerical simulations for the RED head are already presented in chapter 4. From numerical results, it is found that the flow field around the head is governed by the geometry of the head. Significant flow separation is observed on the top and sides (90°) of the head (figure 5.4 (a)). By flow separation we imply geometry induced flow separation (i.e. low pressure regions), it should not be confused with flow separation associated with viscous fluids. The velocity

in the top rear region falls below the free field velocity due to the flow separation effects. The blast wave traversing the head and the blast wave traversing the neck reunites at the back of the head (figure 5.4 (b)). This reunion causes an increase in pressure on the back side of the head. Several other studies [41, 79, 156, 175, 201] have shown that geometry of the head plays an important role in blast wave head interactions and the biomechanical loading of the brain. Our results elucidate that the flow dynamics strongly depend on geometry (shape, curvature) of a specimen and should be considered in understanding biomechanical loading pattern.

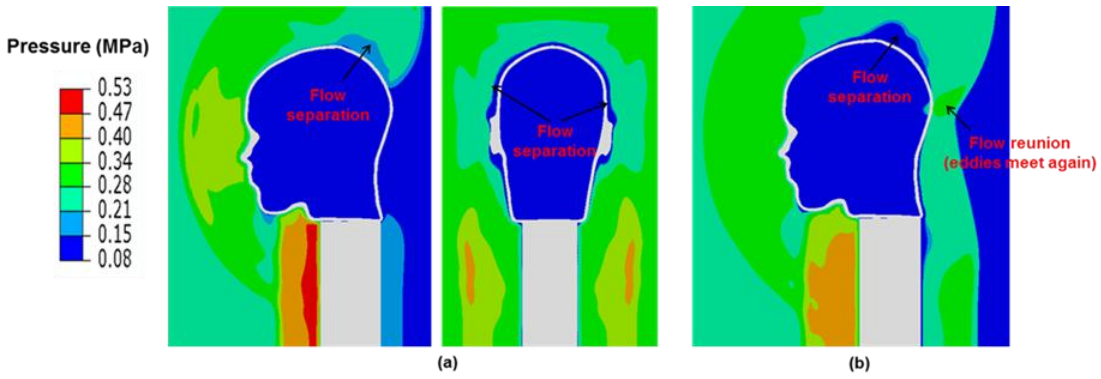

Figure 5.4: Flow mechanics around the head as the shock wave traverses the head

Pressure Amplification at the head interface due to fluid structure interaction:

As mentioned earlier, when a shock wave encounters a solid surface, the incoming shock wave pressure is amplified due to fluid-structure interaction. The amplification factor depends on the incident shock strength, the fluid medium in which shock wave travels, angle of incidence, geometry, elastic and inertial properties of the target and can vary from 2 to 8 (Anderson 2001). The pressure amplification at the interface of head due to incoming blast wave is studied using numerical simulations. The pressure distribution and the pressure history at fluid head interface are shown in figure 5.5. It can be seen that

pressure distribution at the interface of head due to incoming blast wave is non-uniform. Pressure amplification factor is different at different parts of the face depending upon their shape. The maximum peak overpressure is observed near the nasion (corner of the eye socket and the nose wall) with $\Lambda = 4.02$, as shown in figure 5.5. A number of numerical simulations (details not shown for brevity), clearly show that amplification factor is significantly higher for a concave geometry (compared to convex or flat), and further this factor depends on the radius of concavity and incident peak pressure. It is plausible that a concave surface reflects oncoming waves towards each other mutually reinforcing each other leading to a higher overpressure. These reinforcing waves explain why the nasion, which is concave, experiences the highest amplification factor.

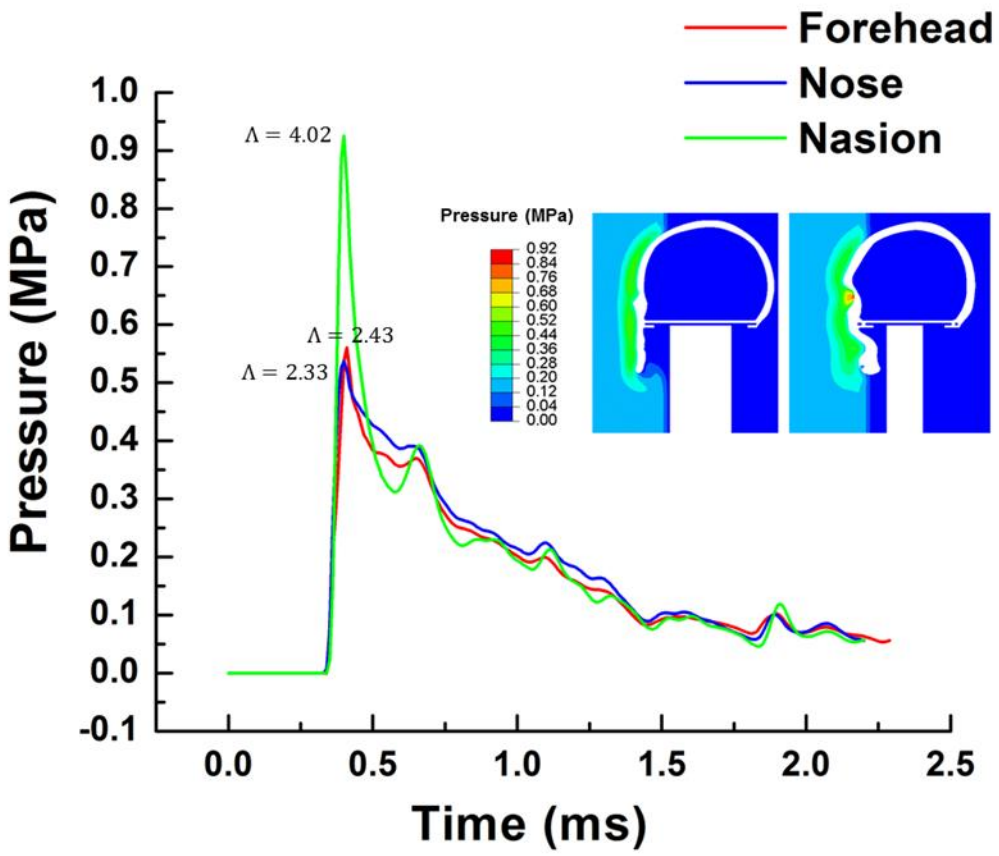

Figure 5.5: Pressure Amplification at the head interface due to fluid structure interaction

5.3.2 Mechanics of Blast wave human head interactions with the helmet

5. 3.2.1 flow field on the surface of the head with the helmet:

Figure 5.6 shows the pressure-time history on the surface of the head with and without the helmets. In general rise time and time to peak is increased and rate of pressure decay is decreased with the helmet. Peak pressures are reduced with the padded helmet at all locations as compared to no helmet case. For the suspension helmet, peak pressure is reduced at the incident blast site (sensor FH); on the contrary, peak pressures are increased on the side away from the incident blast side as compared to no helmet case. The positive phase impulse either remained equivalent or increased with the suspension and padded helmets as time to peak is increased and rate of pressure decay is decreased with the helmets.

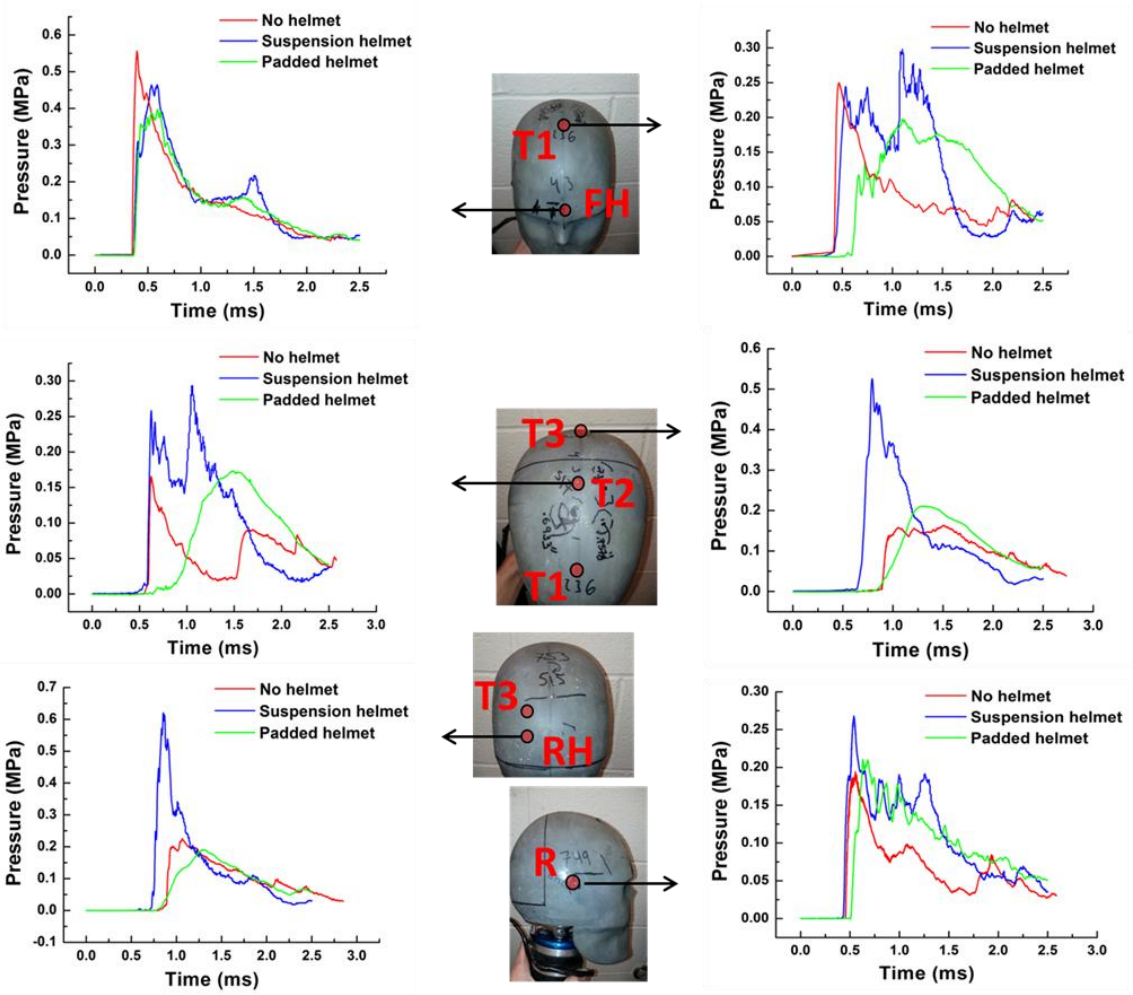

Figure 5.6: Pressure-time history on the surface of the head with and without the helmets

5.3.2.2 Comparison of experiments and numerical simulations for helmeted cases:

Numerical simulations are used to understand mechanics of flow field around the head with the helmet. Before using the numerical simulations for this purpose, numerical results are compared and validated against helmeted experiments. Figure 5.7 (a) and (b) shows comparison of surface pressures on the RED head with suspension and padded helmet respectively. For the suspension helmet, there is a reasonably good agreement between the experiment and numerical simulation, in terms of peak pressures (maximum

difference 26 %, minimum difference 0.3 %) and nonlinear decay. The simulation is able to capture majority of the features well, including the arrival of blast wave at a given location, shock front rise time, underwash (explained in detail in next section) beneath the helmet. For the padded helmet, fair agreement is obtained between the experiment and simulation. The huge difference is seen in the values of peak pressure and total impulse. This is due to the fact that it is very difficult if not impossible to know precise placement of padded helmet on the RED head in the experiments. Blast wave can enter through small gaps, if any, during the mounting of padded helmet on the RED head. In addition, porosity of the foam pads is not modeled in the simulations; which may contribute to the surface pressures.

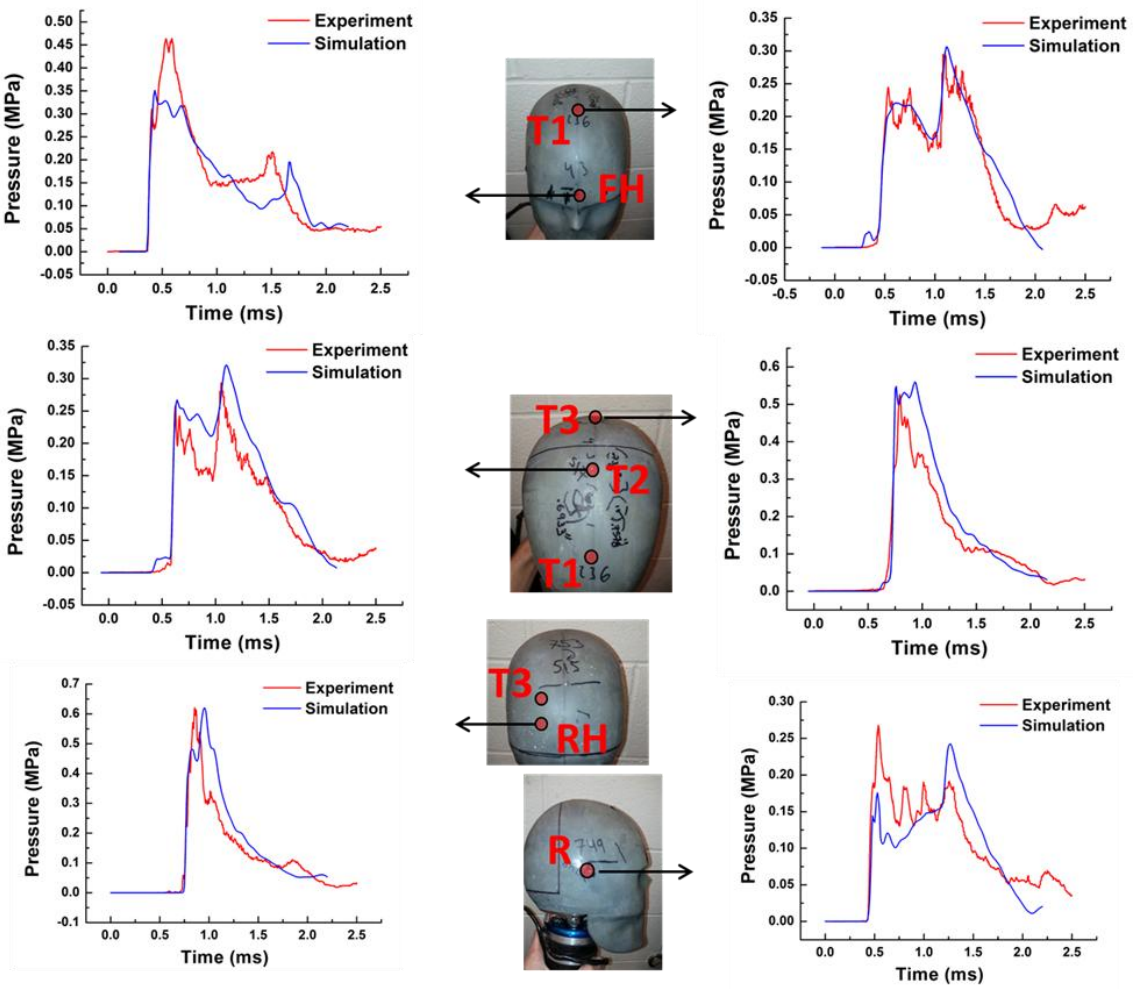
Experiment
Simulation
Pressure (MPa)
Time (ms)
T1
FH
T3
T2
T1
T3
RH
R

(a)

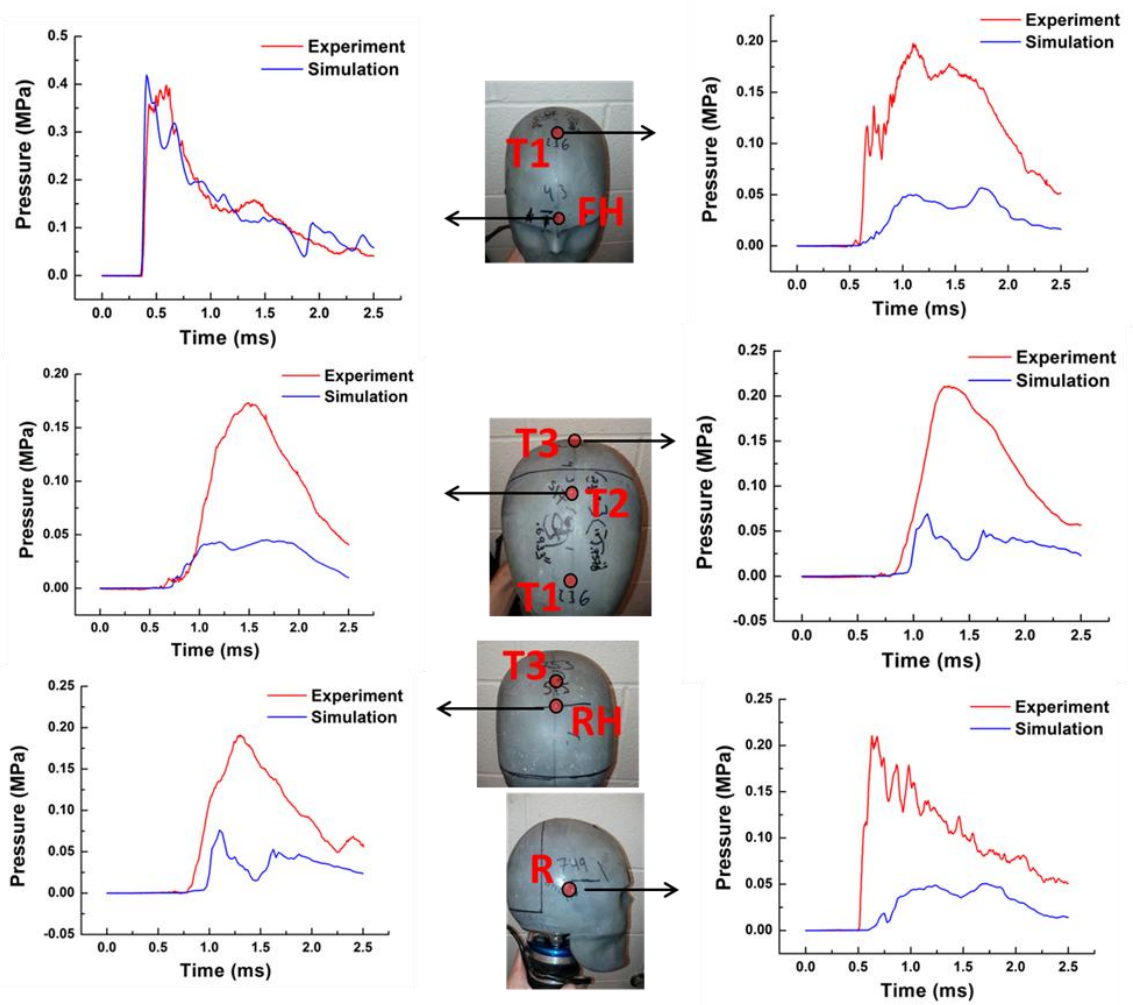

(b)

Figure 5.7: Comparison of surface pressures from experiments and numerical simulations on the RED head with (a) suspension and (b) padded helmet respectively

5.3.2.3 Underwash effect of the helmet

As indicated in previous sections, surface pressures are increased under the suspension helmet on the side away from incident blast side. This is due to the 'underwash' effect of the helmet. This 'underwash' effect is illustrated using numerical

simulations (figure 5.8). The blast front after encountering the head-helmet assembly divides into two fronts: one front travels around the outer perimeter of the helmet while the other front penetrates the gap between the head and the helmet (i.e. head-helmet subspace) and travels underneath the helmet towards the back of the head as shown in the figure 5.8(a). The blast front traveling outside the helmet reaches the rear of the helmet before the blast front traversing through the gap (figure 5.8 (b-i)), and eventually when these two blast fronts meet they focus at a region on the back side of the head (figure 5.8 (b-ii)). This focusing produces higher pressures on the head, away from the incident blast side when the location is shielded by the helmet. After this high pressure is generated, the high pressure air in the head-helmet subspace expands in all the directions (figure 5.8 (b-iii)).

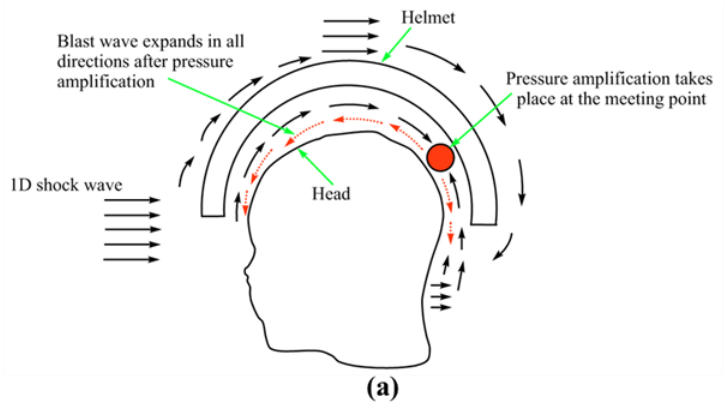

Figure 5.8: Underwash effect of the suspension helmet: (a) schematic explaining underwash effect of the helmet (b) flow field inside and outside of the head-helmet subspace.

To understand how the underwash influences both the local peak pressure and the impulse, it is postulated that the pressure intensification depends on the shape of the helmet (curvature) and the head-helmet subspace gap size with respect to the oncoming pressure wave and its characteristics e.g. pressure, velocity and rise/fall time. These aspects are studied in the following section using simplified two dimensional head models. It should be noted that local peak pressures in the head-helmet subspace and impulse transmitted to the head are analyzed as these quantities determine the effective load on the head.

5.3.2.4 Effect of curvature, head-helmet gap size and incident peak pressure intensity

To examine the effect of geometry, three different cases are considered. In the first case, the head and the helmet are modeled as cylinders, in the second case the head is cylindrical and the helmet flat and in the third case both the helmet and the head are flat (figure 5.9(a)). In all these cases there is constant gap of 13 mm between the helmet and the head. Figure 5.9 (b-i) and (b-ii) shows the pressure and impulse profiles at the back of the head-helmet subspace where the focusing occurs. It is clear from figure 5.9 (b) that the pressure and impulse are increased when both the shapes are cylindrical in comparison with the other two cases. This trend is the same when the incident overpressure is increased from 0.18 MPa to 0.52 MPa.

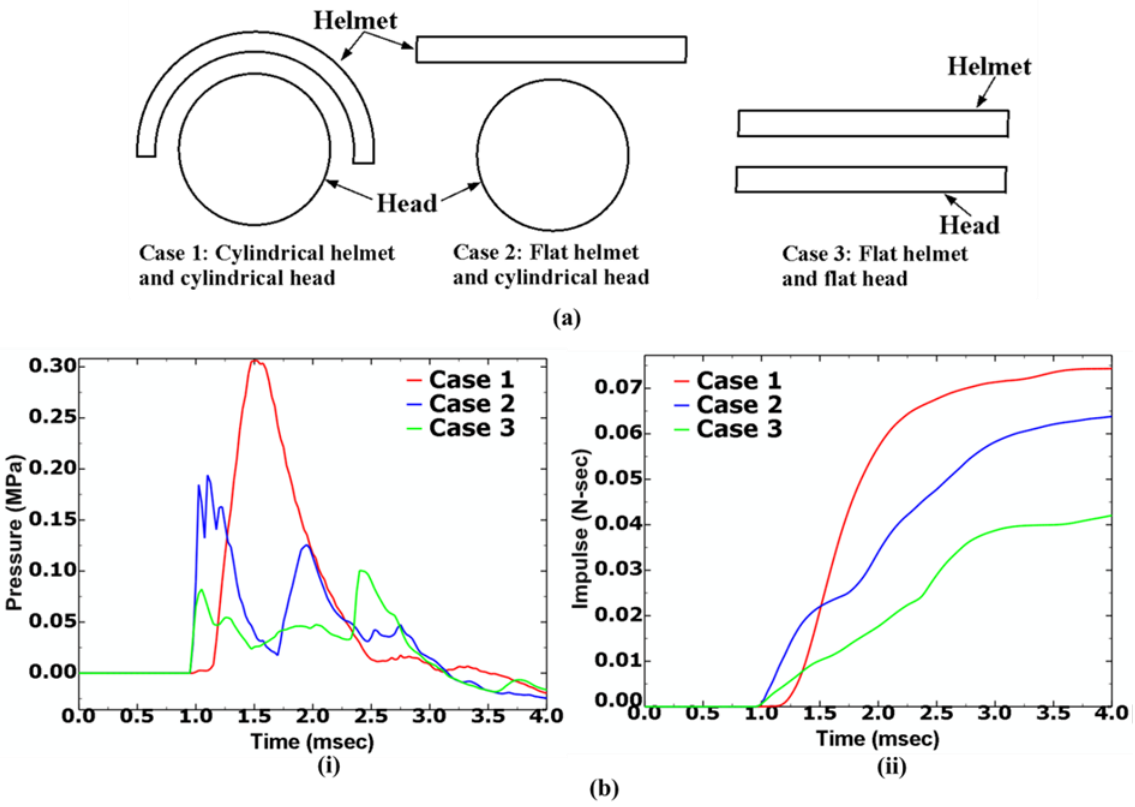

Figure 5.9: Effect of curvature of the helmet and the head: (a) modeling setup for studying curvature effect of the helmet and the head (b) (i) average pressure in the back region of the head-helmet subspace and (ii) total impulse transmitted to the back region of the head. Incident blast intensity 0.52 MPa.

Having identified that the cylindrical case offers the most severe loading conditions, this case is used to study the effect of head-helmet gap size and incident peak pressure intensity on the underwash. Figure 5.10 shows the P_{max}/P^* (normalized peak maximum overpressure) in the head helmet subspace as a function of gap size for different incident peak pressure intensities P*. As the gap is reduced, pressure in the gap increases ($P \alpha 1/V$, V-volume). Thus, P_{max}/P^* increases as the gap size is reduced till certain critical gap

size. Thereafter, the boundary effects become dominant and P_{max}/P^* decreases due to these boundary effects. It should also be noted that the P_{max}/P^* is increased as incident peak pressure intensity P* is increased. Numerical simulations indicate for the ranges tested, the angle θ at which P_{max} occurs is between 140 and 155°.

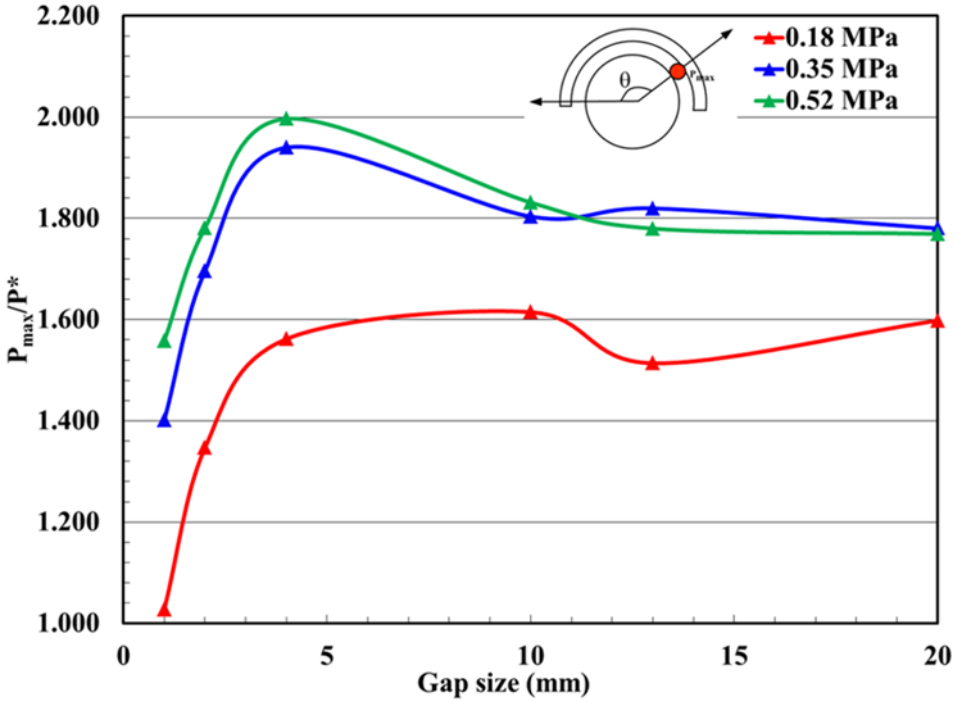

Figure 5.10: Normalized maximum peak overpressure in the head helmet subspace (P_{max}/P^*) as a function of gap size for different incident blast intensities P*

Another quantity of interest is the transmitted impulse, *I*, and depends on the maximum peak pressure, P_{max} and rate of pressure decay (i.e. rate of expansion) once P_{max} is established. Higher the P_{max} and lower the rate of pressure decay the higher is the impulse transmitted. As shown earlier the P_{max} increases as the gap size is reduced till critical gap size. The rate of pressure decay however decreases continuously (no critical gap size) as the gap size is decreased as shown in figure 5.11(a). This is due to fact that as

the gap size is reduced, there is not enough space for expansion and boundary reflection effects become dominant. Similar observations are reported by Rafaels et al. (2010) from their blast experiments on helmeted head. From our simulations it was found that, for a given incident peak pressure intensity P*, rate of pressure decay contributes more to impulse transmitted to the head than P_{max}. Hence, for a given incident peak pressure intensity P*, impulse transmitted to the head continuously increases as the gap size is reduced as shown in figure 5.11(b).

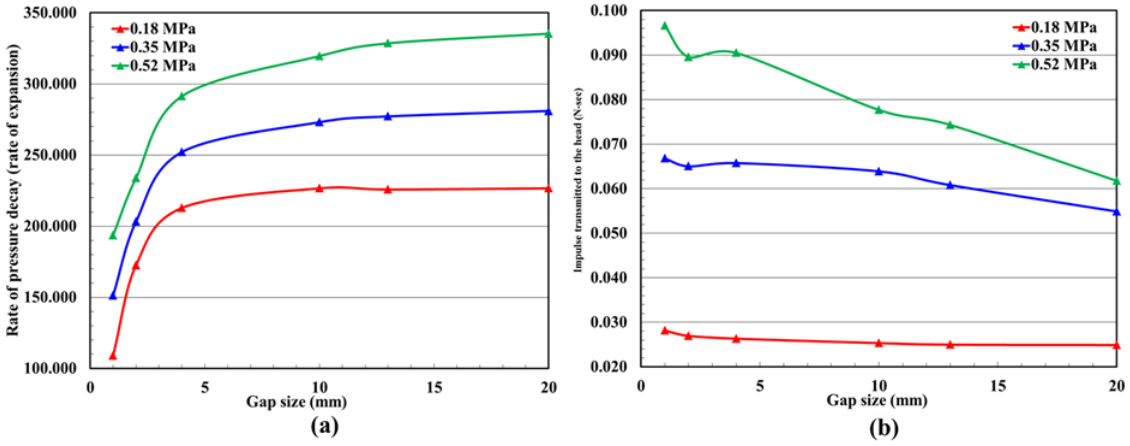

Figure 5.11: (a) rate of pressure decay in head-helmet subspace (b) impulse transmitted to the head as a function of gap size for different incident blast intensities P*

5.3.3 Effect of orientation on blast wave head interactions with and without head protection

As mentioned earlier, to study the effect of orientation on blast wave head interactions experiments were conducted on the RED head with four different orientations to the blast. These orientations are: front, back, side and 45°. The experiments are conducted with and without the helmets and each scenario was repeated

three times. Blast wave head interactions are studied by monitoring surface pressures on the RED head and experimental observations are elucidated with the help of validated numerical models. Role of the head orientations is studied by understanding the mechanics of the blast wave head interactions for no helmet, suspension helmet and padded helmet cases.

5.3.3.1 Peak surface pressures around the head for various head helmet configurations

(a) No helmet case:

Figure 5.12(a) shows the experimentally measured peak pressures for the no helmet case for each head orientation. Pressure at the incident blast site is amplified ($\Lambda = {p_R}/{p_I}$) by 2.40, 2.79, 2.38 and 1.39 times the incident pressure for front, back, side and 45° orientations respectively due to aerodynamic effects. This amplification factor (Λ) is based on the mean values of the incident and reflected pressures for each orientation.

For front orientation, pressure gradually decreases from sensor FH to T1 to T2. Sensors T2 and T3 record equivalent pressures. There is a slight increase in pressure from sensor T3 to sensor RH which is located on the side opposite to the incident blast side. A similar trend is observed for back orientation but in reverse order (i.e. from sensor RH to sensor FH). For these orientations, sensor R records pressure equivalent (within $\pm$ 2 %) to sensor T2. For side orientation, sensor R (i.e. the sensor facing the blast) records the highest pressure; and all sensors in the midsagittal plane record equivalent pressures. Sensor L (i.e. the sensor opposite to the blast side) records marginal pressure. For the 45°

orientation, trend similar to the front orientation is observed; but the flow reunion takes place near sensor T3 (as indicated by increase in pressure) due to tilt.

(b) Suspension helmet case:

Figure 5.12(b) shows experimentally measured peak pressures for the suspension helmet case for each head orientation. With the suspension helmet, pressure at the incident blast site is amplified by 2.03, 0.94, 1.36 and 2.74 times the incident pressure for front, back, side and 45° orientations respectively. The pressure field around the head is complex and does not follow any fixed pattern of variation. In general, pressures are increased on the side away from the incident blast side.

(c) Padded helmet case:

Figure 5.12(c) shows experimentally measured peak pressures for the padded helmet case for each head orientation. With the padded helmet, pressure at the incident blast site is amplified by 1.93, 0.63, 1.26 and 2.68 times the incident pressure for front, back, side and 45° orientations respectively. Sensors FH and R record higher pressures as compared to the other sensors irrespective of the orientation; as these sensors are not fully covered by the foam pads. All other sensors record equivalent pressures for a given orientation.

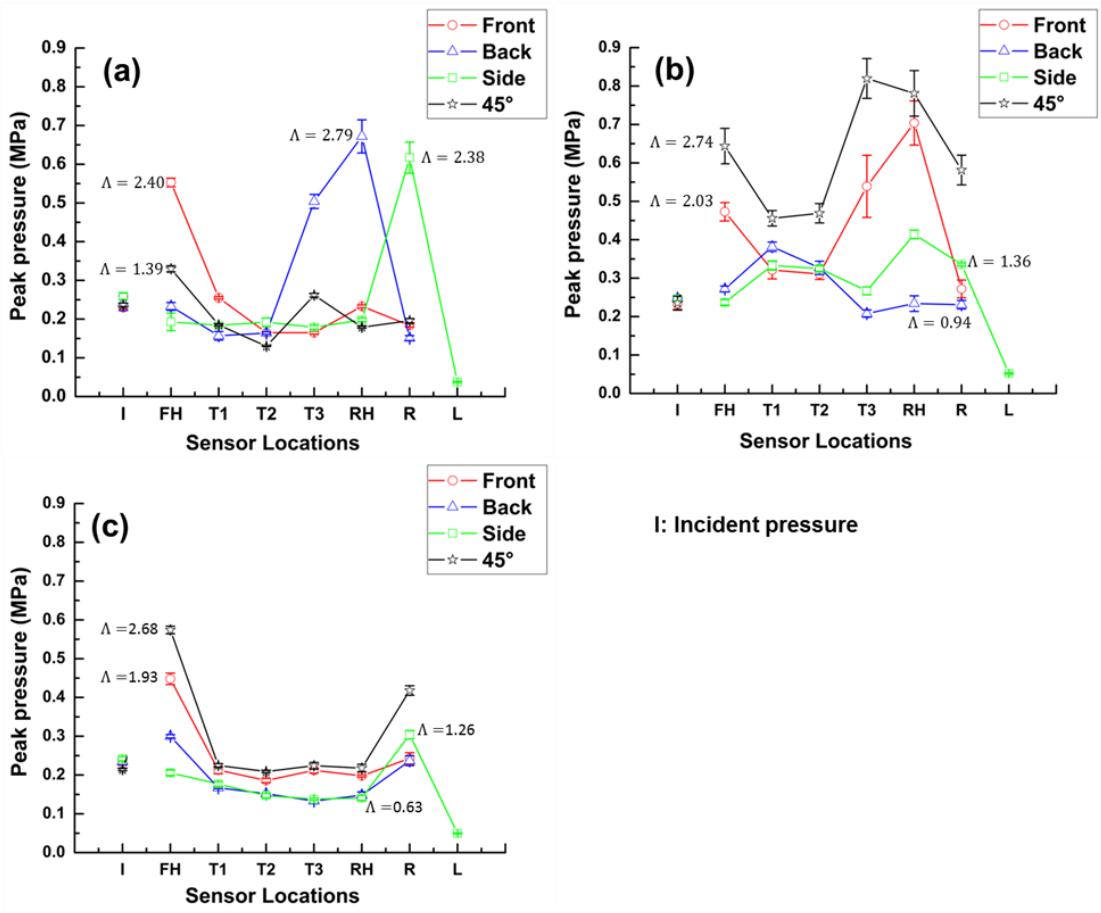

Figure 5.12: Peak pressures recorded by the sensors for various orientations: (a) no helmet (b) suspension helmet (c) padded helmet. (Experiment).

5.3.3.2 Total impulse around the head for various head helmet configurations

Total impulse (positive phase, I^+) is obtained by integrating pressure over time ($\int P\, dt$). Total impulse shows similar trends as peak surface pressures for all head helmet configurations and for all orientations. Total impulse plots are not shown for brevity.

5.3.3.3 Results from Numerical Simulations:

As stated earlier, numerical simulations are conducted to understand and explain some of the experimental observations. Figure 5.13 shows the flow (pressure) field around the head for various head orientations for no helmet case. The flow field around the head is complex. Orientation of the head to the blast wave governs the flow mechanics around the head.

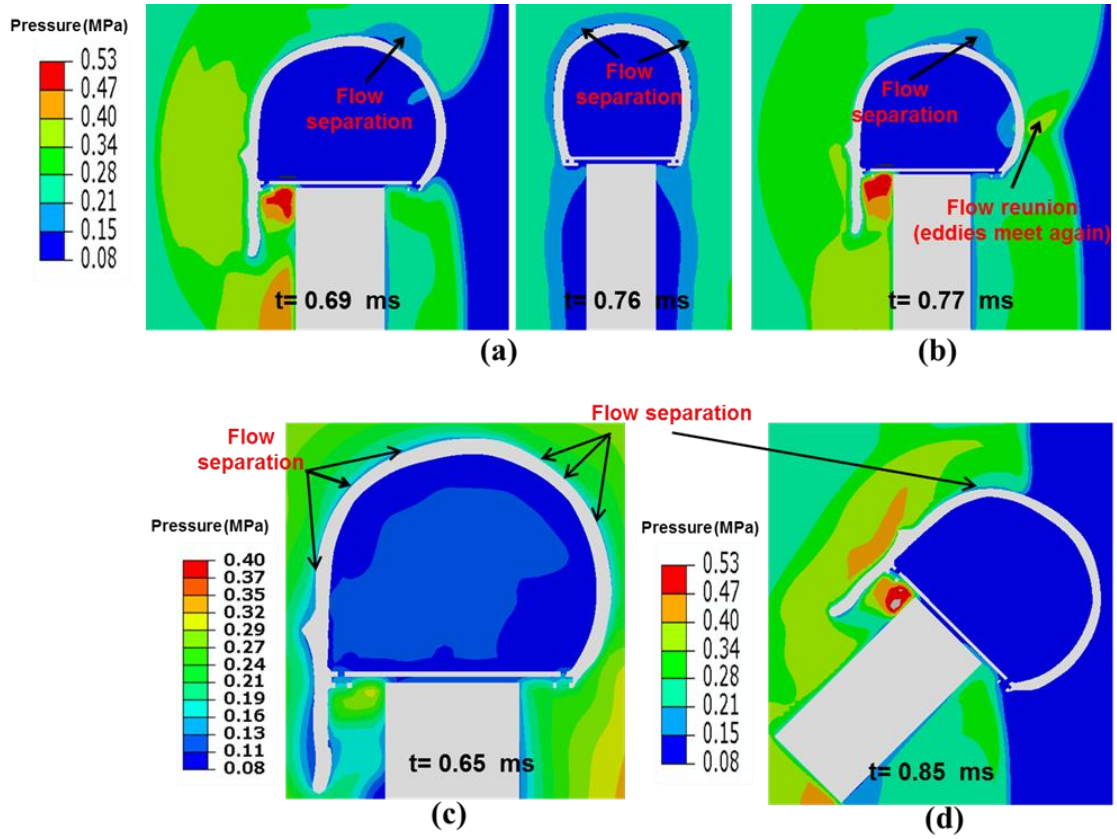

Figure 5.13: Flow mechanics around the head: (a) Flow separation on the top and sides of the head for front orientation (b) flow reunion on the back of the head for front orientation (c) Flow separation along the midsagittal plane for side orientation (d) Flow separation near the face for 45° orientation.

Figure 5.14 shows the pressure field in helmet head subspace (at incident blast site) for each orientation for suspension helmet case. Least pressures in the helmet head subspace at incident blast site are observed for back orientation.

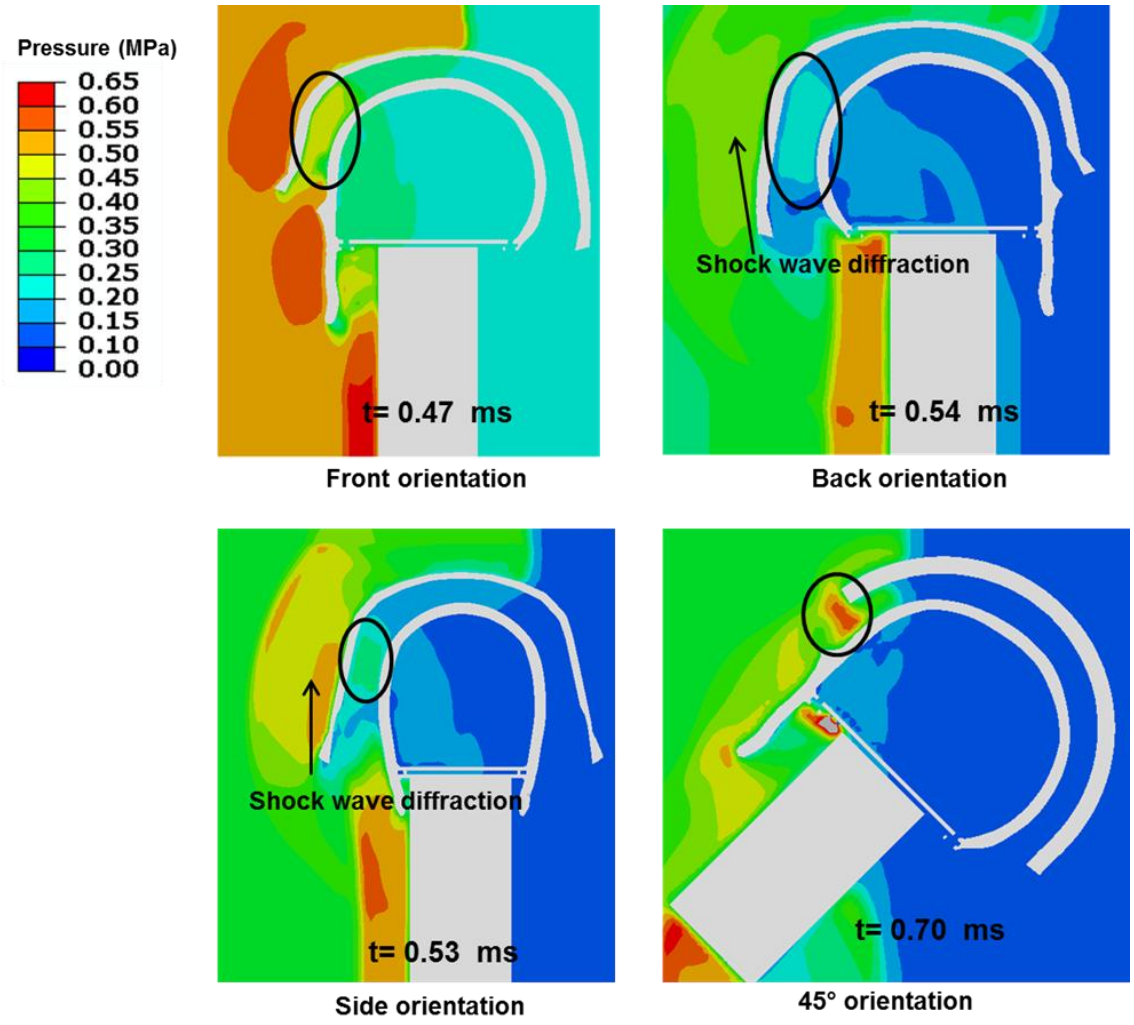

Figure 5.14: Pressure contours in helmet head subspace at incident blast site for each orientation. Least pressures in the helmet head subspace at incident blast site are observed for back orientation due to shock wave diffraction around outer surface of the helmet. Suspension helmet case is used for illustrations.

Figure 5.15 shows pressure field in the head helmet subspace (away from incident blast site) for each orientation for suspension helmet case. From the pressure field it can be seen that, pressures are increased under the suspension helmet on the side away from the incident blast side. This also confirms the presence of underwash effect for back and side orientations. Varying degree of pressure intensification is observed depending upon the orientation of the head and the helmet to the blast wave. The simulation results are consistent with experimental observations.

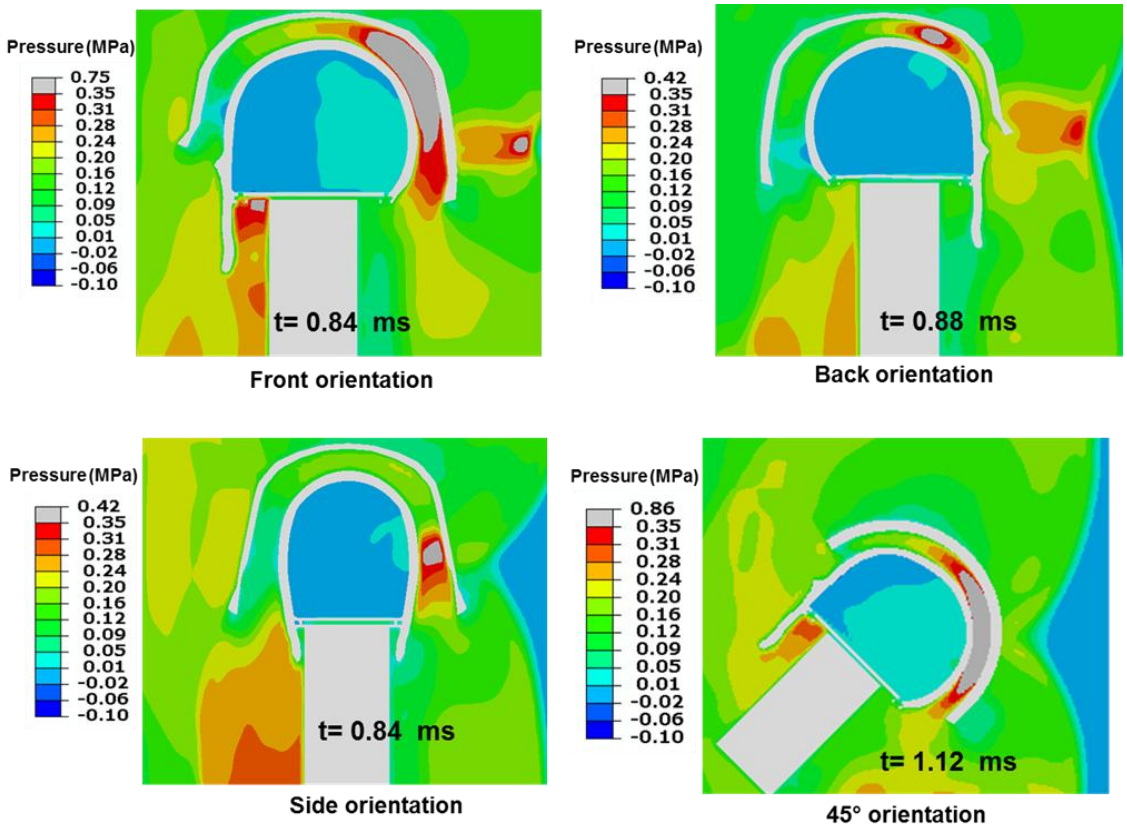

Figure 5.15: Pressure intensification on the side away from incident blast side for the suspension helmet. Varying degree of intensification is observed for various orientations

due to geometric effects which governs flow field within the head-helmet subspace. Maximum intensification is observed for 45° orientation.

5.3.3.4 Discussion on orientation dependent blast wave head interactions:

The present results validate both the hypotheses postulated in this work: (i) external pressure field on the surface of the head depends on whether the wearer has suspension, padded or no helmet. (ii) Orientation of the head to the blast wave governs the pressure field experienced by the head, for a given head helmet configuration. In this section, the results are discussed in the context of these hypotheses.

The blast wave head interactions are quite complex as evident from the surface pressure patterns and the values of Λ at the incident blast site for various orientations for various head helmet configurations (Figure 5.12). For no helmet case (Figure 5.12(a)), statistically similar amplification at the incident blast site is observed for front and side orientations (p=0.81) and a higher amplification for back orientation (p_{max}=0.019). The amplification for 45° orientation is lower (p_{max}=0.006) due to flow separation at the face and as sensor is not present at exact incident site due to 45° tilt (Figure 5.13(d)). The Λ depends on the incident blast intensity, the angle of incidence, the mass and the geometry of the target, boundary conditions and can vary from 2 to 8 [156, 206]. By geometry we imply geometrical features, such as topology and area of exposure. At the plane of specimen blast wave interaction, the different geometrical features have different effects. For suspension and padded helmet cases (Figure 5.12 (b) and (c)), Λ at the incident blast site for each orientation is statistically different. For these cases, Λ is

governed by the geometry of the helmet, the head helmet configuration and its orientation to the blast.

In order to better understand surface pressure patterns and hence the flow fields around the head, numerical simulations are used. First, the flow field around the head for no helmet case is presented. Once the blast wave impinges the head, flow separation occurs, as is evident from the values of the recorded pressure for the senor next to the incident blast site (Figure 5.12 (a)). For example, pressure reductions of 53.89 %, 25 %, 67.91 % and 43.94 % are observed for front, back, side and 45° orientations respectively for the sensor next to the incident blast site. Flow separation causes low pressure zones (e.g. top and sides of the head (Figure 5.13(a))); thus pressures are further reduced as we move away from the incident blast side (Figure 5.13(a)). Blast wave traversing the head and blast wave traversing the neck reunite on the side opposite to the incident blast side (Figure 5.13(b)). This flow reunion causes an increase in pressure; e.g. sensor RH for front orientation, sensor FH for back orientation and sensor T3 for 45° orientation (Figure 5.12(a)). For the side orientation, flow separation occurs before the blast wave reaches the midsagittal plane (Figure 5.13(c)), thus all the sensors on the midsagittal plane record similar pressures (Figure 5.12(a)). This flow separation is further enhanced as the blast wave reaches the side opposite to the incident blast side; hence, the corresponding sensor (sensor L) records very low pressure. Flow separation for the side orientation is attributed to a larger area facing the blast. Numerical simulations clearly show that the surface pressures and the flow field around the head are strongly governed by the geometry of the head. Several other studies [41, 79, 156, 175, 201] have also shown that the geometry of

the head plays an important role in the blast wave head interactions and hence in the biomechanical loading of the brain.

Figure 5.16 shows peak pressure plots for no helmet, suspension helmet and padded helmet cases superimposed on each other for each head orientation. Table 5.2 shows the percentage reduction in peak pressures at the incident blast site for suspension and padded helmet cases as compared to the no helmet case. By comparing the values of peak pressures (Figure 5.16 and Table 5.2) at the incident blast site, it can be seen that varying degrees of pressure reductions at incident blast site are observed for suspension and padded cases as compared to the no helmet case. Back and side orientations show statistically significant reductions ($p<0.05$) in pressure under the helmet, but only marginal reductions are seen under the helmet for front orientation ($p>0.05$). For front orientation, part of the oncoming blast wave contributes to the pressure as the helmet does not cover the forehead completely (Figure 5.14). 45° orientation does not show reduction in peak pressure at the incident blast side (i.e. sensor FH). In contrast, for 45° orientation, peak pressures are increased by 95.13 % and 73.94 % for the suspension and padded helmet cases respectively compared to the no helmet case. This is due to: (i) flow separation at the face for the no helmet case (Figure 5.13(d)) and (ii) In contrast to flow separation for no helmet case, blast wave is directed in the head-helmet subspace for the suspension and padded helmet cases (Figure 5.14). Of all orientations, maximum reduction in pressure (65.18 % and 77.98 % respectively for suspension and padded helmet cases) at the incident blast site compared to no helmet case is observed for the back orientation (Figure 5.16 and Table 5.2). The helmet has a larger area and height on

the back than the front or the side. Thus helmet diffracts and blocks the oncoming blast wave offering maximum protection as shown in Figure 5.14. Zhang and Makwana [202] have also found maximum reduction in peak intracranial pressure for the back orientation from their numerical simulations.

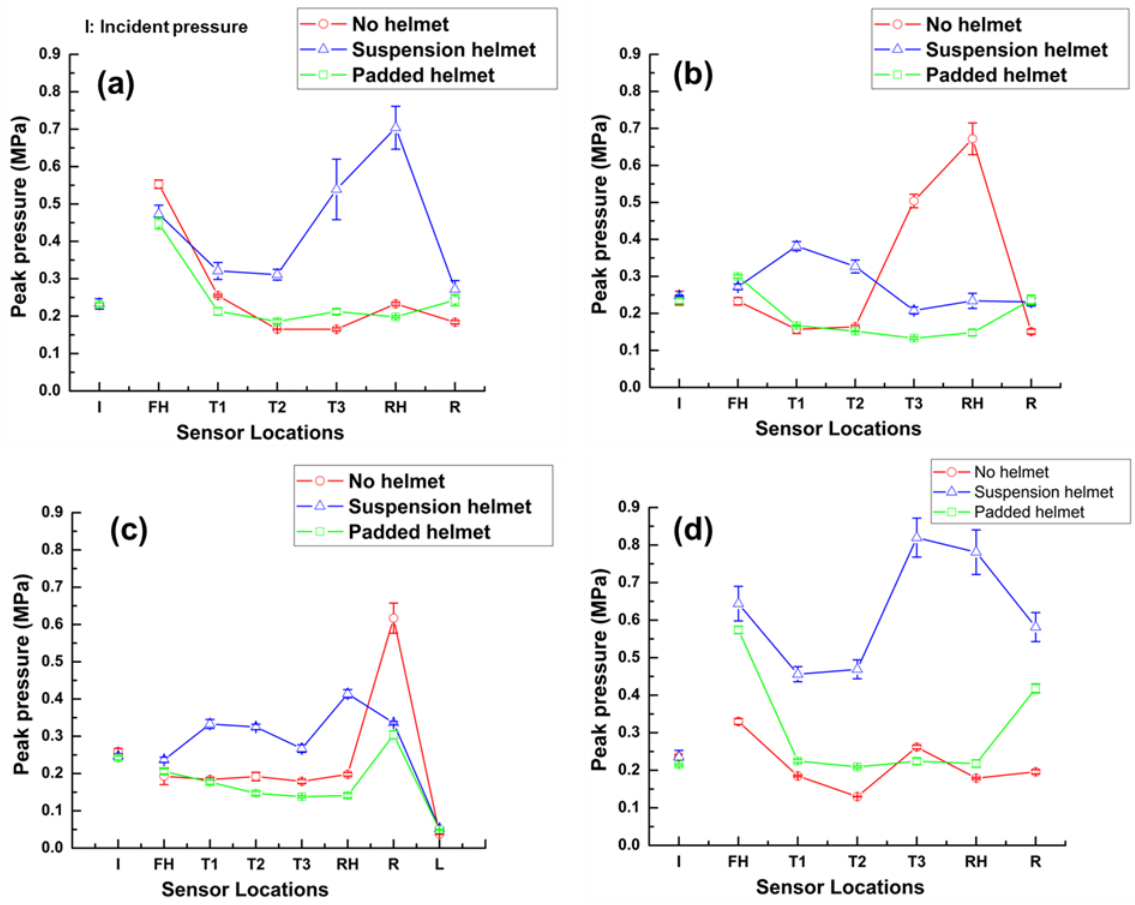

Figure 5.16: Peak pressures for no helmet, suspension helmet and padded helmet cases superimposed on each other for various orientations: (a) front (b) back (c) side (d) 45°

Table 5.2: % reduction in peak pressures at incident blast site for suspension and padded helmet cases as compared to no helmet case. Peak Pressures are based on mean values

Orientation	Peak Pressure incident blast site (MPa)			% reduction in peak pressure	
	No Helmet	Suspension Helmet	Padded Helmet	Suspension Helmet	Padded Helmet
Front	0.55	0.47	0.45	14.47	18.99
Back	0.67	0.23	0.15	65.18	77.98
Side	0.62	0.34	0.30	45.54	50.73
45°	0.33	0.64	0.57	-95.13*	-73.94*

*Negative number suggest increase in pressure as compared to no helmet case

Pressures are increased under the suspension helmet on the side away from the incident blast side (Figure 5.16). This is due to the 'underwash' effect of the helmet. For orientations studied, maximum underwash (i.e. pressure intensification) under the suspension helmet is observed for the 45° orientation followed by the front orientation (see sensor RH Figure 5.16). This is mainly due to two reasons: (i) orientation of the head helmet configuration to the blast; and (ii) the geometry of the helmet. For the 45° orientation, the blast wave penetrates the head-helmet subspace (i.e. gap) more effectively from both sides (Figure 5.15). The blast wave is continuously directed in the head-helmet subspace from the face due to tilt. As mentioned earlier, back of the helmet has larger area and height than the front. Thus, for the front orientation, blast wave traversing the neck and blast wave traversing outside the helmet, after reaching the head-

helmet subspace, engulfs the head-helmet subspace (due to geometric effects) and cause higher intensification. For other orientations, this engulfment is less intense (Figure 5.15) due to the shorter height of the helmet in the corresponding regions. It should be noted that, for front and 45 degree scenarios, the maximum surface pressure recorded by the RED head with the suspension helmet (P_{max} = 0.76 and 0.87 for front and 45° orientations respectively) exceeds the maximum surface pressure recorded in the no helmet case (P_{max} = 0.56 and 0.34 for front and 45° orientations respectively).

Underwash effect is not seen for the padded helmet case, as evident from figure 5.16. However, equivalent pressures are seen on the top region of the head (sensors T1-T3) as compared to no helmet case (figure 5.16). This indicates that additional pathways/modes of energy transfer exist under the padded helmet. Thus, performance of the foam pads under the blast loading conditions needs further investigation to identify these pathways/modes.

5.4 Summary:

The role of helmets in mitigating the effect of primary shock waves is not clearly understood. Though the current helmets have not been specifically designed for preventing blast induced TBIs, understanding the critical issues related to current helmets are important for developing better helmets against shock blasts. In this work, the primary shock-wave interactions for various helmet head configurations were evaluated. Coordinated experimental and computational studies have provided cross-validation and a deeper understanding of the flow physics involved when a blast wave impinges energy onto a helmeted head. The pressure and impulse intensification effects were elucidated as

a function of geometry, head-helmet gap and surface curvature. In addition, the role of orientation on the mechanics of the blast wave head interactions for various head helmet configurations is also studied.

Some of the key findings of this work are:

- When a blast wave encounters the head helmet complex, the flow field around the head is not uniform. The geometry of the head and the helmet, their configurations and their orientations with respect to the blast govern the flow dynamics around the head, the flow separation and the flow reunion; these factors in turn determine the surface pressures. Curvature of the helmet and the head has a significant influence on the pressure and loadings experienced by the head.
- When a shock wave encounters human head, the highest reflected overpressure occurs in the concave region, notably at nasion (the nose-eye cavity). The reflected overpressure increases by 4.02, 2.33 and 2.43 times the incident overpressure at nasion, nosetip and forehead respectively for an incident blast intensity of 0.20 MPa.
- For the no helmet case, surface pressures gradually decrease as the blast wave traverses the head. Maximum flow separation is observed for side orientation as large surface area is exposed to the incoming blast. For front, back and 45° orientations, a slight increase in surface pressure with respect to the top and the side of the head is observed at the site opposite to the incident blast site due to flow reunion.
- In general, the helmet (either suspension or padded) reduces pressure at the incident blast site as compared to no helmet case. Pressure reductions at the incident blast site vary depending on the head helmet configurations and their orientations with respect

to incident blast. Maximum reduction in pressure at the incident blast site is observed for the padded helmet back orientation case.

- When a gap exists between the head and the helmet, blast wave focus under the helmet (underwash) on the side away from incident blast side, increasing surface pressures experienced by the head. The underwash effect is first predicted using numerical simulations and later confirmed by carefully designed shock tube experiments. Simulations and experimental results are in good agreement.
- The degree of underwash is governed by the geometry of the head and the helmet and its orientation to oncoming blast. Maximum underwash is observed for the suspension helmet 45° orientation case.
- When a gap exists between the head and the helmet, there is an increase in overpressure and impulse on the rear side of the head due to underwash. This increase is a non-linear function of gap size and incident overpressure.
- Tight foam pads between the head and the helmet eliminate the impulse and overpressure increase. This case offers the best protection, preventing any pressurization in the head-helmet subspace (gap). The maximum reduction in the overpressure and impulse with the pads are observed to be 86.08 % and 20.15 % respectively.
- Orientation dependent responses predicted by the experiments and numerical models suggest that direction-specific tolerances are needed in the helmet design in order to offer multi-directional protection for the human head under blast loading.

CHAPTER 6

STUDIES ON POST-MORTEM HUMAN SPECIMEN (PMHS) HEADS

6.1 Introduction

In this chapter response of PMHS head is studied using shock tube experiments. As mentioned in chapter 2 on literature review, many warfighters are diagnosed with mTBI or PTSD upon their return from OEF and OIF, and most of them have been exposed to repeated blasts due to IEDs. Since many of the medical outcome measures (e.g. cognitive problems such as impaired learning, forgetfulness, attention and concentration difficulties, changes in personality such as impulsiveness and reduced insight) are common to both mTBI and PTSD, it is not clear whether they suffer from either, both or neither. Since mTBI from blasts should be initiated by mechanical insults at the cellular, tissue or organ levels the basic question is if a subject is exposed to blasts from explosives at a far enough stand-off distance, does the victim experience any mechanical insult in the brain parenchyma. So the basic scientific question is if and how does the shock-blast wave enter the brain past the skull? The mechanical excursion can be in the form of intracranial pressure, shear stress, strain, or energy in the local region and can vary both spatially and temporally when subjected to different levels of incident blast overpressures. Recent works by a number of research groups including some from our own laboratory have clearly shown that animal models experience pressure pulses in the brain when subjected to primary blast conditions [157, 195, 207-218]. However, since the

shape, size, thickness, and the morphology of the skin and skull as well as the structure of the brain are different for animal models compared to humans; these results cannot be directly translated. In addition, simplified models using surrogates may or may not be able to reproduce similar biomechanical response to blast induced mechanical insult as seen by humans. Hence some direct experiments with PMHS heads can at least resolve some of the basic questions. PMHS are the next best surrogate to live humans, and can be subjected to controlled levels of different blast overpressures (BOP). By measuring intracranial pressures directly in different regions of the brain, we can then examine the relationship between BOP and ICP. If ICP is found to be a function of BOP, we can then explore the loading mechanisms and various parameters that affect the magnitude and the spatio-temporal variations of ICP.

In this chapter, the response of PMHS heads is studied using three PMHS heads that are subjected to primary blast of varying peak incident intensities or overpressures (70 kPa, 140 kPa and 200 kPa). The chapter is organized as follows. In section 6.2, we describe the details of the experiments that include PMHS preparation, instrumentation and mounting of gauges, simulated blast loading conditions, data acquisition and analysis. In section 6.3, we present the results of PMHS experiments in terms of time histories of incident, surface and ICP profiles and strain gauges. Analysis of peak ICPs and ICP impulse is next presented. In the final part of this section, results of PMHS experiments with the suspension and padded helmets are presented. In section 6.4, these results are discussed in terms of mechanics of the blast wave head interactions on the surface of the head and subsequent propagation through skin-skull-brain parenchyma.

The key parameters governing ICP response are also discussed. Experimentally obtained peak ICP values are compared against established injury thresholds based on blunt impacts. Shearing and von Mises stress and principal strain values calculated from the validated numerical model are also compared against established injury thresholds. In section 6.5, the key findings of this chapter are summarized.

6.2 Experiments:

6.2.1 PMHS testing in the 28" Shock tube

The details of the shock tube are provided in chapter 5. The PMHS heads are used in conjunction with the Hybrid III neck in these experiments. The head assembly is placed in the test section of the shock tube as shown in figure 6.1(b), and is subjected to frontal blast loading. Experiments are also conducted with the helmets mounted on PMHS heads. The shape, overpressure and duration of the incident blast wave at a given location are known a priori. This is achieved through sample trials in the shock tube, conducted without the surrogate head and the neck.

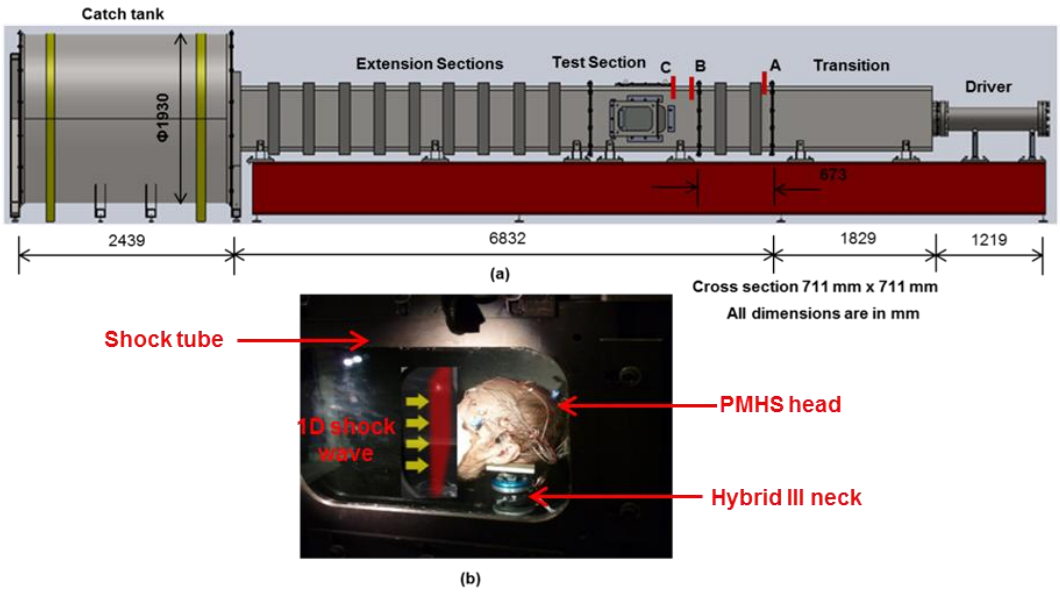

Figure 6.1: Experimental setup (a) Schematic of the 711 mm x 711 mm shock tube system (b) PMHS heads with hybrid III neck placed in the test section of the shock tube

6.2.2 PMHS preparation

A total of three PMHS heads were used in the current study. PMHS heads were obtained from the 'University of Virginia Center for Applied Biomechanics' laboratory. All specimens were handled, prepared and used in accordance with local and federal laws. Ethical guidelines and research protocol approved by the University of Nebraska institutional review panel for PMHS use were also followed. The specimen had no record of osseous disease and pre-existing fractures were not present as confirmed by CT imaging. The age, gender, and basic anthropometry of the specimen are listed in Table 6.1.

PMHS specimens were not fresh and had been kept refrigerated at 'University of Virginia Center for Applied Biomechanics' laboratory for several months. All heads were

thawed/defrosted 24 hours prior to the testing. Since PMHS heads were not fresh, brain was significantly degraded (for each specimen). Thus, the brain was removed from each PMHS head and intracranial space was backfilled with ballistic gelatin. The brain tissue and dura mater were removed through foramen magnum using flat head screw driver. '20% ballistic gelatin' (ballistic gel, from here on) was prepared by dissolving 2 parts of '250 bloom gelatin' into 9 parts of warm (@40 °C) water (by mass), stirring the mixture while pouring in the powdered gelatin. The gelatin is obtained from Gelita USA Inc. (Sioux, IA) in the bloom form. The ballistic gel is poured in the intracranial cavity through foramen magnum and allowed to settle at room temperature. After ballistic gel is settled the entire head was put inside the plastic bags and air bubbles were removed using vacuum cleaner. The foramen magnum was sealed using filler material (Bondo®). Hybrid III neck was attached to the head using base plate. Base plate was screwed to the bottom of the head.

In separate experiments, ballistic gel was characterized by subjecting them to planar blast wave. The experiments were designed such that wave propagation in the ballistic gel was one dimensional (1D). The PCB pressure sensors were mounded on the front and rear planes (ends) of ballistic gelatin. Wave velocity in ballistic gel was calculated from arrival times of blast wave at front and rear planes and distance between them. The calculated wave velocity was 1583±118 m/s, which was close to the longitudinal wave speed of water. Characterization of ballistic gel is important in understanding PMHS results as well as for use in numerical simulations.

Table 6.1: Characteristics of the three PMHS heads tested in this study

PMHS sr. no.	PMHS ID	Sex	Age	Height (cm)	Weight (kg)	Cause of death
1	421	M	72	175	68	prostate cancer, diabetes
2	476	M	75	173	79	cardiovascular disease
3	513	M	65	175	73	Prostate cancer

6.2.3 Instrumentation

Each PMHS head is instrumented to measure surface pressures, surface strains and intracranial pressures (ICP's). A total of 11 sensor measurements are made on each PMHS head. Surface pressures are measured at two locations, surface strains are measured at four locations and ICP's are measured at five locations within the head as shown in figure 6.2 (a). CT images of the instrumented head were also taken using CT machine available at UNL. CT images were used to verify locations of the sensors inside the head (figure 6.2 (b)). In addition, CT images were also useful in identifying precise geometry of skull and the face in the vicinity of the sensor; by geometry we imply anatomical features such as air sinus, eye socket, nasal cavity. For example, huge air sinus was present in front of the certain sensors (see figure 6.2 (b) nose ICP). Surface pressures are measured using Kulite surface mount sensors (model LE-080-250A) and intracranial pressures are measured using Kulite probe sensor (XCL-072-500A). The sensing elements can measure the absolute pressure from 0-250 psi (0-1.72 MPa) with a

nominal calibration of 0.400 mV/psi (58.02 mV/MPa) using 10 volts excitation. Surface strains are measured using Vishay strain gauges (model CEA-13-250UN-350).

In addition to these sensors, PCB pressure gauge (model 134A24) is used to measure incident (side-on) pressure of the blast wave. Incident pressure is measured just before (distance =200 mm) blast wave encounters the PMHS head. Incident pressure gauge is mounted on the wall of the shock tube (at location 'C' of figure 6.1(a)). All pressure sensors utilized in experiments are calibrated under shock loading conditions using a separate 101 mm (4") diameter shock tube. Accurate calibrations are achieved by generating precisely controlled shock wave velocities and invoking the Rankine-Hugoniot jump conditions to relate shock wave velocity to shock wave overpressures.

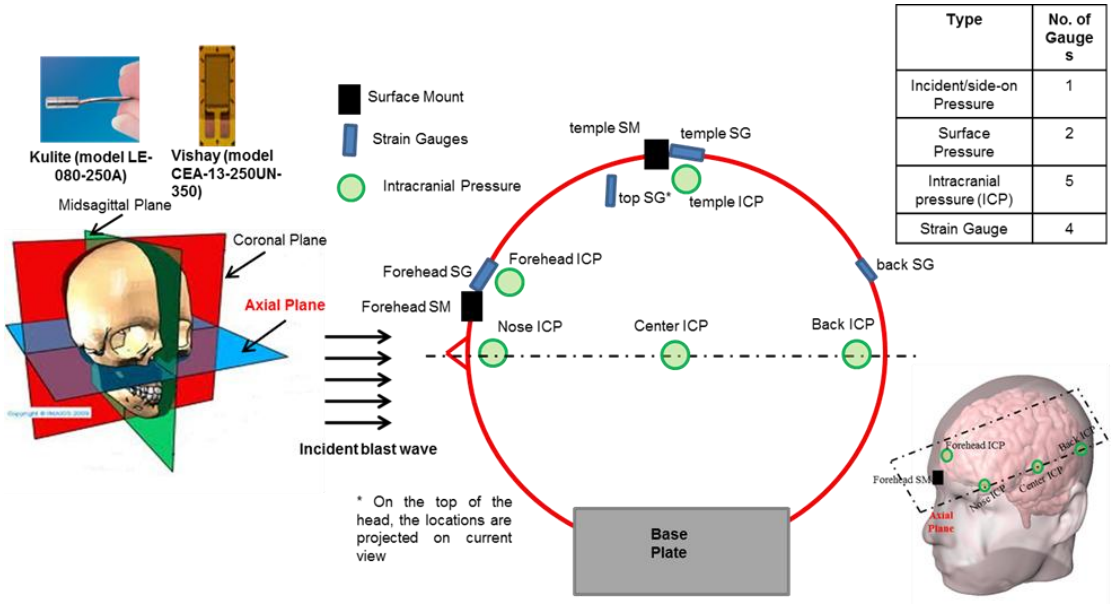

(a)

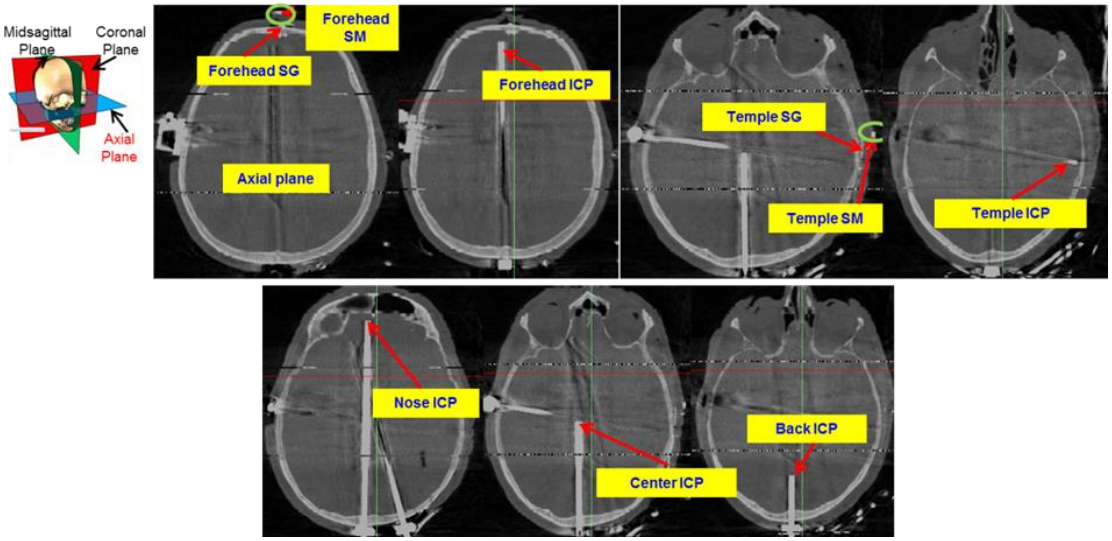

(b)

Figure 6.2: Experimental setup (a) Schematic showing sensor locations on PMHS head (b) CT images of instrumented PMHS showing sensor locations. Anthropometric data was also obtained from these CT images.

Protocol for instrumenting strain gauges and surface pressure sensors on PMHS:

The head was shaved prior to installation of surface pressure and strain gauges. A 2 X 2 cm square of skin was peeled (from three edges) and underlying tissue (Periosteum) was removed with a scalpel. The strain gauge was mounted to the skull bone using superglue (ethyl cyanoacrylate). A small piece of aluminum (of dimensions similar to strain gauge dimensions) was placed on the top surface of the strain gauge using thermal paste (grease). A piece of aluminium acts as a heat sink element and protects the strain gauge from overheating. The (peeled) skin was sutured back using surgical needle. The Kulite surface mount sensor was mounted on the skin using superglue (ethyl cyanoacrylate). The Kulite surface mount sensor was installed at the center of sutured section of the skin. It should be noted that, the strain gauge was mounted on the skull

bone whereas surface mount sensor was mounted on skin. The wires coming from the strain gauges and pressure sensors were stapled to the skin using surgical staple to prevent wire-whip. The strain gauge and surface mount sensors were not mounted until the day of testing. The mounting procedure is schematically shown in figure 6.3(a).

Protocol for instrumenting intracranial pressure sensors for PMHS:

As mentioned earlier, Kulite pressure probes were used for intracranial pressure measurements. Kulite pressure probes were put in the shrink tubing and this assembly is put inside steel tube. The sensing element of the probe sensor was always flush with the open end of the tubing as shown in figure 6.3 (b). The outer surface of the shrink tubing was glued to the inner surface of the steel tube using rubber cement to avoid motion of the probe sensor in the steel tube. 2 mm holes were drilled into the head to allow for the insertion of pressure probes. The temple sensor was inserted through the side of the head and remaining sensors were inserted through the back of the head. Sensors were secured in place using collar which was mounted on the steel tube. Drilled holes were backfilled/closed with mineral oil. The collar was also useful in accurately placing the sensors at desired locations. Nose ICP, center ICP and back ICP are (approximately) in the same axial plane as shown in figure 6.2(a).

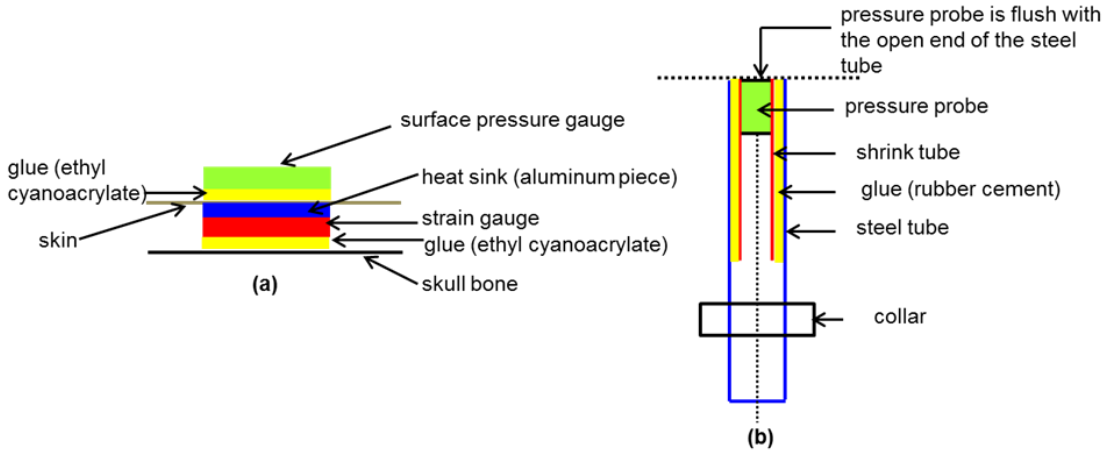

Figure 6.3: (a) Schematic showing protocol used for mounting of strain and surface pressure gauges (b) Preparation of pressure probes that are used for ICP measurements.

6.2.4 Blast wave exposure:

All PMHS heads are subjected to blast waves of three different incident intensities or overpressures (70 kPa, 140 kPa and 200 kPa). This was achieved by changing number of membranes which resulted in different burst pressures. Head was oriented in frontal direction to the blast. Each intensity is repeated three times for each head, so there were total 27 (3x3x3) shots. Experiments were also conducted with the addition of padded and suspension helmets that were mounted on the PMHS head. Same setup and same number of repetitions were used for the padded and suspension helmets experiments. Thus, altogether there were 54 shots. As mention earlier, the PMHS head is placed in the test section of the shock tube located approximately 2502 mm from the driver end; the total length of the shock tube is 12319 mm.

6.2.5 Data acquisition, processing and analysis

Experimental data is collected at the sampling rate of 1MHz using two National Instruments PXI-6133 data acquisition cards, which have eight analog channels each. The data acquisition cards are capable of 14 bit sampling at up to 2.5 MHz. Pressure sensors are connected to the data acquisition system through 1 MHz differential amplifier and strain gauges are connected to data acquisition system through Nicolet® analyzer. No anti-aliasing filters are used during data collection and post processing; instead a simple moving average (SMA) is performed on the raw data to reduce the noise. Experimental data is presented as mean ± Standard error of the mean (SEM). Unpaired two-tailed Student's *t*-test with unequal variance is performed in order to assess statistical significance between various cases, and *p*-values of <0.05 are considered statistically significant.

6.3 Results:

Results are analyzed using three parameters: surface pressures, intracranial pressures (ICP's) and surface strains. In this section only observations are made from the presented results. These observations are discussed in the discussion section.

6.3.1 Analysis of wave velocities:

Table 6.2 shows experimentally obtained wave velocities for each head. Different wave velocities are briefly defined below.

(i) Surface pressure wave: surface pressure wave is a reflected shock wave on the surface of the head. Surface pressure wave indicates where the shock front is at a

given time. In this work, loading induced by the surface pressure wave is considered as a ‘direct load’ as the surface pressure wave transmits energy directly into the brain.

(ii) Pressure wave in the ballistic gel is the wave traveling through ballistic gel as a result of direct transmission of surface pressure wave. In other words, this is the wave propagating through ballistic gel due to 'direct load'.

(iii) Structural wave in the skull: when the blast wave impacts the head, it gives rise to a stress wave traveling through the skin, skull, SAS and brain. Because of its acoustic properties, stress wave in the skull travels much faster than in the other soft tissues of the head. Therefore the stress wave traveling through the skull is monitored in this work and this wave is defined as a structural wave in the skull. The loading induced by structural wave is considered an ‘indirect load’. In addition to stress wave in the skull, load can also be induced/imparted due to skull deflections. The main difference between the stress wave in the skull and skull deflection is that former is characterized by high frequency, low amplitude behavior and latter is characterized by low frequency, high amplitude behavior.

Wave velocities are calculated based on arrival times and distance between respective sensors. Circumferential length is used to calculate wave velocities of surface pressure wave and structural wave in the skull and direct distance (longitudinal) between the sensors is used to calculate wave velocity in the ballistic gel. Of all the wave velocities, highest wave velocity is found in the skull (1081 to 1376 m/s), followed by wave velocity of ballistic gel (657.67 to 875 m/s) (see table 6.2). Least wave velocity is seen for surface pressure wave (406 to 549.67 m/s). This trend is consistent for all heads at all intensities.

As the incident blast intensity is increased wave velocities are slightly increased; however this trend is not statistically significant due to higher values of standard deviation. The wave velocities in the skull and the brain are lower than standard (reported) longitudinal wave velocities; this is expected as the PMHS specimens were not fresh and material properties significantly deteriorate over time [219]. For ballistic gel, curing can change the material properties.

Table 6.2: Experimentally obtained wave velocities

Incident intensity (kPa)		**Wave velocity (m/s)**		
		Surface pressure wave/ external blast wave	**Structural wave in the skull**	**Pressure wave in the ballistic gel**
70	Head 1	430 ± 35	1035 ± 27	620 ± 10
	Head 2	382 ± 17	975 ± 70	793 ± 98
	Head 3	406 ± 13	1233 ± 54	560 ± 31
	Mean of three heads	**406**	**1081**	**657.67**
140	Head 1	500 ± 72	1114 ± 67	651 ± 3
	Head 2	443 ± 11	1052 ± 130	817 ± 55
	Head 3	467 ± 14	1309 ± 21	604 ± 31
	Mean of three heads	**470**	**1158.33**	**690.66**
200	Head 1	561 ± 65	1252 ± 21	792 ± 71
	Head 2	533 ± 42	1158 ± 113	998 ± 190

	Head 3	555 ±13	1720 ± 127	835 ± 93
	Mean of three heads	**549.67**	**1376**	**875**

6.3.2 Sample Pressure-time profiles:

Figure 6.4-6.6 shows sample pressure-time profiles for sensor locations shown in figure 6.2. Sample pressure-time profiles presented here are based on mean of three shots (experiments) for head 1. While presenting sample pressure-time profiles, time axis is shifted so that arrival of blast wave at a given sensor location corresponds to t=0. Incident blast intensity for these profiles is 200 kPa. For brevity, pressure-time profile will be referred as pressure profile from here on. Raw (pressure) data showed oscillations thus profile is smoothed by performing simple moving average (SMA). The number of data points selected for moving average varies from 5 to 20.

Figure 6.4 shows incident pressure profile. The incident pressure is measured 200 mm (upstream) from the PMHS head. The incident profile shows sudden rise in pressure (rise time is 10 μs) followed by nonlinear decay; the peak pressure and positive phase duration are 190 kPa and 5.4 ms respectively. Secondary peaks are also seen in the incident profile. Incident pressure profile is highly repeatable; shot to shot variations in the pressure profile are less than 5%.

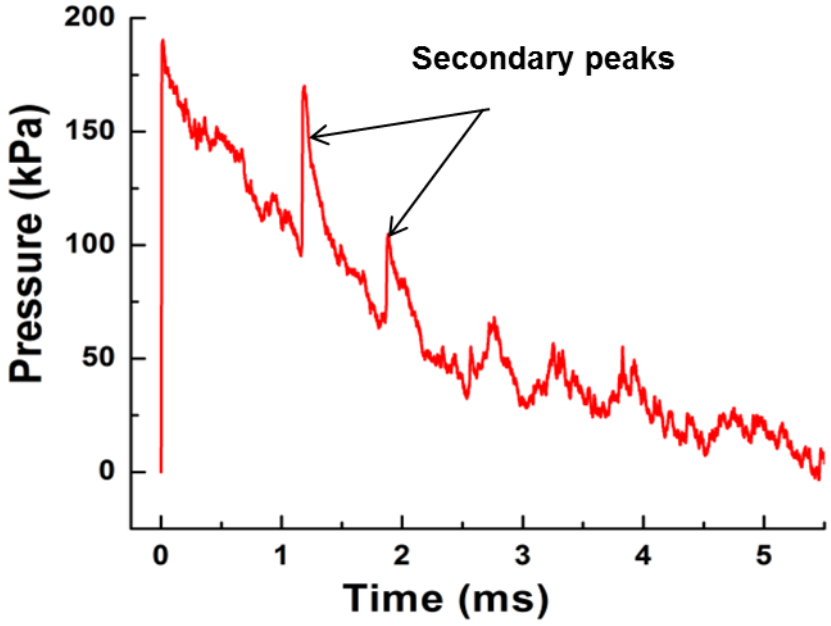

Figure 6.4: Incident pressure profile. Incident pressure profile is measured 200 mm (upstream) from the PMHS head

Figure 6.5 shows pressure profiles on the surface of the head. Surface pressures are measured at the forehead and temple locations (figure 6.2). Profile for forehead location shows sudden rise in pressure (rise time is 30 μs) followed by nonlinear decay. The rate of decay is much faster than that observed in incident pressure profile (e.g. for forehead location peak pressure is decreased by 50% in .17 ms, as opposed to 1.15 ms in the incident pressure profile). The peak pressure and positive phase duration for this profile are 592 kPa and 5 ms respectively. The peak pressure is amplified 3.11 times the peak incident pressure but the positive phase duration remained approximately similar at 5 ms. Raw data of forehead pressure profile show oscillations of the order of 150 kPa during the pressure rise (see insert of the figure 6.5), thus it is difficult to determine the true peak

and the peak value is affected by the number of data points selected for averaging. The pressure profile for temple location also shows sudden rise in pressure (rise time is 30 μs) followed by another spike. This is followed by sudden (instantaneous) decay in pressure with huge oscillations (from t=0.25 to t=0.5). The oscillating profile with much smaller peaks is observed after this time. The peak pressure and positive phase duration for this profile are 295 kPa and 5 ms respectively. The ratio of peak pressure to peak incident pressure is 1.55.

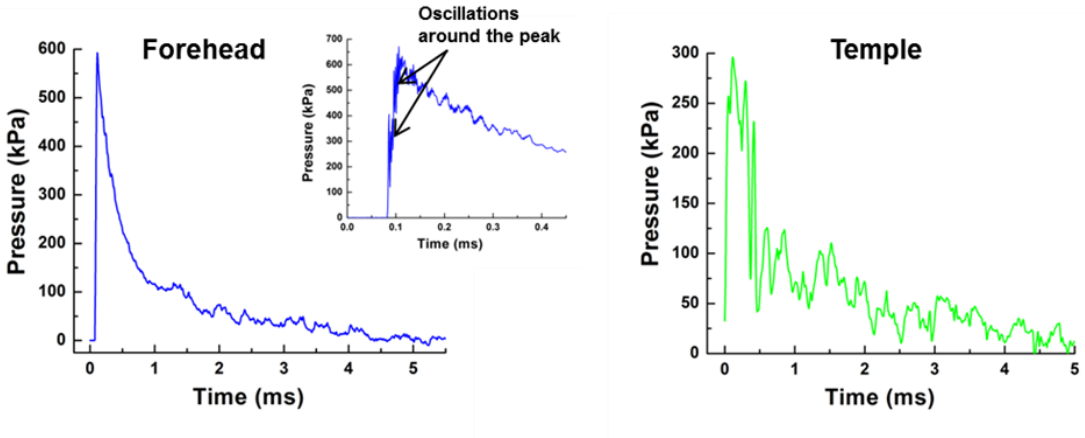

Figure 6.5: Sample pressure profiles on the surface of the head

Figure 6.6 shows the intracranial pressure (ICP) profiles for sensor locations shown in figure 6.2. For ICP profiles, wave action (dynamic events) plays out in very short time. Positive phase duration is 2.5 ms with initial (or majority of) intracranial dynamics playing out within 0.5 ms.

Intracranial pressure sensor forehead ICP (Figure 6.6 (a)) shows sharp rise (rise time = 40 μs) in pressure profile. This is followed by decay in pressure till t=0.15 ms; abrupt pressure increase is also seen during this decay at t=0.07 ms. The decay is not sustained

and there is another rise in the pressure. Secondary (loading) pulse which is similar to pulse observed in impact loading is seen after 1.0 ms. Intracranial pressure sensor nose ICP (Figure 6.6 (b)) also shows sharp rise (rise time = 70 μs) in pressure profile. This is followed by decay in pressure till t=0.5 ms, during this decay distinct pressure increase (like another peak) is seen at t=0.2 ms. After this decay, pressure remains approximately constant with small oscillations till t=1 ms. Secondary pulse which is similar to pulse observed in in the forehead ICP profile is seen after 1 ms. Figure 6.6 (c) shows the pressure profile for center ICP. The pressure rise (rise time = 390 μs) is not as sharp compared to forehead and nose ICP profiles. Pressure pulse seems to repeat itself with damping till the pressure equilibrates. Figure 6.6 (d) shows the pressure profile for temple ICP. The profile has similar features as that of center ICP. It appears that center and temple ICPs experience (see) several waves that are emanating from different sources during the rise. Rise time for temple ICP is 115 μs. Figure 6.6 (e) shows the pressure profile for back ICP. Back ICP shows the negative phase followed by positive phase. The negative phase has a rise time of 100 μs and duration of 0.25 ms. Positive phase of back ICP has features similar to forehead and nose ICP profiles. This is followed by decay in pressure after which pressure equilibrates. Shape of both surface and intracranial pressure profiles remained similar (except temple location) when PMHS head and incident intensity is changed. However, peak values are changed significantly (details in the next section) with change in PMHS head; positive phase durations remain similar.

Analysis of the peak pressures of ICP profiles has led to some interesting observations. Peak pressures are marked with black cross on each ICP profile. The

highest peak pressure is observed behind the forehead. The peak pressures are decreased as we move away from the coup (impact) site towards countercoup (opposite to impact) site. It should also be noted that significant difference in peak pressure is observed for forehead (430 kPa) and nose (310 kPa) ICPs that are in same coronal plane.

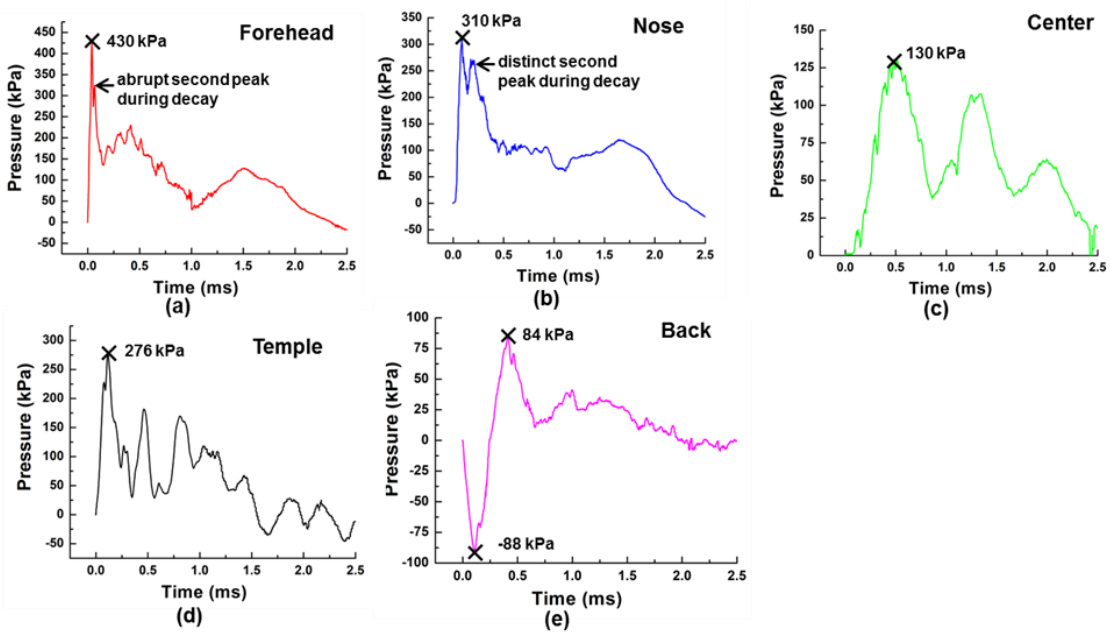

Figure 6.6: Intracranial pressure profiles: (a) forehead ICP (b) nose ICP (c) Center ICP (d) temple ICP (e) back ICP.

6.3.3 Pressure response as a function of incident blast intensity:

The response of PMHS head is studied for three incident blast intensities or overpressures: 70 kPa, 140 kPa and 200 kPa. The results are presented in terms of peak pressure and positive phase impulse as it is impractical to present actual pressure profile for each shot (total 216 measurements). In addition, this helps to evaluate the results using statistical basis. Peak pressure and positive phase impulse are two important parameters in studying mechanical insult to the brain and can be directly related to degree

of injury or injury thresholds. Figure 6.7 shows the peak pressures (for various sensors) as a function of intensity. The peak pressures are increased as the incident blast intensity is increased. This increase is statistically significant ($p< 0.05$) at all sensor locations except back ICP sensor for all heads and temple ICP for head 1. On these graphs, ratio of peak pressure to incident pressure (amplification factor) is also noted for the sensors that are near the coup (impact) site. This ratio is based on mean values for each measurement. The pressure amplification near the impact site (i.e. for forehead and nose surface pressures and ICP's) is linear ($R^2=0.89$) with respect to incident blast intensity except one case (head 3 nose ICP). For other locations this linearity is not seen due to complex wave action and structural effects affecting the peak values. In addition, noticeable head to head variations in the recorded peak pressures are seen. For example, for incident intensity of 200 kPa nose ICP records peak pressures of 310 kPa, 587 kPa and 254 kPa for heads 1, 2 and 3 respectively; which corresponds to variation upto 56 %. Similarly, for a given head, noticeable differences (upto 49.70 %) in forehead and nose ICP's are seen.

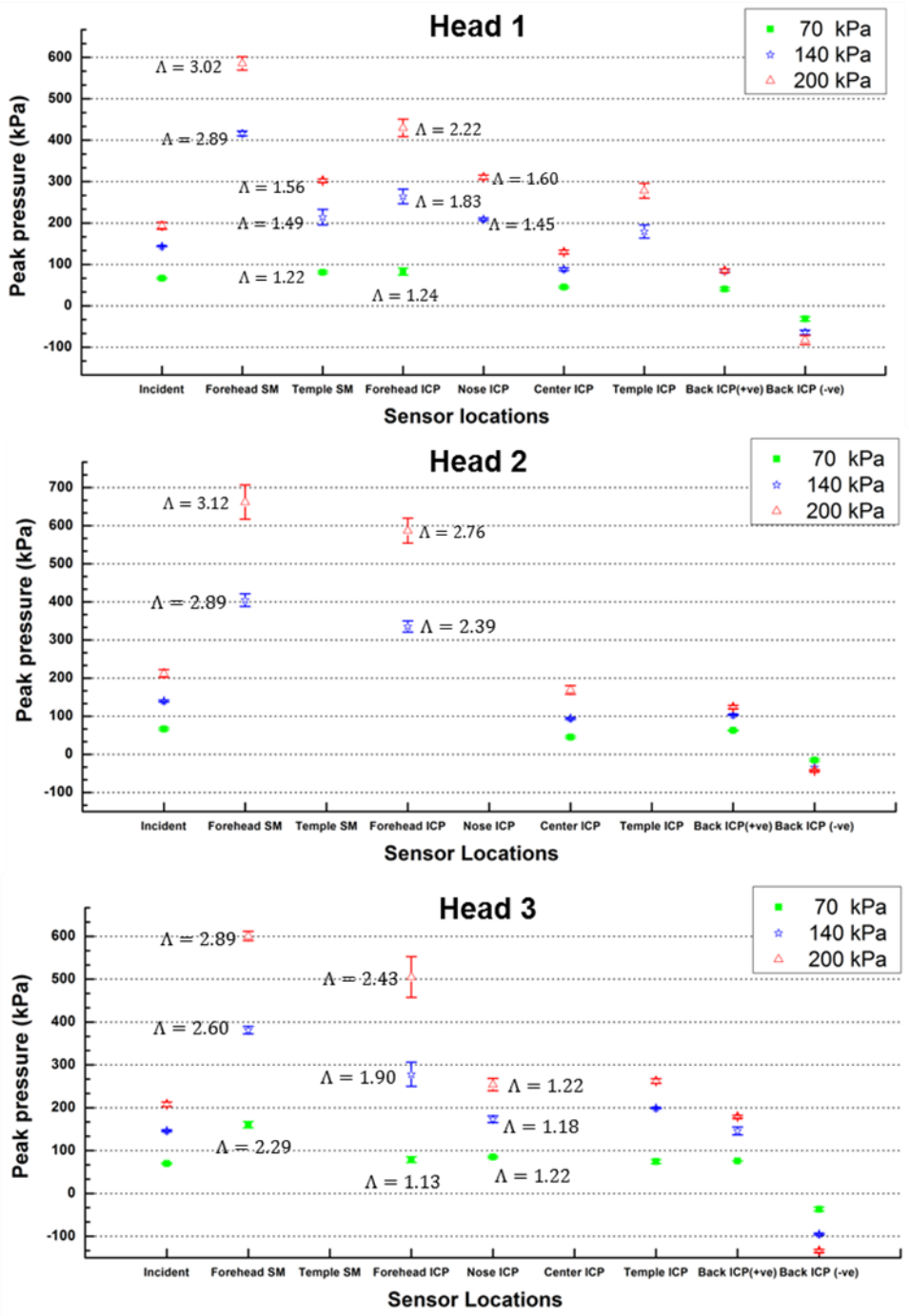

Figure 6.7: Peak pressures for various sensors as a function of intensity

Figure 6.8 shows the positive phase impulse for various sensors as a function of intensity. The positive phase impulse is increased as the incident blast intensity is

increased. The differences are statistically significant ($p < 0.05$) at all sensor locations except back ICP sensor for all heads and temple ICP for head 1. Head to head variations in the positive phase impulse are also significant; impulse variations upto 77% are observed between the heads.

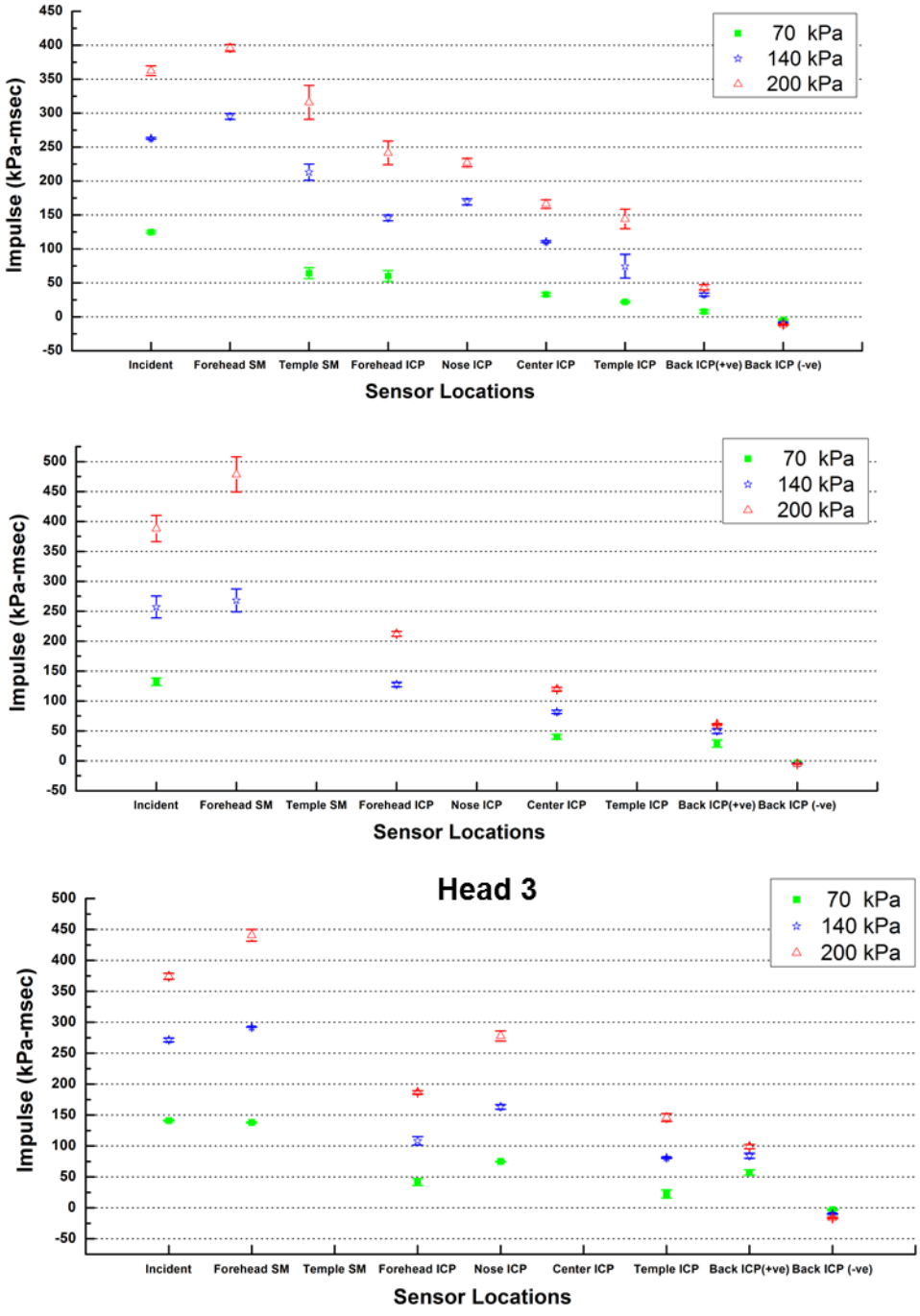

Figure 6.8: Positive phase impulse for various sensors as a function of intensity

6.3.4 Sample strain profiles:

Figure 6.9 show sample (circumferential) strain profiles for strain gauge locations shown in figure 6.2. Incident blast intensity for these profiles is 200 kPa. Negative strain indicates compression and positive strain indicates tension. Front strain gauge shows compressive phase upto 1ms; this is followed by small (equilibrium) oscillations for 0.2 ms, followed by another compressive pulse. Right temple strain gauge shows initial tension followed by compression. This compressive phase is sustained for 0.2 ms only. This is followed by tension-compression phase with higher magnitudes and longer durations. Top and back strain gauges show several compressive phases; each compressive phase is followed by equilibrium oscillations (i.e. small oscillations around zero). Highest circumferential strain is observed for front location at 0.06%. The shape of the strain profiles was not consistent across the heads and incident intensities or in some cases, even from experiment to experiment for a given head. The magnitude of the strain was however on the same order of magnitude. Head to head variation of ±40% is observed in the peak strain.

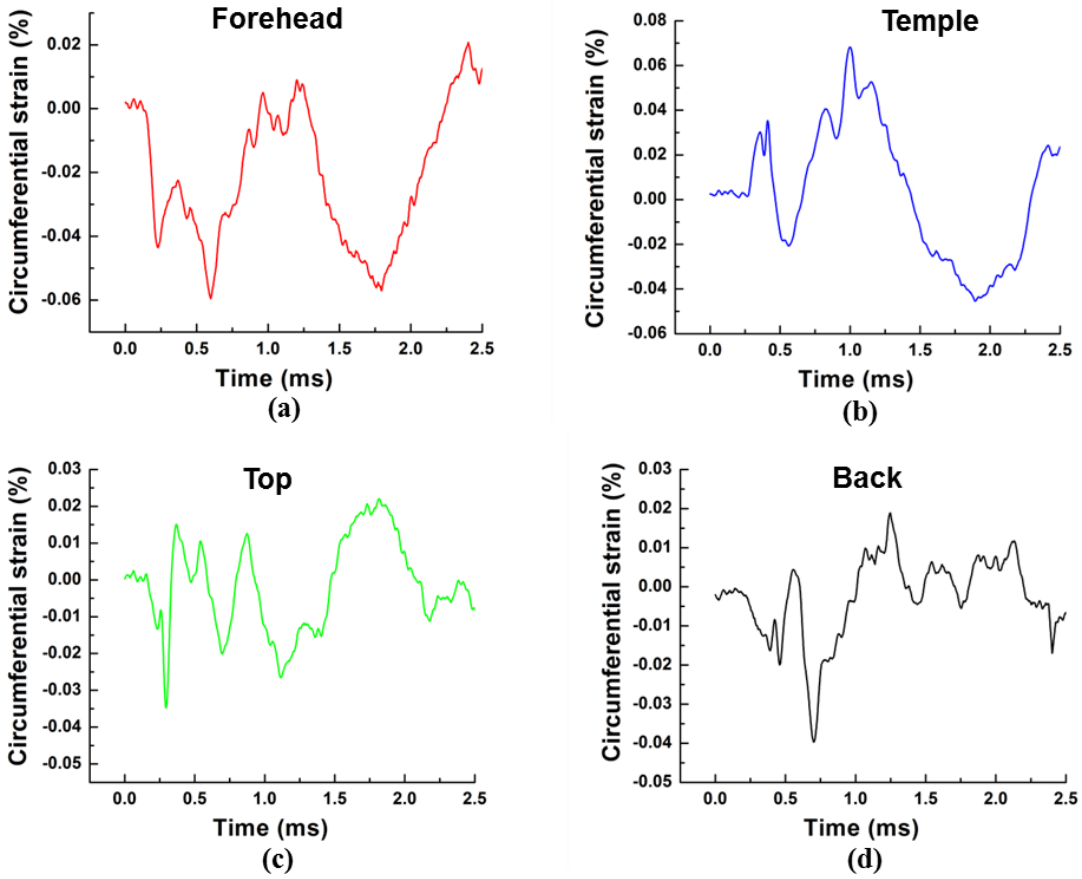

Figure 6.9: Strain profiles for various strain gauge locations

6.3.5 Role of helmet in mechanics of the blast wave head interactions: effect on ICP response:

In the earlier chapter, the role of helmet in the mechanics of the blast wave head interactions is studied in terms of pressure field experienced on the surface of the surrogate dummy head. In this section role of helmet on the ICP response is studied. Padded helmet is used for heads 1 and 2 and suspension helmet is used for head 3. Figure 6.10 shows the comparison of peak ICPs between no helmet and helmeted cases for forehead, nose and center ICP. The observations made are valid at all incident blast

intensities unless stated otherwise. Peak ICP values are reduced with the padded helmet for forehead and nose locations as compared to no helmet case; these reductions are statistically significant for most of the cases ($p < 0.05$). Center and back (not shown) locations show equivalent peak ICP values with the padded helmet, compared to no helmet case. With the suspension helmet, peak ICP value is increased (statistically significant increase) for forehead location at incident blast intensities of 70 kPa and 140 kPa and remained equivalent for incident blast intensity of 200 kPa. With the suspension helmet, statistically significant reduction in peak nose ICP is seen at all intensities. Center and back locations show equivalent peak ICP values with the suspension helmet.

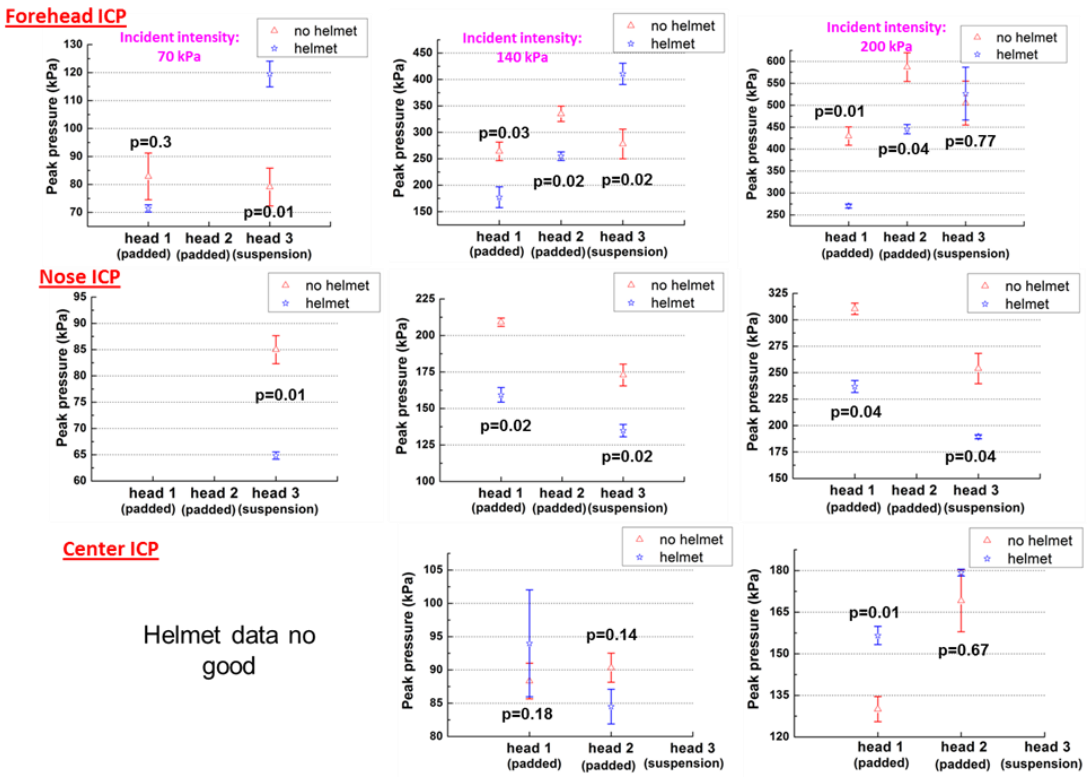

Figure 6.10: Comparison of peak ICPs between no helmet, padded helmet and suspension helmet cases

Figure 6.11 shows the ICP impulse comparison between no helmet and helmeted cases for forehead, nose and center ICP. Equivalent ICP impulse values are seen with the padded helmet at all locations as compared to no helmet but there is no fixed pattern of variation across the heads and/or intensities, making it difficult to draw any concrete conclusions. Increased ICP impulse values are seen with the suspension helmet at all locations compared to no helmet scenarios. This increase in impulse under suspension helmet is statistically significant for most of the scenarios.

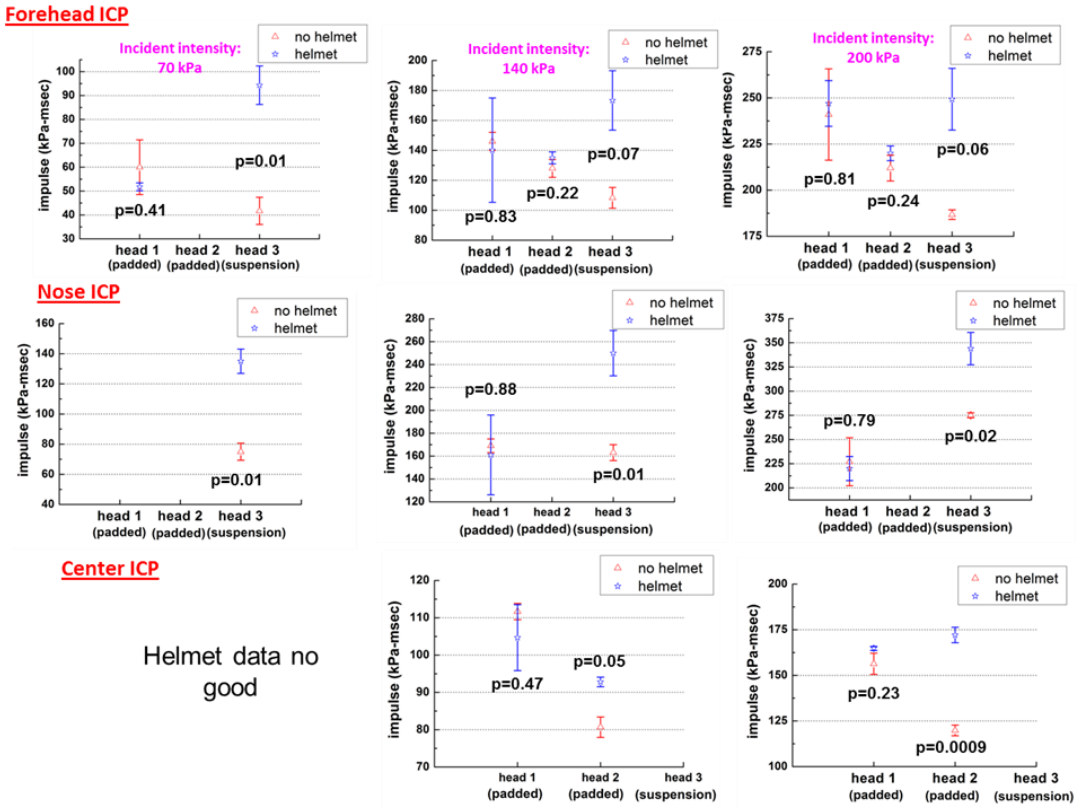

Figure 6.11: Comparison of ICP impulse between no helmet, padded helmet and suspension helmet cases

6.4 Discussions:

One of the lingering questions in medical and scientific communities is whether primary blast waves alone can cause traumatic brain injury? If yes, what is the etiology of blast induced traumatic brain injury? BINT research is yet to answer these fundamental questions. An important requirement of any such BINT study is the ability to produce repeatable and measurable blast loading conditions that can be related to field conditions implicated in bTBI [30, 41, 220-223]. Our blast wave generation facility has been designed and tested to meet this need [173, 224, 225]. The placement of the specimen (PMHS head in this case) is contingent upon the desired blast profile (peak overpressure, duration and impulse) and is typically achieved in the test section [225].

The incident wave profile obtained in this work can be directly related to field conditions implicated in primary BINT as verified using ConWep (see figure 6.12); the match is good barring those secondary peaks. Secondary peaks are due wave reflections from the PMHS head and walls of the shock tube. The incident pressure profiles generated in this work are equivalent to explosion of 7, 20, 30 kilograms of C4 at a distance of 8 meters for incident blast intensities of 70 kPa, 140 kPa and 200 kPa respectively and are comparable to real blast scenarios as proposed by a few researchers [43, 223]. These explosive (charge) weights are equivalent to explosive weights/capacities seen in vest/container bombs, parcel package and pipe bombs/ man-portable explosive device threats as defined by U.S. Technical Support Working Group (TSWG) and unconventional weapons response handbook [226, 227] (see table 6.3). In addition, generated blast wave profile is highly repeatable as standard deviation in peak

pressure and impulse is less than 5% (see figures 6.7 and 6.8). We have also verified, through measurements, that the blast wave is planar at the test section [173]; this is an important aspect of replicating field conditions [224]. Thus, results presented in this study are directly applicable in the analysis and interpretation of primary BINT events.

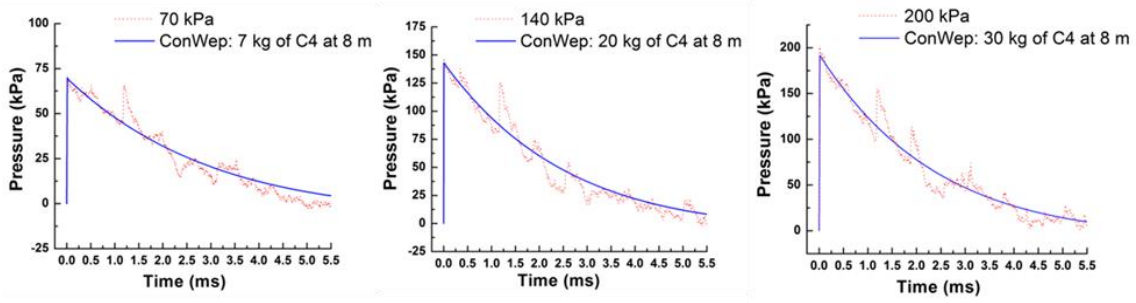

Figure 6.12: Comparison of incident blast profiles with real world blast scenarios

Table 6.3: Comparison of peak incident pressure and positive phase impulse obtained from the UNL shock tube with peak incident pressure and positive phase impulse generated from the IEDs.

IED threat description [226, 227]					**UNL shock tube**	
Threat type	Charge (explosive) weight (kg)	Distance of the target (m)	Peak incident pressure (kPa)	Positive phase impulse (kPa-ms)	Peak incident pressure (kPa)	Positive phase impulse (kPa-ms)
vest/container bombs	7-10	8	70	154	70	125-150

Parcel Package/ briefcase bomb	20	8	143	298	140	250-270
pipe bombs/ man-portable explosive device	30	8	192	385	200	375-400

6.4.1 Shape and related aspects of the pressure profiles:

The analysis of the entire pressure time history is critical as it provides important information regarding interaction of blast wave with the head and subsequent propagation through skin-skull-brain parenchyma. As mentioned earlier, the incident pressure profile/(s) obtained in this work is similar to one obtained in the far field range of typical IED explosion [39-41, 164]. For typical IED explosion (e.g. see ConWep profiles of figure 6.12), the indent profile has sharp rise followed by nonlinear decay (typically exponential); the positive phase duration is close to 5 ms.

The shape and positive phase duration of the surface pressure profile at the forehead location is similar to incident pressure profile. However, peak overpressure is significantly higher due to aerodynamic effects and the rate of decay is much faster as compared to the incident pressure profile; pressure is reduced by 90 % within 2 ms (figure 6.5). Temple location has much smaller peak pressure (50 % decrease) as compared to forehead location. These effects can be explained by studying blast wave head interactions. Flow field around the head is illustrated using numerical simulations (see figure 6.13). At the beginning of the interaction, as the shock front impinges on the

forehead at its most upstream region, a reflected shock propagating in the opposite direction starts to develop. The incident shock starts to propagate around the surface of the head. At the same time, regular reflections occur that propagate radially both in upstream and downstream direction. These reflections continuously interact with incoming tail part of the blast wave. The reflections are tensile in nature and hence compressive pattern of decreasing strength develops as a result of the incident shock reflection over the surface and the forward motion of the shock tail (also known as blast wind) as shown in figure 6.13(a). Thus, forehead surface gauge records faster decay as compared to incident pressure profile. As the shock wave traverses the head shock wave diffractions occur and as a result geometry induced flow separation takes place (figure 6.13(b)). This geometry induced flow separation increases as we move away from the leading edge (or incident blast site) towards downstream. Due to this flow separation temple location shows decrease in peak pressure with respect to forehead location. By geometry induced flow separation we imply that formation of low pressure pockets (regions) in the vicinity of the head; it should not be confused with boundary layer flow separation associated with the viscous fluids. Similar phenomenon of shock wave diffractions and flow separation over cylindrical objects is seen in studies involving shock wave propagation over cylindrical objects [228-230].

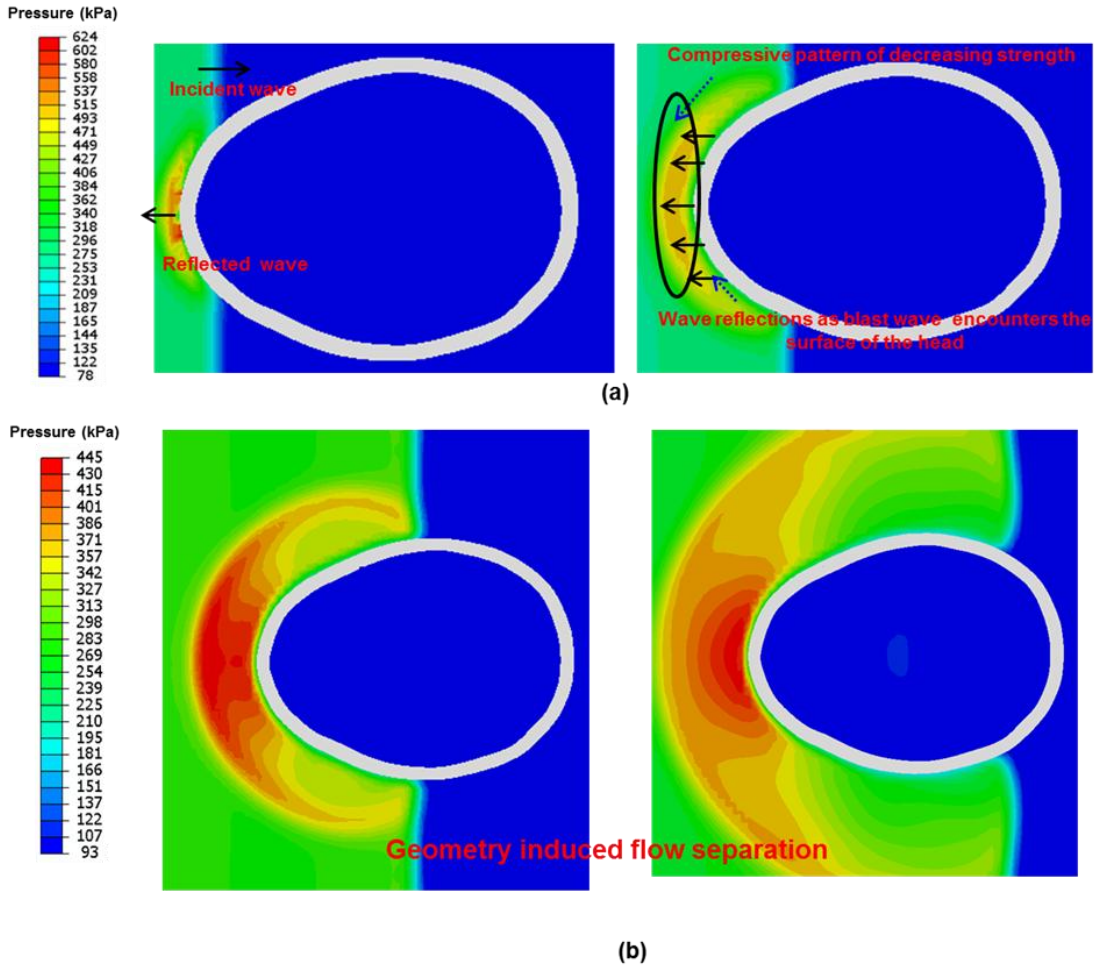

Figure 6.13: Blast wave head interactions as blast wave traverses the head. (a) blast wave head interaction at leading edge or incident blast site (b) illustration of Mach reflection and flow separation as blast wave traverses the head. In all figures cuts are made along axial plane.

The pressure profiles in the brain drastically deviate from surface pressure profiles (see figures 6.5 and 6.6). Intracranial pressure dynamics plays out in much shorter duration as compared to incident or surface pressure profiles. For intracranial pressure (ICP) profiles, positive phase duration is 2.5 ms with initial (or majority of) intracranial

dynamics playing out within 0.5 ms. This is due to wave propagation in skin-skull-brain parenchyma. The impedance mismatch of the layered system (skin-skull-brain) is such that the magnitude of the pressure wave (or input signal) in the skin-skull-brain parenchyma is either amplified or attenuated as it reflects and transmits through these layers. The wave traversal times through the skin and the skull are 52.9 μs and 3.62 μs assuming 10 mm thickness for both skin and skull. Within 506 μs (i.e. 0.506 ms) 2 wave traversals occur in the skin and 29 wave traversals are possible in the skull. Thus, wave action (reflections and transmissions) happens at much shorter time scale and sharp decay in ICP profiles is seen for forehead and nose ICPs. This aspect is further elaborated using one dimensional model of skin-skull-brain parenchyma as shown in figure 6.14. Figure 6.14 (a) shows response of the skull-brain parenchyma when a loading pulse (Heaviside function) of intensity P is applied to the skull. Pressure in the brain is 0.62 (transmission coefficient) times the applied pressure after first transmission from the skull into the brain. Transmission coefficient increases with each transmission and pressure in the brain equilibrates after 5^{th} transmission from the skull into the brain. Figure 6.14 (b) shows response of the skin-skull-brain parenchyma when loading pulse of intensity P is applied to the skin. In this setup (or model), thickness of the skull and skin are designed such that (t_{skull}= 14 t_{skin}) reflection/transmission occurs at same time for skin-skull and skull-brain interfaces. Transmission coefficient is 1.16 after first transmission from the skull into the brain. However, transmission coefficient drastically decreases to 0.15 after second transmission. Subsequent transmissions have transmission coefficients of 1.39, 0.42, 1.32, 0.7. In reality, the thickness of the skin and the skull are almost similar and hence

the wave traversal in the skull is ~14 times faster than the skin based on the wave speeds. The transmitted wave from the skull into the brain equilibrates after 5th transmission (figure 6.14 (a)). Hence, for wave propagation through skin-skull-brain parenchyma in real scenarios skull (thickness) should not play major role in the wave amplification or attenuation and brain should ideally see the pressure that is seen by the skull at the skin-skull interface. Even in that case transmission coefficient in the brain after 2nd transmission is 0.25. This explains sharp decay in intracranial pressure profiles for forehead and nose ICPs (figure 6.6) that are closest to incident blast site wherein initial wave propagation obeys one dimensional theory fairly well (at least in terms of qualitative trends). For forehead ICP, the pressure is decreased from 430 kPa (first transmission) to 138 kPa (second transmission) in 117 μs; the ratio of these pressures is 0.32 which is consistent with the one dimensional theory.

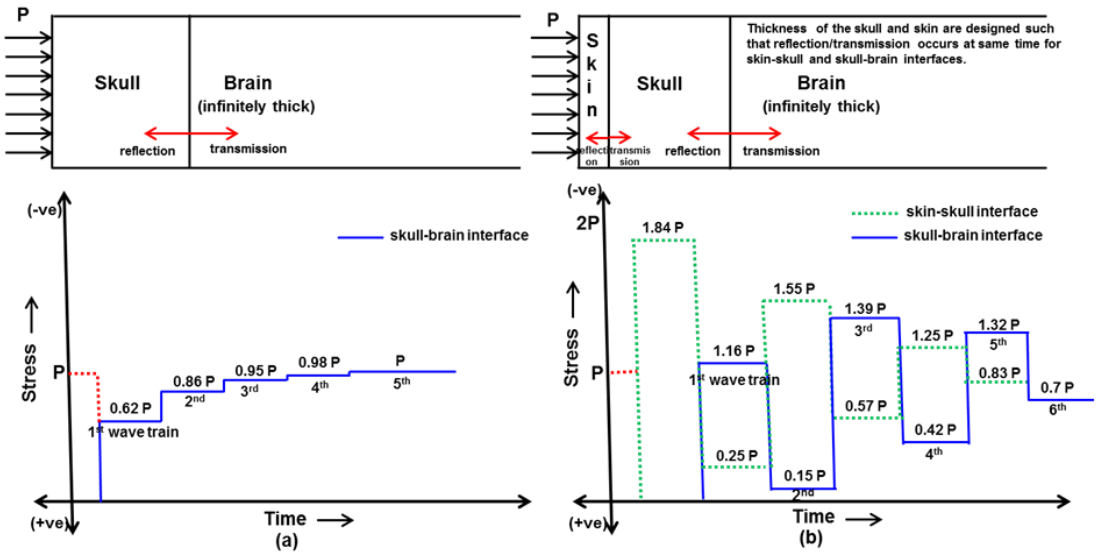

Figure 6.14: Wave propagation in skin-skull-brain parenchyma using one dimensional model. (a) Response of the skull-brain parenchyma to the applied loading pulse of

intensity P (b) Response of the skin-skull-brain parenchyma to the applied loading pulse of intensity P.

The forehead and nose ICP's (figure 6.6) show second peak during the initial decay; the second peak is abrupt in forehead ICP and distinct in nose ICP. This second peak is due to delayed wave transmission from the eyesocket/ eyebrow region as illustrated in figure 6.15. After these initial phases wave reflections from the head boundaries dominate the response and it is not possible to delineate these effects due to complex and highly dynamic nature of the problem. The center and temple ICPs, which are located deep inside the brain probably, experiences many waves emanating from different sources. By the time wave reaches certer ICP the pressure is attenuated. This attenuation can be due to material damping, wave dispersion over larger area and reflections from geometric boundaries and material interfaces. The pressure pattern of the center ICP can be best described as follows. Any given point, the brain experiences a complex set of direct and indirect loadings emanating from different sources (e.g. blast wave transmission, reflections from tissue interfaces, skull deformation) at different points of time. These disturbances continuously propagate into the brain as waves. Constructive and deconstructive interferences of these waves control the pressure history deep inside the brain. Back ICP shows the countercoup effect (negative pressure) initially; as the wave velocity in the skull is higher than the wave velocity in the ballistic gel (see table 6.2). Due to this skull moves forward; displacement of the brain lags displacement of the skull and hence tension or negative pressure is generated in the brain. If tensile loads/forces are not allowed to transfer then separation will take place at the skull-brain

interface. Positive phase begins when longitudinal wave traveling through the brain reaches the back location. The precise source of secondary pulse seen in the some of the ICP profiles is not known at this time, further experiments and investigation is needed to understand this effect. The secondary pulse is not seen in numerical simulations.

The shape of the strain profiles is sinusoidal as opposed to 'blast or Friedlander wave' type. This is due to the frequency response of the strain gauges. Frequency response of the strain gauges is much lower as compared to surface and ICP gauges and hence they do not respond to the induced loading as sharp as necessary. However, strain measurements are useful in calculating structural wave velocity in the skull and in identify flexure modes of the skull.

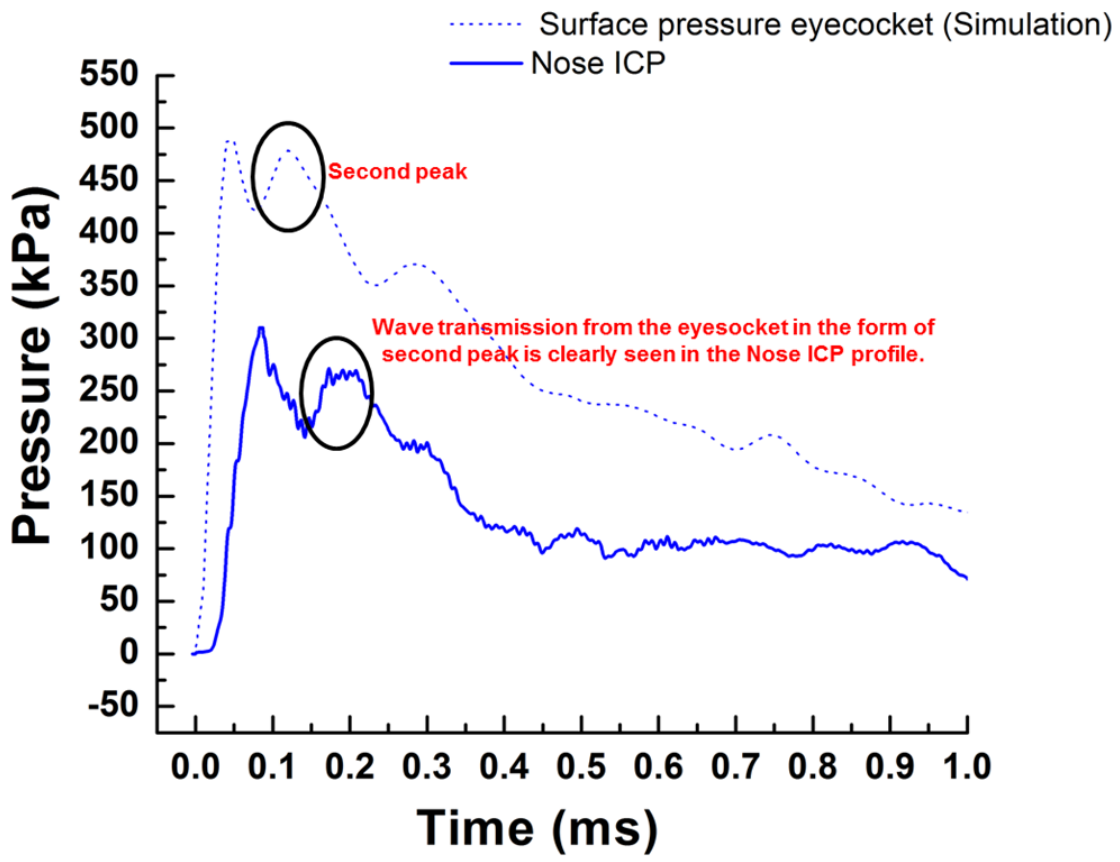

Figure 6.15: Comparison of Surace and ICP profiles near the eyesocket regions

6.4.2 Analysis of peak pressures and pressure distribution within the head

When the blast wave encounters the PMHS head the pressure is amplified as the high velocity particles of the shock front are brought to rest abruptly. The amplification factor Λ (the ratio of reflected pressure to incident pressure) depends on the incident blast intensity, angle of incidence, mass and geometry of the object and boundary conditions, and can vary by a factor of 2 to 8 for air shocks [156, 206]. For PMHS head, the pressure amplification at the incident blast site is in the range of 2.89-3.12 for 200 kPa incident intensity and 2.6-2.89 for 140 kPa incident intensity. The amplification factor for surrogate head is constant at 2.4 (for 200 kPa incident intensity), wherein the skin was not included in the surrogate experiments and surface pressure gauge was mounted on the hard polyurethane skull material. The higher amplification in the PMHS experiments is attributed to the ripple effect of the skin; due to ripple effect oscillations of the order of 150 kPa are seen around the peak and determination of true peak becomes subjective. Similar oscillations in the surface pressure profiles are seen in our experimental studies on the rat [231]. The amplification factor of 2.39 (for 200 kPa incident intensity) is obtained from the numerical simulations for both PMHS and surrogate heads. In PMHS head simulations skin is tied to the skull.

Pressure distribution in the brain shows coup-countercoup pattern typically seen in the impact type of loading [48, 51, 53, 68-70, 74, 80, 84, 94, 232-234]. The maximum peak pressure is seen at the coup site; peak pressure gradually decreases as we move away from coup site towards countercoup site due to wave dispersion over larger area.

ICP in the brain at coup site is higher than the incident pressure but lower than the surface pressure. Few studies suggest that blast waves pass through the (thin) cranium of rats almost unchanged [209]. Our results to the contrary highlight the role of skin-skull parenchyma in governing intracranial pressures. One dimensional model of skin-skull-brain suggests that pressure in the brain should be 1.84 times the surface pressure (Figure 6.14). However, pressure experienced by the brain at coup site (forehead and Nose ICPs) is lower (ratio: 0.3 to 0.5 for different intensities) than the surface pressure (forehead SM). This indicates that the wave propagation becomes multidimensional within short amount of time (<50 μs) due to geometry of the head. In addition, skin and skull are highly heterogeneous materials [81, 235-237] with much complex structure than considered in one dimensional model; one dimensional model assumes homogenous material structure for all tissues. Though forehead and nose ICP's are located in the same coronal plane, nose ICP records significantly lower pressure than forehead ICP. Pressure reductions upto 28 and 50 % are seen for head 1 and head 3 respectively. This is due to presence of air sinus (see figure 6.16); large air sinus (in cranial cavity) is present in front of the nose ICP for head 3 that corresponds to maximum reduction. Role of air sinus in reducing peak pressures is further confirmed using numerical simulations. Air being low impedance material has low transmission coefficient and thus effectively attenuates incoming wave [222]. Blast wave attenuation by impedance mismatch (i.e. by placing low impedance material in front of high impedance material) is widely reported in the literature and low impedance materials such as foam are classically suggested for blast wave attenuation [95, 238-242].

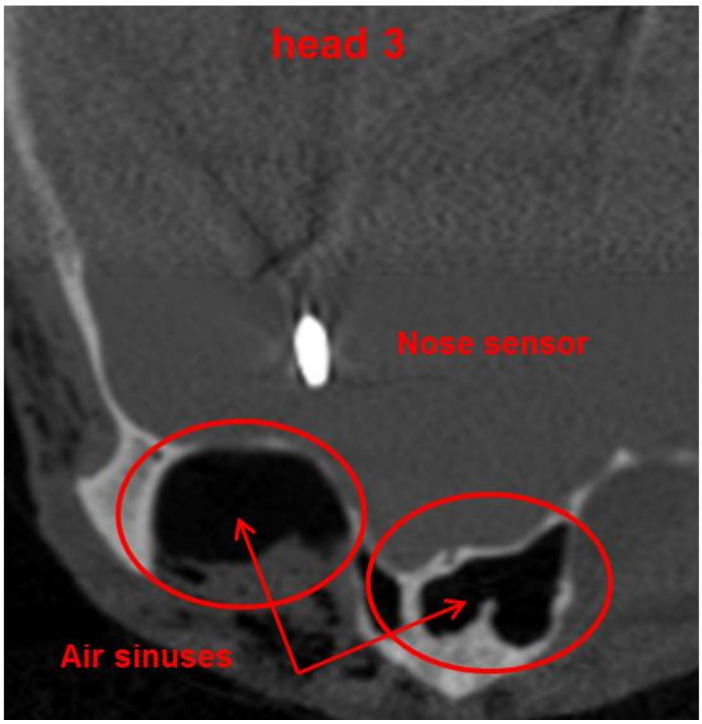

Figure 6.16: Head anatomy in front of the nose sensor. Axial view is shown. Large air sinus (in cranial cavity) is present in front of the nose ICP for head 3; which shows maximum reduction with respect to forehead ICP.

6.4.3 PMHS response as a function of intensity:

As mentioned earlier, one of the lingering questions in front of medical and scientific communities is whether blast waves cause traumatic brain injury? We exposed PMHS head to pure primary blast of varying intensities and observed statistically significant differences in the peak intracranial pressure and total impulse (figure 6.7 and 6.8). This finding supports our hypothesis that intracranial response change with change in incident blast intensity. Thus it is clear that primary blast waves alone can cause mechanical insult to the brain. This potential of this mechanical insult in causing the BINT will be assessed in the following section. Over the past few years, several mechanisms of mechanical

insult have been suggested. These mechanisms are: (a) thoracic mechanism in which blast waves enter the brain through thorax and cause brain injury [64, 65, 243]. (b) translational and rotational head acceleration [65]. (c) blast wave transmission through cranium [34, 78, 79] (d) skull flexure [184, 207] (e) cavitation [43, 244]. Most of these mechanisms are proposed using numerical models alone and experimental evidence is needed to corroborate these proposed mechanisms. Our experimental measurements categorically indicate that the blast wave transmission through cranium induces mechanical insult to the brain of varying degree that changes with change in incident intensity. Thus we propose direct transmission of blast wave into the intracranial cavity as essential loading pathway to the brain. From the current experimental measurements, there is not enough experimental data to establish the possibility of other mechanisms like skull flexure, head acceleration and tissue cavitation. However, potential of some of these mechanisms in causing mechanical insult will be assessed using numerical head model in the next chapter of this dissertation.

Significant head to head variations (upto ~60 %) are seen in Peak ICP's as well as positive phase impulse. Head to head variations highlights the importance local effects (e.g. geometric and (micro) structural) in transmission of blast wave to intracranial contents. In addition, significant head to head variations support the hypothesis that stress wave action governs the intracranial response under blast loading conditions. Similar variations in the ICP response (variations upto 80 %) are seen by Leonardi [62] and Bolander [61] who exposed fresh PMHS heads to blast overpressures of 69, 88 and 120

kPa. This also highlights the need for large amount of testing and data analysis needed before establishing injury risk curves for primary TBI.

6.4.4 Comparison with the blunt impact event:

In the impact induced injuries the loading experienced by the head is governed by the momentum transfer from the impacting body to the head that is dependent on the mass, velocity and material of the impacting surface; which in turn decide the force and duration of the contact. In the blast induced injuries loading experienced by the head is governed by the amount of explosive and distance of the target from the explosive source. For impact event, duration of impact is typically 30 to 50 ms [245] and input pulse assumes parabolic shape [48, 49, 53] . For blast type of loading duration of blast is 2 to 5 ms with pressure profile assuming Friedlander waveform [30, 36, 164]. The rate of loading is 200-300 times faster in blast event as compared to the impact event. In addition, blast load is a moving load experienced by the entire head as opposed to impact load that is experienced by small portion of the head.

Table 6.4 shows the comparison of input loads in impact and blast type of loading for frontal loading scenario. In the simulated impacts, velocities of impact are in the range of 3 to 7 ms with impactor area around 1500 mm^2. This produces the peak input pressure of 2000 to 7000 kPa with applied impulse of 21 to 27 N-s. In the simulated primary blast of present work, the peak input pressure is in the range of 70 to 200 kPa which is 10 to100 times smaller than peak forces/pressures seen in the impact event. However, area of exposure in blast loading is much larger as compared to area in impact loading. For example, area of exposure in blast is approximately 60,000 mm^2 (frontal region of the

head) as opposed to 1500 to 2000 mm^2 in the impact. Thus net applied impulse in the blast loading is 8 to 22 N-s; this input impulse is comparable to input impulse in the impact type of loading. Table 6.5 shows comparison of peak intracranial pressures and impulse for impact and blast loading. The ICP data is available for only one impact scenario. The peak ICPs are higher whereas ICP impulse is lower in the blast loading as compared to the impact loading. The higher peak ICPs in the blast loading scenario are due to the much faster rate of loading as compared to blunt impact; the rate of loading in blast 10^5 s^{-1} as opposed to 500 s^{-1} in blunt impact). In blunt impact, due to low rate of loading pressure is distributed over larger area before significant amount of energy is transferred. In blast loading wave transmission governs the ICP profile as opposed to head motion in impact event.

Table 6.4: Comparison of input loads in impact and blast type of loadings for frontal loading scenario

Impact					**Blast**	
Velocity of impactor (m/s)	**Peak input pressure (kPa)**	**Input impulse (N-s)**	**Peak head acceleration (g)**	**HIC**	**Peak input pressure (kPa)**	**Applied impulse (N-s)**
3.8	1906	21.3	43	31	70	8
4.63	3940	22.9	122	251	140	16
6.2	5153	22.9	194	627	200	22.5
7.05	5846	26.3	236	845		

7.21	7220	23.1	281	1443		

Table 6.5: Comparison of resulted intracranial pressures in impact and blast type of loading for frontal loading scenario

(a) impact loading

Velocity of impactor (m/s)	Peak input pressure (kPa)	Input impulse (N-s)	Peak ICP (kPa)			Total ICP impulse (kPa-ms)		
			Front	Parietal	Back	Front	Parietal	Back
7.05	5846	26.3	141	74	-60	449	212	-179

(b) blast loading

Peak input pressure (kPa)	Applied impulse (N-s)		Peak ICP (kPa)			Total ICP impulse (kPa-ms)		
			Forehead	Temple	Back (-ve)	Forehead	Temple	Back (-ve)
70	8	Head 1	83	-	-32	60	22	-5
		Head 2	-	-	-15	-	-	-4
		Head	79	74	-37	42	22	-3

		3						
140	16	Head 1	264	180	-64	146	74	-8
		Head 2	335	-	-34	128	-	-5
		Head 3	278	199	-95	108	81	-10
200	22.5	Head 1	430	276	-88	241	144	-12
		Head 2	587	-	-43	212	-	-5
		Head 3	505	262	-134	187	146	-16

6.4.5 Assessment of brain injury:

Over the last five decades, several brain injury criterions were developed (details in chapter 2). Different researchers used different mechanical parameters to relate mechanical insult to the degree of injury. The fundamental parameters defining mechanical insult are: head acceleration, strain, intracranial pressure (ICP) and shearing stress. Choice of parameter is usually dictated by type of mechanism deemed responsible for the brain injury. Basically, there are three widely regarded mechanisms of brain injury; these mechanisms corresponding bio-mechanical parameter (in parenthesis) are: 1) Contusion (increase in ICP) 2) DAI (shear strain and stress, von Mises stress) 3)

subdural hematoma (relative motion between the skull and brain and/or increase in ICP). The PMHS response is compared against these mechanical parameters. Out of these parameters, only ICP values are available from PMHS experiments. Values of other parameters (i.e. shear strain and stress, von Mises stress) are obtained from validated numerical model in order to compare them with known injury thresholds. Table 6.6 summarizes the mechanical response of PMHS head at various incident blast intensities. ICP impulse based injury thresholds are not developed thus far but we believe that there is strong need for impulse based thresholds; especially for short duration blast events wherein the peak ICP alone may not be sufficient to predict the injury outcome. In addition, it is recently shown that impulse (pulse duration) and not the peak pressure govern the gene expression in cultured microglia subjected to blast overpressures of varying intensities [246].

Table 6.6 : Mechanical response of PMHS head at various incident blast intensities

(a) Peak ICP and total ICP impulse at various incident blast intensities (experiments)

Peak input pressure (kPa)	**Applied impulse (N-s)**		**Mean peak ICP (kPa)**						**Mean total ICP impulse (kPa-ms)**					
			Forehead	**Nose**	**Center**	**Temple**	**Back (+ve)**	**Back (-ve)**	**Forehead**	**Nose**	**center**	**Temple**	**Back (+ve)**	**Back (-ve)**
70	8	Head 1	83	-	45	-	40	-32	60	-	33	22	8	-5
		Head 2	-	-	45	-	63	-15	-	-	40	-	29	-4
		Head 3	79	85	-	74	76	-37	42	75	-	22	57	-3
		Mean of three heads	**81**	**85**	**45**	**74**	**59.67**	**-28**	**51**	**75**	**36.5**	**22**	**31.33**	**-4**

140	16	Head 1	264	209	88	180	85	-64	146	169	111	74	33	-8
		Head 2	335	-	94	-	104	-34	128	-	82	-	50	-5
		Head 3	278	173	-	199	146	-95	108	163	-	81	84	-10
		Mean of three heads	**271**	**191**	**91**	**189.5**	**111.67**	**-64.33**	**127.33**	**166.00**	**96.50**	**77.50**	**55.67**	**-7.67**
200	22.5	Head 1	430	310	130	276	84	-88	241	227	166	144	43	-12
		Head 2	587	-	169	-	124	-43	212	-	120	-	61	-5
		Head 3	505	254	-	262	179	-134	187	278	-	146	99	-16

		Mean of three heads	**467.5**	**282.5**	**149.5**	**306.5**	**129.33**	**-89.33**	**213.33**	**252.50**	**143.00**	**145.00**	**67.67**	**-11.00**

(b) Peak shear and von Mises stresses at various incident blast intensities (numerical simulation)

Peak input pressure (kPa)	**Applied impulse (N-s)**	**Peak shear stress (kPa)**					**Peak von Mises stress (kPa)**				
		Forehead	**Center**	**Temple**	**Back (+ve)**	**Back (-ve)**	**Forehead**	**Center**	**Temple**	**Back (+ve)**	**Back (-ve)**
70	8	0.27	0.02	-0.18	0.14	-0.21	1.76	0.47	1.66	1.53	-
140	16	0.70	-0.04	-0.39	0.34	-0.49	4.37	1.83	3.16	3.5	-
200	22.5	1.20	-0.06	-0.60	0.56	-0.57	7.9	3.0	4.54	4.4	-

(c) Peak maximum principal strain (numerical simulation)

Peak input pressure (kPa)	**Applied impulse (N-s)**	**Maximum principal strain (%)**				
		Forehead	**Center**	**Temple**	**Back (+ve)**	**Back (-ve)**
70	8	0.11	0.05	0.13	0.09	-
140	16	0.25	0.2	0.27	0.18	-
200	22.5	0.5	0.3	0.38	0.24	-

When looking at the biomechanical parameters for the tissue injury predictors, pressure has the highest correlation with concussion based on R^2 and log likelihood values [138]. However, as mentioned in chapter 2, there is only one study by Ward et al. [50] that directly correlates ICPs with degree of injury. Ward et al. [50] developed brain injury criterion based on occurrence of brain contusion and hemorrhage. The criterion was derived from combined experimental and analytical investigations of intracranial pressures and contusions. It was hypothesized that increase in intracranial pressure is a cause of contusion and hemorrhage. Overall injury severity obtained from the experiments was correlated with intracranial pressures. It was proposed that no brain injury will occur when the ICP<173 kPa, moderate to severe injury will occur when 173 kPa<ICP<235 kPa and severe injury will occur when ICP>235 kPa for blunt impacts. This criterion is used to assess brain injury severity from our data; during our analysis it was assumed that mean pressure values of at least three sensor locations should pass (either above or below) the specified threshold value while assigning the severity. Based on this criterion, no injury will occur at incident blast overpressure level of 70 kPa, moderate to severe injuries will occur at 140 kPa and severe head injury will occur at the incident blast overpressure intensity of 200 kPa. Yao et al. [141] proposed ICP value of 256 ± 76 kPa as an indicator of AIS 3 (severe) brain injury from finite element reconstruction of 10 real-world adult pedestrian accident cases. Based on this criterion severe injury will occur for incident blast overpressure of 200 kPa. Baumgartner [247], from finite element reconstruction of 66 real world accidents (includes motorcyclists,

pedestrians and American football, and impacts of ballistic projectiles), proposed brain pressure of 200 kPa as an indicator of brain contusion, edema and hematoma . Based on this criterion contusion, edema and hematoma will occur for incident blast overpressure of 200 kPa. For incident overpressure of 140 kPa there is a probability that contusion, edema and hematoma will occur as two senor locations record mean values of 191 and 189.5 kPa while other sensor records mean value of 271 kPa.

Shear and von Mises stresses are often regarded as biomechanical parameter for diffuse axonal injury (DAI). Correlation between von Mises stress and observed neurological injuries (e.g. location of injury) was previously shown in sheep [142, 248] and other animals as well as for human [249]. Various researchers, over the years, have developed injury criteria for diffuse axonal injury purely based on numerical investigations (These studies are described in chapter 2). However, despite five decades of blunt induced brain injury research, shear strain/stress is never measured experimentally due to inherent difficult in measuring shear strains. Anderson et al.[248], from their combined experimental and computational studies on sheep have suggested that von Mises stress in the range of 8 to 16 kPa will result in axonal injury with a severity AIS 1 that corresponds to mild DAI. Yao et al. [141] proposed von Mises stress value of 14.8 ± 4.5 kPa and shear stress value of 7.9 ± 1.6 kPa as an indicator of AIS 3 (severe) brain injury from finite element reconstruction of 10 real-world adult pedestrian accident cases. Zhang et al. [80] proposed shear stress value of 7.8 kPa for 50% Probability of mild TBI from finite element reconstruction of 24 football collisions occurred in professional football games. When our results are compared against these

thresholds most of the peak von Mises and peak shear stress values are below these thresholds, thus there is only slight possibility that any DAI will occur under blast overpressures simulated. It should be noted that in our analysis peak von Mises and peak shear stress values are based on first 2 ms response. During this short time period relative motion between the skull and the brain is negligible and hence significant shearing stresses are not developed. It is possible that significant shear stresses can develop at later times. At present time, no such data is available. Similar pattern/values of ICP and shearing stress are seen in other computational investigations studying blast [79, 95].

Stalnaker et al. [139] developed mean strain criterion based on head impact experiments on subhuman primates and then extrapolated to humans by dimensional analysis. They proposed value of 0.329 % as a value of maximum tolerable strain above which severe brain injury will occur. Based on this criterion, severe injury will occur for incident blast intensity of 200 kPa for which maximum principal strain values at three locations will exceed this strain limit of 0.329%. However, values of maximum principal strain obtained in this work are two orders of magnitude smaller than cellular injury thresholds. For example, values of 13% and 14% were suggested as a threshold values for functional impairment and morphological damage respectively by Bain and Meany [134], from their experiments on dynamic stretching of the right optic nerve of an adult male guinea pig. Highest principal strain value of 0.5% is obtained from our validated numerical model for incident blast overpressure of 200 kPa. Cellular injury thresholds overestimate the actual brain injury seen in in-vivo studies using PMHS as well as animals; serious concerns are raised regarding in-vitro cellular injuries [16]. Negligible

gross head motion and negligible differential head accelerations are seen from our numerical model hence the differential acceleration values do not exceed acceleration based thresholds (i.e. peak linear head acceleration of 300 g's and HIC_{15} of 700).

6.4.6 Effect of helmet on ICP response:

In the earlier chapter and also in our published works [250, 251] role of helmet in mechanics of the blast wave head interactions is studied in terms of pressure field experienced on the surface of the surrogate dummy head. In those studies, surface pressures were measured at five different locations (front, top (3 locations) and back) in the midsagittal plane. It was shown that the peak surface pressures were reduced at incident blast site (i.e. site closest to impact) for both for padded and suspension helmet configurations and these reductions were statistically significant. At other locations surface pressures were marginally reduced for padded helmet configuration and increased for suspension helmet configuration. Increase in surface pressures under the suspension helmet were due to focusing of blast wave under the suspension helmet. Impulse values were either equivalent or were marginally reduced for both padded and suspension helmet configurations. In addition, for suspension helmet, statistically significant increase in impulse was seen for locations that were directly below focused region. How the external pressure field measured on the surface of the head translates to intracranial contents is currently not known. Some of the interesting questions are: what dose increase in surface pressures under suspension helmet imply in terms of brain injury? Does blast wave focusing affect injury outcome and injury severity? In this section we attempt to address these questions by studying ICP response with and without the helmets. We

believe, this is the first experimental attempt to study intracranial response with and without the helmets under the primary blast.

For the padded helmet, peak ICP values at forehead, nose and temple locations are reduced and these reductions are statistically significant; center and back locations do not show significant reductions in peak ICP values. ICP Impulse values are either equivalent or marginally reduced with the padded helmet (see figure 6.17 (a)). This suggests that the face is important pathway of load transfer to the brain. The area of face is ~25-30 % as that of the area of the forehead. Thus significant amount of impulse/energy is transferred through the face; this is further confirmed using numerical simulations. The face has been identified as an important pathway of load transfer by Nyein et al. [78] and face shield was proposed for blast mitigation; peak pressure reductions upto 80 % were prosed with the face shield. However, some of the major limitations of the Nyein et al.'s study are total simulation time and military/field relevance of their input data. Authors simulated entire blast event for 0.76 ms only; this time period is not sufficient to truly evaluate role of face shield in blast mitigation as face shield delays the blast wave transmission into intracranial cavity. In addition, incident blast pressures and durations used as an input for numerical simulations were not representative of realistic blast. In addition to role of face in blast wave transmission; marginal impulse reductions seen with the padded helmet from our experiments also highlight the role that structure/geometry of the head plays in governing the ICP response.

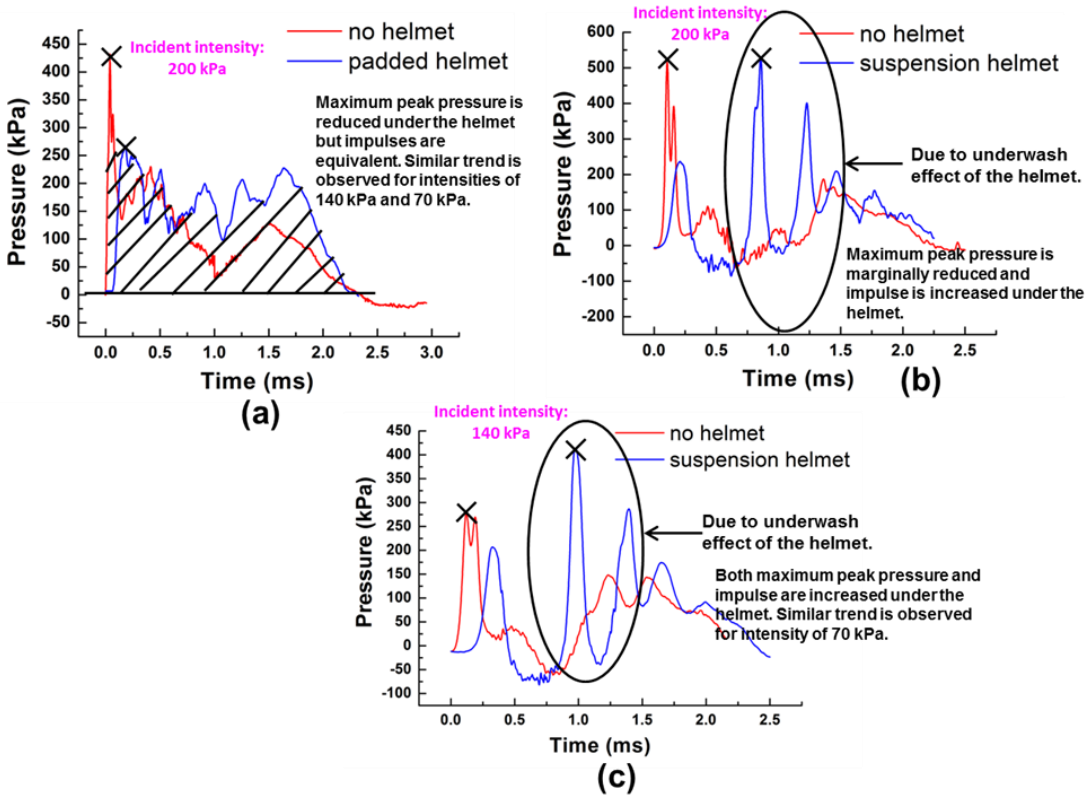

Figure 6.17: Pressure time histories with and without the helmet. (a) Padded helmet @ incident intensity of 200 kPa. Similar trend is seen for intensities of 70 kPa and 140 kPa. (b) Suspension helmet @ incident intensity of 200 kPa. (c) Suspension helmet @ incident intensity of 140 kPa. Similar trend is seen at incident intensity of 70 kPa.

With the suspension helmet, peak ICP values are reduced for nose ICP and these reductions are statistically significant. On the contrary, peak values are increased for forehead ICP at incident blast intensities of 70 and 140 kPa and remained equivalent for blast intensity of 200 kPa due to focusing/underwash effect as shown in figure 6.17 (b) & (c). In addition, temple, center and back locations show equivalent peak ICP values with the suspension helmet. Statistically significant increase in impulse values are seen with

the suspension helmet at all locations compared to no helmet scenarios. Thus it is clear that focusing effect seen under the suspension helmet translates to the intracranial contents and adversely affects the ICP response (see figure 6.18). This does imply that for suspension helmet configuration wearing helmet can be worse than not wearing the helmet for primary blast, wherein, blast waves can potentially focus under the helmet. However this does not preclude the use of helmets that provide critical protection against blunt and penetrating conditions. Comparison of peak ICP values seen with the suspension helmet against injury threshold values of ward et al. [50] suggest that, though peak ICP values are increased under suspension helmets they do not alter injury severity. Ward et al.'s injury threshold however provides threshold values for peak ICPs only. Injury criterion based on ICP impulse is not yet available hence assessment of ICP impulse values with suspension helmet against the injury threshold is not possible.

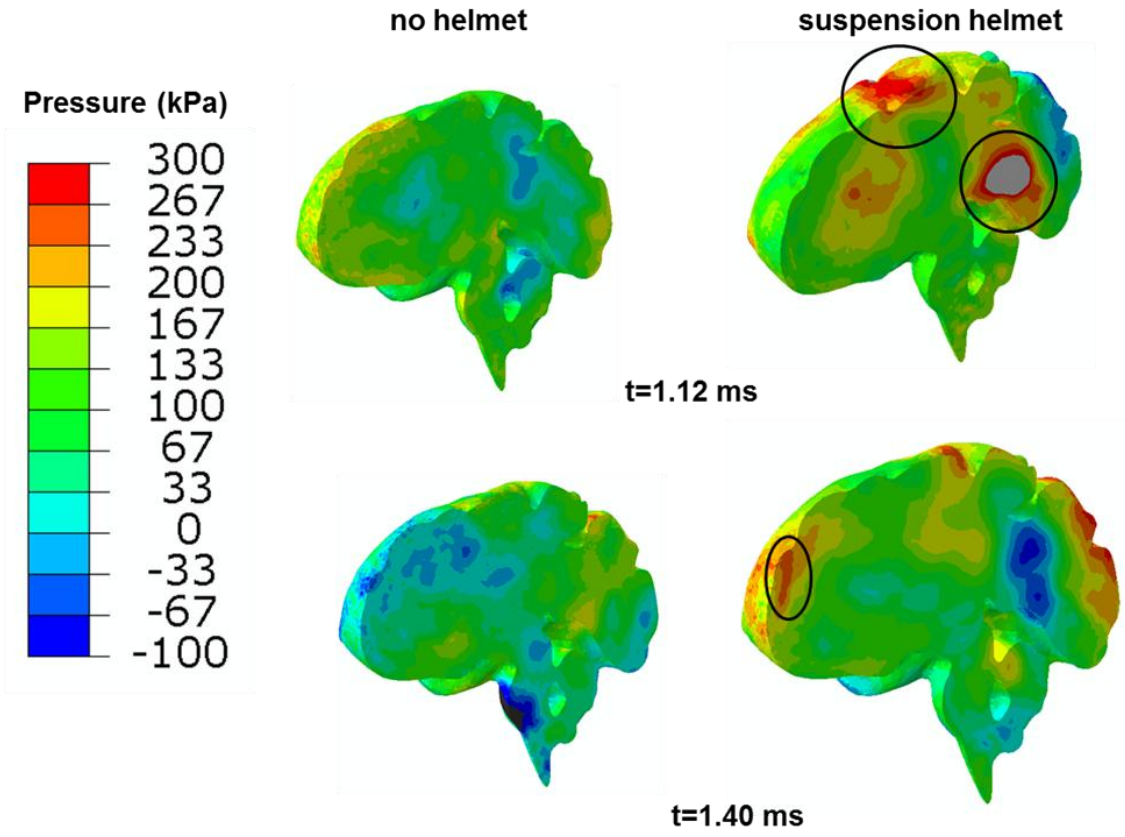

Figure 6.18: Focusing effect seen under the suspension helmet translates to the intracranial contents. Intracranial regions with increased pressure with respect to no helmet counterpart are highlighted with the ellipse.

6.5 Summary:

In this chapter response of PMHS heads that are next best surrogate to humans is studied. Three PMHS heads are subjected to pure primary blast of varying peak incident intensities or overpressures (70 kPa, 140 kPa and 200 kPa). We believe this is one of the very first attempts to understand mechanical insult experienced by the brain under pure primary blast loading conditions. Further, blast loading conditions simulated in this work are comparable to field blast loading conditions. Each specimen is filled with a brain

simulant prior to the experiments. Intracranial pressures (ICPs), surface pressures, and surface strains are measured at 11 different locations on each PMHS specimen. Analysis is based on a total of 54 experiments that included 594 measurements. Thus statistical significance of the results and findings is established. Computational studies have further provided cross-validation and a deeper understanding of the mechanics of the blast wave head interaction and subsequent wave propagation through skin-skull-brain parenchyma. Some of the key findings of this work are:

- When the incident blast wave impinges on the head, the surface pressures experienced by the head are amplified due to aerodynamic effects and amount of amplification varies from location to location; which is governed by the geometry of the head. The amplification factor is increased as the incident blast intensity is increased.
- Experimental results show that significant levels of ICP occur throughout the brain for all three incident blast intensities studied. The maximum peak ICP is measured at the coup site (nearest to the blast) that gradually decreases towards the countercoup site. When the incident blast intensity is increased, there is a statistically significant increase in the peak ICP and total impulse ($p<0.05$). Thus pure primary blast alone can cause mechanical insult of varying degree to the brain depending on incident blast intensities.
- The shape (or pressure-time history) of the ICP profiles is drastically different from the shape of surface pressure profiles and the shape of the ICP profiles is governed by

the wave propagation through skin-skull-brain parenchyma. Air sinus attenuates the peak ICP values.

- When ICP values are compared with the existing injury thresholds available in the literature, it is seen that no injury will occur at incident blast overpressure level of 70 kPa, moderate to severe injuries will occur at 140 kPa and severe head injury will occur at the incident blast overpressure intensity of 200 kPa.
- Shearing and von Mises stress values computed from numerical simulations are below the axonal injury thresholds proposed in the literature.
- Analyses of the helmeted experiments on PMHS head show that the peak ICPs and the ICP impulse are only marginally reduced with the padded helmet as compared to the no helmet case.
- Focusing of the blast wave under a suspension helmet accompanies a corresponding increase in ICP beneath focused regions as compared to the no helmet case. Overall, these results suggest that based only on ICP blast mitigation offered by the current helmets may be marginal, if at all.

CHAPTER 7

MECHANICS OF BTBI: PARAMETRIC STUDIES

7.1 Introduction:

In this chapter, we try to elucidate some of the experimental observations/variations (seen in the PMHS experiments) by performing parametric studies on the validated head model. In addition, role of wave transmission and skull deformations, which are hypothesized as the mechanisms of bTBI, on ICP response is also studied. In section 7.2, effect of bulk modulus of the brain on the ICP response is studied. In section 7.3, effect of skull thickness on the ICP response is studied. In section 7.4, the role of face in load/energy transfer to the brain is studied by adding face shield to the head-helmet assembly. In section 7.5, role of wave transmission and skull deformations on ICP response is studied by changing Young's modulus of the skull. The key observations from these parametric studies are summarized in section 7.6 on summary. Parametric studies are carried out for incident blast intensity of 200 kPa. The results of parametric studies are presented in terms ICP profiles at various locations (see figure 7.1) along the centerline of the brain in the axial plane, this section is selected as a representative section.

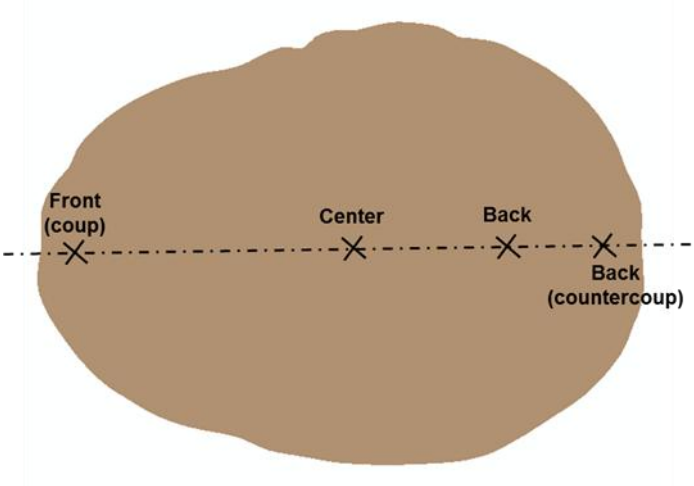

Figure 7.1: Results of parametric studies are presented at marked locations along the centerline of the brain in the axial plane

7.2 Effect of bulk modulus on ICP response:

A critical scientific aspect of bTBI is the knowledge of spatial and temporal variation of ICP. The bulk modulus of the brain tissue is one of the important parameter of the computational head models and huge variations in the value of bulk modulus have been reported. Thus it is necessary to understand response of head subjected to primary blast for various bulk moduli. In this work, three bulk moduli values are chosen: widely used [69, 70, 77, 84] value of 2.19 GPa, intermediate value of 560 MPa as used by Takhounts et al. [83] and recently reported [117] value of 10 MPa based on testing of porcine gray/white tissue in unconfined compression over a wide range of strain-rate (0.01 to 3000 s^{-1}). Figure 7.2 shows the ICP profiles along the centerline of the brain in the axial plane for various bulk moduli. In general, wave speed is increased and time to peak is reduced as the bulk modulus is increased. Thus the arrival of compressive wave at a given location in the brain is earlier for higher bulk modulus.

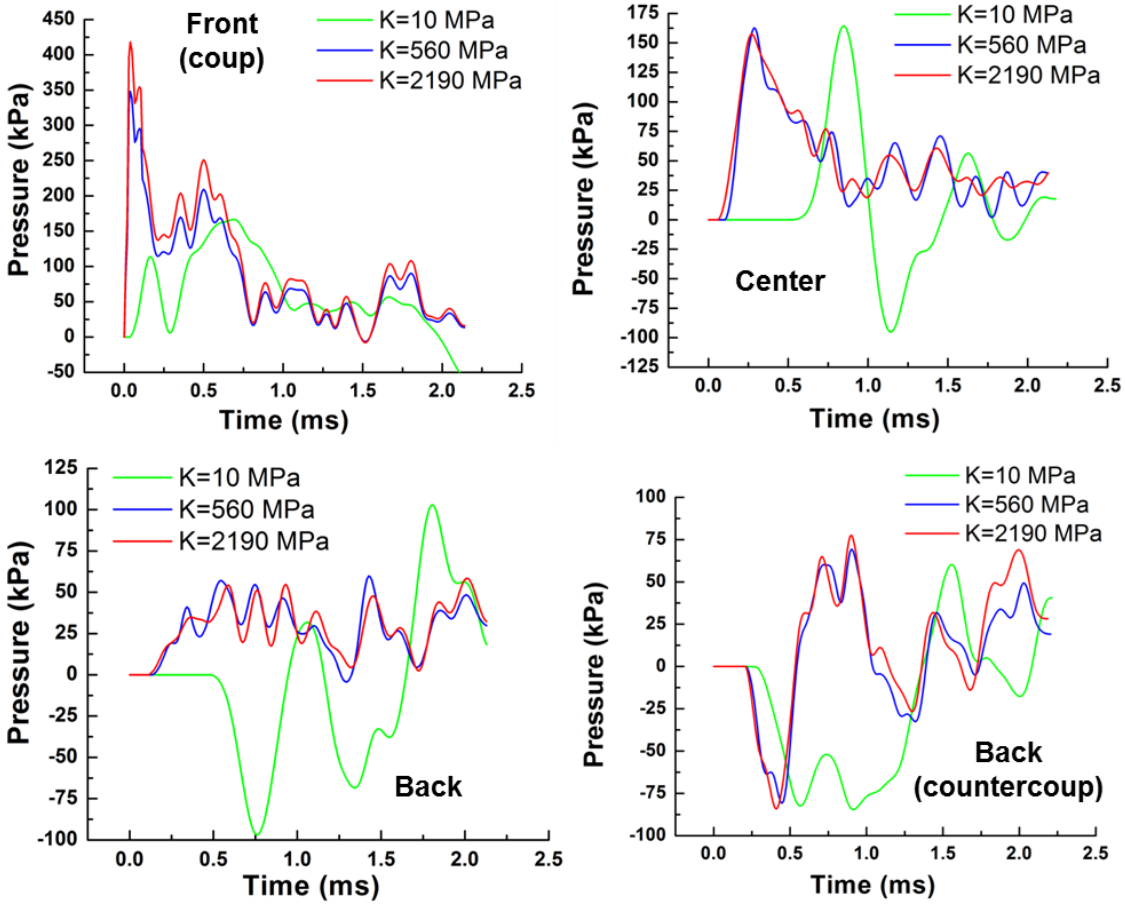

Figure 7.2: Pressure profiles in the brain as a function of bulk modulus

The peak ICP value at coup site is increased as bulk modulus is increased. The peak ICP values are increased by 231 % and 20 % when the bulk modulus is changed from 10 MPa to 560 MPa and from 560 MPa to 2190 MPa respectively. The positive phase impulse values are increased by 38 % and 20 % when bulk modulus is changed from 10 MPa to 560 MPa and from 560 MPa to 2190 MPa respectively. This increase in peak ICP value and positive phase impulse are attributed to higher transmission coefficient that increases with increase in bulk modulus. The transmission coefficient is calculated using following equation:

$$\frac{\sigma_T}{\sigma_I} = \frac{2\rho_2 c_2}{\rho_1 c_1 + \rho_2 c_2} \qquad \text{.....} \qquad (7.1)$$

Where,

σ_I is incident wave, σ_T is transmitted wave, ρ is the density and c (=$\sqrt{K/\rho}$) is the wave speed. Subscript 1 and 2 indicate the material 1 and thus material 2 respectively. The incident wave is applied to material 1 and material 2 receives the transmitted wave. Above equation is based on one dimensional theory. Table 7.1 shows theoretical transmission coefficients (based on one dimensional theory) from the skull to the brain for various bulk moduli of the brain. From table 7.1 it is clear that as the bulk modulus is increased, transmission coefficient is increased. This finding is consistent with findings of other studies who studied the response of head for various bulk moduli. Ruan et al. [68] from their parametric studies, using three dimensional head model, on brain bulk modulus (modulus was varied in the range of three orders of magnitude 10^6 MPa to 10^9 MPa) found that peak ICP value at coup site increased with increase in brain bulk modulus. Moss et al. [68] have also drawn similar conclusions from their parametric studies.

Table 7.1: Transmission coefficient as a function of bulk moduli

Brain Bulk Modulus (MPa)	**Brain density (kg/m^3)**	**Longitudinal wave speed (m/s)**	**Transmission coefficient, σ_T**
2190	1040	1451	0.64
560	1040	734	0.39
10	1040	98	0.06

Peak ICP value in the center region remains unaltered (or equivalent) with change in bulk modulus. Zhu et al. [175] studied the response of egg shaped surrogate filled with gel under blast loading conditions using experiments and computational modeling; they reported that the peak pressure in the central region of the gel remained approximately constant as bulk modulus of gel is changed from 500 MPa to 2000 MPa. The positive phase impulse values are increased by 304 % and 8 % when bulk modulus is changed from 10 MPa to 560 MPa and from 560 MPa to 2190 MPa respectively. Positive phase impulse is much smaller for 10 MPa case as shape of the ICP profile is sinusoidal as opposed to sharp rise followed by exponential decay for other two scenarios. For bulk modulus of 10 MPa wave action in the brain and reflections from head boundaries govern the ICP response; which is evident from sinusoidal shape of pressure profile. In addition, tensile wave front from the countercoup side erodes the compressive wave front. For back region the 10 MPa case do not show initial positive phase. This is because the arrival of tensile front from countercoup site is earlier than the arrival of compressive front from coup site. For other two cases (i.e. bulk moduli of 560 MPa and 2190 MPa) positive phase do exist and peak ICP values and positive phase impulse values are similar (or equivalent) for these bulk moduli. Extreme back or countercoup region show initial tension for all the bulk moduli. In this region, negative peak ICP values are unaltered/equivalent when the bulk modulus is changed. Negative phase impulse is equivalent for bulk moduli of 560 and 2190 MPa. However, with bulk modulus of 10 MPa the negative phase impulse is increased by 307% as compared to bulk moduli of 560 and 2190 MPa. This is logical considering tensile phase is sustained for longer time in 10

MPa case because of compressive front initiated at coup site traverses at low wave speed (98 m/s).

Figure 7.3 shows the pressure distribution in the brain for various bulk moduli. Pressure distribution shows typical coup (compression)-countercoup (tension) pattern. Thus there are multiple wave fronts in the brain; a compressive wave front from the incident blast side and a tensile wave front from the side opposite to the incident blast side. For brain moduli of 2190 MPa and 560 MPa compressive wave front traverses the brain tissue at speeds of 1451 m/s and 734 m/s respectively. These speeds are comparable to wave speed of 1857 m/s in the skull; the ratio of brain speed to skull speed is 0.78 and 0.40 for bulk moduli of 2190 MPa and 560 MPa respectively. Thus for bulk moduli of 2190 MPa and 560 MPa the compressive wave front that originates at coup site dominate the initial ICP response throughout the brain and compressive wave front effectively erodes the tensile wave front originating from countercoup side. On the contrary, for bulk modulus of 10 MPa wave speed being much smaller (98 m/s), the tensile wave front that originates at countercoup side and wave reflections from the boundaries/material interfaces dominate the ICP response. These disturbances continuously propagate into the brain as waves. Constructive and deconstructive interferences of these waves control the ICP history in the brain. Due to these reasons, for bulk modulus of 10 MPa maximum peak pressure is found at intermediate location (in between the front and center) as opposed to coup site for bulk moduli of 2190 MPa and 560 MPa.

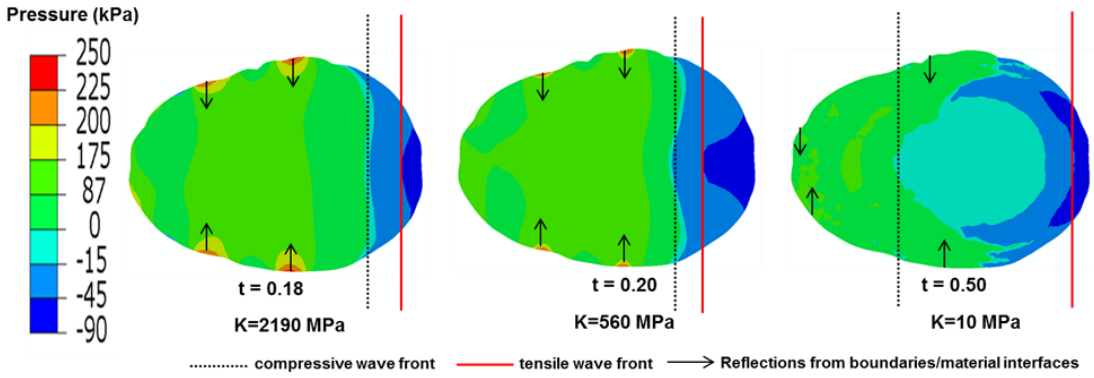

Figure 7.3: Pressure distribution in the brain for various bulk moduli

Shearing stress does not have significant effect as bulk modulus is changed. Shearing stress varies by < 2 kPa as bulk modulus is changed from 10 MPa to 2190 MPa. This is mainly because low value of shear modulus (G_0= 41 kPa, G_∞= 7.8 kPa) used in this work. Shearing strains upto 5 % (at front location) is found when bulk modulus is 10 MPa and shearing strain upto 2 % (at front location) is found when bulk modulus is 2190 MPa. Corresponding peak stresses are 3 kPa and 1.2 kPa for bulk modulus of 10 MPa and 2190 MPa respectively; which corresponds to < 2 kPa variation. This variation is further reduced to when shear properties of Nicolle et al. [112] are used, in which material relax faster and long term modulus is less than <1 kPa.

7.3 Effect of skull thickness on ICP response:

The PMHS experiments showed significant head to head variations in the peak ICP and positive phase impulse values. To study the sources of these variations skull thickness is hypothesized as one of the variable governing the ICP values. The thickness of the skull in the head model is changed while remaining components of the head model were kept same. Figure 7.4 shows the ICP profiles for two different skull thicknesses; 4

mm and 8 mm. As the skull thickness is increased the peak ICP and positive phase impulse values are reduced. Table 7.2 summarizes the peak ICP and positive phase impulse values for skull thickness of 4 mm and 8 mm and % reduction in these values when skull thickness is changed from 4 mm to 8 mm. The highest reductions upto 29 % (at front location) in peak ICP and 11 % (at center location) in positive phase impulse are seen. The least reduction in peak ICP (5.37 %) and positive phase impulse (5%) is seen at back location (countercoup site). This also explains the variations seen in experimental data as skull thickness is varying across PMHS heads.

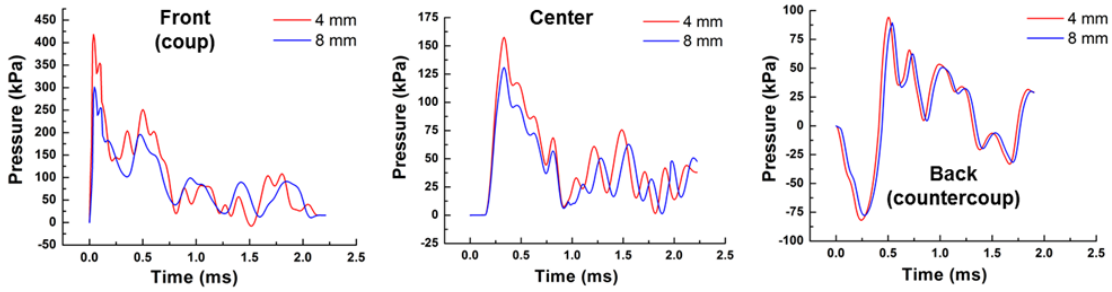

Figure 7.4: ICP response as a function of skull thickness

Table 7.2: Peak ICP and positive phase impulse values at various locations in the brain as a function of skull thickness

Location	**Peak ICP (kPa)**			**Impulse (kPa-ms)**		
	Skull thickness 4 mm	**Skull thickness 8 mm**	**% difference**	**Skull thickness 4 mm**	**Skull thickness 8 mm**	**% difference**
Front	416	295	29	218	194	11
Center	156	129	17	107	90	16

Back (+ve phase)	93	88	5	38	35	8
Back (-ve phase)	-82	-75	9	-20	-19	5

7.4 Role of face in load transfer to the brain:

In the earlier chapter it was seen from the experiments that the padded helmet only marginally reduces peak ICPs and ICP impulse values in the brain. To explain this pattern it was hypothesized that face is important pathway of load/energy transfer to the brain. In order to evaluate role of face in load/energy transfer to the intracranial contents, additional simulations are carried out with the face shield. Figure 7.5 shows the ICP profiles at three different locations for no helmet, padded helmet and padded helmet with face shield cases and table 7.3 summarizes the peak ICP and positive phase impulse values for those scenarios. With the padded helmet, peak ICP and positive phase impulse values are reduced; reductions upto 39.78 % in peak ICP and 38.36 % in ICP impulse are seen. However, peak ICP value at front location seen with the padded helmet still exceeded the peak ICP threshold values available in the literature. In addition, it is not known if impulse reductions seen with the padded helmet are sufficient to mitigate the TBI as injury thresholds values for impulse are not available. To investigate this further we hypothesized that face remains important pathway of load transfer to the intracranial contents and face shield was added to padded helmet-head assembly to study load/energy transfer to the brain. With the face shield much higher reductions upto 93.75 % in peak

ICP and 93.18 % in ICP impulse are seen. With the face shield, peak ICP values seen in the brain are below the injury threshold values.

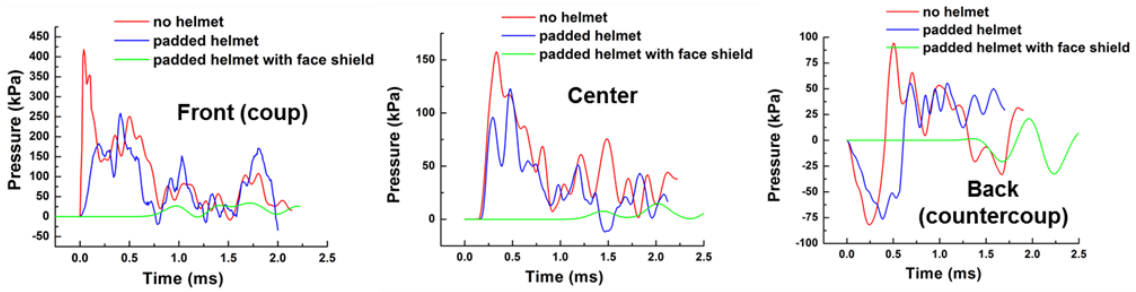

Figure 7.5: Comparison of ICP profiles for no helmet, padded helmet and padded helmet with face shield scenarios.

Table 7.3: Comparison of (a) peak ICPs and (b) ICP impulse for no helmet, padded helmet and padded helmet with face shield scenarios.

(a)

Location	Peak ICP (kPa)				
	No helmet	Padded helmet	Padded helmet with face shield	% reduction compared to no helmet scenario	
				Padded helmet	Padded helmet with face shield
Front	416	255	26	38.70	93.75
Center	156	123	14.65	21.15	90.61
Back (+ve phase)	93	56	21	39.78	77.42

Back (-ve phase)	-82	-75.44	-32	8.00	60.98

(b)

Location	**ICP impulse (kPa-ms)**				
	No helmet	**Padded helmet**	**Padded helmet with face shield**	**% reduction compared to no helmet scenario**	
				Padded helmet	**Padded helmet with face shield**
Front	218	166	28	23.85	87.16
Center	107	65.96	7.3	38.36	93.18
Back (+ve phase)	38	38.21	3.16	-0.55	91.68
Back (-ve phase)	-20	-26.83	-4.45	-34.15	77.75

7.5 Role of skull deformations on ICP response:

Skull flexure is proposed as one of the potential mechanisms of brain injury [61, 62, 184, 207]. In order to study the role of skull deformations in governing ICP response, following hypotheses are made: 1) Initial ICP response is solely governed by the transmission of the blast wave into the brain. 2) Magnitude of peak ICP is not proportional to radial displacement and radial strain of the skull. 3) For higher (normal) skull modulus values, high frequency, low amplitude oscillations are present and these oscillations originate from stress wave in the skull and not by skull deflections. 4) For

lower skull modulus values, high amplitude, low frequency oscillations are present and these oscillations originate from skull deflections. The hypotheses are investigated in this section.

Figure 7.6 shows the ICP time history in the brain and corresponding radial strain and radial displacement in the skull for front and temple locations for various Young's moduli of the skull. The bulk modulus of the brain is kept constant at 2190 MPa. The time histories are filtered using 10 kHz filter to reduce the noise/oscillations. It can be seen that, as the Young's modulus of the skull is reduced the peak ICP is increased. This is logical considering as the Young's modulus is decreased impedance mismatch between the skull and the brain is increased thus increasing transmission coefficient (see equation 7.1). Radial strain is also increased as Young's modulus of the skull is reduced. However, magnitude of peak ICP increase is not proportional to increase in radial strain of the skull as shown in table 7.4. In addition, when the impedance mismatch (hence transmission coefficient) between the skull and the brain is kept constant (while changing the Young's modulus of the skull), the peak ICP values remain changed. Impedance of the skull is kept constant by simultaneously varying density and Young's modulus of the skull. This clearly indicates that change in ICP with change in skull modulus at the initial stages (i.e. associated with the direct load) is governed solely by wave transmission, and not the skull flexure. For temple location, the amplitude of secondary oscillations (associated with the indirect load) is increased as the skull modulus is decreased, this trend is especially evident for the skull modulus of 800 MPa (see figure 7.6). Thus it is possible that initial ICP response is governed by the wave transmissions (direct load) and response

at later time is governed by the deformations or oscillations of the skull (indirect load), especially if skull modulus is order of magnitude smaller (e.g. E=800 MPa) than skull modulus value reported in the literature. Fast Fourier Transform (FFT) of unfiltered radial strain and ICP data also showed that low amplitude, high frequency oscillations are also present for skull moduli values of 4400 and 8000 MPas due to higher longitudinal wave speeds. From these parametric studies it is seen that all the hypotheses postulated above hold true.

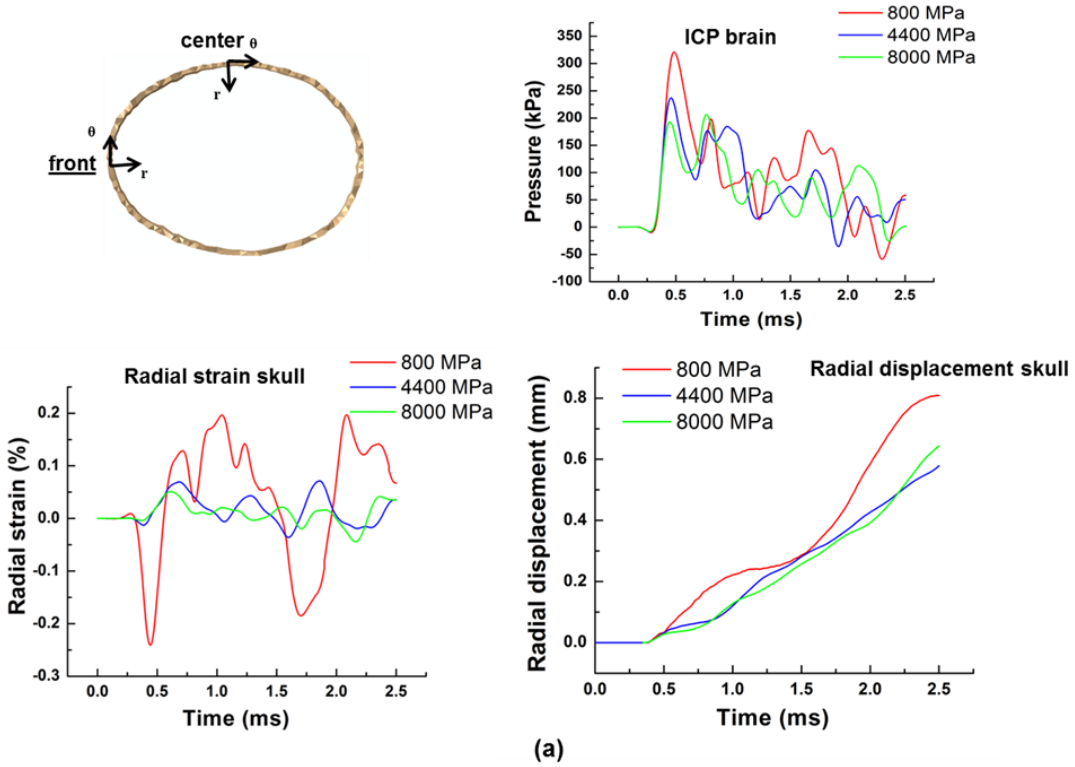

(a)

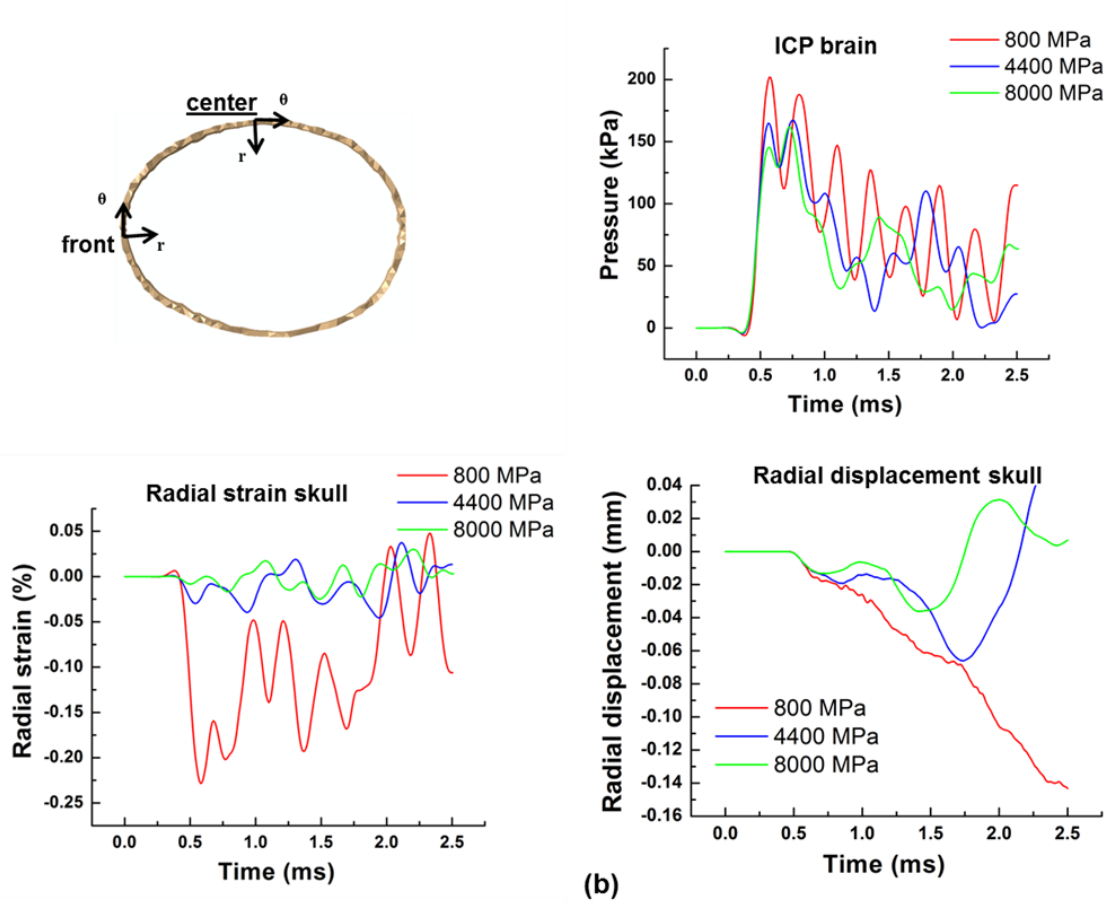

Figure 7.6: ICP time history in the brain and corresponding radial strain and radial displacement in the skull for various Young's moduli of the skull. (a) front location (b) temple location

Table 7.4: % change in peak radial strain and peak ICP as a function of skull Young's modulus

Location	Skull Young's modulus (MPa)	Peak radial strain (%)	Peak ICP (kPa)	% increase in radial strain	% increase in ICP
Front	8000	-0.004	192	-	-
	4400	-0.012	236	200	22.92
	800	-0.24	321	1900	36.02
Center	8000	-0.007	144	-	-
	4400	-0.029	163	314.29	13.19
	800	-0.227	201	682.76	23.31

7.6 Summary:

In this chapter, parametric studies are performed to identify/confirm loading mechanisms and loading pathways through which energy is imparted to intracranial contents under primary blast loading conditions. In addition, role of geometric and material parameters such as skull thickness, skull and brain moduli on ICP response is also studied in order to understand head to head variations seen in the PMHS experiments. With these goals in mind, some of the key findings of this chapter are:

- Face is the important pathway of energy transfer to the intracranial contents. With face shield significant reductions upto 93.75 % in peak ICP and 93.18 % in ICP impulse are seen. In addition, peak ICP values with the face shield were below traumatic brain injury thresholds available in the literature.
- Role of skull deformation on ICP response is studied by varying Young's modulus of the skull. The results show that the initial ICP response is solely governed by the transmission of the blast wave into the intracranial contents and that the magnitude of peak ICP is not proportional to radial displacement and radial strain of the skull. For higher (normal) modulus values, the high frequency, low amplitude oscillations are seen in the skull strain and ICP profiles. These oscillations originate from the stress wave in the skull and not by skull deflections. On the contrary, for lower modulus values (e.g. E=800 MPa), high amplitude, low frequency oscillations are seen. These oscillations originate from the skull deflections.
- As the skull thickness is increased the peak ICPs and ICP impulse values are decreased; however these reductions are not significant in the countercoup region.
- With change in bulk modulus ICP response is changed, however perceptible differences in the ICP response are only seen for very low bulk modulus value of 10 MPa; which is ~200 times smaller than widely accepted value of 2190 MPa in the literature.

CHAPTER 8

CONCLUSIONS AND FUTURE WORK

8.1 Conclusions of this work:

Blast-induced traumatic brain injury is the most prevalent military injury in Iraq and Afghanistan, yet little is known about if and how blast waves induce brain injury. Whether the primary blast waves alone can cause mechanical insult that is comparable to existing traumatic brain injury thresholds is still an open question. A comprehensive knowledge of the loading mechanics of brain tissue is crucial in understanding the pathophysiology of BINT as well as in designing effective mitigation strategies. In this work, blast wave head interactions are studied, under pure primary blast loading conditions on PMHS and surrogate dummy heads, using an integrated experimental and numerical approach. The critical factors in biomechanical loading of the head-brain complex are identified. Some of the contributions of this work are:

- It has been conclusively shown that the primary blast waves alone can cause mechanical insult in PMHS. The magnitude of this mechanical insult increases with increase in incident blast intensity, duration and impulse. The ICPs exceed brain injury thresholds available in the literature for blast overpressures as low as 200 kPa. The animal work carried out at TMRF, UNL also show neuronal damage at that intensity.
- The intracranial response is studied in terms of the wave transmission (direct load) and the skull deflections (indirect load). The wave transmission has been identified as

the main loading mechanism of mechanical insult to the brain. The role of wave propagation through skin-skull-brain parenchyma in governing ICP response is also established. In addition, the role of head geometry and head orientations in governing pressure field on the surface of the head is also established.

- The role of helmets in blast wave head interactions is extensively studied. The focusing of blast waves under the helmet is shown for certain head helmet configurations with a gap between the head and the helmet. It is also shown that the focusing of the blast wave under the helmet accompanies a corresponding increase in ICP beneath focused regions as compared to the no helmet case. It is shown that with the presence of helmets, significant mechanical insult is induced in the brain through the face.

8.2 Recommendations for the future work:

This dissertation was aimed at understanding the response of PMHS and surrogate heads to the primary blast. Some of the ideas of mechanics of the blast wave head interactions with and without the helmets are established and verified in this work. However, there is a strong need to translate these ideas to better understand neuronal degeneration at macroscopic and microscopic levels. In addition, a lot more work needs to be done in terms of design of personal protective equipment for protection of head against blast. Some of the recommendations for the future work are:

- In order to develop bTBI thresholds, a lot more testing needs to be done in terms of PMHS as significant variations exist from specimen to specimen.

- In this work, ballistic gel was used as a brain simulant. Experiments should also be conducted with fresh PMHS heads with intact brain. Intracranial response with intact brain should then be compared with intracranial response with ballistic gel.
- Various means of blast wave mitigation (e.g. adding a face shield) should be critically explored and evaluated.

References:

[1] Tanielian, T., and Jaycox, L.H., 2008, Invisible wounds of war, RAND Corporation, Santa Monica, CA.

[2] Anderson, R. J., 2008, "Shell shock: an old injury with new weapons," Mol Interv, 8(5), pp. 204-218.

[3] Warden, D., 2006, "Military TBI During the Iraq and Afghanistan Wars," The Journal of Head Trauma Rehabilitation, 21(5), pp. 398-402.

[4] Thurman, D. J., Alverson, C., Dunn, K. A., Guerrero, J., and Sniezek, J. E., 1999, "Traumatic brain injury in the United States: A public health perspective," J Head Trauma Rehabil, 14(6), pp. 602-615.

[5] Thurman, D. J., Sniezek, J. E., and Johnson, D., 1995, "Guidelines for Surveillance of Central Nerous System Injury. Centers for Disease Control and Prevention, Atlanta."

[6] Teasdale, G., and Jennett, B., 1974, "Assessment of coma and imparied consciousness : A Practical Scale," The Lancet, 304(7872), pp. 81-84.

[7] Ling, G., Bandak, F., Armonda, R., Grant, G., and Ecklund, J., 2009, "Explosive Blast Neurotrauma," Journal of Neurotrauma, 26(6), pp. 815-825.

[8] 2003, "Centers for Disease Control and Prevention. Explosions and Blast Injuries: A Primer for Clinicians. CDC, Atlanta, GA.."

[9] Kraus, M. F., Susmaras, T., Caughlin, B. P., Walker, C. J., Sweeney, J. A., and Little, D. M., 2007, "White matter integrity and cognition in chronic traumatic brain injury: a diffusion tensor imaging study," Brain, 130(Pt 10), pp. 2508-2519.

[10] Okie, S., 2005, "Traumatic brain injury in the war zone," N. Engl. J. Med., 352(20), pp. 2043-2047.

[11] Kennedy, J. E., Jaffee, M. S., Leskin, G. A., Stokes, J. W., Leal, F. O., and Fitzpatrick, P. J., 2007, "Posttraumatic stress disorder and posttraumatic stress disorder-like symptoms and mild traumatic brain injury," J Rehabil Res Dev, 44(7), pp. 895-920.

[12] Alexander, M. P., 1995, "Mild traumatic brain injury: pathophysiology, natural history, and clinical management," Neurology, 45(7), pp. 1253-1260.

[13] Schneiderman, A. I., Braver, E. R., and Kang, H. K., 2008, "Understanding sequelae of injury mechanisms and mild traumatic brain injury incurred during the conflicts in Iraq and Afghanistan: persistent postconcussive symptoms and posttraumatic stress disorder," Am J Epidemiol, 167(12), pp. 1446-1452.

[14] Heitger, M. H., Jones, R. D., Macleod, A. D., Snell, D. L., Frampton, C. M., and Anderson, T. J., 2009, "Impaired eye movements in post-concussion syndrome indicate suboptimal brain function beyond the influence of depression, malingering or intellectual ability," Brain, 132(Pt 10), pp. 2850-2870.

[15] Rao, V., and Lyketsos, C., 2000, "Neuropsychiatric sequelae of traumatic brain injury," Psychosomatics, 41(2), pp. 95-103.

[16] Leung, L. Y., VandeVord, P. J., Dal Cengio, A. L., Bir, C., Yang, K. H., and King, A. I., 2008, "Blast related neurotrauma: a review of cellular injury," Mol Cell Biomech, 5(3), pp. 155-168.

[17] Beauchamp, K., Mutlak, H., Smith, W. R., Shohami, E., and Stahel, P. F., 2008, "Pharmacology of traumatic brain injury: where is the "golden bullet"?," Mol Med, 14(11-12), pp. 731-740.

[18] Xiong, Y., Mahmood, A., and Chopp, M., 2009, "Emerging treatments for traumatic brain injury," Expert Opin Emerg Drugs, 14(1), pp. 67-84.

[19] Svetlov, S. I., Larner, S. F., Kirk, D. R., Atkinson, J., Hayes, R. L., and Wang, K. K. W., 2009, "Biomarkers of Blast-Induced Neurotrauma: Profiling Molecular and Cellular Mechanisms of Blast Brain Injury," Journal of Neurotrauma, 26(6), pp. 913-921.

[20] Langlois, J. A., Rutland-Brown, W., and Thomas, K. E., 2006, "Traumatic brain injury in the United States: Emergency department visits, hospitalizations, and deaths. Centers for Disease Control and Prevention, National Center for Injury Protection, Atlanta,GA, 2006.."

[21] U.S. Government Accountability Office 2008, "Mild traumatic brain injury screening and evaluation implemented for oef/oif veterans, but challenges remain."

[22] Terrio, H., Brenner, L. A., Ivins, B. J., Cho, J. M., Helmick, K., Schwab, K., Scally, K., Bretthauer, R., and Warden, D., 2009, "Traumatic Brain Injury Screening: Preliminary Findings in a US Army Brigade Combat Team," J. Head Trauma Rehabil., 24(1), pp. 14-23.

[23] Defense and Veterans Brain Injury Center February 2007, "Operation Iraqi Freedom (OIF)/Operation Enduring Freedom (OEF) Fact Sheet."

[24] Clark, M. E., Bair, M. J., Buckenmaier, C. C., 3rd, Gironda, R. J., and Walker, R. L., 2007, "Pain and combat injuries in soldiers returning from Operations Enduring Freedom

and Iraqi Freedom: implications for research and practice," J Rehabil Res Dev, 44(2), pp. 179-194.

[25] Galarneau, M. R., Woodruff, S. I., Dye, J. L., Mohrle, C. R., and Wade, A. L., 2008, "Traumatic brain injury during Operation Iraqi Freedom: findings from the United States Navy-Marine Corps Combat Trauma Registry," J Neurosurg, 108(5), pp. 950-957.

[26] Department of defense (DoD). Accessed January 2012., "DoD Worldwide Numbers for Traumatic Brain Injury. http://www.health.mil/Research/TBI_Numbers.aspx."

[27] Terrio, H., Brenner, L. A., Ivins, B. J., Cho, J. M., Helmick, K., Schwab, K., Scally, K., Bretthauer, R., and Warden, D., 2009, "Traumatic brain injury screening: preliminary findings in a US Army Brigade Combat Team," J Head Trauma Rehabil, 24(1), pp. 14-23.

[28] Jones, E., Fear, N. T., and Wessely, S., 2007, "Shell shock and mild traumatic brain injury: A historical review," American Journal of Psychiatry, 164(11), pp. 1641-1645.

[29] Bhattacharjee, Y., 2008, "Neuroscience - Shell shock revisited: Solving the puzzle of blast trauma," Science, 319(5862), pp. 406-408.

[30] Taber, K. H., Warden, D. L., and Hurley, R. A., 2006, "Blast-related traumatic brain injury: what is known?," The Journal of Neuropsychiatry and Clinical Neurosciences, 18(2), pp. 141-145.

[31] Murray, C. K., Reynolds, J. C., Schroeder, J. M., Harrison, M. B., Evans, O. M., and Hospenthal, D. R., 2005, "Spectrum of care provided at an echelon II Medical Unit during Operation Iraqi Freedom," Mil Med, 170(6), pp. 516-520.

[32] Gawande, A., 2004, "Casualties of war--military care for the wounded from Iraq and Afghanistan," N Engl J Med, 351(24), pp. 2471-2475.

[33] DePalma, R. G., Burris, D. G., Champion, H. R., and Hodgson, M. J., 2005, "Blast Injuries," N. Engl. J. Med., 352(13), pp. 1335-1342.

[34] Moore, D. F., Jerusalem, A., Nyein, M., Noels, L., Jaffee, M. S., and Radovitzky, R. A., 2009, "Computational biology - Modeling of primary blast effects on the central nervous system," Neuroimage, 47, pp. T10-T20.

[35] Moore, D. F., Radovitzky, R. A., Shupenko, L., Klinoff, A., Jaffee, M. S., and Rosen, J. M., 2008, "Blast physics and central nervous system injury," Future Neurology, 3(3), pp. 243-250.

[36] Ritzel, D., Parks S., Roseveare J., Rude G. and Sawyer T.,, 2011, "Experimental Blast Simulation for Injury Studies. RTO-MP-HFM-207.," RTO Human Factors and Medicine Panel (HFM) Symposium Halifax, Canada.

[37] Warden, D. L., French, L. M., Shupenko, L., Fargus, J., Riedy, G., Erickson, M. E., Jaffee, M. S., and Moore, D. F., 2009, "Case report of a soldier with primary blast brain injury," Neuroimage, 47 Suppl 2, pp. T152-153.

[38] "ConWep version: 2.1.0.8, USAE Engineer Research & Development Center, CEERD-GS-S, 3909 Halls Ferry Road, Vicksburg, Mississippi.."

[39] Bauman, R. A., Ling, G., Tong, L., Januszkiewicz, A., Agoston, D., Delanerolle, N., Kim, Y., Ritzel, D., Bell, R., Ecklund, J., Armonda, R., Bandak, F., and Parks, S., 2009, "An Introductory Characterization of a Combat-Casualty-Care Relevant Swine Model of

Closed Head Injury Resulting from Exposure to Explosive Blast," Journal of Neurotrauma, 26(6), pp. 841-860.

[40] Formby, S. A., and Wharton, R. K., 1996, "Blast characteristics and TNT equivalence values for some commercial explosives detonated at ground level," Journal of Hazardous Materials, 50(2-3), pp. 183-198.

[41] Mott DR, S. D., Young TR, Levine J, Dionne JP, Makris A, Hubler G, "Blast-induced pressure fields beneath a military helmet," Proc. 20th international symposium on military aspects of blast and shock, Oslo, Norway, September 1st – 5th, 2008.

[42] Kinney, G. F., and Graham, K. J., 1985, Explosive shocks in air, Springer-Verlag, New York.

[43] Panzer, M. B., Myers, B. S., Capehart, B. P., and Bass, C. R., 2012, "Development of a finite element model for blast brain injury and the effects of CSF cavitation," Ann Biomed Eng, 40(7), pp. 1530-1544.

[44] Goldsmith, W., and Monson, K. L., 2005, "The state of head injury biomechanics: past, present, and future part 2: physical experimentation," Crit Rev Biomed Eng, 33(2), pp. 105-207.

[45] O'Connor, W. T., Smyth, A., and Gilchrist, M. D., 2011, "Animal models of traumatic brain injury: A critical evaluation," Pharmacology & Therapeutics, 130(2), pp. 106-113.

[46] Xiong, Y., Mahmood, A., and Chopp, M., 2013, "Animal models of traumatic brain injury," Nat Rev Neurosci, 14(2), pp. 128-142.

[47] Goldsmith, W., 2001, "The state of head injury biomechanics: past, present, and future: part 1," Crit Rev Biomed Eng, 29(5-6), pp. 441-600.

[48] Nahum, A., Smith, R., and Ward, C., "Intracranial pressure dynamics during head impact," Proc. Proc. 21st Stapp Car Crash Conf., pp. 339-366.

[49] Nahum, A., and Smith, R., 1976, "An Experimental Model for Closed Head Impact Injury," SAE Technical Paper 760825.

[50] Ward, C. C., Chan, M. , Nahum, A.M., "Intracranial Pressure - a Brain Injury Criterion," Proc. Proc. 24th Stapp Car Crash Conference SAE No. 801304, p. 161.

[51] Trosseille, X., Tarriére, C., Lavaste, F., Guillon, F., and Domont, A., "Development of a F.E.M. of the Human Head According to a Specific Test Protocol. SAE Technical Paper 922527," Proc. Stapp Car Crash Conference.

[52] Hardy, W. N., Foster, C. D., Mason, M. J., Yang, K. H., King, A. I., and Tashman, S., 2001, "Investigation of Head Injury Mechanisms Using Neutral Density Technology and High-Speed Biplanar X-ray," Stapp Car Crash J, 45, pp. 337-368.

[53] Hardy, W. N., Mason, M. J., Foster, C. D., Shah, C. S., Kopacz, J. M., Yang, K. H., King, A. I., Bishop, J., Bey, M., Anderst, W., and Tashman, S., 2007, "A study of the response of the human cadaver head to impact," Stapp Car Crash J, 51, pp. 17-80.

[54] Stalnaker, R., Melvin, J., Nusholtz, G., and Alem, N., 1977, "Head Impact Response," SAE Technical Paper, 770921.

[55] Nusholtz, G., Lux, P., Kaiker, P., and Janicki, M., 1984, "Head impact Response—Skull Deformation and Angular Accelerations," SAE Technical Paper, 841657.

[56] Walsh, M. J., Kelleher, B. J., and Severin, C. M., 1985, "Head and Neck Injuries in Human Cadavers From Lateral Impacts," SAE Technical Paper, 856032.

[57] McIntosh, A., Kallieris, D., Mattern, R., and Miltner, E., 1993, "Head and Neck Injury Resulting from Low Velocity Direct Impact," SAE Technical Paper 933112.

[58] Rizzetti, A., Dimitrios, K., Schiemann, P., and Rainer, M., 1997, "Response and injury severity of the head-neck unit during a low velocity head impact," Proceedings of the International Research Council on the Biomechanics of Injury conference, 25, pp. 193-206.

[59] Got, C., Patel, A., Fayon, A., and Tarrière, C., 1978, "Results of Experimental Head Impacts on Cadavers: The Various Data Obtained and Their Relations to Some Measured Physical Parameters," SAE Technical Paper, 780887.

[60] Bir, C., Bolander R., Leonardi A., Ritzel D., VandeVord P. and Dingell J.,, 2011, "A Biomechanical Prospective of Blast Injury Neurotrauma. RTO-MP-HFM-207.," RTO Human Factors and Medicine Panel (HFM) Symposium Halifax, Canada.

[61] Bolander, R., 2012, "A multi-species analysis of biomechanical responses of the head to a shock wave," Ph.D. dissertation, Wayne State University.

[62] Leonardi, A. D., 2011, "An investigation of the biomechanical response from shock wave loading to the head," Ph.D. dissertation, Wayne State University.

[63] Rafaels, K. A., Shridharani, J., Bass, C. R., Salzar, R. S., Walilko, T. J., and Panzer, M. B., 2010, "Blast wave attenuation: ballistic protective helmets and the head," Personal Armor Safety Symposium (PASS)Washington, DC.

[64] Cernak, I., Wang, Z. G., Jiang, J. X., Bian, X. W., and Savic, J., 2001, "Ultrastructural and functional characteristics of blast injury-induced neurotrauma," Journal of Trauma-Injury Infection and Critical Care, 50(4), pp. 695-706.

[65] Courtney, A. C., and Courtney, M. W., 2009, "A thoracic mechanism of mild traumatic brain injury due to blast pressure waves," Medical Hypotheses, 72(1), pp. 76-83.

[66] Anzelius, A., 1943, "The effect of an impact on a spherical liquid mass," Acto path. microbial. scond. Suppl., 48, pp. 153-159.

[67] Voo, K., Kumaresan, S., Pintar, F. A., Yoganandan, N., and Sances, A., Jr., 1996, "Finite-element models of the human head," Med Biol Eng Comput, 34(5), pp. 375-381.

[68] Ruan, J. S., Khalil, T., and King, A. I., 1994, "Dynamic response of the human head to impact by three-dimensional finite element analysis," Journal of Biomechanical Engineering, Transactions of the ASME, 116(1), pp. 44-50.

[69] Zhang, L., Yang, K. H., Dwarampudi, R., Omori, K., Li, T., Chang, K., Hardy, W. N., Khalil, T. B., and King, A. I., 2001, "Recent advances in brain injury research: A new human head model development and validation," Stapp Car Crash Journal, 45, pp. 369-394.

[70] Zhang, L. Y., Yang, K. H., and King, A. I., 2001, "Comparison of brain responses between frontal and lateral impacts by finite element modeling," Journal of Neurotrauma, 18(1), pp. 21-30.

[71] Zhou, C., Khalif, T. B., and King, A. I., "New model comparing impact responses of the homogeneous and inhomogeneous human brain," Proc. Proceedings of the 39th Stapp Car Crash Conference, November 8, 1995 - November 10, 1995, SAE, pp. 121-137.

[72] Kang H.S., W., R., Diaw B.M., Chinn, B., "Validation of a 3D Anatomic Human Head Model and Replication of Head Impact in Motorcycle Accident by Finite Element Modeling," Proc. Proceedings, 41st Stapp Car Crash Conf., SAE Paper No. 973339.

[73] Belingardi, G., Chiandussi, G., and Gaviglio, I., "Development And Validation Of A New Finite Element Model Of Human Head," Proc. 19th International Technical Conference on the Enhanced Safety of Vehicles, Washington, D.C.

[74] El Sayed, T., Mota, A., Fraternali, F., and Ortiz, M., 2008, "Biomechanics of traumatic brain injury," Computer Methods in Applied Mechanics and Engineering, 197(51–52), pp. 4692-4701.

[75] Ganpule, S., Alai, A., Plougonven, E., and Chandra, N., 2012, "Mechanics of blast loading on the head models in the study of traumatic brain injury using experimental and computational approaches," Biomech Model Mechanobiol.

[76] Horgan, T. J., and Gilchrist, M. D., 2003, "The creation of three-dimensional finite element models for simulating head impact biomechanics," International Journal of Crashworthiness, 8(4), pp. 353-366.

[77] Kleiven, S., and Hardy, W. N., 2002, "Correlation of an FE Model of the Human Head with Local Brain Motion--Consequences for Injury Prediction," Stapp Car Crash J, 46, pp. 123-144.

[78] Nyein, M. K., Jason, A. M., Yu, L., Pita, C. M., Joannopoulos, J. D., Moore, D. F., and Radovitzky, R. A., 2010, "In silico investigation of intracranial blast mitigation with relevance to military traumatic brain injury," Proceedings of the National Academy of Sciences.

[79] Taylor, P. A., and Ford, C. C., 2009, "Simulation of Blast-Induced Early-Time Intracranial Wave Physics leading to Traumatic Brain Injury," Journal of Biomechanical Engineering-Transactions of the Asme, 131(6), p. 061007.

[80] Zhang, L. Y., Yang, K. H., and King, A. I., 2004, "A proposed injury threshold for introduction mild traumatic brain injury," Journal of Biomechanical Engineering-Transactions of the Asme, 126(2), pp. 226-236.

[81] Hubbard, R. P., 1971, "Flexure of layered cranial bone," Journal of Biomechanics, 4(4), pp. 251-263.

[82] Claessans, M., Sauren, F., and Wismans, J., "Modeling of the human head under impact conditions: A parametric study," Proc. Proceedings of the 1997 41st Stapp Car Crash Conference, November 13, 1997 - November 14, 1997, SAE, pp. 315-328.

[83] Takhounts, E. G., Eppinger, R. H., Campbell, J. Q., Tannous, R. E., Power, E. D., and Shook, L. S., 2003, "On the development of the SIMon Finite Element Head Model," Stapp Car Crash Journal, 47, pp. 107-133.

[84] Willinger, R., Kang, H. S., and Diaw, B., 1999, "Three-dimensional human head finite-element model validation against two experimental impacts," Annals of Biomedical Engineering, 27(3), pp. 403-410.

[85] Cheng, L. Y., Rifai, S., Khatua, T., and Piziali, R. L., "Finite element analysis of diffuse axonal injury," Proc. Electronic Diesel Engine Controls - Papers presented at the 1990 SAE International Congress and Exposition, Febrary 26, 1990 - March 2, 1990, Publ by SAE, pp. 14p 900547-900514p 900547.

[86] Claessens, M., Sauren, F., and Wismans, J., "Modeling of the human head under impact conditions: a parametric study," Proc. Proc. 41st Stapp Car Crash Conf., pp. 315-328.

[87] Miller, R. T., Meaney, D. F., Smith, D. H., Chen, X., Nonaka, M., Leoni, M., and Margulies, S. S., 1998, "Finite element modeling approaches for predicting injury in an experimental model of severe diffuse axonal injury. SAE Technical Paper 983154."

[88] Chafi, M., Karami, G., and Ziejewski, M., 2010, "Biomechanical Assessment of Brain Dynamic Responses Due to Blast Pressure Waves," Annals of Biomedical Engineering, 38(2), pp. 490-504.

[89] Zoghi-Moghadam, M., and Sadegh, A. M., 2009, "Global/local head models to analyse cerebral blood vessel rupture leading to ASDH and SAH," Computer Methods in Biomechanics and Biomedical Engineering, 12(1), pp. 1-12.

[90] McElhaney, J., Melvin, J. W., Roberts, V. L., and Portnoy, H. D., "Dynamic characteristics of the tissues of the head," Proc. In: Perspectives in Biomedical Engineering, pp. 215-222.

[91] Stalnaker, R. L., 1969, "Mechanical properties of the head, Ph.D. Dissertation," West Virginia University.

[92] Khalil, T. B., and Viano, D. C., 1982, "Critical Issues in Finite Element Modeling of Head Impact," Proc. 26th Stapp Car Crash Conf., SAE Paper No. 821150.

[93] Nusholtz, G. S., Kaiker, P. S., and Gould, W. S., 1987, "Two factors critical in the pressure response of the impacted head," Aviat Space Environ Med., 58(12), pp. 1157-1164.

[94] Kleiven, S., and von Holst, H., 2002, "Consequences of head size following trauma to the human head," Journal of Biomechanics, 35(2), pp. 153-160.

[95] Grujicic, M., Bell, W., Pandurangan, B., and Glomski, P., 2011, "Fluid/Structure Interaction Computational Investigation of Blast-Wave Mitigation Efficacy of the Advanced Combat Helmet," Journal of Materials Engineering and Performance, 20(6), pp. 877-893.

[96] Sharma, S., and Zhang, L., "Prediction of Intracranial Responses from Blast Induced Neurotrauma using a validated finite element model of human head," Proc. Proceedings of Injury Biomechanics Symposium (IBS).

[97] Zhang, L., Makwana, R., and Sharma, S., "Comparison of the head response in blast insult with and without combat helmet," Proc. Proceedings of HFM-207 Symposium on Survey of Blast Injury across the Full Landscape of Military Science NATO OTAN Research & Technology Organisation.

[98] Estes, M. S., McElhaney, J.H., "Response of brain tissue of compressive loading," Proc. 4th ASME Biomechanics Conf., number 70-BHF-13.

[99] Shuck, L. Z., and Advani, S. H., 1972, "Rheological response of human brain-tissue in shear," Journal of Basic Engineering, 94(4), pp. 905-911.

[100] Donnelly, B. R., and Medige, J., 1997, "Shear properties of human brain tissue," Journal of Biomechanical Engineering-Transactions of the Asme, 119(4), pp. 423-432.

[101] Arbogast, K. B., Meaney, D., and Thibault, L., 1995, "Biomechanical Characterization of the Constitutive Relationship for the Brainstem. SAE Technical Paper 952716."

[102] Arbogast, K. B., and Margulies, S. S., 1997, "Regional Differences in Mechanical Properties of the Porcine Central Nervous System. SAE Technical Paper 973336."

[103] Arbogast, K. B., and Margulies, S. S., 1998, "Material characterization of the brainstem from oscillatory shear tests," Journal of Biomechanics, 31(9), pp. 801-807.

[104] Bilston, L. E., Liu, Z. Z., and Nhan, P. T., 1997, "Linear viscoelastic properties of bovine brain tissue in smear," Biorheology, 34(6), pp. 377-385.

[105] Bilston, L. E., Liu, Z. Z., and Phan-Thien, N., 2001, "Large strain behaviour of brain tissue in shear: Some experimental data and differential constitutive model," Biorheology, 38(4), pp. 335-345.

[106] Brands, D. W. A., Bovendeerd, P.H.M., Peters, G.W.M., Wismans, J.S.H.M., Paas, M.H.J.W., van Bree, J.L.M.J. , "Comparison of the dynamic behavior of the brain tissue and two model materials," Proc. Proceedings of the 43rd Stapp Car Crash Conference, number SAE 99SC21 pp. 57-64.

[107] Brands, D. W. A., Bovendeerd, P.H.M., Peters, G.W.M., Wismans, J.S.H.M., 2000, "The large shear strain dynamic behavior of in-vitro porcine brain tissue and the silicone gel model material," Proceedings of the 44th Stapp Car Crash Conference, number SAE 200001-SC17, pp. 249-260.

[108] Miller, K., and Chinzei, K., 1997, "Constitutive modelling of brain tissue: Experiment and theory," Journal of Biomechanics, 30(11-12), pp. 1115-1121.

[109] Miller, K., and Chinzei, K., 2002, "Mechanical properties of brain tissue in tension," Journal of Biomechanics, 35(4), pp. 483-490.

[110] Darvish, K. K., and Crandall, J. R., 2001, "Nonlinear viscoelastic effects in oscillatory shear deformation of brain tissue," Medical Engineering & Physics, 23(9), pp. 633-645.

[111] Lippert, S. A., Rang, E. M., and Grimm, M. J., 2004, "The high frequency properties of brain tissue," Biorheology, 41(6), pp. 681-691.

[112] Nicolle, S., Lounis, M., and Willinger, R., 2004, "Shear Properties of Brain Tissue over a Frequency Range Relevant for Automotive Impact Situations: New Experimental Results," Stapp car crash journal, 48, pp. 239-258.

[113] Nicolle, S., Lounis, M., Willinger, R., and Palierne, J. F., 2005, "Shear linear behavior of brain tissue over a large frequency range," Biorheology, 42(3), pp. 209-223.

[114] Hrapko, M., van Dommelen, J. A. W., Peters, G. W. M., and Wismans, J. S. H. M., 2006, "The mechanical behaviour of brain tissue: Large strain response and constitutive modelling," Biorheology, 43(5), pp. 623-636.

[115] Franceschini, G., Bigoni, D., Regitnig, P., and Holzapfel, G. A., 2006, "Brain tissue deforms similarly to filled elastomers and follows consolidation theory," Journal of the Mechanics and Physics of Solids, 54(12), pp. 2592-2620.

[116] Pervin, F., and Chen, W. W., 2009, "Dynamic mechanical response of bovine gray matter and white matter brain tissues under compression," Journal of Biomechanics, 42(6), pp. 731-735.

[117] Prevost, T. P., Balakrishnan, A., Suresh, S., and Socrate, S., 2011, "Biomechanics of brain tissue," Acta Biomaterialia, 7(1), pp. 83-95.

[118] Lissner, H. R., Lebow, M., and Evans, F. G., 1960, "Experimental studies on the relation between acceleration and intracranial pressure changes in man," Surg Gynecol Obstet, 111, pp. 329-338.

[119] Gadd, C., "Use of weighted-impulse criterion for estimating injury hazard," Proc. 10th Stapp Car Crash Conference, pp. 164-174.

[120] Eppinger, R., Sun, E., Bandak, F., Haffner, M., Khaewpong, N., Maltese, M., Kuppa, S., Nguyen, T., Takhounts, E., and Tannous, R., 1999, "Development of improved injury criteria for the assessment of advanced automotive restraint systems–II," National Highway Traffic Safety Administration.

[121] Funk, J. R., Rowson, S., Daniel, R. W., and Duma, S. M., 2012, "Validation of Concussion Risk Curves for Collegiate Football Players Derived from HITS Data," Annals of Biomedical Engineering, 40(1), pp. 79-89.

[122] Funk, J. R., Duma, S. M., Manoogian, S. J., and Rowson, S., 2007, "Biomechanical risk estimates for mild traumatic brain injury," Annu Proc Assoc Adv Automot Med, 51, pp. 343-361.

[123] Forbes, J. A., Awad, A. J., Zuckerman, S., Carr, K., and Cheng, J. S., 2012, "Association between biomechanical parameters and concussion in helmeted collisions in American football: a review of the literature," Neurosurgical Focus, 33(6).

[124] Pellman, E. J., Viano, D. C., Tucker, A. M., Casson, I. R., and Waeckerle, J. F., 2003, "Concussion in professional football: reconstruction of game impacts and injuries," Neurosurgery, 53(4), pp. 799-812; discussion 812-794.

[125] Guskiewicz, K. M., Mihalik, J. P., Shankar, V., Marshall, S. W., Crowell, D. H., Oliaro, S. M., Ciocca, M. F., and Hooker, D. N., 2007, "Measurement of head impacts in collegiate football players: relationship between head impact biomechanics and acute clinical outcome after concussion," Neurosurgery, 61(6), pp. 1244-1252; discussion 1252-1243.

[126] Brolinson, P. G., Manoogian, S., McNeely, D., Goforth, M., Greenwald, R., and Duma, S., 2006, "Analysis of linear head accelerations from collegiate football impacts," Curr Sports Med Rep, 5(1), pp. 23-28.

[127] Rowson, S., and Duma, S. M., 2012, "The Virginia Tech Response," Annals of Biomedical Engineering, 40(12), pp. 2512-2518.

[128] Broglio, S. P., Eckner, J. T., and Kutcher, J. S., 2012, "Field-based measures of head impacts in high school football athletes," Current Opinion in Pediatrics, 24(6), pp. 702-708.

[129] Broglio, S. P., Surma, T., and Ashton-Miller, J. A., 2012, "High School and Collegiate Football Athlete Concussions: A Biomechanical Review," Annals of Biomedical Engineering, 40(1), pp. 37-46.

[130] Ono, K., Kikuchi, A., Nakamura, M., Kobayashi, H., and Nakamura, H., "Human head tolerance to sagittal impact reliable estimation deduced from experimental head injury using sub-human primates and human cadaver skulls," Proc. 24th Stapp Car Crash Conf, pp. 101-160.

[131] Gurdjian, E. S., Lissner, H. R., and Patrick, L. M., "Concussion mechanism and pathology," Proc. Proceedings, 7th Stapp Car Crash Conf., pp. 470–482.

[132] Ommaya, A. K., and Hirsch, A. E., 1971, "Tolerances for Cerebral Concussion from Head Impact and Whiplash in Primates," Journal of Biomechanics, 4(1), pp. 13-17.

[133] Margulies, S. S., and Thibault, L. E., 1992, "A Proposed Tolerance Criterion For Diffuse Axonal Injury In Man," Journal of Biomechanics, 25(8), pp. 917-923.

[134] Bain, A. C., and Meaney, D. F., 2000, "Tissue-level thresholds for axonal damage in an experimental model of central nervous system white matter injury," J Biomech Eng, 122(6), pp. 615-622.

[135] Morrison, B., III, Cater, H. L., Wang, C. C., Thomas, F. C., Hung, C. T., Ateshian, G. A., and Sundstrom, L. E., 2003, "A tissue level tolerance criterion for living brain developed with an in vitro model of traumatic mechanical loading," Stapp Car Crash J, 47, pp. 93-105.

[136] Ellis, E. F., McKinney, J. S., Willoughby, K. A., Liang, S., and Povlishock, J. T., 1995, "A new model for rapid stretch-induced injury of cells in culture: characterization of the model using astrocytes," J Neurotrauma, 12(3), pp. 325-339.

[137] Deck, C., and Willinger, R., 2008, "Improved head injury criteria based on head FE model," International Journal of Crashworthiness, 13(6), pp. 667-678.

[138] Kleiven, S., 2007, "Predictors for traumatic brain injuries evaluated through accident reconstructions," 51st Stapp Car Crash J, pp. 81-114.

[139] Stalnaker, R. L., and McElhaney, J., "Head Injury Tolerance for Linear Impacts by Mechanical Impedance Methods," Proc. American Society of Mechanical Engineers, Winter Annual Meeting.

[140] Viano, D. C., and Lovsund, P. E. R., 1999, "Biomechanics of Brain and Spinal-Cord Injury: Analysis of Neuropathologic and Neurophysiology Experiments," Journal of Crash Prevention and Injury Control, 1(1), pp. 35-43.

[141] Yao, J. F., Yang, J. K., and Otte, D., 2008, "Investigation of head injuries by reconstructions of real-world vehicle-versus-adult-pedestrian accidents," Safety Science, 46(7), pp. 1103-1114.

[142] Anderson, R. W. G., Brown, C. J., Scott, G., Blumbergs, P. C., Finnie, J. W., Jones, N. R., McLean, A. J., "Mechanisms of Axonal Injury: an Experimental and Numerical Study of Sheep Model of Head Impact," Proc. Proc., Int. Conf. on the Biomechanics of Impact, pp. 107-120.

[143] Shreiber, D. I., Bain, A. C., and Meaney, D. F., "In vivo thresholds for mechanical injury to the blood-brain barrier," Proc. Proceedings of the 1997 41st Stapp Car Crash Conference, November 13, 1997 - November 14, 1997, SAE, pp. 277-291.

[144] Kleiven, S., "Biomechanics and thresholds for MTBI in humans," Proc. MTBI Pre-Congress Symposium IBIA CONGRESS.

[145] Willinger, R., Diaw, B. M., Baumgartner, D., and Chinn, B., 2002, "Full face protective helmet modelling and coupling with a Human head model," International Journal of Crashworthiness, 7(2), pp. 167-178.

[146] Pinnoji, P. K., Mahajan, P., Bourdet, N., Deck, C., and Willinger, R., 2010, "Impact dynamics of metal foam shells for motorcycle helmets: Experiments & numerical modeling," International Journal of Impact Engineering, 37(3), pp. 274-284.

[147] Warden, D., 2006, "Military TBI during the Iraq and Afghanistan wars," J. Head Trauma Rehabil., 21(5), pp. 398-402.

[148] Elder, G. A., and Cristian, A., 2009, "Blast-Related Mild Traumatic Brain Injury: Mechanisms of Injury and Impact on Clinical Care," Mount Sinai Journal of Medicine, 76(2), pp. 111-118.

[149] Abdul-Wahab, R., Swietek, B., Mina, S., Sampath, S., Santhakumar, V., and Pfister, B. J., "Precisely controllable traumatic brain injury devices for rodent models," Proc. Bioengineering Conference (NEBEC), 2011 IEEE 37th Annual Northeast, pp. 1-2.

[150] Alley, M. D., Schimizze, B. R., and Son, S. F., 2011, "Experimental modeling of explosive blast-related traumatic brain injuries," NeuroImage, 54(Supplement 1), pp. S45-S54.

[151] Bolander, R., Mathie, B., Bir, C., Ritzel, D., and VandeVord, P., 2011, "Skull Flexure as a Contributing Factor in the Mechanism of Injury in the Rat when Exposed to a Shock Wave," Annals of Biomedical Engineering, pp. 1-10.

[152] Cernak, I., Wang, Z., Jiang, J., Bian, X., and Savic, J., 2001, "Cognitive deficits following blast injury-induced neurotrauma: possible involvement of nitric oxide," Brain Injury, 15(7), pp. 593-612.

[153] Chavko, M., Koller, W. A., Prusaczyk, W. K., and McCarron, R. M., 2007, "Measurement of blast wave by a miniature fiber optic pressure transducer in the rat brain," Journal of Neuroscience Methods, 159(2), pp. 277-281.

[154] Cheng, J., Gu, J., Ma, Y., Yang, T., Kuang, Y., Li, B., and Kang, J., 2010, "Development of a rat model for studying blast-induced traumatic brain injury," Journal of the Neurological Sciences, 294(1-2), pp. 23-28.

[155] Desmoulin, G. T., and Dionne, J. P., 2009, "Blast-Induced Neurotrauma: Surrogate Use, Loading Mechanisms, and Cellular Responses," The Journal of Trauma, 67(5), pp. 1113-1122 1110.1097/TA.1110b1013e3181bb1118e1184.

[156] Ganpule, S., Gu, L., Alai, A., and Chandra, N., 2011, "Role of helmet in the mechanics of shock wave propagation under blast loading conditions," Computer Methods in Biomechanics and Biomedical Engineering, pp. 1-12.

[157] Long, J. B., Bentley, T. L., Wessner, K. A., Cerone, C., Sweeney, S., and Bauman, R. A., 2009, "Blast Overpressure in Rats: Recreating a Battlefield Injury in the Laboratory," Journal of Neurotrauma, 26(6), pp. 827-840.

[158] Rafaels, K., 2010, "Blast brain injury risk, PhD dissertation," Ph.D., University of Virginia.

[159] Saljo, A., Bolouri, H., Mayorga, M., Svensson, B., and Hamberger, A., 2010, "Low-Level Blast Raises Intracranial Pressure and Impairs Cognitive Function in Rats: Prophylaxis with Processed Cereal Feed," Journal of Neurotrauma, 27(2), pp. 383-389.

[160] Säljö, A., Mayorga, M., Bolouri, H., Svensson, B., and Hamberger, A., 2011, "Mechanisms and pathophysiology of the low-level blast brain injury in animal models," NeuroImage, 54(Supplement 1), pp. S83-S88.

[161] Duff, R. E., and Blackwell, A. N., 1966, "Explosive Driven Shock Tubes," Review of Scientific Instruments, 37(5), pp. 579-586.

[162] Courtney, A. C., Andrusiv, L., P, and Courtney, M. W., 2012, "Oxy-acetylene driven laboratory scale shock tubes for studying blast wave effects," Rev. Sci. Instrum., 83(4).

[163] Bleakney, W., and Taub, A. H., 1949, "Interaction of shock waves," Reviews of Modern Physics, 21(4), pp. 584-605.

[164] Baker, W. E., 1973, Explosions in air, University of Texas Press, Austin, TX.

[165] Arakeri, J. H., Das, D., Krothapalli, A., and Lourenco, L., 2004, "Vortex ring formation at the open end of a shock tube: A particle image velocimetry study," Physics of Fluids, 16(4), pp. 1008-1019.

[166] Honma, H., Ishihara, M., Yoshimura, T., Maeno, K., and Morioka, T., 2003, "Interferometric CT measurement of three-dimensional flow phenomena on shock waves and vortices discharged from open ends," Shock Waves, 13(3), pp. 179-190.

[167] Jiang, Z., Onodera, O., and Takayama, K., 1999, "Evolution of shock waves and the primary vortex loop discharged from a square cross-sectional tube," Shock Waves, 9(1), pp. 1-10.

[168] Jiang, Z., Wang, C., Miura, Y., and Takayama, K., 2003, "Three-dimensional propagation of the transmitted shock wave in a square cross-sectional chamber," Shock Waves, 13(2), pp. 103-111.

[169] Kashimura, H., Yasunobu, T., Nakayama, H., Setoguchi, T., and Matsuo, K., 2000, "Discharge of a shock wave from an open end of a tube," Journal of Thermal Science, 9(1), pp. 30-36.

[170] Onodera, O., Jiang, Z. L., and Takayama, K., 1998, "Holographic interferometric observation of shock waves discharged from an open-end of a square cross-sectional shock tube," Jsme International Journal Series B-Fluids and Thermal Engineering, 41(2), pp. 408-415.

[171] Setoguchi, T., Matsuo, K., Hidaka, F., and Kaneko, K., "Impulsive noise induced by a weak shock wave discharged from an open end of a tube: Acoustic characteristics and its passive control," Proc. Proceedings of the 1993 ASME Winter Meeting, November 28, 1993 - December 3, 1993, Publ by ASME, pp. 57-64.

[172] Chandra, N., Holmberg, A., and Feng, R., 2011, "Controlling the shape of the shock wave profile in a blast facility, U.S. Provisional patent application no. 61542354."

[173] Kleinschmit, N. N., 2011, "A shock tube technique for blast wave simulation and studies of flow structure interactions in shock tube blast experiments,"Master's thesis, University of Nebraska-Lincoln, Lincoln.

[174] Jiang, Z., Takayama, K., and Skews, B. W., 1998, "Numerical study on blast flowfields induced by supersonic projectiles discharged from shock tubes," Physics of Fluids, 10(1), pp. 277-288.

[175] Zhu, F., Wagner, C., Dal Cengio Leonardi, A., Jin, X., VandeVord, P., Chou, C., Yang, K., and King, A., 2012, "Using a gel/plastic surrogate to study the biomechanical response of the head under air shock loading: a combined experimental and numerical investigation," Biomechanics and Modeling in Mechanobiology, 11(3-4), pp. 341-353.

[176] 2009, "The Visible Human Project, National Library of Medicine."

[177] Bourdin, X., Beillas, P., Petit, P., and Troseille, X., "Comparison Of Tetrahedral And Hexahedral Meshes For Human Finite Element Modelling: An Application To Kidney Impact," Proc. In: 20th Enhanced Safety of Vehicles Conference: Innovations for safety: opportunities and challenges.

[178] Baker, T. J., 2005, "Mesh generation: Art or science?," Progress in Aerospace Sciences, 41(1), pp. 29-63.

[179] Schneiders, R., "Algorithms for quadrilateral and hexahedral mesh generation," Proc. In Proceedings of the VKI Lecture Series on Computational Fluid Cynamics.

[180] Wieding, J., Souffrant, R., Fritsche, A., Mittelmeier, W., and Bader, R., 2012, "Finite Element Analysis of Osteosynthesis Screw Fixation in the Bone Stock: An Appropriate Method for Automatic Screw Modelling," PLoS ONE, 7(3), p. e33776.

[181] Cifuentes, A. O., and Kalbag, A., 1992, "A performance study of tetrahedral and hexahedral elements in 3-D finite element structural analysis," Finite Elements in Analysis and Design, 12(3–4), pp. 313-318.

[182] Ramos, A., and Simões, J. A., 2006, "Tetrahedral versus hexahedral finite elements in numerical modelling of the proximal femur," Medical Engineering & Physics, 28(9), pp. 916-924.

[183] Chen, Y., and Ostoja-Starzewski, M., 2010, "MRI-based finite element modeling of head trauma: spherically focusing shear waves," Acta Mechanica, 213(1-2), pp. 155-167.

[184] Moss, W. C., King, M. J., and Blackman, E. G., 2009, "Skull Flexure from Blast Waves: A Mechanism for Brain Injury with Implications for Helmet Design," Physical Review Letters, 103(10), p. 108702.

[185] "Humanetics - 575-1000, Humanetics Innovative Solutions, Plymouth MI."

[186] Kennedy, E. A., 2007, "The development and validation of a biofidelic synthetic eye for the facial and ocular countermeasure safety (FOCUS) headform,"PhD dissertation, Virginia Polytechnic Institute and State University, Blacksburg, Virginia.

[187] Hossain, S. G. M., 2010, "Material modeling and analysis for the development of a realistic blast headform,"Master's thesis, University of Nebraska - Lincoln, Lincoln, NE.

[188] Tanielian, T., and Jaycox, L. H., 2008, Invisible Wounds of War, RAND Corp, Santa Monica, CA.

[189] 2012, "http://www.health.mil/Research/TBI_Numbers/TBI_Numbers_Totals.aspx."

[190] Pun, P. B., Kan, E. M., Salim, A., Li, Z., Ng, K. C., Moochhala, S. M., Ling, E. A., Tan, M. H., and Lu, J., 2011, "Low level primary blast injury in rodent brain," Frontiers in neurology, 2:19.

[191] Rafaels, K., Bass, C. R., Salzar, R. S., Panzer, M. B., Woods, W., Feldman, S., Cummings, T., and Capehart, B., 2011, "Survival Risk Assessment for Primary Blast Exposures to the Head," Journal of Neurotrauma, 28(11), pp. 2319-2328.

[192] Rafaels, K. A., 2010, "Blast Brain Injury Risk,"PhD dissertation, University of Virginia.

[193] Risling, M., Plantman, S., Angeria, M., Rostami, E., Bellander, B. M., Kirkegaard, M., Arborelius, U., and Davidsson, J., 2011, "Mechanisms of blast induced brain injuries, experimental studies in rats," Neuroimage, 54, pp. S89-S97.

[194] Saljo, A., Arrhen, F., Bolouri, H., Mayorga, M., and Hamberger, A., 2008, "Neuropathology and Pressure in the Pig Brain Resulting from Low-Impulse Noise Exposure," Journal of Neurotrauma, 25(12), pp. 1397-1406.

[195] Svetlov, S. I., Prima, V., Kirk, D. R., Gutierrez, H., Curley, K. C., Hayes, R. L., and Wang, K. K. W., 2010, "Morphologic and Biochemical Characterization of Brain Injury in a Model of Controlled Blast Overpressure Exposure," The Journal of Trauma, 69(4), pp. 795-804 710.1097/TA.1090b1013e3181bbd1885.

[196] Lew, H. L., Poole, J. H., Alvarez, S., and Moore, W., 2005, "Soldiers with Occult Traumatic Brain Injury," American Journal of Physical Medicine & Rehabilitation, 84(6), pp. 393-398 310.1097/1001.phm.0000163703.0000191647.a0000163707.

[197] Xydakis, M. S., Bebarta, V. S., Harrison, C. D., Conner, J. C., Grant, G. A., and Robbins, A. S., 2007, "Tympanic-Membrane Perforation as a Marker of Concussive Brain Injury in Iraq," N. Engl. J. Med., 357(8), pp. 830-831.

[198] Gennarelli, T. A., Thibault, L. E., Adams, J. H., Graham, D. I., Thompson, C. J., and Marcincin, R. P., 1982, "Diffuse axonal injury and traumatic coma in the primate," Ann Neurol, 12(6), pp. 564-574.

[199] Kleiven, S., 2005, "Influence of direction and duration of impacts to the human head evaluated using the finite element method," International Research Council on the Biomechanics of Impact - 2005 International IRCOBI Conference on the Biomechanics of Impact Prague, Czech Republic pp. 41-57.

[200] Zhou, C., Khalil, T., and King, A., 1995, "A New Model Comparing Impact Responses of the Homogeneous and Inhomogeneous Human Brain," 39th Stapp Car Crash Conference, SAE Technical Paper 952714, pp. 121-137.

[201] Chavko, M., Watanabe, T., Adeeb, S., Lankasky, J., Ahlers, S. T., and McCarron, R. M., 2010, "Relationship between orientation to a blast and pressure wave propagation inside the rat brain," Journal of Neuroscience Methods, 195(1), pp. 61-66.

[202] Zhang, L., and Makwana, R., 2011, "Comparison of the Head Response in Blast Insult with and without Combat Helmet," RTO Human Factors and Medicine Panel (HFM) Symposium Halifax, Canada

[203] Reynosa, M. A., 1999, The Personnel Armor System Ground Troops (PASGT) helmet, Atglen (PA): Schiffer Military History.

[204] 2012, "Archived Content. Ministry of Defence.," http://webarchive.nationalarchives.gov.uk/+/http://www.mod.uk/DefenceInternet/DefenceNews/EquipmentAndLogistics/NewHelmetsAndArmourForTroopsInAfghanistan.htm.

[205] Aare, M., and Kleiven, S., 2007, "Evaluation of head response to ballistic helmet impacts using the finite element method," International Journal of Impact Engineering, 34(3), pp. 596-608.

[206] Anderson, J., 2001, Fundamentals of aerodynamics, McGraw-Hill, New York.

[207] Bolander, R., Mathie, B., Bir, C., Ritzel, D., and Vandevord, P., 2011, "Skull Flexure as a Contributing Factor in the Mechanism of Injury in the Rat when Exposed to a Shock Wave," Annals of Biomedical Engineering, 39(10), pp. 2550-2559.

[208] Wang, Y., Wei, Y. L., Oguntayo, S., Wilkins, W., Arun, P., Valiyaveettil, M., Song, J., Long, J. B., and Nambiar, M. P., 2011, "Tightly Coupled Repetitive Blast-Induced Traumatic Brain Injury: Development and Characterization in Mice," Journal of Neurotrauma, 28(10), pp. 2171-2183.

[209] Chavko, M., Watanabe, T., Adeeb, S., Lankasky, J., Ahlers, S. T., and McCarron, R. M., 2011, "Relationship between orientation to a blast and pressure wave propagation inside the rat brain," Journal of Neuroscience Methods, 195(1), pp. 61-66.

[210] Risling, M., Plantman, S., Angeria, M., Rostami, E., Bellander, B. M., Kirkegaard, M., Arborelius, U., and Davidsson, J., 2011, "Mechanisms of blast induced brain injuries, experimental studies in rats," NeuroImage, 54 Suppl 1, pp. S89-97.

[211] Cernak, I., Merkle, A. C., Koliatsos, V. E., Bilik, J. M., Luong, Q. T., Mahota, T. M., Xu, L., Slack, N., Windle, D., and Ahmed, F. A., 2011, "The pathobiology of blast injuries and blast-induced neurotrauma as identified using a new experimental model of injury in mice," Neurobiology of Disease, 41(2), pp. 538-551.

[212] Vandevord, P. J., Bolander, R., Sajja, V. S., Hay, K., and Bir, C. A., 2012, "Mild neurotrauma indicates a range-specific pressure response to low level shock wave exposure," Ann Biomed Eng, 40(1), pp. 227-236.

[213] Koliatsos, V. E., Cernak, I., Xu, L., Song, Y., Savonenko, A., Crain, B. J., Eberhart, C. G., Frangakis, C. E., Melnikova, T., Kim, H., and Lee, D., 2011, "A mouse model of blast injury to brain: initial pathological, neuropathological, and behavioral characterization," J Neuropathol Exp Neurol, 70(5), pp. 399-416.

[214] Svetlov, S. I., Prima, V., Glushakova, O., Svetlov, A., Kirk, D. R., Gutierrez, H., Serebruany, V. L., Curley, K. C., Wang, K. K., and Hayes, R. L., 2012, "Neuro-glial and systemic mechanisms of pathological responses in rat models of primary blast overpressure compared to "composite" blast," Front Neurol, 3, p. 15.

[215] Garman, R. H., Jenkins, L. W., Switzer, R. C., 3rd, Bauman, R. A., Tong, L. C., Swauger, P. V., Parks, S. A., Ritzel, D. V., Dixon, C. E., Clark, R. S., Bayir, H., Kagan, V., Jackson, E. K., and Kochanek, P. M., 2011, "Blast exposure in rats with body shielding is characterized primarily by diffuse axonal injury," J Neurotrauma, 28(6), pp. 947-959.

[216] Abdul-Muneer, P. M., Schuetz, H., Wang, F., Skotak, M., Jones, J., Gorantla, S., Zimmerman, M. C., Chandra, N., and Haorah, J., 2013, "Induction of Oxidative and Nitrosative damage leads to Cerebrovascular Inflammation in Animal Model of Mild Traumatic Brain Injury Induced by Primary Blast," Free Radic Biol Med.

[217] Skotak, M., Wang, F., Alai, A., Holmberg, A., Harris, S., Switzer Iii, R. C., and Chandra, N., 2013, "Rat injury model under controlled field-relevant primary blast conditions: Acute response to a wide range of peak overpressures," J Neurotrauma.

[218] Readnower, R. D., Chavko, M., Adeeb, S., Conroy, M. D., Pauly, J. R., McCarron, R. M., and Sullivan, P. G., 2010, "Increase in Blood-Brain Barrier Permeability, Oxidative Stress, and Activated Microglia in a Rat Model of Blast-Induced Traumatic Brain Injury," Journal of Neuroscience Research, 88(16), pp. 3530-3539.

[219] Gottsauner-Wolf, F., Grabowski, J. J., Chao, E. Y. S., and An, K.-N., 1995, "Effects of freeze/thaw conditioning on the tensile properties and failure mode of bone-muscle-bone units: A biomechanical and histological study in dogs," Journal of Orthopaedic Research, 13(1), pp. 90-95.

[220] Cernak, I., 2005, "Animal Models of Head Trauma," NeuroRX, 2(3), pp. 410-422.

[221] Elder, G. A., and Cristian, A., 2009, "Blast-related mild traumatic brain injury: mechanisms of injury and impact on clinical care," Mount Sinai Journal of Medicine: A Journal of Translational and Personalized Medicine, 76(2), pp. 111-118.

[222] Nakagawa, A., Manley, G. T., Gean, A. D., Ohtani, K., Armonda, R., Tsukamoto, A., Yamamoto, H., Takayama, K., and Tominaga, T., 2011, "Mechanisms of Primary Blast-Induced Traumatic Brain Injury: Insights from Shock-Wave Research," Journal of Neurotrauma, 28(6), pp. 1101-1119.

[223] Moss, W. C., King, M. J., and Blackman, E. G., 2011, "Distinguishing realistic military blasts from firecrackers in mitigation studies of blast-induced traumatic brain

injury," Proceedings of the National Academy of Sciences of the United States of America, 108(17), pp. E82-E82.

[224] Chandra, N., Ganpule, S., Kleinschmit, N. N., Feng, R., Holmberg, A. D., Sundaramurthy, A., Selvan, V., and Alai, A., 2012, "Evolution of blast wave profiles in simulated air blasts: experiment and computational modeling," Shock Waves, 22(5), pp. 403-415.

[225] Sundaramurthy, A., Alai, A., Ganpule, S., Holmberg, A., Plougonven, E., and Chandra, N., 2012, "Blast-induced biomechanical loading of the rat: experimental and anatomically accurate computational blast injury model " Journal of Neurotrauma, 29(13), pp. 2352-2364.

[226] National Academies and the Department of Homeland Security, "IED Attack Improvised Explosive Devices, A fact sheet from the National Academies and the Department of Homeland Security."

[227] Sullivan, J. P., Bunker, R. J., and Lorelli, E. J., 2002, Jane's Unconventional Weapons Response Handbook, Jane’s Information Group, Alexandria, VA.

[228] Ripley, R. C., Lien, F. S., and Yovanovich, M. M., 2006, "Numerical simulation of shock diffraction on unstructured meshes," Computers & Fluids, 35(10), pp. 1420-1431.

[229] Ofengeim, D. K., and Drikakis, D., 1997, "Simulation of blast wave propagation over a cylinder," Shock Waves, 7(5), pp. 305-317.

[230] Gonor, A. L., Gottlieb, J. J., and Hooton, I., 2004, "Shock wave diffraction over wedges, cylinders, and spheres in gases, liquids, and condensed matter," J. Appl. Phys., 95(3), pp. 1577-1585.

[231] Skotak, M., Wang, F., Alai, A., Holmberg, A., Harris, S., Switzer, R., and Chandra, N., ahead of print, "Rat injury model under controlled field-relevant primary blast conditions: Acute response to a wide range of peak overpressures " Journal of Neurotrauma.

[232] King, A. I., 2000, "Fundamentals of impact biomechanics: Part I--Biomechanics of the head, neck, and thorax," Annu Rev Biomed Eng.(2), pp. 55-81.

[233] Ruan, J. S., Khalil, T., and King, A. I., 1991, "Human head dynamic-response to side impact by finite-element modeling," Journal of Biomechanical Engineering-Transactions of the Asme, 113(3), pp. 276-283.

[234] Takhounts, E. G., Ridella, S. A., Hasija, V., Tannous, R. E., Campbell, J. Q., Malone, D., Danelson, K., Stitzel, J., Rowson, S., and Duma, S., 2008, "Investigation of Traumatic Brain Injuries Using the Next Generation of Simulated Injury Monitor (SIMon) Finite Element Head Model," Stapp Car Crash Journal, 52, pp. 1-31.

[235] Clarke, B., 2008, "Normal bone anatomy and physiology," Clin J Am Soc Nephrol, 3 Suppl 3, pp. S131-139.

[236] Kanitakis, J., 2002, "Anatomy, histology and immunohistochemistry of normal human skin," Eur J Dermatol, 12(4), pp. 390-399.

[237] McElhaney, J. H., Fogle, J. L., Melvin, J. W., Haynes, R. R., Roberts, V. L., and Alem, N. M., 1970, "Mechanical properties of cranial bone," Journal of Biomechanics, 3(5), pp. 495-511.

[238] Goel, R., Vechart, A., Schimizze, B., Christou, G., Jérusalem, A., Young, L. R., and Son, S., "Design of an Advanced Helmet Liner to Reduce TBI: The Case for

Simulations " Proc. Proceedings of the IMPLAST 2010 Conference, Society for Experimental Mechanics.

[239] Grujicic, A., LaBerge, M., Grujicic, M., Pandurangan, B., Runt, J., Tarter, J., and Dillon, G., 2012, "Potential Improvements in Shock-Mitigation Efficacy of a Polyurea-Augmented Advanced Combat Helmet," Journal of Materials Engineering and Performance, 21(8), pp. 1562-1579.

[240] Grujicic, M., d'Entremont, B. P., Pandurangan, B., Runt, J., Tarter, J., and Dillon, G., 2012, "Concept-Level Analysis and Design of Polyurea for Enhanced Blast-Mitigation Performance," Journal of Materials Engineering and Performance, 21(10), pp. 2024-2037.

[241] Nesterenko, V. F., "Shock (blast) mitigation by" soft" condensed matter," Proc. MATERIALS RESEARCH SOCIETY SYMPOSIUM PROCEEDINGS, Cambridge Univ Press, pp. 135-146.

[242] Petel, O. E., Jetté, F. X., Goroshin, S., Frost, D. L., and Ouellet, S., 2011, "Blast wave attenuation through a composite of varying layer distribution," Shock Waves, 21(3), pp. 215-224.

[243] Cernak, I., Savic, J., and Lazarov, J., 1997, "Relations among plasma prolactin, testosterone, and injury severity in war casualties," World Journal of Surgery, 21(3), pp. 240-246.

[244] Goeller, J., Wardlaw, A., Treichler, D., O'Bruba, J., and Weiss, G., 2012, "Investigation of cavitation as a possible damage mechanism in blast-induced traumatic brain injury," J Neurotrauma, 29(10), pp. 1970-1981.

[245] SAE, 2011, "Human Tolerance to Impact Conditions as Related to Motor Vehicle Design (STABILIZED Feb 2011). SAEJ885 ".

[246] Kane, M. J., Angoa-Pérez, M., Francescutti, D. M., Sykes, C. E., Briggs, D. I., Leung, L. Y., VandeVord, P. J., and Kuhn, D. M., 2012, "Altered gene expression in cultured microglia in response to simulated blast overpressure: Possible role of pulse duration," Neuroscience Letters, 522(1), pp. 47-51.

[247] Baumgartner, D., 2001, "Mécanismes de lésion et limites de tolérance au choc de la tête humaine – Reconstruction numérique et expérimentale de traumatismes crâniens," Ph.D. Dissertation. Université Louis Pasteur Strasbourg.

[248] Anderson, R. W., Brown, C. J., Blumbergs, P. C., McLean, A. J., and Jones, N. R., 2003, "Impact mechanics and axonal injury in a sheep model," J Neurotrauma, 20(10), pp. 961-974.

[249] Marjoux, D., Baumgartner, D., Deck, C., and Willinger, R., 2008, "Head injury prediction capability of the HIC, HIP, SIMon and ULP criteria," Accident Analysis & Prevention, 40(3), pp. 1135-1148.

[250] Ganpule, S., Gu, L., Alai, A., and Chandra, N., 2012, "Role of helmet in the mechanics of shock wave propagation under blast loading conditions," Computer Methods in Biomechanics and Biomedical Engineering, 15(11), pp. 1233-1244.

[251] Ganpule, S., Gu, L., and Chandra, N., 2010, "Modeling shock response of helmeted head using fluid structure interaction," 16th US National Congress of Theoretical and Applied MechanicsJune 27 - July 2, 2010, State College, Pennsylvania.

APPENDIX

Comparison of flow fields obtained by modeling the entire shock tube (technique (a)) vs. modeling partial shock tube with measured pressure boundary condition as a input (technique (b)):

One of the important aspects of studying head response under blast loading conditions is to accurately simulate the shock wave dynamics. Technique (a) is computationally prohibitive in terms of memory and CPU time. However, before using technique (b) it is necessary to verify that this modeling approach is capable of capturing the pressure/impulse/momentum boundary conditions corresponding to the physics of the problem. Towards this end, field variables obtained from technique (b) are compared with technique (a) (i.e. full scale model where events of burst and expansion are explicitly modeled) as shown in Figure A1. As seen in the figure, the agreement between field variables is good. Thus potential (in the form of pressures), kinetic (in the form of velocities) and thermal (in the form of temperatures) energy components associated with the flow are represented correctly in technique (b).

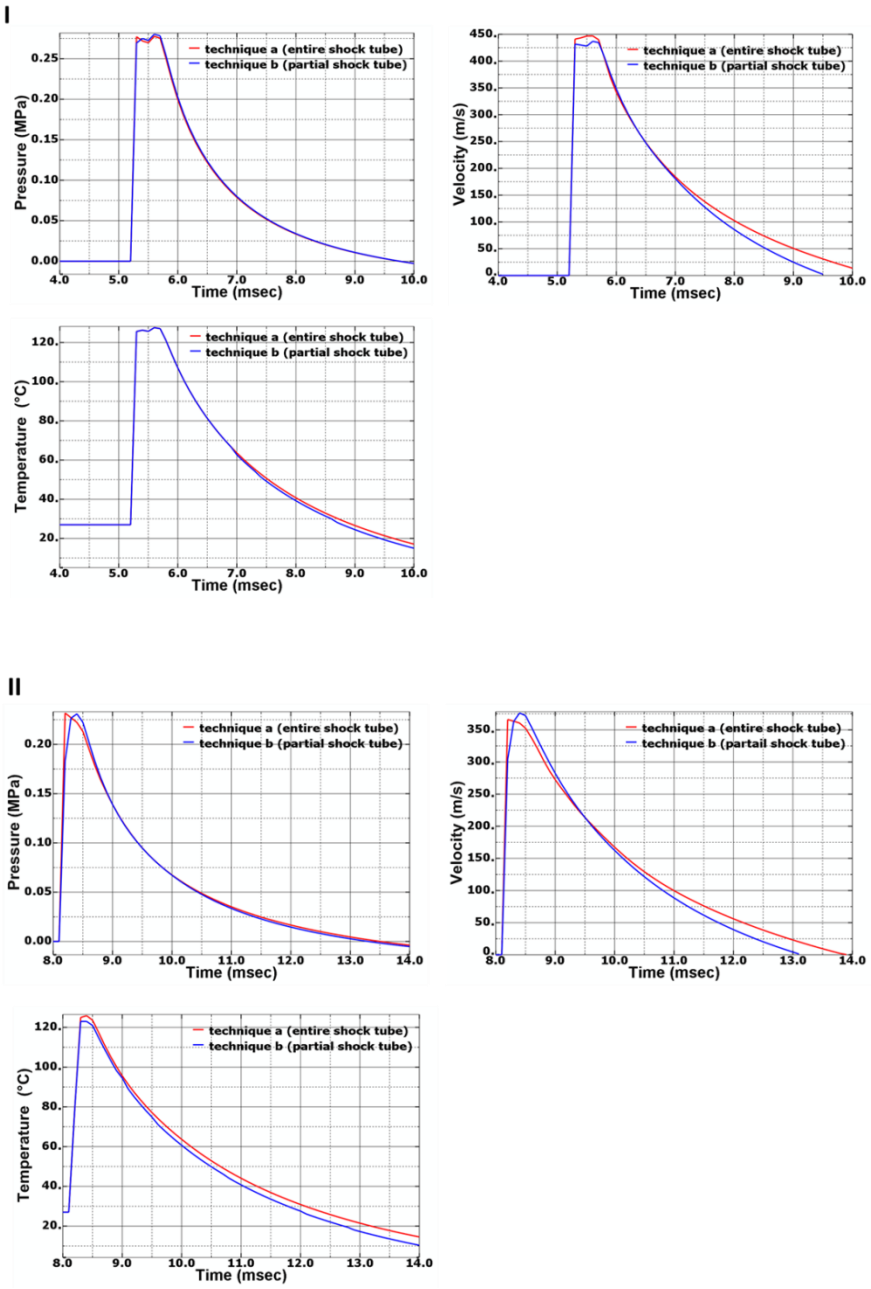

Figure A1: Comparison of pressure, velocity and temperature profiles with modeling technique (a) (i.e. entire shock tube) vs. modeling technique (b) (i.e. partial shock tube with pressure boundary condition as input). (I) shows profiles at truncation location (II) shows profiles at downstream location.